Gesellschaft für Mikroelektronik

The Society for Microelectronics

Annual Report

2000

Vienna, October 2001

Gesellschaft für Mikroelektronik

The Society for Microelectronics

Annual Report

2000

Gesellschaft für Mikroelektronik
c/o Technische Universität Wien
Institut für Industrielle Elektronik und Materialwissenschaften
Gußhausstraße 27-29/366, A-1040 Wien

Vienna, October 2001

Editor: Karl Riedling

Layout: Claudia Benedela
Karl Riedling

c/o Technische Universität Wien
Institut für Industrielle Elektronik und Materialwissenschaften
Gußhausstraße 27-29/366, A-1040 Wien

The Society for Microelectronics (GMe — Gesellschaft für Mikroelektronik)

G. Bauer, K. Riedling

Gesellschaft für Mikroelektronik,
c/o Institut für Industrielle Elektronik und Materialwissenschaften,
TU Wien
Gußhausstraße 27 – 29, A-1040 Wien

1. Goals of the Society for Microelectronics

The Society for Microelectronics (GMe) was founded in 1985 with the aim to "*support microelectronics technology and its applications*" in Austria. The GMe defines its tasks as follows:

- Support of university-based "high-tech" research in the areas of microelectronics, semiconductor technology, sensors, and opto-electronics;
- Operation of research facilities;
- Support and consulting for industry, in particular, for small and medium enterprises, within the area of microelectronics.

The central task of the GMe is to provide an internationally competitive *infra-structure* in the area of microelectronics technology. The GMe allocates funds to maintain research projects in the fields of semiconductor technology, sensors, opto-electronics, and ASIC design. Thus the infra-structure support generates a base for research projects that are funded by other funding agencies.

2. Activities of the Society

The present focal point activities of the GMe are:

- Operation of university-based laboratories for microelectronics technology;
- Design of application specific integrated circuits (ASICs) —TMOe.

The GMe currently supports mainly the first focal point activity but also coordinates the Austria-wide activities of the TMOe program.

The main task of the GMe in the area of microelectronics technology is the operation of the cleanroom laboratories in Vienna and Linz. The GMe has coordinated the construction of the Microstructure Center (MISZ — Mikrostrukturzentrum) in Vienna; the funds were supplied by the Austrian Federal Ministry of Science and Research. The GMe now finances a significant part of the operation costs for the cleanroom laboratories in Vienna and Linz.

2.1 Microelectronics Technology — Cleanroom Vienna

The following university institutes receive support within this focal point activity:

- TU Wien:
  - Institut für Festkörperelektronik
  - Institut für Industrielle Elektronik und Materialwissenschaften

2.2 Microelectronics Technology — Cleanroom Linz

The following university institutes receive support within this focal point activity:

- Johannes Kepler Universität Linz:
  - Institut für Halbleiter- und Festkörperphysik
  - Institut für Mikroelektronik

3. Other Activities of the Society

In 2000, the GMe prepared its biennial seminar which took place at the Vienna University of Technology on April 5 and 6, 2001 under the title "*GMe Forum 2001*". The seminar presented twelve invited lectures given by international experts, and 37 oral and poster contributions which resulted from work supported by the GMe. Great emphasis was put into making the seminar more attractive to an industrial audience, thus contributing to an improved knowledge transfer between universities and industry.

One of the declared tasks of the GMe is to provide information on current Austrian academic activities in the field of microelectronics to industry, in particular to Austrian small- and medium enterprises (SMEs). To enhance the distribution of the results of the research work done with GMe support, the GMe has put the contents of its annual reports — 1995 through 2000 — and the proceedings of the latest seminars organized by the GMe in 1999 and 2001 on its Web server. In late 2000, a new GMe Web server has been introduced. This server now provides a variety of search facilities into the reports, thus acting as a Microelectronics Knowledge Base. The server has apparently been fairly well accepted by the international community. Access statistics show an average of 72 requests per day; an amazingly large percentage of the accesses to the GMe server — about two thirds — originates from net domains outside Austria. The new GMe Web server is available under the address:

http://gme.tuwien.ac.at/

4. The Annual Report for 2000 of the Society for Microelectronics

The GMe is currently supporting the microelectronics technology activities of the cleanroom laboratories in Vienna and Linz. All projects described in this report were carried out in the cleanrooms in Vienna and Linz, respectively. They are *not* specific projects of the GMe but were funded by a variety of other sources. They all have in common that they use the infra-structure provided by the GMe. It would therefore not have been possible to carry out these projects without the support by the GMe.

Contents

Microelectronics Technology — Cleanroom Vienna

Cleanroom Vienna

G. Strasser

**Mikrostrukturzentrum der Technischen Universität Wien,
Floragasse 7, A-1040 Vienna, Austria**

This report intends to review the main activities of the MISZ TU Wien (Mikrostrukturzentrum der Technischen Universität Wien) in the year 2000. In the cleanroom facility available technologies for the production of optoelectronic and microelectronic prototype devices include state of the art growth of III-V nanostructures, standard contact lithography, the production of patterned masks to be used in standard lithography, various structuring techniques like dry etching and plasma enhanced chemical vapor deposition, electron beam writing, focused ion beam etching and depositing, and. different metallization techniques. State of the art silicon processing started 1998 and will need further activities to mature. A variety of device characterization techniques like transport measurements, spectroscopic techniques for optoelectronic devices and surface probing like scanning tunneling microscopy are available. An atomic force microscopy system with the possibility to probe capacitance locally was brought into the cleanroom in the year 2000. In this report, a short description of research projects with a high need of technological input, using the equipment in the cleanroom and the cleanroom environment is given.

The following reports represent the main research efforts of the solid state electronics institute (Festkörperelektronik TU Wien) within the last twelve months. All the projects described below like transport studies in low dimensional semiconductor nanostructures, scanning probe spectroscopy, realization of new and improved optoelectronic devices, quantum cascade lasers, THz sources, and the characterization of microelectronic devices, take full advantage of the technologies installed in the cleanroom of the MISZ (Reinraum Mikrostrukturzentrum der TU Wien).

To satisfy this variety of topics, state of the art growth of semiconductor nanostructures (molecular beam epitaxy) is needed as well as a complete process line including structure definition (lithography), structure transfer (reactive ion etching, focussed ion beam etching, ion milling, wet chemical etching techniques) and coating with metals and/or dielectrics (plasma-enhanced chemical vapor deposition, sputtering, electron gun evaporation, focussed ion beam deposition). All the equipment necessary for the above mentioned technologies needs the cleanroom environment (cooling, filtered air, constant temperature and humidity, high quality water, different inert gases) as well as periodic maintenance of the equipment and the cleanroom itself, e.g. pumping systems (rotary pumps, turbo pumps), exhaust filtering, liquid nitrogen, and cleaning and repair. Testing of the cleanroom quality and adjustment (laminar airflow, filters, cooling, humidity, and temperature) is done periodically.

In addition to the above mentioned technologies further equipment was installed in the cleanroom in 2000. The installations include an extended compressed air system, new or totally refurbished rotary pumps for the plasma enhanced CVD and the reactive ion etching system, exchanged turbo pumping systems for the metallization units, and an extension of the liquid nitrogen supply.

From the scientific point of view a new technique to explore surface morphology as well as local carrier concentrations was installed. This is done with a conventional Atomic Force Microscope (AFM) in combination with a Scanning Capacitance Microscopy (SCM) extension. A detailed description of this new equipment as well as the additional technological possibilities is given in the following.

The main research activities making use of the cleanroom itself or using samples grown, structured and tested in the MISZ are described. These activities are not the only projects running in the MISZ, but are intended to show a representative overview of the basic research as well as applied projects which need the cleanroom infrastructure. For a more general overview the listed projects and the attached publication list may give more insides on the broad range of activities in our facility.

Project Information

Project Manager

ao.Univ.Prof. Dr. G. Strasser

Reinraum MISZ TU Wien, Floragasse 7, A-1040 Wien

Project Group

Last Name	First Name	Status	Remarks
Basnar	Bernhard	postdoc	
Bertagnolli	Emmerich	o. prof.	
Boxleitner	Winfried	postdoc	
Bratschitsch	Rudolf	dissertation	
Coquelin	Michael	student	
Dzigal	Elvira	technician	
Fasching	Gernot	student	
Fehlmann	Gerhard	student	
Finger	Norman	dissertation	
Fischler	Wolfgang	dissertation	
Fürböck	Christoph	dissertation	
Gianordoli	Stefan	dissertation	
Golka	Sebastian	student	
Gornik	Erich	o. prof.	
Harasek	Stefan	dissertation	
Heer	Rudolf	dissertation	
Hirner	Heimo	student	
Hobler	Gerhard	ao. prof.	
Hofer	Stefan	dissertation	
Hvozdara	Lubos	dissertation	
Kamvar	Parvis	student	
Kast	Michael	dissertation	
Kellermann	Peer	dissertation	
Kröll	Peter	technician	
Langfischer	Helmut	dissertation	GMe
Litzenberger	Martin	dissertation	
Lugstein	Alois	univ. ass.	

Last Name	First Name	Status	Remarks
Maier	Harald	student	
Maier	Thomas	dissertation	GMe
Müller	Thomas	dissertation	
Pacher	Christoph	dissertation	
Patz	Sybille	student	
Ploner	Guido	postdoc	
Pogany	Dionyz	univ. ass.	
Prinzinger	Johannes	technician	
Rakoczy	Doris	dissertation	
Riegler	Erich	technician	
Schinnerl	Markus	technician	
Schenold	Helmut	technician	
Schrenk	Werner	dissertation	
Smoliner	Jürgen	ao. prof.	
Strasser	Gottfried	univ. ass.	
Ulrich	Jochen	dissertation	
Unterrainer	Karl	ao. prof.	
Wanzenböck	Heinz	univ. ass.	
Zobl	Reinhard	dissertation	

Books and Contributions to Books

1. J.Smoliner, G.Ploner, Electron transport and confining potentials in nanostructures, Handbook of Nanostructured Materials and Nanotechnology, Vol.3, p1-91, ed. H.Nalwa, Academic Press (2000)

Publications in Reviewed Journals

1. J. Ulrich, R. Zobl, K. Unterrainer, G. Strasser, E. Gornik; "Magnetic field enhanced quantum cascade emission"; Appl. Phys. Lett. **76**, 19 (2000)
2. W. Schrenk, N. Finger, S. Gianordoli, L. Hvozdara, G. Strasser, E. Gornik; "GaAs/AlGaAs distributed feedback quantum cascade lasers"; Appl. Phys. Lett. **76**, 253 (2000)
3. R. Kersting, R. Bratschitsch, G. Strasser, K. Unterrainer, J.N. Heyman; "Sampling a terahertz dipole transition with subcycle time resolution"; Opt. Lett. **25**, 272 (2000)
4. T. Maier, G. Strasser, E. Gornik; "Monolithic integration of vertical-cavity laser diodes and resonant photodetectors with hybrid Si_3N_4/SiO_2 top Bragg mirrors"; IEEE Phot. Tech. Lett. **12**, 119-121 (2000)

5. J. Smoliner, R. Heer, G. Ploner and G. Strasser; "k//=0 filtering effects in ballistic electron transport through sub-surface GaAs-AlGaAs double barrier resonant tunneling structures"; Physica **E6**, 339-342 (2000)
6. G.Ploner, H.Hirner, T.Maier, G.Strasser, J.Smoliner, E.Gornik; "A novel device layout for tunneling spectroscopy of low-dimensional electron systems"; Physica **E6**, 343-347 (2000)
7. G. Strasser, S. Gianordoli, L. Hvozdara, W. Schrenk, E. Gornik; "Intersubband and interminiband GaAs/AlGaAs quantum cascade lasers"; Physica **E7**, 1-7 (2000)
8. O. Gauthier-Lafaye, B. Seguin-Roa, F.H. Julien, P. Collot, C. Sirtori, J.Y. Duboz, G. Strasser; "High power tunable quantum fountain unipolar lasers"; Physica **E7**, 12-19 (2000)
9. S. Gianordoli, L. Hvozdara, G.Strasser, T. Maier, N. Finger, K. Unterrainer, E. Gornik; "GaAs/AlGaAs microresonator quantum cascade lasers"; Physica **E7**, 29-32 (2000)
10. L. Hvozdara, S. Gianordoli, G.Strasser, W. Schrenk, K. Unterrainer, E. Gornik, C.S.S.S. Murthy, M. Kraft, V. Pustogow, B. Mizaikoff; "GaAs/AlGaAs quantum cascade laser – a source for gas absorption spectroscopy"; Physica **E7**, 37-39 (2000)
11. M. Helm, W. Hilber, G. Strasser, R. DeMeester, F. M Peeters, A. Wacker; "Interminiband spectroscopy of biased superlattices"; Physica **E7**, 274-278 (2000)
12. S. Gianordoli, L. Hvozdara, G. Strasser, W. Schrenk, J. Faist, and E. Gornik; "Long-Wavelength (10 μm) Quadrupolar Shaped GaAs/AlGaAs Microlasers"; IEEE J. Quantum Electron. **36**, 458 (2000)
13. R. Zobl, K. Unterrainer, G. Strasser, E. Gornik, "Magneto-optical terahertz emission from plasmons in parabolic quantum wells"; Semicond. Sci. and Technol. **15**, 315-321 (2000)
14. G. Strasser, G. Ploner, C. Rauch and E. Gornik; "Transport Spectroscopy of Quantum Wires and Superlattices"; Thin Solid Films **367**, 267-276 (2000)
15. S. Gianordoli, W. Schrenk, G.Strasser, L. Hvozdara, N. Finger, and E. Gornik; "Strained InGaAs/AlGaAs/GaAs-Quantum Cascade Lasers"; Appl. Phys. Lett. **76,** 3361 (2000)
16. K. Unterrainer, R. Kersting, R. Bratschitsch, G. Strasser, J. N. Heyman, K.D. Maranowski, A.C. Gossard; " Few-Cycle THz spectroscopy of nanostructures"; Physica **E7**, 693-697 (2000)
17. G. Strasser, L. Hvozdara, S. Gianordoli, W. Schrenk, K.Unterrainer, E. Gornik, M. Helm; "Intersubband and interminiband GaAs/AlGaAs quantum cascade lasers at 10 μm"; Physica **E7**, 709-712 (2000)
18. L. Hvozdara, S. Gianordoli, G. Strasser, W. Schrenk, K.Unterrainer, E. Gornik; "GaAs/AlGaAs unipolar mid-infrared quantum cascade lasers"; Inst. Phys. Conf. Ser. **166**, 363v (2000)
19. L. Hvozdara, A. Lugstein, S. Gianordoli, W. Schrenk, G. Strasser, K. Unterrainer, E. Bertagnolli, and E. Gornik; "Self-aligned coupled cavity GaAs/AlGaAs mid infrared quantum cascade lasers"; Appl. Phys. Lett. **77**, 1077 (2000)

20. S. Gianordoli, R. Hainberger, A. Köck, N. Finger, E. Gornik, L. Korter, and C. Hanke, “Optimization of the emissioncharacteristics of light emitting diodes by surface plasmons and surface waveguide modes”, Appl. Phys. Lett. **77**, 2295 (2000)

21. R. Bratschitsch, T. Müller, R. Kersting, G. Strasser, K. Unterrainer; "Coherent THz emission from optically pumped intersubband plasmons in parabolic quantum wells"; Appl. Phys. Lett. **76**, 3501 (2000)

22. K. Esmark, C. Fürböck, H. Gossner, G. Groos, M. Litzenberger, D. Pogany, R. Zelsacher, M. Stecher, E. Gornik, "Simulation and experimental study of temperature distribution during ESD stress in smart-power technology ESD protection structures", Proc. IRPS 2000, pp. 304-309.

23. C. Fürböck, D. Pogany, M. Litzenberger, E. Gornik, N. Seliger, H. Gossner, T. Müller-Lynch, M. Stecher, W. Werner, "Interferometric temperature mapping during ESD stress and failure analysis of smart power technology ESD protection devices", J. Electrostatics 49 (3-4), pp. 195-213 (2000)

24. M. Litzenberger, K. Esmark, D. Pogany, C. Fürböck, H. Gossner, E. Gornik, W. Fichtner, "Study of triggering inhomogeneities in gg-nMOS ESD protection devices via thermal mapping using backside laser interferometry", Microel. Reliab. 40 (8-10), pp.1359-1364 (2000)

25. C. Fürböck, K. Esmark, M .Litzenberger, D. Pogany, G. Groos, R. Zelsacher, M. Stecher, E. Gornik, "Thermal and free carrier concentration mapping during ESD event in smart power ESD protection devices using a modified laser interferometry technique", Microel. Reliab. 40 (8-10), pp.1365-1370 (2000)

26. D. Pogany, K. Esmark, M. Litzenberger, C. Fürböck, H. Gossner, E. Gornik, "Bulk and surface degradation mode in 0.35µm technology gg-nMOS ESD protection devices", Microel. Reliab. 40 (8-10), pp.1467-1472 (2000).

27. M. Litzenberger, C. Fürböck, D. Pogany, E. Gornik, K. Esmark, H. Gossner, "Investigation of 3D phenomena in the triggering of gg-nMOS electrostatic discharge protection devices", Proc. ESSDERC'2000, Cork, Ireland, 11-13 Sept 2000, pp. 520-523.

28. L. Hvozdara, A. Lugstein, N. Finger, S. Gianordoli, W. Schrenk, K. Unterrainer, E. Bertagnolli, G. Strasser, and E. Gornik; "Quantum cascade lasers with monolithic air-semiconductor Bragg reflectors", Appl. Phys. Lett. **77**, 1241 (2000).

29. S. Gianordoli, W. Schrenk, L. Hvozdara, N. Finger, K. Unterrainer, G. Strasser, and E. Gornik, “Improved performance of GaAs/AlGaAs superlattice quantum cascade lasers emitting beyond $\lambda = 13$ µm”, IEEE Photon. Techn. Lett. **12**, 1144 (2000)

30. W. Schrenk, N. Finger, S. Gianordoli, G. Strasser, E. Gornik; "AlGaAs/GaAs distributed feedback quantum cascade lasers"; Material Research Society Symposium Proceedings, Vol 607, ISBN 1-55899-515-3, pp. 141-146 (2000).

31. W. Schrenk, N. Finger, S. Gianordoli, L. Hvozdara, G. Strasser, E. Gornik; "Surface emitting distributed feedback quantum cascade lasers”, Appl. Phys. Lett. **77**, 2086 (2000)

32. R. Folman, P. Krüger, D. Cassettari, B. Hessmo, T. Maier, J. Schmiedmayer, "Controlling Cold Atoms using Nanofabricated Surfaces: Atom Chips", Phys. Rev. Lett, **84**, 4749 (2000).

33. R. Kersting, G. Strasser, K. Unterrainer, "Demonstration of a THz phase modulator", Electron. Lett. **36**, 1156 (2000).

34. W. Fischler, R. Bratschitsch, R.A. Höpfel, G. Zandler, G. Strasser, K. Unterrainer, "The lower branch of plasmon-phonon couples modes", Semicond. Sci. Technol. **15**, 813 (2000).

35. D. Rakoczy, J. Smoliner, R. Heer, G. Strasser; "Ballistic Transport through GaAs-AlGaAs Superlattices in Transverse Magnetic Fields"; Journ. Appl. Phys. **88**, 3495 (2000)

36. P.O. Kellermann, N. Finger, E. Gornik, M. Ost, F. Scholz and H. Schweizer "Wavelength-graded horizontal cavity laser array with postgrowth adjustment of wavelength", IEEE Phot. Tech. Lett. **12**, 1138 (2000)

37. J. Ulrich, R. Zobl, W. Schrenk, G. Strasser, K. Unterrainer, and E. Gornik, "Terahertz quantum cascade structures: Intra- versus interwell transition", Appl. Phys. Lett. **77**, 1928 (2000).

38. R. Bratschitsch, T. Müller, R. Kersting, G. Strasser, K. Unterraine ; "Coherent THz emission from optically pumped parabolic quantum wells", CLEO/QELS ´2000 Technical Digest, p 254, 2000.

39. J.E. Golub, R. Eichmann, G. Strasser, G. Bernatz, S. Nau, W. Stolz, P. Thomas; "Observations of interaction-assisted hopping transport in GaAs/$Ga_{1-x}Al_xAs$ quantum wells"; Journ. of Luminescence **91**, 7 (2000)

40. W. Schrenk, N. Finger, S. Gianordoli, L. Hvozdara, G. Strasser, E. Gornik; "First- and second-order distributed feedback AlGaAs/GaAs quantum cascade lasers"; CLEO Europe/IQEC 2000 Technical Digest, 85 (2000)

41. N. Finger, W. Schrenk, E. Gornik; "Surface-Grating Coupled Quantum Cascade Laser Structures"; CLEO Europe/IQEC 2000 Technical Digest, 85 (2000)

42. J. Ulrich, G. Strasser, K. Unterrainer, and E. Gornik; "Terahertz-quantum-cascade emitters: interwell versus intrawell transitions"; CLEO Europe/IQEC 2000 Technical Digest, 86 (2000)

43. P. O. Kellermann, N. Finger, E. Gornik, M. Ost, F. Scholz, H. Schweizer; "Wavelength-Graded Surface-Emitting Laser Array With Contradirectional Surface-Mode Coupling" CLEO Europe/IQEC 2000 Conference Digest, 38 (2000)

44. L. Hvozdara, A. Lugstein, S. Gianordoli, N. Finger, G. Strasser, W. Schrenk, K. Unterrainer, E. Bertagnolli, E. Gornik; "Quantum cascade lasers with monolithic photonic bandgap mirrors"; CLEO Europe/IQEC 2000 Technical Digest, 219 (2000)

45. R. Bratschitsch, T. Müller, R. Kersting, G. Strasser, K. Unterrainer ; "Coherent THz emission from optically pumped intersubband plasmons in parabolic quantum wells",in "Ultrafast Phenomena XII", Springer Series in Chemical Physics **66**, 203 (2000).

46. R. Kersting, R. Bratschitsch, G. Strasser, K. Unterrainer, "Excitation Dynamics beyound Slowly-Varying Envelope Approximation", in "Ultrafast Phenomena XII", Springer Series in Chemical Physics **66**, 235 (2000).

47. W. Schrenk, N. Finger, S. Gianordoli, E. Gornik, G. Strasser; "Continuous-Wave Operation of AlAs/GaAs Superlattice Quantum Cascade Lasers"; Appl. Phys. Lett. **77**, 3328 (2000)

48. L. Hvozdara, S. Gianordoli, G. Strasser, W. Schrenk, K. Unterrainer, E. Gornik, C.S.S.S. Murthy, M. Kraft, V. Pustogow, B. Mizaikoff, N. Croitoru; "Spectroscopy in the Gas Phase with GaAs/AlGaAs Quantum-Cascade Lasers"; Appl. Opt. **39**; 6926 (2000)

49. N. Finger, W. Schrenk, and E. Gornik, "Analysis of TM-polarized laser structures with metal surface gratings", IEEE J. Quantum Electron. **QE-36**, 780 (2000)

50. K. Unterrainer, J. Ulrich, R. Zobl, G. Strasser, "THz sources based on Semiconductor quantum structures", Proc. of the 8th Int. Conf. on Terahertz Electronics, VDE Verlag, Berlin (2000), p. 37.

51. T. Klaffs, A.A. Ivanov, A.S. Bakin, D. Piester, M. Ursu, A. Schlachetzki, L. Hvozdara, G. Strasser, B. Güttler; "Intersubband Absorption In Delta-Doped GaInAs-InP multi quantum wells"; Proc. 3rd Int. Euroconference on Advanced Semiconductor Devices and Microsystems (ASDAM 2000); ISBN 0-7803-5939-9

52. D. Cassettari, B. Hessmo, R. Folman, T. Maier, J. Schmiedmayer, " Beam Splitter for Guided Atoms", Phys. Rev. Lett. **85**, 5483 (2000).

53. G. Hobler, L. Pelaz, and C. S. Rafferty, "Dose, energy, and ion species dependence of the effective plus-factor for transient enhanced diffusion", J. Electrochem. Soc., **147**, 3494-3501 (2000).

54. H.-H. Vuong, Y.-H. Xie, M. R. Frei, G. Hobler, L. Pelaz, and C. S. Rafferty, "Use of transient enhanced diffusion to tailor boron out-diffusion", IEEE Trans. Electron Dev., **47**, 1401-1405 (2000).

55. G. Hobler and V. Moroz, "Simple formulae for the effective plus-factor for transient enhanced diffusion", In ESSDERC 2000, pp. 168-171. Frontier Group, 2000.

56. H.D. Wanzenboeck, H. Langfischer, A. Lugstein, E. Bertagnolli, "Improved Materials for Direct Writing of Microelectronic Interconnects“, AVS Proceedings of the 2nd Intl. Conf. On Advanced Materials and Processes for Microelectronics, 7.-14. Feb. 2000, Sta Clara, pp. 67.

57. H. Bachhofer, H. Reisinger, H. von Philipsborn and E. Bertagnolli, “On the Erase Mechanism in SONOS Nonvolatile Memories“, Proc. 17th IEEE Nonvolatile Semiconductor Memory Workshop (NVSMW), Monterey, CA, Feb. 2000, pp. 124-128.

58. H.D. Wanzenboeck, A. Lugstein, H. Langfischer, E. Bertagnolli, M. Gritsch, H. Hutter, „Ion Beam Induced Chemical Vapor Deposition of Dielectric Materials“, Proceedings of the 2000 Material Research Society Spring-Meeting (MRS), San Francisco, 24.-28. April 2000, p. 354.

59. H. D. Wanzenboeck, S. Harasek, H. Langfischer, A. Lugstein, E. Bertagnolli, M. Gritsch, H. Hutter, C. Tomastik, J. Brenner, H. Stoeri, "Local Deposition of Dielectrics for the deep sub-µm range", Proc.17th International VLSI Multilevel Interconnection Conference (VMIC), VMIC 2000, Sta Clara, CA, 27.-29. June 2000, pp.127-142.

60. H. Langfischer, E. Bertagnolli, A. Lugstein, H. D. Wanzenboeck, H. Hutter, M. Gritsch, C. Tomastik, "Improvement of FIB based Tungsten Metallization", Proc.17th International VLSI Multilevel Interconnection Conference (VMIC),Sta Clara, CA, 27.-29. June 2000, pp.439-441.

61. H.D. Wanzenboeck, M. Verbeek, W. Maurer, E. Bertagnolli, FIB Based Local Deposition of Dielectrics for Phaseshift Mask Modification“,20th Annual BACUS Symposium on Photomask Technology, Monterey, 13.-15. Sept. 2000, Proceedings of SPIE – International Society for Optical Engineering, **4186**, p.148 –157

62. H.D. Wanzenboeck, A. Lugstein, H. Langfischer, E. Bertagnolli, M. Gritsch, H. Hutter, „Ion Beam Induced Deposition of Dielectric Nanostructures“, 8th Int. Conference on Dielectric Materials, Measurement and Application (DMMA), DMMA 2000, 17.-21. Sept. 2000, Edinburgh, IEE Conference Publication No. 473 (ISBN 0 85296 730 6) pp. 485-490.

63. H. D. Wanzenboeck, S. Harasek, H. Langfischer, A. Lugstein, E. Bertagnolli, "Rapid Prototyping by Local Deposition of Siliconoxide and Tungsten Nanostructures for Interconnect Rewiring", 47th AVS Symposium , Boston, 2.-6. Oct. 2000, 47th International Symposium of the American Vacuum Society, p.114.

64. H. D. Wanzenboeck, H. Langfischer, E. Bertagnolli, H. Stoeri, M. Gritsch, H. Hutter, "Material and Interface Characterisation of Locally Deposited Dielectrics and Metals with a focused Ion Beam (FIB)" 47th AVS Symposium, Boston, 2.-6. Oct. 2000, 47th International Symposium of the American Vacuum Society, p.227.

65. J. Smoliner, R. Heer, G. Strasser, C.Strahberger, Magnetic field effects and $k_{//}$-filtering in BEEM on GaAs-AlGaAs resonant tunneling structures, Applied Physics (accepted).

66. K. Kempa, E. Gornik, K. Unterrainer, M. Kast and G. Strasser; " Resonant Tunneling mediated by resonant emission of inter-subband plasmons"; Phys. Rev. Lett. (accepted).

67. C. Strahberger, J. Smoliner, R. Heer, G. Strasser; "Enhanced $k_{//}$ filtering effects in ballistic electron emission experiments"; Phys. Rev. B (accepted)

68. G. Strasser, S. Gianordoli, W. Schrenk, E. Gornik, A. Mücklich, M. Helm; "MBE-grown GaAs/AlGaAs and strained InGaAs/AlGaAs/GaAs quantum cascade lasers"; Journal of Crystal Growth (accepted)

69. M. Helm, G. Strasser; "Correlation of vertical transport and infrared absorption in GaAs/AlGaAs superlattices"; proceedings ICPS25(accepted).

70. K. Unterrainer, R. Bratschitsch, T. Müller, R. Kersting, J.N. Heyman, G. Strasser, "Time domain THz spectroscopy of semiconductor quantum structures", Proc. of the ICPS 25 (accepted).

71. C. Pacher, G. Strasser, E. Gornik, F. Elsholz, A. Wacker, E. Schöll, "Optics with ballistic electrons: Anti-reflection coatings for GaAs/AlGaAs superlattices", Proc. of the ICPS 25 (accepted).

72. J. Ulrich, R. Zobl, G. Strasser, K. Unterrainer, “Terahertz emission from semiconductor nanostructures” in “Terahertz Sources and Systems”, Kluwer academic publisher (accepted).

73. D. Pogany, J. A. Chroboczek, G. Ghibaudo, "Random telegraph signal noise mechanisms in reverse base current of hot carrier degraded submicron bipolar transistors: Effect of carrier trapping during stress on noise characteristics", J. Appl. Phys., (accepted)

74. W. Boxleitner, G. Hobler, V. Klüppel, and H. Cerva, "Dynamic simulation of topography evolution and damage formation in TEM sample preparation using focused ion beams", Nucl. Instr. Meth., B (accepted).

75. W. Boxleitner and G. Hobler, "FIBSIM -- Dynamic Monte Carlo simulation of compositional and topography changes caused by focused ion beam milling", Nucl. Instr. Meth., B (accepted).

76. G. Hobler and G. Betz, "On the useful range of application of molecular dynamics simulations in the recoil interaction approximation", Nucl. Instr. Meth., B (accepted).

77. G. Hobler and C. S. Murthy, "Towards a comprehensive model of electronic stopping in amorphous and crystalline silicon", In Proc. 13th Int. Conf. Ion Implantation Technology, IIT-2000 (accepted).

78. L. Palmetshofer, M. Gritsch, and G. Hobler, "Range of ion-implanted rare earth elements in Si and SiO2", Proc. EMRS-2000 (accepted)

79. K. Unterrainer, R. Bratschitsch, R. Kersting , T. Müller, G. Strasser, J.N. Heyman, "Few-Cycle THz spectroscopy of semiconductor quantum structures" Physica E (accepted)

80. D. Pogany, E. Gornik, M. Stecher, W. Werner, "Random telegraph noise and leakage current in smart power technology DMOS devices", Microel. Reliab. (accepted).

81. C. Kranz, G. Friedbacher, B. Mizaikoff, A. Lugstein, J. Smoliner, E. Bertagnolli, "An Integrated Ultramicroelectrode in an AFM Cantilever – Combined Power for Enhanced Information" Anal. Chem. (accepted)

82. H. Bachhofer, H. Reisinger, E. Bertagnolli, H. von Philipsborn, "Transient conduction in multidielectric silicon-oxide-nitride-oxide-semiconductor structures. J. Appl. Phys(accepted)

83. F. Elsholz, A. Wacker, E. Schöll, M. Kast, G. Strasser, E. Gornik; "Magnetotransport through semiconductor superlattices"; submitted to Phys. Rev. B 9/2000

84. R. Bratschitsch, T. Müller, N. Finger, G. Strasser, K. Unterrainer, C. Sirtori; "Monitoring the ultrafast electric field change at a mid-infrared plasma Bragg mirror"; submitted to Appl. Phys. Lett. 12/2000

85. J.Smoliner, R. Heer, G.Strasser, BEEM/S on GaAs-AlGaAs resonant tunneling structures and quantum wires, submitted to Surface and Interface Analysis

86. H. R. K. Maier, P. O. Kellermann, N. Finger, E. Gornik, R. Winterhoff and F. Scholz; "Visible red surface-emitting distributed feedback lasers with a surface grating"; submitted to Appl. Phys. Lett. 2000

87. D.Rakoczy, G.Strasser, J.Smoliner; "Ballistic Electron Emission Microscopy of "on-surface" Self Assembled InAs Dots and Wetting Layers"; submitted to J. Vac. Sci. Technol. B 12/2000
88. H. Wanzenboeck, A. Lugstein, H. Langfischer, S. Harasek, E. Bertagnolli; U. Grabner, P. Pongratz, B. Basnar, J. Smoliner, E. Gornik; "Effects of Ga-ion irradiation on chemical and electrical properties of materials processed by a Focused Ion Beam (FIB)", Material Research Society MRS 2000 – Fall Meeting, Boston, 27. Nov. - 1. Dec 2000, submitted 12/2000
89. S. Gianordoli, W. Schrenk, G.Strasser, L. Hvozdara, and E. Gornik; "Low threshold AlAs—GaAs Superlattice Quantum Cascade Laser"; submitted to IEEE Photon. Techn. Lett. 12/2000
90. B. Goebel, E. Bertagnolli, and D. Schumann, "Vertical N-Channel MOSFETs for Extremely High Density Memories: The Impact of Interface Orientation on Device Performance", submitted to IEEE Trans Electron Devices.
91. A. Lugstein, E. Bertagnolli, C. Kranz, B. Mizaikoff, „Fabrication of a Ring-Nanoelectrode Integrated in an AFM-Tip: A Novel Approach Towards Simultaneous Electochemical and Topographical Imaging", Surface and Interface Analysis, submitted 10/2000
92. C. Kranz, B. Mizaikoff, A. Lugstein, E. Bertagnolli, „Integrating an Ultramicroelectrode in an AFM Cantilever: Towards the Development of a Combined Microsensing-Imaging Tool", ACS Symposium Book on Electrochemical Methods for the Environmental Analysis of Trace Element Biogeochemistry (Eds. Martial Taillefert and Tim Rozan) submitted 12/2000.
93. A. Lugstein, M. Stockinger, G. Hobler, S. Selberherr, E. Bertagnolli, Sublithographic Channel Profile Tayloring of MOSFETS, IEEE Electron Device Letters submitted 12/2000

Presentations

1. G. Strasser; "GaAs-based superlattice quantum cascade lasers"; Workshop on Quantum Heterostructures and THz Electronics, Regensburg, Germany, 27.1.2000
2. H.D. Wanzenboeck, H. Langfischer, A. Lugstein, E. Bertagnolli, "Improved Materials for Direct Writing of Microelectronic Interconnects",AVS Proceedings of the 2nd Intl. Conf. On Advanced Materials and Processes for Microelectronics, Sta Clara, USA, 7.-14. Feb. 2000
3. K. Unterrainer , R. Bratschitsch, R. Kersting , T. Müller, G. Strasser, J.N. Heyman (invited), "Few-Cycle THz spectroscopy of semiconductor quantum structures", 11th Int. Winterschool on New Developments in Solid State Physics,Low dimensional Systems: Fundamentals and Applications, Mauterndorf, Austria, 21-25 February 2000.
4. D. Rakoczy, R. Heer, J. Smoliner, G. Ploner, G. Strasser, E. Gornik; "A Metal-Insulator-Metal Injector for Ballistic Electron Emission Spectroscopy", 11th Int. Winterschool on New Developments in Solid State Physics,Low-dimensional Systems: Fundamentals and Applications, Mauterndorf, Austria, 21-25 February 2000.

5. K. Unterrainer, R. Bratschitsch, J. Ulrich , G. Strasser (invited), "THz emission from semiconductor nano structures“,18th General Conf. Condensed Matter Division of the European Physical Society; Montreux, Switzerland, 13-17.3.2000.
6. G. Strasser, S. Gianordoli, W. Schrenk, E. Gornik; "Single mode GaAs/AlGaAs QCLs"; 18th General Conf. Condensed Matter Division of the European Physical Society; Montreux, Switzerland, 13-17.3.2000.
7. F. Elsholz, A. Wacker, E. Schöll, C. Pacher, C. Rauch, G. Strasser und E. Gornik, “Magnetotransport durch rauhe Halbleiterübergitter“,DPG Frühjahrstagung, Regensburg, Deutschland, 27.03. - 31.03.2000
8. S. Schmult, W. Wegscheider, J. Raabe, S. Gianordoli, G. Strasser, M. Bichler, G. Abstreiter; "Eigenschaften von AlGaAs/GaAs-Quantenkaskadenlasern"; DPG Frühjahrstagung, Regensburg, Deutschland, 27.-31.3.2000
9. K. Esmark, C. Fürböck, H. Gossner, G. Groos, M. Litzenberger, D. Pogany, R. Zelsacher, M. Stecher, and E. Gornik, “Simulation and experimental study of temperature distribution during ESD stress in smart-power technology ESD protection structures”, International Reliability Physics Symposium, San Jose, California, April 10-13 2000.
10. H.D. Wanzenboeck, A. Lugstein, H. Langfischer, E. Bertagnolli, M. Gritsch, H. Hutter, „Ion Beam Induced Chemical Vapor Deposition of Dielectric Materials“,2000 MRS Spring-Meeting, San Francisco, USA, 24.-28. April 2000
11. R. Bratschitsch, T. Müller, R. Kersting, G. Strasser, and K. Unterrainer: “Coherent THz emission from optically pumped parabolic quantum wells”, CLEO/QELS 2000, San Francisco, USA, 7.-12. 5. 2000.
12. G. Strasser, S. Gianordoli, W. Schrenk, E. Gornik (invited); "GaAs based quantum cascade microcavities"; European material research society E-MRS Spring Meeting 2000, Strasbourg, France, 31.5.-2.6. 2000.
13. L. Palmetshofer, M. Gritsch, and G. Hobler, "Range of ion-implanted rare earth elements in Si and SiO2", European material research society E-MRS Spring Meeting 2000, Strasbourg, France, 31.5.-2.6. 2000.
14. K. Unterrainer "THz generation from intersubband devices", NATO Advanced Research Workshop "Terahertz Sources and Systems", Chateau de Bonas, France, 21 -28 June.
15. H. D. Wanzenboeck, S. Harasek, H. Langfischer, A. Lugstein, E. Bertagnolli, M. Gritsch, H. Hutter, C. Tomastik, J. Brenner, H. Stoer,i "Local Deposition of Dielectrics for the deep sub-µm range", 17th Int. VLSI Multilevel Interconnection Conf. (VMIC), S^{ta} Clara, CA, 27.-29. June 2000
16. J. Ulrich, G. Strasser, K. Unterrainer, “Terahertz quantum cascade emission: intra- versus interwell transition” INTERACT-meeting, Chateau de Bonas, France, 29 -30 June.
17. R. Bratschitsch, T. Müller, R. Kersting, G. Strasser, and K. Unterrainer: “Coherent THz emission from optically pumped intersubband plasmons in parabolic quantum wells”, Ultrafast Phenomena 2000, Charleston, USA, 9.-13. 7. 2000.

18. R. Kersting, R. Bratschitsch, G. Strasser, K. Unterrainer; "Excitation Dynamics beyond the Slowly-Varying Envelope Approximation"; 12th Int. Conf. On Ultrafast Phenomena; Charleston, USA, 9.-13.7.2000

19. W. Boxleitner and G. Hobler, "FIBSIM -- Dynamic Monte Carlo simulation of compositional and topography changes caused by focused ion beam milling", 5th Int. Conf. Computer Simulation of Radiation Effects in Solids, Penn State University, USA, 24.-28. Juli 2000.

20. G. Hobler and G. Betz, "On the useful range of application of molecular dynamics simulations in the recoil interaction approximation", 5th Int. Conf. Computer Simulation of Radiation Effects in Solids, Penn State University, USA, 24.-28. Juli 2000.

21. J.Smoliner, R. Heer, G. Strasser, C.Strahberger, Effective mass effects and $k_{//}$-filtering in BEEM on GaAs-AlGaAs resonant tunneling structures, SPS2000, Hamburg (2000)

22. G. Strasser, W. Schrenk, S. Gianordoli, L. Hvozdara, N. Finger, K. Unterrainer, and E. Gornik; "Single mode emission from GaAs/AlGaAs intersubband and interminiband QCLs"; European Semiconductor Laser Workshop, Berlin, Germany, 1.-2.9. 2000

23. W. Boxleitner, G. Hobler, V. Klüppel, and H. Cerva, "Dynamic simulation of topography evolution and damage formation in TEM sample preparation using focused ion beams", 12th Int. Conf. Ion Beam Modification of Materials, Gramado-Canela, Brasil, 3.-8. September 2000.

24. L. Hvozdara, A. Lugstein, S. Gianordoli, N. Finger, G. Strasser, W. Schrenk, K. Unterrainer, E. Bertagnolli, E. Gornik; "Quantum cascade lasers with monolithic photonic bandgap mirrors"; CLEO Europe 2000, Nice, France, 10 - 15 September 2000

25. W. Schrenk, N. Finger, S. Gianordoli, L. Hvozdara, G. Strasser, E. Gornik; "First- and second-order distributed feedback AlGaAs/GaAs quantum cascade lasers"; CLEO Europe 2000 , Nice, France, 10 - 15 September 2000

26. N. Finger, W. Schrenk, E. Gornik; "Surface-Grating Coupled Quantum Cascade Laser Structures"; CLEO Europe 2000 , Nice, France, 10 - 15 September 2000

27. J. Ulrich, G. Strasser, K. Unterrainer, “Terahertz-Quantum-Cascade Emitters: Interwell Versus Intrawell Transitions” CLEO Europe 2000, Nice, France, 10 - 15 September 2000

28. G. Strasser, S. Gianordoli, W. Schrenk, E. Gornik (invited); "MBE-grown GaAs/AlGaAs and strained InGaAs/AlGaAs/GaAs quantum cascade lasers"; MBE XI, Peking, China, 10.-15.9.2000

29. P.O. Kellermann, N. Finger, E. Gornik, M. Ost, F. Scholz, H. Schweizer; ”Wavelength-graded surface-emitting laser array with contradirectional surface-mode coupling“; oral presentation CLEO/Europe 2000, Nice, France, 10 - 15 September 2000

30. M. Litzenberger, C. Fürböck, D. Pogany, E. Gornik, K. Esmark and H. Gossner: “Investigation of 3D Phenomena in the Triggering of gg-nMOS Electrostatic

Discharge Protection Devices", ESSDERC 2000, Cork, IRL, 11.-13. September 2000.

31. G. Hobler and V. Moroz, "Simple formulae for the effective plus-factor for transient enhanced diffusion", ESSDERC 2000, Cork, IRL, 11.-13. September 2000.

32. K. Unterrainer (invited), "Coherent and photon assisted transport in vertical quantum structures", TMR Advanced Research School, Space-, Frequency- and Time resolved Quantum Transport, Hamburg, September 3-9, 2000.

33. R. Bratschitsch, T. Müller, R. Kersting, G. Strasser, and K. Unterrainer; "Coherent THz emission from optically pumped parabolic quantum wells"; CLEO/IQEC 2000 Europe Konferenz, Nizza, Frankreich, 10.-15. 9. 2000.

34. H.D. Wanzenboeck, M. Verbeek, W. Maurer, E. Bertagnolli, „FIB Based Local Deposition of Dielectrics for Phaseshift Mask Modification",20th Annual BACUS Symposium on Photomask Technology, Monterey, USA, 13.-15. Sept. 2000

35. R. Bratschitsch, T. Müller, R. Kersting, G. Strasser, and K. Unterrainer (invited); "Nonadiabatic Intersubband Spectroscopy"; ITW 2000, Sandbjerg Estate, Dänemark, 17.-19. 9. 2000

36. R. Bratschitsch, T. Müller, R. Kersting, G. Strasser, and K. Unterrainer; "Coherent THz emission from optically pumped parabolic quantum wells"; ITW 2000, Sandbjerg Estate, Dänemark, 17.-19. 9. 2000

37. T. Müller, R. Bratschitsch, G. Strasser, K. Unterrainer, and A. Poppe; "Few-cycle mid-infrared emission from quantum beats in semiconductor nanostructures"; ITW 2000, Sandbjerg Estate, Dänemark, 17.-19. 9. 2000.

38. G. Hobler and C. S. Murthy, "Towards a comprehensive model of electronic stopping in amorphous and crystalline silicon", 13th Int. Conf. Ion Implantation Technology, Alpbach, Austria, 17.-22. September 2000.

39. H.D. Wanzenboeck, A. Lugstein, H. Langfischer, E. Bertagnolli, M. Gritsch, H. Hutter, „Ion Beam Induced Deposition of Dielectric Nanostructures", 8th Int. Conference on Dielectric Materials, Measurement and Application (DMMA), DMMA 2000, Edinburgh, UK, 17.-21. Sept. 2000,

40. K. Unterrainer, R. Bratschitsch, T Müller, R. Kersting, J.N. Heyman, G. Strasser (invited); "Time domain THz spectroscopy of semiconductor quantum structures"; ICPS25, Osaka, 18-22.9.00

41. G. Strasser, L. Hvozdara, W. Schrenk, S. Gianordoli, N. Finger, A. Lugstein, and E. Gornik; "Single mode GaAs/AlGaAs quantum cascade lasers"; ICPS25, Osaka, 18-22.9.00

42. C. Pacher, G. Strasser, C. Rauch, E. Gornik, F. Elsholz, and A. Wacker; "Optics with Ballistic Electrons: Anti-Reflection Coatings for GaAs-AlGaAs Superlattices"; ICPS25, Osaka, 18.-22.9.00

43. R. Kersting, R. Bratschitsch, G. Strasser, and K. Unterrainer; "Sampling the dynamics of intersubband transitions"; ICPS25, Osaka, 18.-22.9.00

44. S. Gianordoli, W. Schrenk, L. Hvozdara, G. Strasser, and E. Gornik; "GaAs/AlGaAs superlattice - and strained InGaAs/GaAs/AlGaAs quantum cascade lasers"; ICPS25, Osaka, 18-22.9.00

45. M. Helm and G. Strasser; "Correlation of vertical transport and infrared absorption in GaAs/AlGaAs superlattices"; ICPS25, Osaka, 18-22.9.00

46. J. Ulrich, G. Strasser, K. Unterrainer, and E. Gornik; "Intrawell versus interwell THz emission"; ICPS25, Osaka, 18-22.9.00

47. T. Schwarzl, W. Heiß, G. Springholz, S. Gianordoli, G. Strasser, M. Aigle, H. Pascher; "Strongly detuned IV-VI microcavity and microdisk resonances: mode splitting and lasing"; ICPS25, Osaka, 18-22.9.00

48. D. Rakoczy, J. Smoliner, R. Heer, and G. Strasser; "Ballistic electron emission spectroscopy on biased GaAs-AlGaAs superlattices in transverse magnetic fields"; ICPS25, Osaka, 18-22.9.00

49. J.Smoliner, R. Heer, G. Strasser, C.Strahberger, BEEM/S on GaAs-AlGaAs resonant tunneling structures and quantum wires, SXM4, Münster (2000)

50. C. Kranz, G. Friedbacher, B. Mizaikoff, A. Lugstein, J. Smoliner, E. Bertagnolli, Combining SECM and AFM – Integration of an Ultramicroelectrode in an AFM-Tip, SXM4 4th International Conference on the Development and Technological Application of Scanning Probe Methods, Münster, FRG, 25-27. September 2000

51. G. Strasser; "Single mode GaAs quantum cascade laser"; Österreichische Physikalische Gesellschaft, 50. Jahrestagung, Graz, Austria 28.-29.9.2000

52. K. Unterrainer, J. Ulrich, R. Zobl, G. Strasser, E. Gornik (invited), "THz sources based on semiconductor nanostructures", 8th International Conference on THz-Electronics, Darmstadt, 28.-29. September 2000.

53. R. Bratschtisch, T. Müller, R. Kersting, G. Strasser, K. Unterrainer, "Few-cycle THz-generation, from semiconductor quantum structures", 8th International Conference on THz-Electronics, Darmstadt, 28.-29. September 2000.

54. C. Fürböck, K. Esmark, M. Litzenberger, D. Pogany, G. Groos, R. Zelsacher, M. Stecher, and E. Gornik; "Thermal and free carrier concentration mapping during ESD event in Smart Power ESD protection devices using a modified laser interferometry technique", ESREF 2000, Dresden, Germany, 2.-6.10.2000.

55. M. Litzenberger, K. Esmark, D. Pogany, C. Fürböck ,H. Gossner, E. Gornik, and W. Fichtner; "Study of triggering inhomogeneities in gg-nMOS ESD protection devices via thermal mapping using backside laser interferometry", ESREF 2000, Dresden, Germany, 2.-6.10.2000.

56. D. Pogany, K. Esmark, M. Litzenberger, C.Fürböck, H. Gossner, and E. Gornik: "Bulk and surface degradation mode in 0.35µm technology gg-nMOS ESD protection devices", ESREF 2000, Dresden, Germany, 2.-6.10.2000.

57. H. D. Wanzenboeck, S. Harasek, H. Langfischer, A. Lugstein, E. Bertagnolli, "Rapid Prototyping by Local Deposition of Siliconoxide and Tungsten Nanostructures for Interconnect Rewiring", 47th Int. Symp. of the American Vacuum Society, Boston, USA, 2.-6. Oct. 2000

58. H. D. Wanzenboeck, H. Langfischer, E. Bertagnolli, H. Stoeri, M. Gritsch, H. Hutter, "Material and Interface Characterisation of Locally Deposited Dielectrics and Metals with a focused Ion Beam (FIB)" 47th International Symposium of the American Vacuum SocietyBoston, USA, 2.-6. Oct. 2000

59. A. Lugstein, E. Bertagnolli, C. Kranz, B. Miziaikoff „FIB Based Microfabrication Technique For A Novel Type of Scanning Electrochemical Microscopy Probes“, European FIB User Group Meeting, Dresden, Germany 4.10.2000
60. H. D. Wanzenboeck, A. Lugstein, S. Harasek, H. Langfischer, E. Bertagnolli, “Advances in Material Properties of Focused Ion Beam Deposited Dielectrics “, 4th European FIB Users Group Meeting (EFUG), Dresden, Germany 4.10.2000
61. T. Klaffs, A.A. Ivanov, A.S. Bakin, D. Piester, M. Ursu, A. Schlachetzki, L. Hvozdara, G. Strasser, B. Güttler “Intersubband absorption in delta-doped GaInAs-InP multi quantum wells” Advanced Semiconductor Devices And Microsystems, Smolenice-Castle, Slovakia 16-.18.10.2000
62. L. Hvozdara, S. Gianordoli, G. Strasser, W. Schrenk, K. Unterrainer, E. Gornik, V. Pustogov, C. Murthy, B. Mizaikoff, A. Inberg, N. Croitoru, “Gas Absorption Spectroscopy using GaAs/AlGaAs quantum cascade lasers and a hollow waveguide absorption cell”; SPIE – Environmental and Industrial Sensing, Boston, USA, 5-8 Nov. 2000
63. H. Wanzenboeck, A. Lugstein, H. Langfischer, S. Harasek, E. Bertagnolli; U. Grabner, P. Pongratz, B. Basnar, J. Smoliner, E. Gornik; “Effects of Ga-ion irradiation on chemical and electrical properties of materials processed by a Focused Ion Beam (FIB)”, MRS 2000 – Fall Meeting, Boston, USA, 27. Nov. - 1. Dec 2000

Patents

1. C. Kranz, B. Mizaikoff, A. Lugstein, E. Bertagnolli, „Vorrichtung für die gleichzeitige Durchführung einer elektrochemischen und einer topografischen Nahfeld-Mikroskopie,Austrian Patent pending, A 1011/2000 G01N, June 2000.
2. A. Lugstein, E. Bertagnolli, C. Kranz, B. Mizaikoff, „Verfahren zur Herstellung einer Vorrichtung für die gleichzeitige Durchführung einer elektrochemischen und einer topografischen Nahfeld-Mikroskopie“, Austrian Patent pending, A 1011/2000 G01N, June 2000
3. E. Gornik, N. Finger, „Gittergekoppelter oberflächenemittierender Quantenkaskadenlaser“,Austrian Patent pending, A 1141/2000 H01S, July 2000
4. G. Hobler, M. Mastrapasqua, M. R. Pinto, and E. Sangiorgi, "Monolithically integrated static random access memory device", U.S. Patent Number 6144073, 7 Nov 2000.

Doctor's Theses

1. Rudolf Heer: "Ballistic Electron Emission Spectroscopy on Buried Semiconductor Heterostructures", TU Wien, 2000.
2. Norman Finger: "Grating-Coupled Semiconductor Structures", TU Wien, 2000.
3. Thomas Maier: "Integration von oberflächenemittierenden Laserdioden und resonanten Photodetektoren für interferometrische Messungen", TU Wien, 2000.
4. Stefan Gianordoli: "Quantum cascade lasers on AlGaAs-GaAs for the mid-infrared regime", TU Wien, 2000.

5. Lubos Hvozdara: "Unipolar GaAs/AlGaAs MID-Infrared Lasers for Spectroscopic Applications", TU Wien, 2000.

Cooperations

1. Universität Linz, W. Heiss, F. Schäffler, H. Thim, L. Palmetshofer, W. Jantsch
2. Universität Wien, H. Kauffmann
3. Universität für Bodenkultur Wien, U.Sleytr, D. Pum
4. AMS-Unterbremstätten, H.Enichlmair, M.Schatzmayr, K. Tschernay F. Unterleitner
5. Philips Consumer Electronics, E. Kaun
6. Siemens AG, E. Wolfgang, G. Sölkner, W. Maurer
7. Infineon, M. Stoisiek, D. Schuhmann, J. Willer, R. Zelsacher
8. Femtolasers, Wien, A. Stingl
9. Plansee AG, Reutte, Dr. P. Willhartitz
10. High Q Laser, Hohenems, Dr. D. Kopf
11. TU-München, G. Abstreiter, P. Vogl, C. Strahberger, Deutschland
12. Universität Regensburg, W. Wegscheider, Deutschland
13. LMU München, N. Hecker, Deutschland
14. TU Braunschweig, D. Schneider, A. Schlachetzki
15. Technische Universität Berlin, A. Wacker, Deutschland
16. Heinrich Hertz Institut, Berlin, H. Künzel, Deutschland
17. Paul Drude Institut, Berlin, H. Grahn, Deutschland
18. Universität Bremen, D. Hommel, Deutschland
19. Universität Stuttgart, M.H. Pilkuhn, Deutschland
20. Forschungszentrum Rossendorf, Dresden, M. Helm, Deutschland
21. Mütek Infrared Laser Systems, H. Wachernig, Deutschland
22. Centre National de la Recherche Scientific, Laboratoire de Microstructures et de Microelectronique, B. Etienne, Cedex, Frankreich
23. Thomson-CSF LCR, Orsay , C. Sirtori, D. Corbin, Frankreich
24. Universite Paris Sud, F. Julien, Frankreich
25. Institute National des Sciences Appliques de Lyon, VilleUrbanne, Frankreich
26. Interuniversity Microelectronics Center (IMEC), Leuven, Belgien
27. Ioffe Physico-Technical Institute, St. Petersburg, Y. Ivanov, Rußland
28. Sub-Micron Center, Weizmann Institute, Rehovot, M. Heiblum, Israel
29. Univ. of California, Lawrence Berkeley Laboratories, E. E. Haller , USA
30. Univ. of California, Santa Barbara, J. Allen, A. Gossard, USA

31.Columbia University, New York, H. Störmer, USA

32.Princeton University, S. Lyon, USA

33.IBM Fishkill, C.S. Murthy, USA

34.Lucent Technologies, C. Gmachl, USA

35.Boston College, Boston, MA, K. Kempa, P. Bakshi, USA

36.EPI MBE Components, St. Paul, Minnesota, USA

37.Univ. Osaka, C. Hamaguchi, Japan

38.Univ. Nagoya, N. Sawaki, Japan

39.Herriot Watt University, Edinburgh, C. Pidgeon, Schottland

40.Univ. Glasgow, C. Ironside, Schottland

41.Univ. Nottingham, M. Chamberlain, England

42.University of Sheffield, M. Skolnick, J. Coburn, England

43.University of Surrey, B.N. Murdin, England

44.INFM-SNS Pisa, F. Beltram, Italien

45.Technische Universität Delft, Wenckebach, Holland

46.University Neuchatel, J. Faist, Schweiz

47.EPFL Lausanne, M. Ilegems, Schweiz

48.ETH Zürich, W. Fichtner, Schweiz

49.Orbisphere Semiconductor Lasers, Schweiz

50.Alpes Lasers, Neuchatel, A. Müller, Schweiz

51.Slovak Academy of Sciences, Bratislava, Slowakei

Focused Ion Beam Induced Local Tungsten Deposition

H. Langfischer, B. Basnar, E. Bertagnolli

Institute for Solid State Electronics, Vienna University of Technology, Floragasse 7, 1040 Wien, Austria

H. Hutter

Institute of Analytical Chemistry, Vienna University of Technology Getreidemarkt 9, 1060 Wien, Austria

Direct writing of metal lines is a widely used approach to interconnect prototype circuits and to rewire defective circuits at the very backend of the process line. However, the application of these direct written metal structures to contact devices is actually an open topic. In the presented metallization process a metal organic compound is decomposed by a focused ion beam (FIB) to form metal layers on several substrates. A variety of test structures allows the application of analytical methods and to quantify electrical properties. In addition, the detection of secondary electrons gives rise to time resolved *in situ* surface imaging of deposited metal layers. A direct characterization of the layers is obtained by atomic force microscopy (AFM).

1. Introduction

A widely used approach to interconnect prototype circuits and to rewire defective circuits is direct writing of metal lines at the very backend of the process line by means of FIB induced deposition. Primary beam related contaminations, intermixing effects, and unintentional local charging are the most important issues to be overcome if an application of FIB is viable close to the frontend. In this work we investigate the ion beam induced metallization process focusing on nucleation, intermixing, and growth, involving in situ characterization, AFM topography, SIMS, and electrical measurements.

2. Experimental

2.1 Layer Formation and Characterization

Based on a volatile metal organic tungsten compound ($W(CO)_6$) W-layers were deposited on thermal oxide layers by a Ga^+ ion beam [1]. Time resolved *in situ* surface imaging of the growth process addressing the primary steps in layer formation including nucleation and nuclei coalescence are involved. Characterization of the surface topography of the layers is done by atomic force microscopy (AFM). The chemical composition of the layers and the intermixing effects are both evaluated by secondary ion mass spectroscopy (SIMS) measurements.

2.2 Electrical Characterization

Electrical measurements are issuing the onset of the electrical conductivity, the specific resistance, and the maximum current densities the deposited material is capable to carry. To quantify the ohmic resistivity and maximum current densities in the metal, specific test structures were developed. Figure 1 shows a typical van der Pauw test structure for measuring sheet resistances. In the left viewgraph, the structure is already crossectioned by FIB to determine the associated layer thickness.

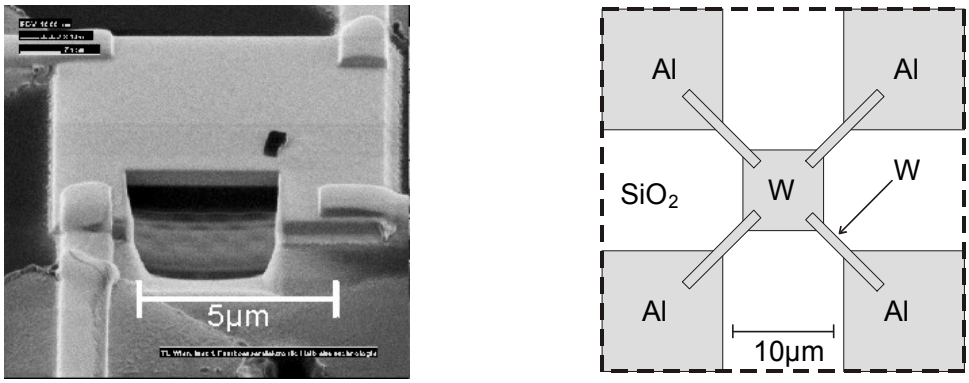

Fig. 1: Van der Pauw structure with FIB cross-sectional view and schematic illustration.

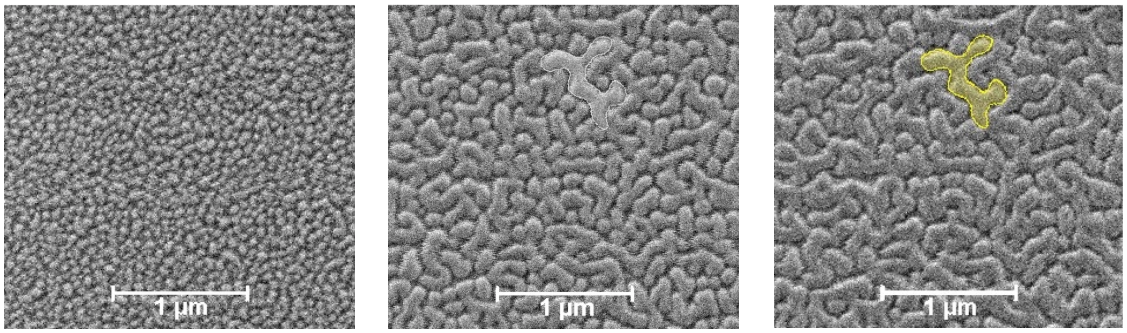

(2a) (2b) (2c)

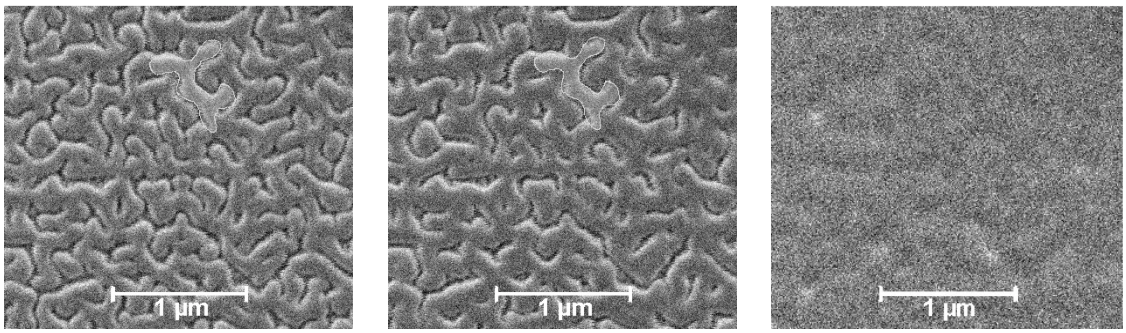

(2d) (2e) (2f)

Fig. 2: Evolution of an ion beam induced CVD tungsten process on thermal silicon dioxide.

3. Results and Discussion

3.1 FIB Induced Growth Process

In order to determine the evolution of the tungsten deposition process, *in situ* observations of the developing nanoscale structures are done by detecting the secondary charges (electrons or ions) emitted from the surface during focused ion beam irradiation. After each ion induced deposition step, an image scan over the same sample region is done. By the way, time resolved *in situ* surface images of the evolving metal layers are obtained. Figures 2a to 2f are a sequence of images showing how the process of tungsten layer formation proceeds.

At the beginning of the deposition process (Fig. 2a) the time resolved investigation shows nucleation at spots that are stochastically but homogeneously distributed over the area exposed to the ion beam. Then the nuclei grow during the deposition and start to collapse to form larger connected structures. Its remarkable that the formations grown in the early deposition steps are preserved in their shape during the consecutively following steps. They are not destroyed by the ion beam. This can be verified observing the weakly enlightened region in the upper part of Figs. 2b – 2e. After the exposure to an accumulated ion dose of about 1.7 10^{16} ions/cm^2 the merging process of formerly separated "islands" results in a closed metal surface (Fig. 2f).

3.2 Topography

Direct characterizations of the surface topography of the layers are obtained by atomic force microscopy (AFM). Figure 3 shows a three dimensional plot of the AFM data corresponding to a tungsten layer deposited with the same ion dose as the one in Fig. 2c. As seen in this figure, the topographic view is in close correspondence with the FIB imaging.

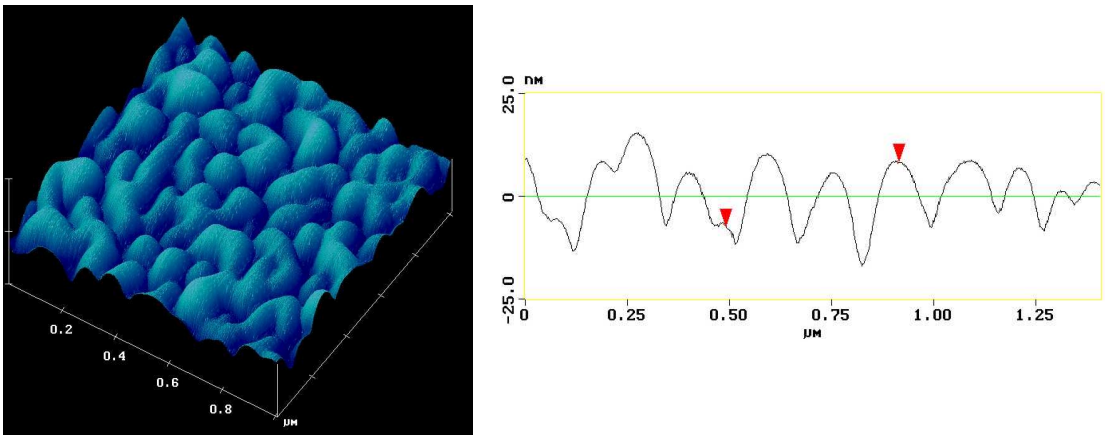

Fig. 3: Three dimensional plot of AFM surface scan (left). AFM analysis of the as grown tungsten surface (right).

The AFM section analysis of a tungsten surface in Fig. 3 exhibits a surface roughness value of up to 40 nm peak to peak.

3.2.1 Chemical

A SIMS based chemical analysis confirms a tungsten layer on the top of the substrate. In addition, however, to the direct observation, SIMS evidences, that no sharp interface to the substrate is formed. The exposure to the Ga beam leads to an intermixing region. Approaching the interface a clear pile up in the WSi concentration is seen, demonstrating the presence of a 50 nm interface layer between the tungsten layer and the substrate (Fig. 4).

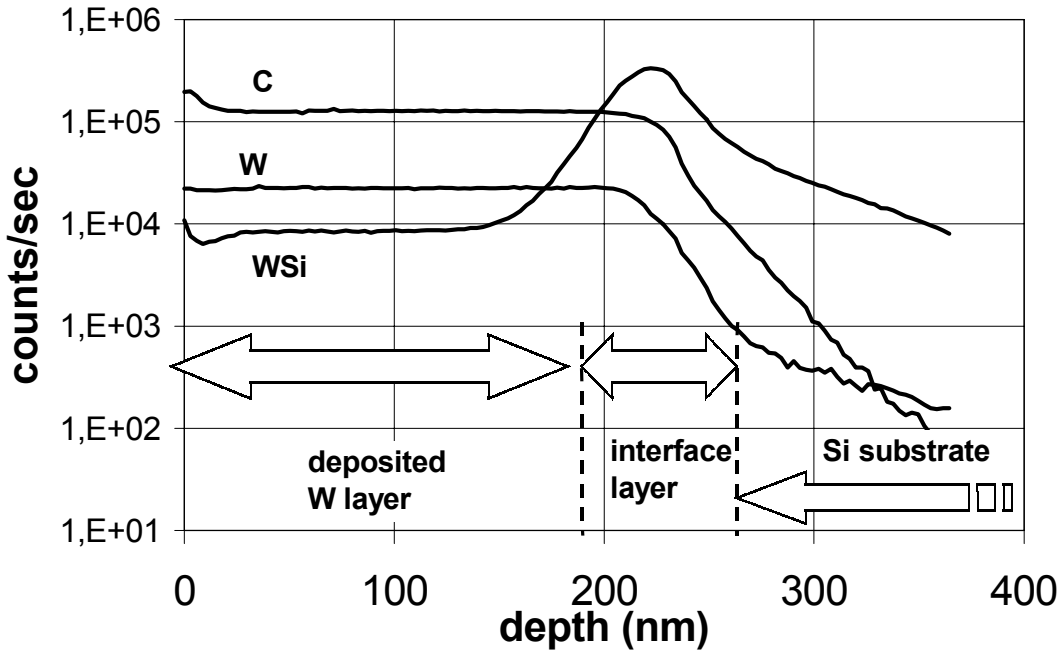

Fig. 4: SIMS profiles of C, W and WSi.

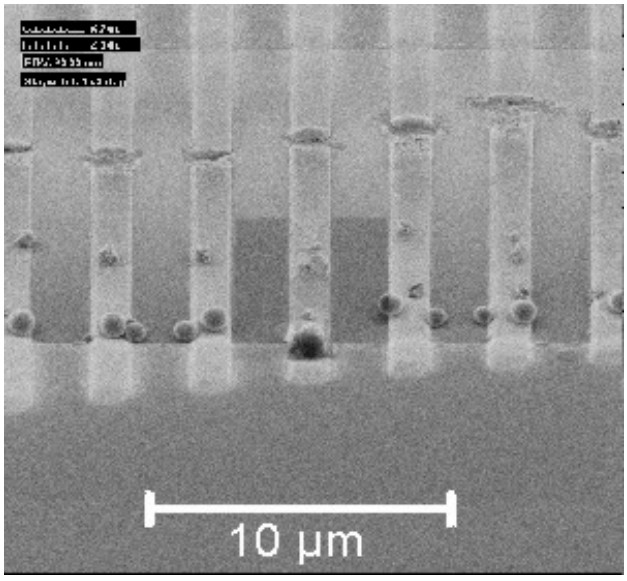

Fig. 5: Current stressed tungsten lines.

3.2.2 Electrical

The sheet resistance of a 280 nm layer is typically 3 Ω/square. The resistivity of the metal was calculated to be in a typical range of 200 – 300 μΩcm. The maximum current densities, indicating the robustness of the material were estimated using arrays of identical parallel W-lines (1 μm wide, 280 nm thick) connecting two contact pads. Maximum current densities up to 3.5 10^6 A/cm^2 were obtained. The array of current stressed tungsten lines is depicted in Fig. 5. A remarkable feature are the spherical hillocks visible at the lower ends of the lines because they give a strong indication for the fact that electromigration took place before the lines broke down due to the local ohmic heating.

4. Summary and Conclusion

Direct writing of metal lines is a suitable approach to interconnect prototype circuits and to rewire defective circuits at the very backend of line. The application of these direct written metal structures to contact devices is actually an open topic. In the presented metallization process a metal organic compound is decomposed by a focused ion beam (FIB) to form metal layers on several substrates. A variety of test structures allows the application of analytical methods and to quantify electrical properties. In addition, the detection of secondary electrons gives rise to time resolved *in situ* surface imaging of deposited metal layers. A direct characterization of the layers is obtained by atomic force microscopy (AFM).

References

[1] T. Kodas, M. Hampden-Smith, *The Chemistry of Metal, CVD*, VCH, Weinheim (1994).

FIB Based Micro Fabrication Technique for a Novel Type of Scanning Electrochemical Microscopy Probes

A. Lugstein[1], C. Kranz[2], E. Bertagnolli[1]

[1] Institute for Solid State Electronics, TU Wien, Floragasse 7, 1040 Vienna, Austria

[2] Institute for Analytical Chemistry, TU Wien, Getreidemarkt 9, 1060 Vienna, Austria

Scanning Electrochemical Microscopy is a powerful technique to obtain *in situ* information of a wide range of processes occurring at interfaces. However, one major drawback of this technique is the lack of high spatial resolution compared with AFM or STM, due to the interference of the currents originated by the topographical and the electrochemical effects, respectively. Hence, a simultaneous but independent sensing of both, the topographical and the electrochemical information with high spatial resolution is a major issue in the field of scanning electrochemical microscopy (SECM). In this paper, we present a Focused Ion Beam (FIB) based technology, which, for the first time, enables the realization of an independent, simultaneous sensing of both the topography and the electrochemically active interface [1]. By remodeling an AFM-cantilever, an isolated ring-shaped electroactive metallic surface was integrated in the probe, whereas the residual AFM-tip was applied to gain the topographic information.

1. Introduction

Miniaturization of electrodes and electrochemical transducers by microfabrication processes is one of the fundamentals in modern electroanalytical chemistry [2]. Laterally resolved information on a sub-micrometer scale was added to electroanalytical chemistry with the invention of Scanning Electrochemical Microscopy (SECM) [3], [4]. This analytical method provides spatially resolved information on interface processes, which can be obtained by the possibility to use all common electrochemical methods, such as amperometry, potentiometry or cyclic voltammetry. The changes of the diffusion limited Faraday current at the microelectrode due to hemispherical diffusion of a redox mediator is recorded while scanning in constant height in the x,y-plane within a distance of a few electrode radii above the sample surface. The current response as a function of the microelectrode position is mainly influenced by the morphology and the reactivity of the investigated surface and the distance between microelectrode and sample. One major drawback of this technique is the lack of sufficient spatial resolution compared to AFM or STM, as long as a current dependent mode for positioning of the micro-electrode is used. Any further progress in information quantification and qualification has to address (i) sub-micrometer to nanometer-sized electrodes (nanoelectrodes) for improved lateral resolution, (ii) the integration of current independent height information and (iii) the precise knowledge of the distance between the electrode tip and the sample surface. Consequently, the combination of SECM with other scanning probe techniques such as

Scanning Tunneling Microscopy (STM), Atomic Force Microscopy (AFM), Scanning Nearfield Optical Microscopy (SNOM), etc. is of particular interest in order to overcome the current limitations and to obtain complementary surface information. Several approaches have been reported so far to overcome the "fixed height problem in conventional SECM experiments". A constant current mode combined with a vertical tip position modulation was already described in 1992 [5], [6]. A second approach based on electrochemical signaling uses convective effects when the microelectrode is moved with high speed perpendicular to the sample surface [7]. However, both methods do not provide current independent information on the tip-to-sample distance. Though, this approach is restricted to a few practical applications. An innovative possibility to circumvent this drawback is to integrate an electroactive area within a defined distance to the sample surface in a conventional AFM tip. In the present paper we discuss this novel approach applying a Focused Ion Beam (FIB) technique to produce a microelectrode integrated in a standard AFM tip. Thus, for the first time a precisely defined and constant held distance between the microelectrode and the sample surface can be obtained, thus allowing a simultaneous independent recording of the topographic and electrochemical information.

2. Experimental

The formation of the SECM electrode comprises coating of the AFM cantilever with thin conductive and insulating layers by RF sputtering respectively plasma enhanced chemical vapor deposition (PECVD) and the modeling of the integrated ultramicroelectrode by FIB cutting.

Conventional silicon nitride cantilevers were initially subjected to a RF-sputter coat forming a 5 nm chromium layer to ensure good adhesion of the subsequently deposited metal layer. The electrode material in form of a thin gold layer (100 nm to 400 nm) was then sputtered onto the cantilever. Finally a thin insulating and chemically inert SiO_2/Si_3N_4 sandwich layer was deposited (PECVD) onto the metal coated cantilever (Fig. 1). In order to produce homogeneous, dense films without pinholes the cantilever had to be annealed at 300 °C.

The well-defined microelectrode integrated in an AFM tip at a certain distance above the apex of the tip was generated by a FIB pattern process as shown in Fig. 1. The electrode formation includes several diametrically opposed cuttings, which are repeated several times in order obtain the demonstrated tip geometry. A major prerequisite for a simultaneous electrochemical and high resolution topographical imaging is the quality and stability of the re-modeled AFM tip. In order to ensure high resolution imaging, the original tip is re-established by FIB. Even smaller curvatures than usual for conventional Si_3N_4 tips are achieved and thereby the quality of the AFM image after the entire modification procedure could be improved. As a final step, re-deposited material was removed from the electrically active part of the tip.

The electrical contact was provided by an insulated copper wire (diameter: 0.2 mm) glued with a conducting silver epoxy resin to a small exposed area of gold layer at the end of the cantilever mount.

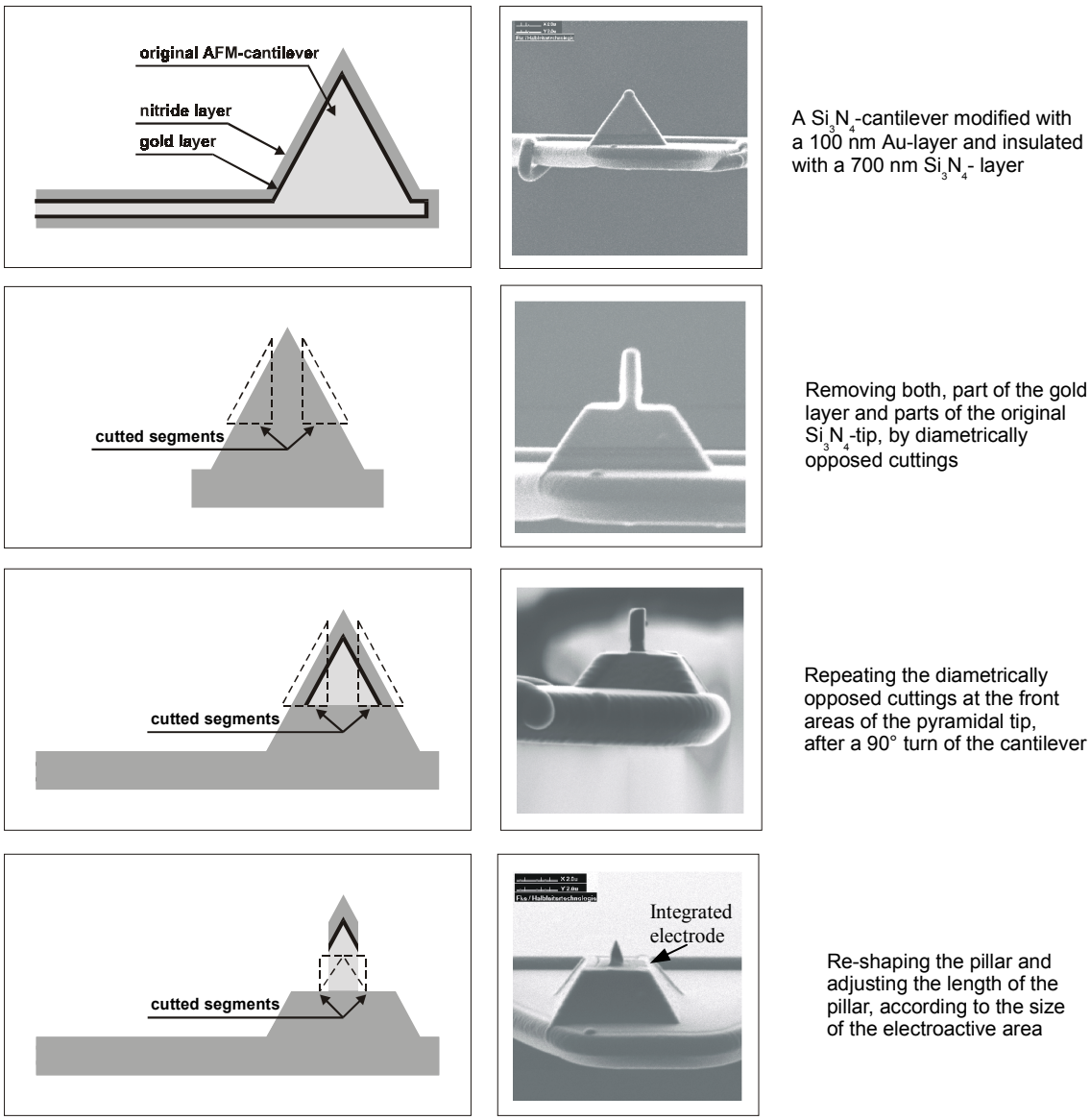

Fig. 1: Ion beam assisted modification of the AFM-tip. Schematic view of the processing steps (left) and the corresponding FIB-images (right).

AFM imaging was performed using a Nanoscope III atomic force microscope. The electrochemical investigations were performed in a fluid cell using an NPI VA10 potentiostat. All images were obtained in contact mode operation. The electrochemical setup was located in a Faraday cage. First results of simultaneous topographical and electrochemical measurement are shown in Fig. 2. A micromachined gold grating on gallium arsenide with a periodicity of 4.2 µm and a height of 0.45 µm was used as a model surface.

3. Conclusion

We present a novel technique which enables for the first time the integration of a microelectrode into an conventional AFM tip using an ion beam assisted approach, allowing simultaneous mapping of topographical and laterally resolved electrochemical informa-

tion. This development allows to position the electroactive area in a precisely defined and deliberately chosen distance to the very end of a scanning probe tip. Based on the opportunity to exactly adjust the distance of the electroactive area to the sample surface by adapting the length of the topographical probe with a micromachining technique like FIB, an optimized and defined working distance is ensured without theoretical fitting of current/distance approach curves. This procedure ensures high resolution topographical imaging and a precisely defined and constant distance between the integrated electrode and the sample surface within the working distance for electrochemical mapping. The demonstrated design is not limited to amperometric electrodes but can be extended to potentiometric electrodes or integrated electrochemical sensors, which are particularly difficult to position in a defined distance above a sample surface.

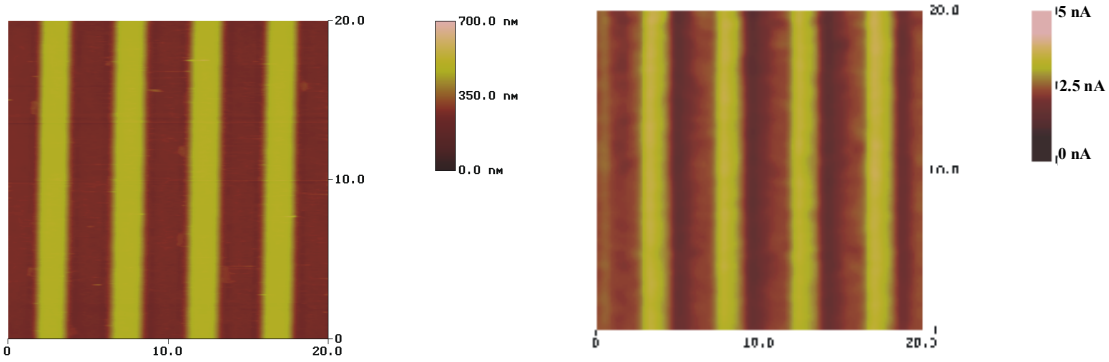

(a) (b)

Fig. 2: Imaging of a gold grating (periodicity 4,2 µm). Simultaneously recorded AFM image (a) and corresponding SECM signal (b).

Acknowledgements

The authors thank Gernot Friedbacher (Institute of Analytical Chemistry, Vienna University of Technology) for the possibility to use the AFM-SECM facilities.

References

[1] Patents pending, A 1011/2000 G01N, June 09, 2000; A 1012/2000 G01N, Jun. 09, 2000.

[2] M.I. Montenegro, A.A. Queiros, J.D. Daschbach, Microelctrodes: Theory and Applications, Kluwer: Dordrecht, NL, 1990.

[3] H.Y. Liu, F.-R.F Fan, C.W. Lin, A.J. Bard, J. Am. Chem. Soc. 1986, 108, 3838.

[4] R.C. Engstrom, M. Webber, D.J. Wunder, R. Burgess, S. Winquist, Anal. Chem. 1986, 58, 844.

[5] D.O. Wipf, A.J. Bard, Anal. Chem. 1992, 64, 1362.

[6] D.O. Wipf, A.J. Bard, D.E. Thallman, Anal. Chem. 1993, 65, 1373.

[7] K. Borgwarth, D.G. Ebling, J. Heinze, Ber. Bunsen-Ges. Phys. Chem. 1994, 98, 1317.

Ultrathin Silicon Dioxide: Growth and Characterization

S. Harasek, S. Golka, J. Smoliner and E. Bertagnolli

**Institute for Solid State Electronics, TU Wien,
Floragasse 7, 1040 Wien, Austria**

The technology of ultrathin solid films represents a key issue in microelectronic manufacturing. The continued shrinking of lateral dimensions has to be accompanied by an appropriate reduction of vertical dimensions to control short channel effects. As far as dielectric layers are concerned, silicon dioxide remains in the center of interest. In this work we investigate silicon dioxide layers of a few nanometers thickness grown by thermal oxidation. Electrical characterization of the oxide layers is performed by capacitance-voltage and current-voltage measurements. Comparison of the measured C-V curves with simulated curves shows that the simple MOS-capacitor model used for the simulation is well applicable within the ultrathin regime.

1. Introduction

The formation and characterization of ultrathin dielectric layers is of major importance in microelectronics. Due to the continuing reduction of lateral device dimensions, scaling of the vertical dimensions is required to maintain an appropriate gate control over the channel. In the field of dielectrics silicon dioxide still is the most important material. The gate oxide thickness of MOSFET devices is about to enter the ultrathin layer regime by now. Therefore the electrical properties of ultrathin layers with a thickness of only a few nanometers are of immanent technological interest. These properties are influenced by the growth process itself and post-oxidation processing steps. In this work, ultrathin oxides were thermally grown at intermediate temperatures. The oxidized substrates were integrated into a metal-oxide-semiconductor (MOS) capacitor scheme. Electrical characteristics of ultrathin silicon dioxide were investigated by capacitance-voltage (C-V) and current-voltage (I-V) measurements. The measured C-V characteristics were compared to curves resulting from simulation based on a simple analytical MOS model.

2. Experimental

P-type silicon (ρ = 14 Ωcm) wafers were oxidized by dry thermal oxidation in pure oxygen after a thorough RCA-clean. To investigate the influence of the oxidation temperature, oxidations were carried out at temperatures from 700 to 800 °C. Oxidation times were adjusted to yield the same oxide thickness (2.8 nm) in each experiment. The oxidized substrates were covered with aluminum by thermal evaporation and patterned using optical lithography and wet etching to form gate electrodes with an area of 1.2×10^{-4} cm^2. Al was sputtered for good backside contacts. The samples were subjected to a pre-metallization anneal at the temperature of the previous oxidation process in an inert atmosphere (N_2). The patterned samples were annealed in forming gas (post-metallization anneal) at 400 °C. Annealing times were varied from zero to a maximum of 30 minutes.

A HP 4156B semiconductor parameter analyzer and a HP 4284A LCR meter were used for electrical testing. Oxide thickness was determined from C-V curves at strong accumulation region without any correction and showed good agreement with ellipsometric thickness evaluation.

3. Simulation

In order to simulate the C-V characteristics of a MOS capacitor, the device is modeled as a series connection of a constant capacitance caused by the insulator (C_{Ox}) and the variable capacitance of the semiconductor depletion layer (C_D) [1]. C_D is accessible from (1):

$$C_D = \frac{\partial Q_S}{\partial \psi_S} \tag{1}$$

Q_S.....space charge
ψ_S.....surface potential

The space charge is related to the electric field at the surface of the semiconductor ($\mathscr{E}_S$) by (2):

$$Q_S = -\varepsilon_S \mathscr{E}_S \tag{2}$$

ε_S....dielectric constant of the semiconductor

Finally equation (3) describes the ideal relation between the electric field $\mathscr{E}$ and the potential ψ of the material:

$$\mathscr{E}^2 = \left(-\frac{d\psi}{dx}\right)^2 = \left(\frac{2kT}{q}\right)^2 \left(\frac{q p_{p0} \beta}{2\varepsilon_S}\right) \left[\left(e^{-\beta\psi} + \beta\psi - 1\right) + \frac{n_{p0}}{p_{p0}}\left(e^{\beta\psi} - \beta\psi - 1\right)\right] \tag{3}$$

ψ.....potential
x.....distance from surface
k.....Boltzmann's constant
T.....absolute temperature
ε_S.....dielectric constant of the semiconductor
q.....elementary charge
p_{p0}...equ. density of holes
n_{p0}....equ. density of electrons
$\beta = q/kT$

Knowing the values of C_D and C_{Ox} the overall capacitance and the voltage between gate and bulk is easily computed in dependence of the surface potential ψ_S. The exact position of the calculated curve along the voltage axis is determined from the difference in the work function of the gate metal and the silicon substrate. Since the areas of the stacked capacitors are relatively large, rim induced effects may be neglected in the simulation of the C-V characteristics.

4. Results and Discussion

The variation of the oxidation temperature shows that the C-V characteristic of the gate oxide is drastically improved if the oxidation temperature is increased. Fig. 1 shows the C-V curves of oxide layers grown at 700°C and 800°C respectively. Apart from this both samples underwent the same procedures including pre- and post-metallization anneal. The higher oxidation temperature leads to a well-behaved C-V curve with striking correspondence to the simulated characteristic (dashed line) thereby suggesting that the

simulated curve is valid as a measure of oxide quality. The oxide grown at 700°C on the other hand displays several imperfections like a shifted position along the voltage axis and a nearly constant capacitance from weak to strong accumulation which can be interpreted as a consequence of insulator leakage [2]. The shift of the curve from the ideal position, however, is due to a fixed charge (N_f) of about 1.10^{12} cm^{-2} in the oxide layer. This charge is obviously nearly totally absent when the oxidation is carried out at the higher temperature. Also the post-oxidation annealing procedures were found to be of major influence on the device behavior (Fig. 2).

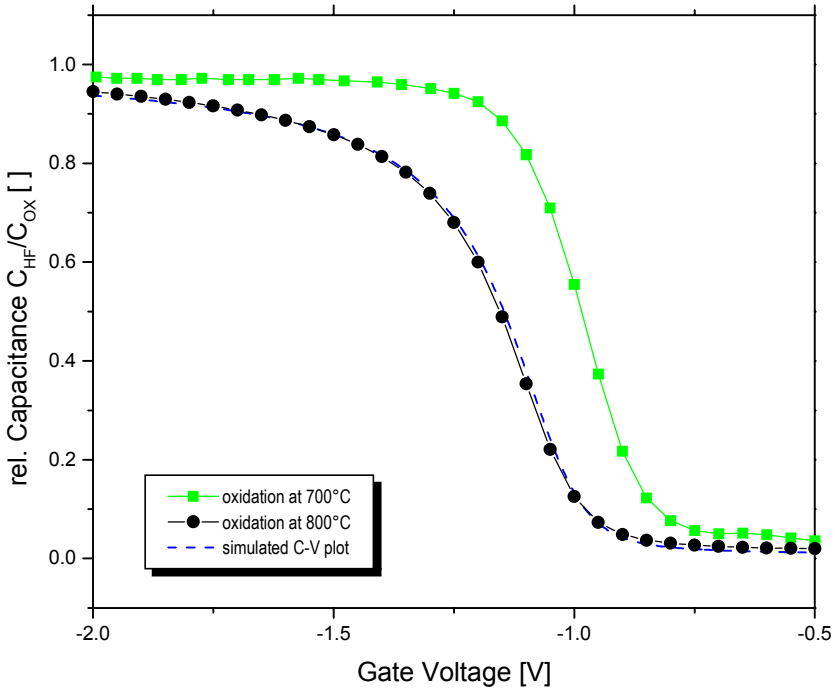

Fig. 1: Typical C-V characteristics showing the effect of different oxidation temperatures.

Without any further temperature treatment after the oxidation, the C-V plot displays a relatively large amount of fixed charge as well as a high density of interface traps which cause the typical stretch-out of the plot (squares). These defects are reduced by a pre-metallization anneal of 30 minutes (circles). Further improvement of the curve to almost the ideal shape of the simulation is achieved by a post-metallization anneal of 10 minutes. Longer heating times are of no desired effect since they in some cases lead to strongly increased gate leakage likely due to metal diffusion through the oxide. Fig. 3 displays a typical current-voltage plot recorded using a sample grown at 800 °C and annealed before and after metallization. The measured current densities are well within the expected range. The much smaller gate currents at positive voltage are due to formation of the depletion layer.

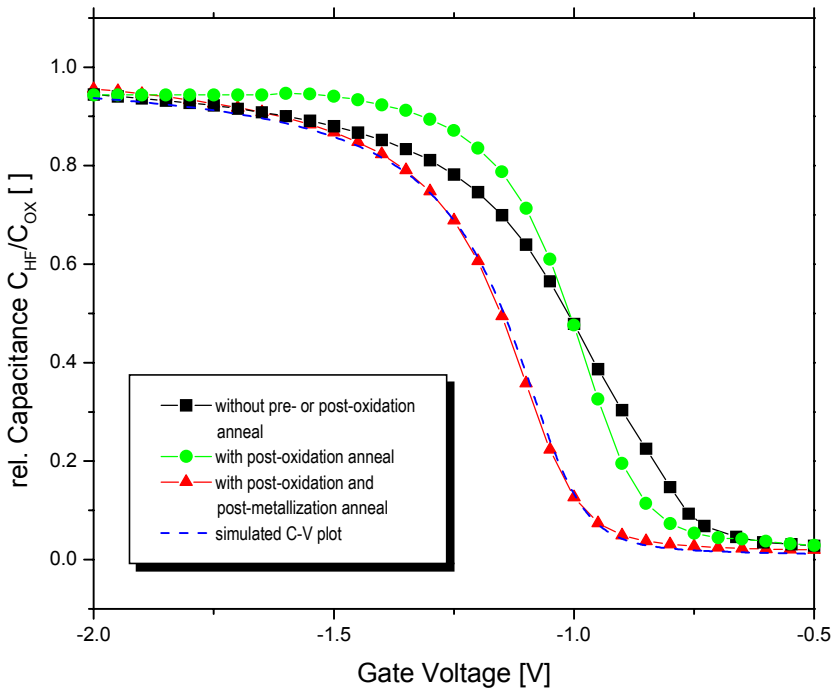

Fig. 2: The effect of annealing processes on C-V characteristics.

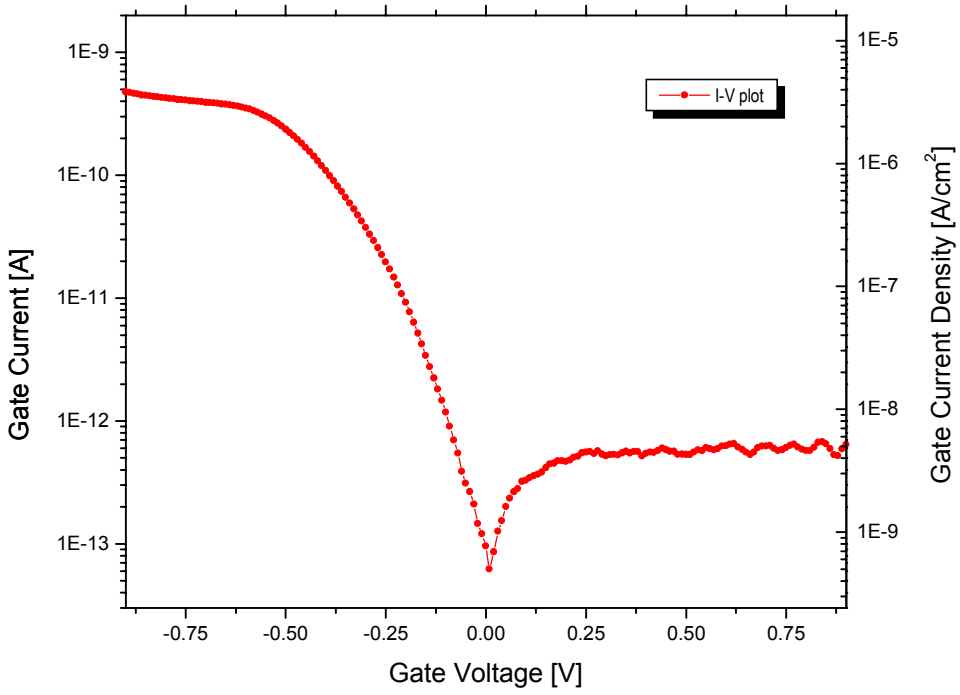

Fig. 3: I-V curve measured on a fully annealed sample grown at 800°C.

5. Conclusion

Ultrathin silicon dioxide films were thermally grown on p-type silicon at intermediate temperatures ranging from 700 °C to 800 °C and subjected to different pre- and post-metallization annealing steps. Electrical characterizations were performed by capacitance-voltage and current-voltage measurements and compared with simulated curves based on a simple MOS-capacitor model. Excellent agreement of simulation and measurements proved high predictability of electrical behavior and demonstrated applicability to the ultrathin regime. Thus these films are well suited for and have already facilitated pioneering work in demanding applications like scanning capacitance microscopy (SCM) [3].

References

[1] S.M. Sze: “Physics of Semiconductor Devices”, John Wiley, New York, 1981.

[2] W.K. Henson, K.Z. Ahmed, E.M. Vogel, J.R. Hauser, J.J. Wortman, R.D. Venables, M. Xu and D. Venables: "Estimating Oxide Thickness of Tunnel Oxides Down to 1.4 nm Using Conventional Capacitance-Voltage Measurements on MOS Capacitors", *IEEE Electron Device Lett.*, vol. 20, 1999, 179 – 181.

[3] B. Basnar, S. Golka, E. Gornik, S. Harasek, E. Bertagnolli, M. Schatzmayer and J. Smoliner: "Quantitative Scanning Capacitance Microscopy Investigations on p-doped Si-Multilayers", *J. Vac. Sci. Technol. B*, accepted for publication.

Coherent Terahertz Emission from Optically Pumped Parabolic Quantum Wells

R. Bratschitsch, T. Müller, G. Strasser, and K. Unterrainer

**Institut für Festkörperelektronik, TU Wien,
Floragasse 7, 1040 Wien, Austria**

We report on few-cycle terahertz (THz) emission from modulation-doped parabolic quantum wells. The quantum wells are optically excited by near-infrared femtosecond laser pulses. The observed THz emission corresponds to the intersubband plasmon of the parabolic quantum well. The emission frequency is independent of the number of optically generated carriers. We identify the excitation mechanism of the intersubband plasmon and hence THz emission to be ultrafast field screening. This mechanism allows for an optically driven THz emission from a completely symmetric nanostructure, in contrast to quantum beats which require a broken symmetry for their excitation.

1. Introduction

Recently, Sekine et al. [1] reported on the optically pumped emission of THz radiation from grating-coupled *intra*subband plasmons in a doped single quantum well. We present experiments which show that *modulation doped* parabolic quantum wells (PQWs) emit coherent THz radiation corresponding to the *inter*subband plasmon when excited by near infrared femtosecond laser pulses.

2. Experimental

The samples used in the experiments are modulation doped GaAs/AlGaAs PQWs, with widths in the range of 1200 – 2000 Å and carrier sheet densities of $1.7\text{x}10^{11}$ – $5\text{x}10^{11}$ cm^{-2}. We perform THz autocorrelation (AC) measurements where two temporarily delayed visible femtosecond laser pulses hit the sample. The emitted THz radiation is collected by parabolic mirrors and detected by a bolometer. The Fourier transform of the recorded AC signal then gives the spectrum of the coherent radiation emitted by the source. The samples are mounted in a continuous flow cryostat to cool them to approximately 5 K, and the whole setup is purged with nitrogen gas to avoid absorption of the THz radiation by water vapor.

Figure 1 shows an AC trace of a modulation doped PQW (W=1400 Å, n_{2D} = $5\text{x}10^{11}$ cm^{-2}) excited by 780 nm (τ_{FWHM} = 80 fs) laser pulses. The density of the optically generated carriers is kept well below the carrier density inside the PQW due to the modulation doping.

The spectrum of the emitted THz radiation (inset of Fig. 1) consists of two components, a broad one around 0.8 THz and a narrow one (FWHM: 0.3 THz) with a center frequency of 2.55 THz. These two emission peaks can be observed within a wide range of excitation wavelengths (815 – 760 nm).

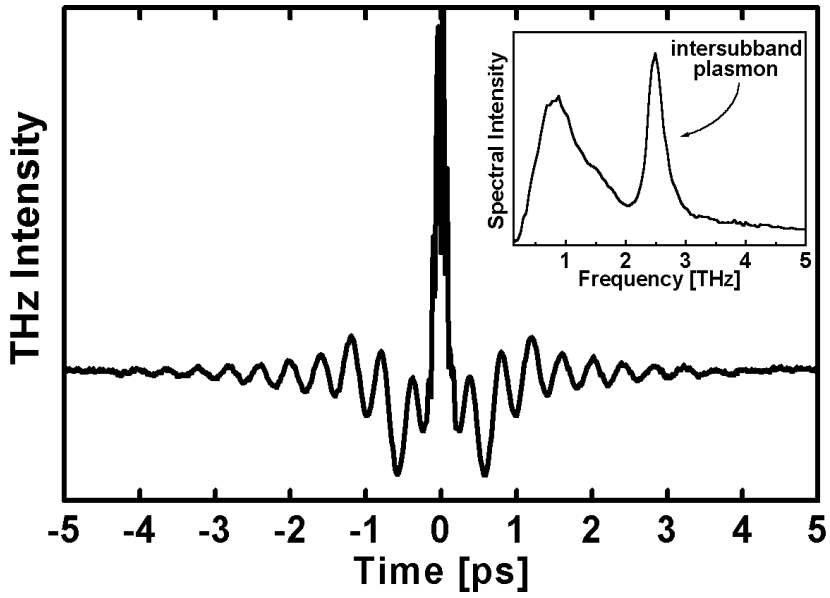

Fig. 1: THz autocorrelation signal of the 1400 Å PQW excited by 780 nm laser pulses (T = 5 K). Inset: Fourier transform of the recorded AC.

While the broadband component varies in frequency, the emission at 2.55 THz doesn't change. The low frequency broadband component is found with all the different PQW samples and shows roughly the same frequency dependence, i.e. it is independent of the PQW sample structure. The origin of the broadband component is due to THz generation at the surface of the sample [2].

The narrowband emission results from the oscillation of the carriers inside the PQW [3]. FTIR absorption and THz-Time Domain Spectroscopy measurements [4] show nearly the same resonance frequency of 2.2 THz which is the characteristic frequency of the intersubband plasmon of this PQW. The width of the THz emission line is as narrow as 0.2 THz for the 2000 Å PQW sample.

The excitation mechanism for the intersubband plasmon is due to screening of the surface depletion field by the electron-hole pairs injected by the ultrafast laser pulse [5]. In this way the electrons inside the quantum well experience a kick and begin to oscillate with their *eigenfrequency* (Fig. 2).

This is supported by the fact that the oscillation can be excited over a large wavelength range of the femtosecond pulses (815 – 760 nm). This large range implies that the excitation mechanism is clearly a non-resonant phenomenon, in contrast to THz quantum beat experiments. The difference between the two excitation mechanisms — quantum beats and ultrafast field screening — is also discernible when we perform THz emission experiments on an *undoped* PQW of the same width (L = 1400 Å). In this case no THz emission associated with the PQW can be observed, i.e. no quantum beats can be excited.

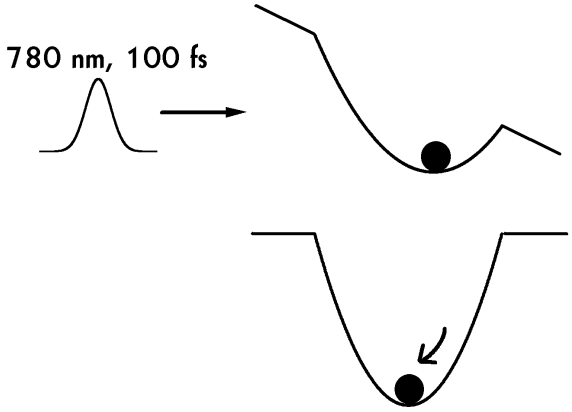

Fig. 2: Schematic drawing of the excitation mechanism: An oscillation of the carriers in the parabolic potential is initiated by ultrafast field screening.

3. Conclusion

We have demonstrated optically driven THz emission from intersubband plasmons in modulation-doped parabolic quantum wells. The excitation mechanism is due to screening of the surface depletion field by electron-hole pairs injected by an ultrafast laser pulse. Due to this non-resonant excitation mechanism, a completely symmetric nanostructure can emit optically driven THz radiation. THz emission due to quantum beats can be excluded since we observe no THz radiation from an identical but undoped PQW. The combination of the designability of the transition frequency, the narrowband emission, and the absence of any processing of the sample make modulation-doped PQWs attractive and easy-to-use THz emitters.

Acknowledgements

This work has been supported by the *Fond zur Förderung der Wissenschaftlichen Forschung* (START-Y47).

References

[1] N. Sekine, K. Yamanaka, K. Hirakawa, M. Voßebürger, P. Haring-Bolivar, and H. Kurz: "Observation of terahertz radiation from higher-order two-dimensional plasmon modes in GaAs/AlGaAs single quantum wells", *Appl. Phys. Lett.*, Vol. 74, 1999, 1006 – 1008.

[2] X.-C. Zhang, B. B. Hu, J. T. Darrow, and D. H. Auston: "Generation of femtosecond electromagnetic pulses from semiconductor surfaces", *Appl. Phys. Lett.*, Vol. 56, 1990, 1011 – 1013.

[3] R. Bratschitsch, T. Müller, R. Kersting, and K. Unterrainer: "Coherent terahertz emission from optically pumped intersubband plasmons in parabolic quantum wells", *Appl. Phys. Lett.*, Vol. 76, 2000, 3501 – 3503.

[4] R. Kersting, R. Bratschitsch, G. Strasser, K. Unterrainer, and J. N. Heyman: "Sampling a terahertz dipole transition with subcycle time resolution", *Opt. Lett.*, Vol. 25, 2000, 272 – 274.

[5] R. Kersting, K. Unterrainer, G. Strasser, H. F. Kauffmann, and E. Gornik: "Few-cycle THz emission from cold plasma oscillations", *Phys. Rev. Lett.*, Vol. 79, 1997, 3038 – 3041.

Band Structure Engineering for Terahertz Quantum Cascade Lasers

J. Ulrich, R. Zobl, W. Schrenk, G. Strasser, K. Unterrainer, E. Gornik

Institut für Festkörperelektronik,TU Wien,
Floragasse 7, 1040 Wien, Austria

We have investigated intra- and interwell transition schemes in magnetotransport and intersubband electroluminescence experiments regarding their potential as a central part of a terahertz quantum cascade laser. The conductivity of the interwell structure is smaller, indicating a reduced nonradiative scattering rate compared to the intrawell structure. The interwell transition exhibits a Stark shift, as expected. The intrawell transition shows a smaller shift which agrees with band structure calculations.

1. Introduction

The need of compact sources of coherent radiation in the frequency regime between 1 and 10 THz has stimulated the development of a terahertz (or far-infrared) quantum cascade (QC) laser [1] – [3]. A simple scaling of successful band structure concepts of mid-infrared QC-lasers [4] is impracticable because resonant emission of longitudinal optical (LO) phonons (in GaAs at 8.7 THz, 36 meV) cannot be utilized likewise, and fast non-radiative intersubband relaxation counteracts population inversion [1]. The relaxation rate decreases as initial and final subband of the laser transition are spatially separated by a barrier. Two band structure schemes (emission around 18 meV, 4.4 THz) have been compared, one based on an intrawell transition between the second and the first subband of one quantum well, the other based on an interwell transition between the first subbands of two adjacent quantum wells separated by a barrier [5].

2. Experimental

The samples consist of 50 periods of a 3-well system with GaAs wells and $Al_{0.15}Ga_{0.85}As$ barriers grown on n+-doped GaAs substrates employing molecular beam epitaxy. The central well of each period is lightly n-doped ($1x10^{16}$ cm-3). On top of the layer system is a 100 nm thick n+-doped GaAs contact layer. Calculated conduction band profiles of the two samples are shown in Fig. 1. The structures were designed for emission between the subbands denominated as |i> (initial) and |f> (final). The narrower quantum wells serve as an energy filter to extract electrons from |f> and inject them into the subband |i'> of the adjacent period. We processed emission samples as 4 (intrawell) or 32 (interwell) parallel ridge mesas, each of the dimensions 25 µm x 1000 µm, with 25 µm distance between them. These ridges are connected on both ends with two perpendicular mesas of 175 µm x 80 µm (intrawell) or 1575 µm x 80 µm (interwell), which serve as bond pads. The total surface of the mesas is 0.112 mm^2 (intrawell) or 0.924 mm^2 (interwell). The mesas were shaped by 4.3 µm deep reactive ion etching through the whole layer system into the substrate. Ohmic AuGe contacts were then produced on top of the mesa structure and on the backside of the substrate.

The magnetotransport- and electroluminescence measurements were performed in the same set-up [2]. The spectral response of an InSb cyclotron resonance photodetector was tuned in the magnetic field B of a superconducting magnet from 8.7 meV (B = 1 T) up to 26 meV (B = 3.4 T). The detector and the sample were located in a closed waveguide immersed in liquid He. A second magnet controlled the magnetic field oriented perpendicular to the epitaxial layers at the position of the sample. In all measurements we applied 22 µs long voltage pulses at 23 kHz repetition rate between the top and the back contact.

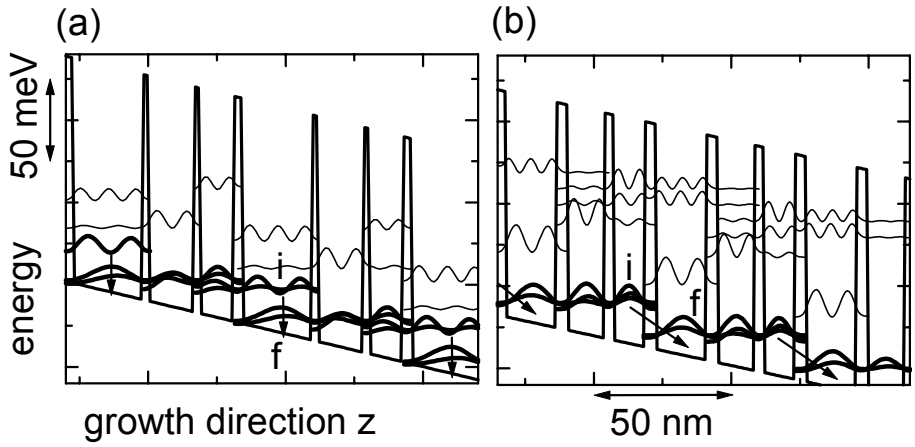

Fig. 1: Band structure calculation for 2½ periods of (a) the intrawell and (b) the interwell structure at an electric bias of 3.6 kV/cm. The moduli squared of the envelope wavefunctions of the involved subbands (thick lines) and of higher subbands (thin lines) are plotted at their energies. The radiative |i>-|f>-transitions are marked with arrows. The well- and barrier (underlined) widths in nm are: (a) 25.0 / 2.7 / 16.0 / 2.5 / 12.4 / 2.8 and (b) 18.5 / 4.0 / 13.5 / 3.3 / 11.4 / 4.0.

The conductivity of the two samples is remarkably different, for example, the current densities at a bias of 5 kV/cm are 419 A/cm^2 in the intrawell sample and 31 A/cm^2 in the interwell sample. This is a direct consequence of the different spatial overlaps between the |i> and |f> subbands. We conclude that the |i> – |f>-transition rate governs the transport through the whole structure. In a magnetic field the current is quenched in an oscillatory manner as depicted in Fig. 2(a). The quenching originates from a suppression of intersubband scattering caused by Landau quantization of the in-plane electron motion. The maxima in the current resemble magneto-intersubband resonances [6]. The knowledge of the resonance positions allows a determination of the subband energy difference. Identifying the current maxima with a change of Landau index of M = 2, 3, 4, 5 and using the GaAs effective mass $m^* = 0.0667\ m_e$, we derived the transition energies plotted in Fig. 2(c) versus the electric field. The data should be compared with the center frequency of the electroluminescence peak (solid circles). Some original spectra are given in Fig. 2(b). For a pure intrawell transition no first order Stark shift is expected since the centers of charge of |i> and |f> are at the same position. In the high bias region (F > 6 kV/cm) the energy of the transition is fairly field-independent (left panel of Fig. 2), whereas at low biases it changes from 17 meV (at 2 kV/cm) to 20 meV (at 6 kV/cm). The transition energy was calculated (Fig. 2(c), line) solving Poisson's and Schödinger's equations. Apart from an offset of 1.8 meV the experimental data are well

described by the calculation. The energy of the interwell transition (right panel of Fig. 2) suffers a clear Stark shift, visible in the magnetotransport as well as in the electroluminescence data. The linewidth is on the average 0.4 meV broader than that of the intrawell transition. This is consistent with the argument of alloy scattering in the barrier. The slope of the measured Stark shift is somewhat smaller than the one predicted by the calculation under the assumption of a homogeneous electric field.

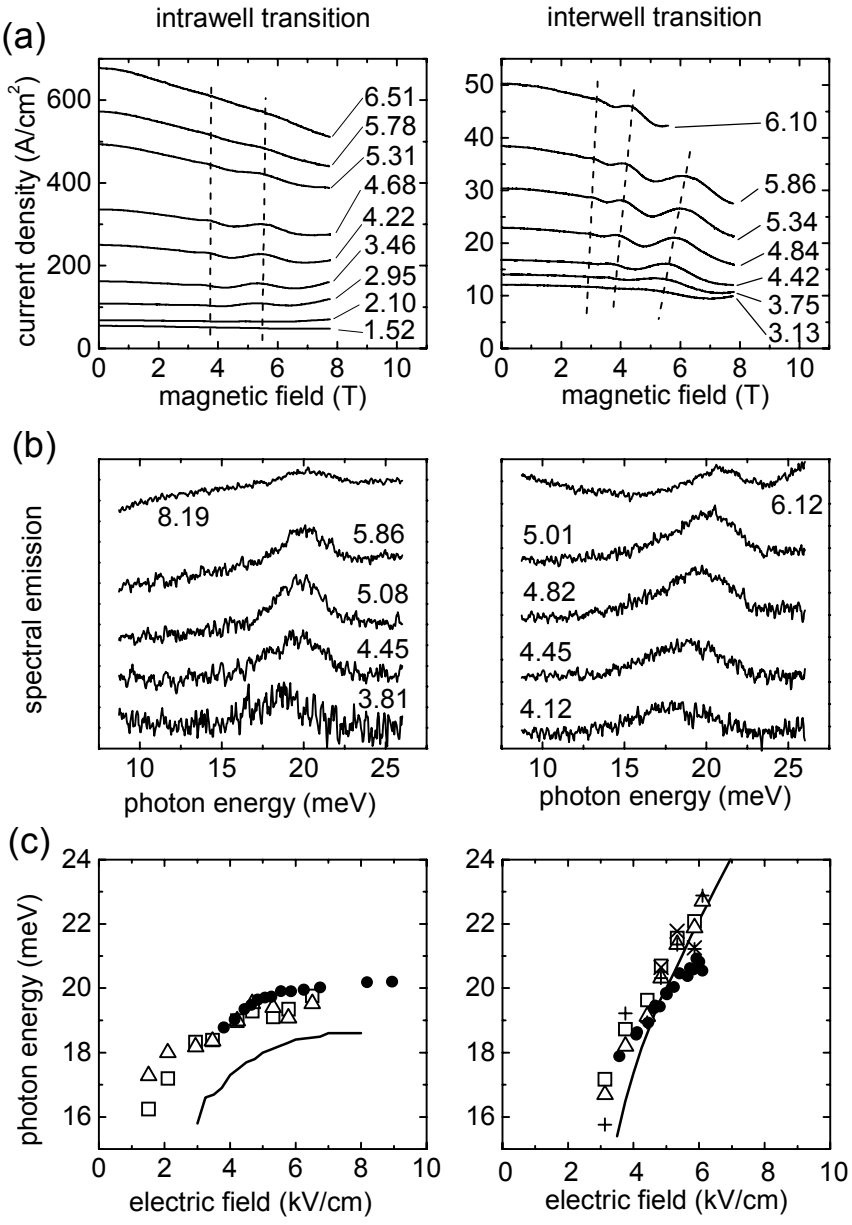

Fig. 2: (a) Current density versus magnetic field for various values of the electric field given in kV/cm. The dashed lines mark the magneto-intersubband resonances. (b) Electroluminescence spectra at electric fields as indicated in kV/cm. The spectra are plotted with arbitrary offsets. (c) Transition energy versus electric field extracted from the positions of the magneto-intersubband resonances for M = 2 (open squares), 3 (open triangles), 4 (+) and 5 (x); photon energy from the electroluminescence spectra (solid circles); and transition energy $E_i - E_f$ from Poisson-Schrödinger caculations (line).

3. Conclusion

Our comparison of an intrawell and an interwell quantum cascade structure yields: The interwell sample exhibits a Stark shift. This transition scheme could therefore form the basis of an electrically tunable source. The energy of the intrawell transition is also blue shifted in an electric field as the mixing of the transition subbands with those of the injectors is reduced. The lower current density of the interwell sample at an emission intensity, comparable to that of the intrawell sample, demonstrate the reduction of non-radiative scattering by spatial separation of the |i> and |f> subbands. A low scattering rate is an essential condition for population inversion and hence for lasing.

Acknowledgements

This work was supported by the Austrian Science Foundation (START Y47, Wittgenstein Award) and by the EU-TMR Program (INTERACT).

Reference

[1] M. Rochat, J. Faist, M. Beck, U. Oesterle, M. Ilegems: "Far-infrared (λ= 88 μm) electroluminescence in a quantum cascade structure" *Appl. Phys. Lett.*, vol. 73, pp. 3724 – 3726, 1998.

[2] J. Ulrich, R. Zobl, N. Finger, K. Unterrainer, G. Strasser, E. Gornik: "Terahertz electroluminescence in a quantum cascade structure", *Physica,* vol. B 272, pp. 216 – 218, 1999.

[3] B. S. Williams, B. Xu, Q. Hu, M. R. Melloch: "Narrow-linewidth terahertz intersubband emission from three-level systems", *Appl. Phys. Lett.,* vol. 75, pp. 2927 – 2929, 1999.

[4] J. Faist, F. Capasso, D. L. Sivco, C. Sirtori, A. L. Hutchinson, A. Y. Cho: "Quantum cascade laser", *Science,* vol. 264, pp. 553 – 556, 1994.

[5] J. Ulrich, R. Zobl, W. Schrenk, G. Strasser, K. Unterrainer, E. Gornik: "Terahertz quantum cascade structures: Intra- versus interwell transition", *Appl. Phys. Lett.,* vol. 77, 1928 – 1930, 2000.

[6] J. Ulrich, R. Zobl, K. Unterrainer, G. Strasser, E. Gornik: "Magnetic-field-enhanced quantum-cascade emission", *Appl. Phys. Lett.* vol. 76, pp. 19 – 21, 2000.

Ballistic Electron Spectroscopy of Quantum Mechanical Anti-reflection Coatings for GaAs/AlGaAs Superlattices

C. Pacher, M. Kast, C. Coquelin, G. Fasching, G. Strasser, E. Gornik

Institut für Festkörperelektronik, TU Wien,
Floragasse 7, 1040 Wien, Austria

It is demonstrated that a standard concept for optics, anti-reflection coatings, can be transferred to ballistic electron transport in semiconductor superlattices. This constitutes a further manifestation of the electronic wave nature in nanoscale devices. We demonstrated the counter-intuitive effect that the transmission through a superlattice is increased by a factor of 2.4 if two further barriers are added at both sides of the structure. Additionally we designed a new injector for ballistic electrons which increases the energy resolution of ballistic electron spectroscopy to approx. 10 meV for further studies.

1. Introduction

Ballistic electron spectroscopy is a suitable method to investigate both semiconductor bulk and heterostructure material properties. In Fig. 1 the scheme of a typical application, the spectroscopy of superlattice minibands [1], is shown.

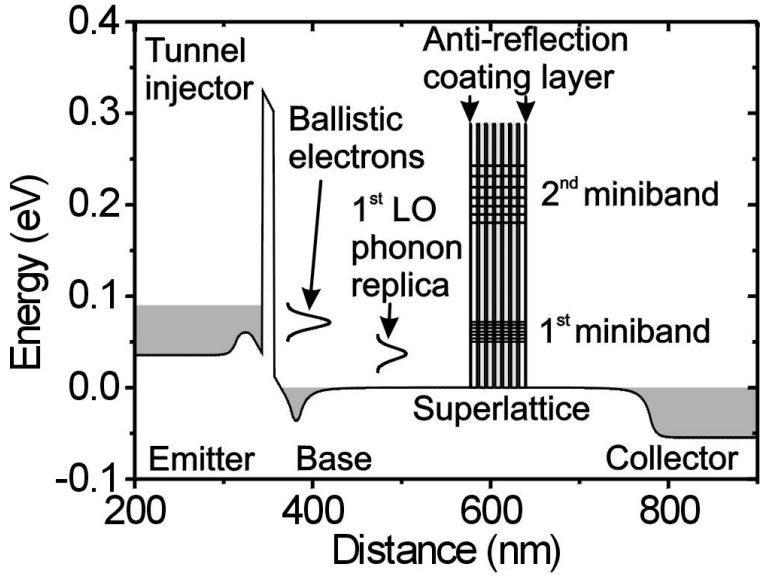

Fig. 1: Schematic bandstructure of a three-terminal device for ballistic electron spectroscopy.

By applying a DC voltage between the emitter and the base contact of a three-terminal device (3TD) hot electrons with a tunable energy are injected through a tunnel barrier

into a first drift region. This drift region serves the purpose to reduce quantum-confinement effects originating from the well formed by the injector barrier and the superlattice structure. After traversing the drift region the hot electrons hit the superlattice. In a third contact the electrons which have been transmitted through the superlattice are detected as collector current. From the ratio $\alpha = I_C/I_E$ of the measured currents at T = 4.2 K an energy-resolved spectrum of the superlattice transmission is obtained. The measured transfer ratio $\alpha(V_{BE})$ corresponds to the transmission function T(E) but peaks of T(E) get broadened due to the injected electron distribution, thus limiting the energy resolution of the spectrum.

2. Quantum Mechanical Anti-Reflection Coating

2.1 Theory

A quantum mechanical anti-reflection coating (ARC) for a superlattice (SL) consists in the simplest case of two additional barriers, one in front and one after the superlattice separated from the superlattice by a quantum well. In order to increase the transmission through the superlattice minibands these additional barriers have to be thinner than the barriers forming the superlattice. Using the transfer-matrix method in envelope function approximation including non-parabolicity we studied the transmission through a $GaAs/Al_{0.3}Ga_{0.7}As$-superlattice with five periods (barrier width 25 Å, well width 65 Å) while varying the width of the additional barrier and the distance to the superlattice. As a measure for the transmission we integrate the transmission *T(E)* over the width of the first superlattice miniband: $T_I = \int T(E) dE$. For the case where the well width between the superlattice and the ARC equals one superlattice well width (65 Å) the maximum of the transmission T_I is achieved when the barrier width equals *half* the width of the barriers constituting the superlattice (12.5 Å). From the calculations of T(E) for both samples shown in Fig. 2, a very strong enhancement of the integrated transmission for the first miniband (by a factor of 3.1) and a significant enhancement for the second miniband (+79 %) due to the additional barriers can be seen.

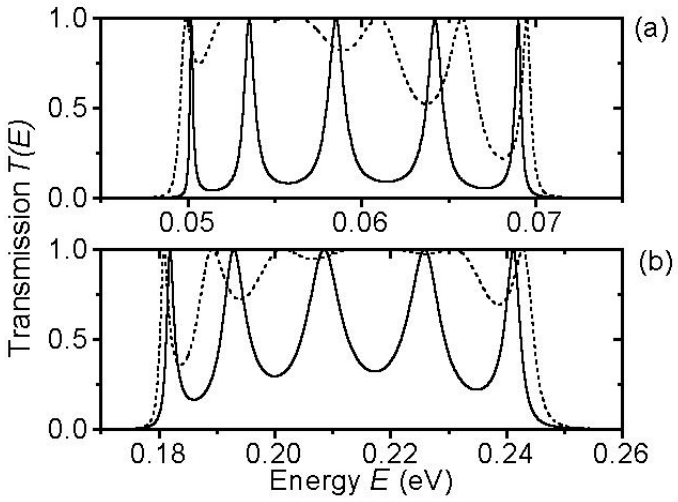

Fig. 2: Calculated transmission T(E) through a superlattice with (dotted line) and without (full line) anti-reflection coating. (a) first miniband, (b) second miniband.

2.2 Experiment

In Fig. 3 the measured transfer ratio α at T = 4.2 K as a function of the applied base-emitter voltage V_{BE}, which specifies the injection energy, is plotted for both structures. In both samples the first peak from the left corresponds to ballistic transport through the first miniband whereas the following peak originates from electrons that have emitted one LO phonon in the drift region in front of the superlattice structure. From the shape of the first peak we deduce that the miniband width and position are not influenced by the anti-reflection coating as is predicted by our calculations. From the peak values an increase of the transfer ratio by a factor of 2.4 is found. This agrees quite well with the average increase of 3.1 estimated from the envelope function calculation, thus showing the validity of the concept of anti-reflection coating for superlattice transport. For the second miniband we measured an increase in the transmission by a factor of 1.35 as can be seen in Fig. 3(b).

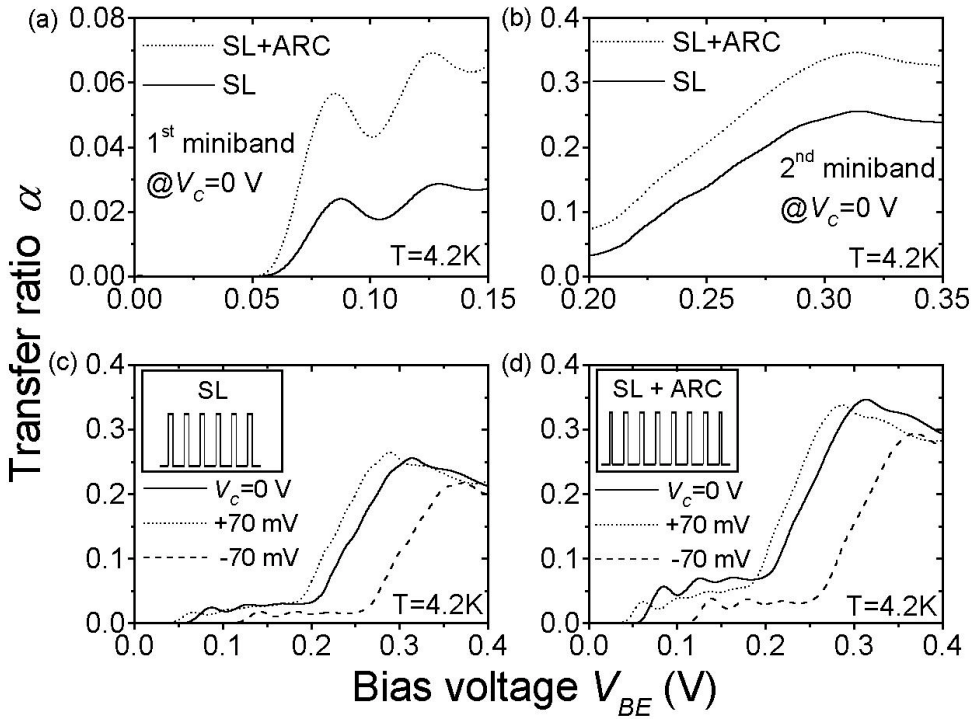

Fig. 3: Measured transfer ratios vs. bias voltage for superlattices with and without anti-reflection coating.

By applying a positive or negative voltage to the collector, the influence of an electric field on the electron transport has been studied. Fig. 3(c) and (d), show the transmission of both samples at collector bias voltages of +70 mV (dotted line), 0 mV (full line), and –70 mV (dashed line), respectively. The absolute value of the transmission of the first miniband (Δ_1 = 20 meV) does not depend on the direction of the applied electric field since the transmission time is much shorter than the dominant interface roughness scattering time ($\tau_I \approx 1$ ps). This situation is different for the second miniband. Since the miniband width (Δ_2 = 65 meV) exceeds the energy of an LO phonon ($\hbar\omega_{LO}$ = 36 meV), LO phonon scattering becomes the dominant scattering mechanism. For a positively biased superlattice LO phonon enhanced transport leads to an additional current in for-

ward direction. This is the reason for the asymmetric transmission in the second miniband with respect to the applied electric field (peak maximum in the positive bias case is larger than in the negative bias case) as can be seen in Fig. 3 (c) and (d). This effect can be observed in both samples, but is weaker in the sample with anti-reflection coating, although the superlattice is about 33% longer. The LO phonon scattering inside the second miniband leads to a phase loss of the electrons and is therefore the reason why the effect of the anti-reflection coating is reduced for the second miniband.

3. Injector Improvements

The aim of this work is to reduce the width of the ballistic electron distribution by optimizing the layer structure of the electron injector. This was achieved by a special doping profile in the injector. To measure the energetic width of the ballistic electron beam, a three terminal device was designed using a special triple barrier RTD as a narrow energy filter between base and collector. It consists of three $Al_{0.3}Ga_{0.7}As$ barriers and two GaAs wells. To get a transmission of the analyzer that forms a sharp energy filter with a FWHM of 1 meV at 100 meV we choose both well widths to be 4.2 nm and the center barrier (8 nm) twice as thick as the neighboring barriers (4 nm). The complete conduction band structure of the three terminal device is shown in the left part of Fig. 4.

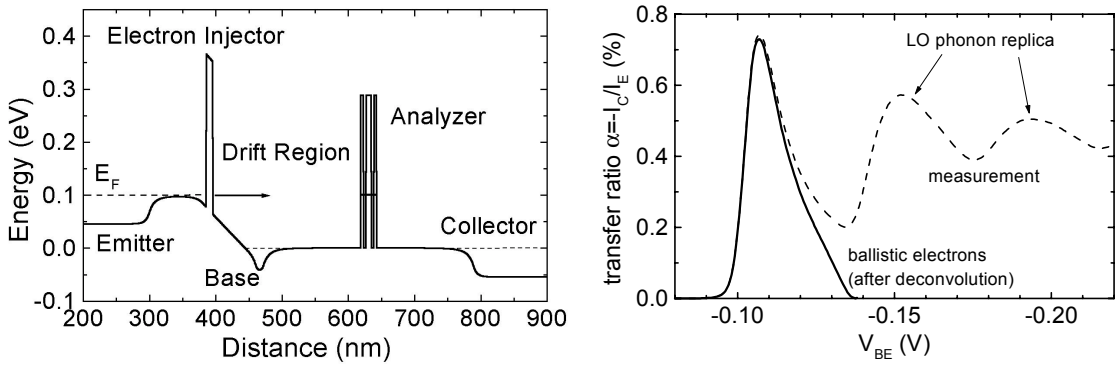

Fig. 4: Schematic bandstructure and transfer ratio for a three-terminal device with optimized injector and analyzer.

The transfer ratio vs. emitter bias is shown in the right part of Fig. 4. Due to the nearly δ-shaped transmission T(E) of the analyzer the first peak of the transfer ratio reflects almost directly the energy distribution of the ballistic electrons. The following peaks in the transfer ratio are due to electrons which are scattered by LO-phonons while traversing the drift region and which have lost 36 meV during the scattering processes. After deconvoluting [2] (thus removing the LO phonon replica) the transfer ratio and estimating the broadening due to the analyzer (≈3 meV) we get a full width at half maximum (FWHM) of the injected electrons of 10 meV.

4. Conclusion

In conclusion, we have demonstrated that the optical concept of anti-reflection coatings is of relevance for electron transport in semiconductor superlattices as well. We have shown that an increase of the transmission by a factor of 2.4 is possible by adding addi-

tional barriers of suitable width on both sides of the structure. These concepts will allow for a better design of various devices such as the quantum cascade lasers [3], where the introduction of such anti-reflection coatings may increase the transmission through the injectors significantly. We developed an injector with an ballistic electron distribution with a FWHM of 10 meV to increase the energy resolution for further experiments.

References

[1] C. Rauch et al., "Transition Between Coherent and Incoherent Electron Transport in GaAs/GaAlAs Superlattices**"**, *Phys. Rev. Lett.* vol. 81, pp. 3495 – 8, Oct. 1998.

[2] W. S. M. Werner, "Slowing down of medium energy electrons in solids", *Phys. Rev. B*, vol. 55, pp. 14925 – 34, June 1997.

[3] J. Faist et al., "Quantum cascade laser", *Science*, vol. 264, pp. 553 – 6, April 1994.

Ballistic Electron Emission Spectroscopy on Biased GaAs-AlGaAs Superlattices in Transverse Magnetic Fields

D. Rakoczy, G. Strasser, J. Smoliner

**Institut für Festkörperelektronik, TU-Wien,
Floragasse 7, 1040 Wien, Austria**

In this work, we introduce a metal-insulator-metal (MIM) injector structure as a solid-state version of ballistic electron emission spectroscopy (BEES) and utilize this structure for the investigation of the lowest miniband of a biased GaAs-AlGaAs superlattice in a transverse magnetic field. The ballistic electron current measured as a function of the collector bias shows a peak at flatband condition indicating coherent transport through the superlattice miniband. With increasing transverse magnetic field, the coherent transport decreases, i.e. the peak is quenched. Using an extended transfer matrix method, the observed effects are explained quantitatively.

1. Introduction

Ballistic electron emission spectroscopy (BEES) is a method to probe metal-semiconductor interfaces as well as the band structure of semiconductor heterostructures. In the form of a three-terminal extension of scanning tunneling microscopy (STM) [1], [2], BEES was initially used to determine Schottky barrier heights [3] – [6]. Later BEES was also applied to study subsurface structures, such as buried GaAs-AlGaAs double barrier resonant tunneling diodes [7], superlattices [8], [9], and self-assembled InAs quantum dots [10], [11]. The main advantage of STM-based BEES is an excellent spatial resolution, which can also be used for imaging nanostructures with ballistic electrons (BEEM). However, in some experimental environments, e.g. high transverse magnetic fields or temperatures in the mK range, conventional STM equipment is difficult to use. To avoid these obstacles one can replace the STM tip by a solid-state injector which is directly integrated on the sample under investigation. As spatial resolution is usually not required for purely spectroscopic applications, device based BEES is a useful supplement to STM-based BEES. In the literature there are several reports on devices for BEES, such as hot electron transistors on the basis of GaAs–AlGaAs heterostructures [12] or the injector structures introduced by Rauch et al. [13]. Yet one has to keep in mind that all these experiments were carried out on highly specialized molecular beam epitaxy (MBE) grown structures and, in addition, required an advanced sample processing. Therefore, we were looking for a versatile, robust and easy-to-produce solid-state emitter for ballistic electrons. A very promising candidate is a metal-insulator-metal (MIM) injector based on Al–Al_2O_3–Al, which can be used on virtually any substrate material, provided the quality of the Schottky contact between the aluminum base layer and the semiconductor is good enough. The first MIM injector for ballistic electrons was realized on bulk germanium by Spratt et al. [14], whose device proved to be suitable for operation as a hot electron transistor. First tests of our MIM injector [15] were carried out on various heterostructures, which we had previously investigated with

STM-based BEES. After proving that this type of injector is a suitable tool for BEES, we applied it to a sample with a superlattice and investigated its behavior in a transverse magnetic field.

2. Sample Preparation and Experimental Setup

To test our new emitter concept we compared two different types of MBE-grown GaAs–AlGaAs samples. The first consisted of GaAs only, while the other one had a single, 10 nm thick AlGaAs barrier 30 nm below the surface. All samples (also the superlattices) were grown with a very thin region of highly p-doped GaAs ("δ-doping") in the otherwise nominally undoped GaAs to provide a "flatband" condition at the surface. The pattern of our injector structure was defined by optical lithography and is shown in Fig. 1(a). To process the MBE grown samples, first ohmic contacts to the n^+ collector region were established using a standard Ge–Au–Ni–Au metallization. Prior to the evaporation of the Al base layer, the native surface oxide was removed by dipping the samples in a 1:1 solution of HCl (35%) and de-ionized water. Then a 150 Å thick Al layer was evaporated onto the sample, which serves both as a base electrode and for the growth of the Al_2O_3 tunneling barrier. The base metallization was oxidized at ambient conditions (cleanroom environment) for 30 min at 50 °C to form a protective layer on the Al base layer for the subsequent lithography step. To fabricate the tunneling barrier, a second oxidation step of 3 min duration at 100 °C was carried out after the lithography for the emitter pattern. As a last step, a 600 Å thick Al emitter electrode was sputtered on top of the sample. For the measurements the samples were cooled down to T = 4.2 K and, in case of the superlattices, exposed to transverse magnetic fields of up to 8 T (see Fig. 1(b)). In the following, V_E denotes the voltage between emitter and base, I_t the corresponding tunneling current, and I_c the collector current. V_c, the bias voltage between base and collector, causes a tilt in the conduction band profile.

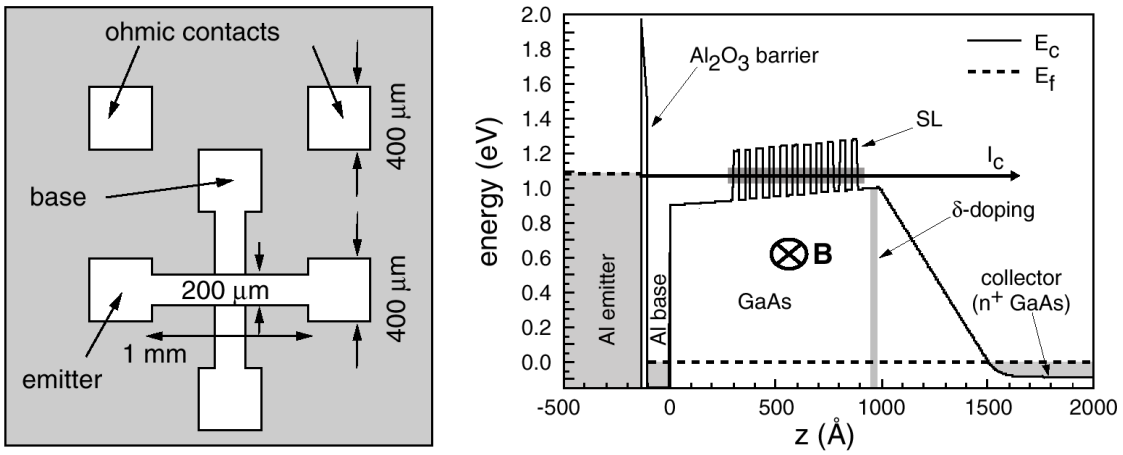

(a) (b)

Fig. 1: (a) Sample layout. (b) Schematic conduction band profile of our device applied to a sample with a superlattice. Below the AlGaAs barrier height only ballistic electrons with the proper energy to pass through the miniband (indicated by the gray area in the superlattice) contribute to the collector current I_c.

3. Experimental Results

For all samples the BEE spectra ($\alpha = I_c/I_t$ vs. V_E) show that the transfer ratio α is negligible up to a certain threshold in V_E and increases rapidly after this onset. The measured onset voltages agree very well with the values expected from the band profile parameters. For $V_c = 0$ V we obtain $V_{onset} = -0.803$ V for the sample without any barrier and $V_{onset} = -1.113$ V for the sample with one AlGaAs barrier [15]. The measured height of the AlGaAs barrier (i.e. the difference of the two onset voltages) is thus 310 meV, in good agreement with the results obtained by STM-based BEES on the same samples. The onset voltages and the shape of the BEE spectra were reproduced on several samples and also agree excellently with the calculated results. On the other hand the total amount of the ballistic current shows large deviations when measured on different samples. This seems to originate from variations of the quality of the Al_2O_3 barrier.

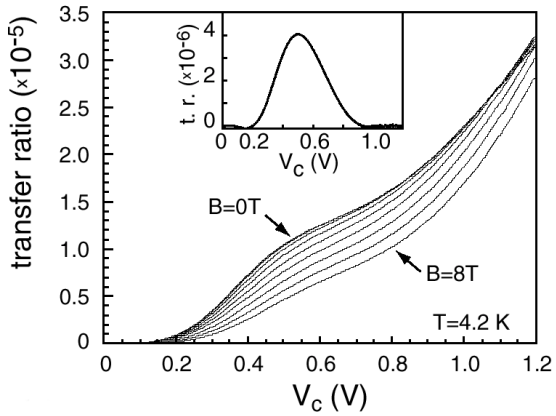

(a)

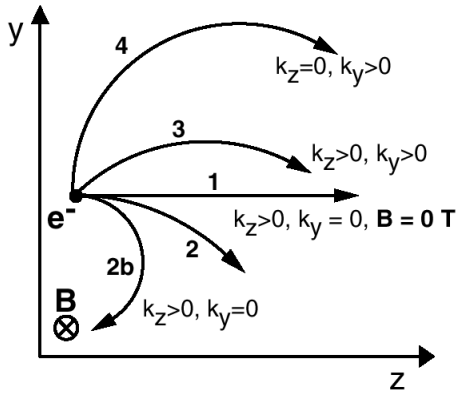

(b)

Fig. 2: (a) Measured transfer ratios vs. V_c for $V_E = -1.06$ V. The curves are measured at various B-fields from B = 0 T to 8 T in steps of 1 T (from left to right). At B = 0 T a peak at flatband condition is observed, which is quenched with increasing field. The inset shows the data for B = 0 T after background subtraction.
(b) Classical trajectories of electrons in a transverse magnetic field. Curve 1 shows a path without any B-field, the other trajectories are influenced by a B-field parallel to the x-axis. k_y, k_z denote the initial values of the momentum components. Curves 2 and 2b have identical initial momenta, but for 2b the B-field is higher.

Applying a positive voltage to the collector of the sample with the single barrier shifts the onset to smaller absolute values in V_E, just as expected from the band profile: $V_c > 0$ V means a lowering of the collector Fermi level which leads to a tilt of the band profile and therefore reduces the effective height of the AlGaAs barrier. The measured decrease in V_{onset} agrees very well with results from self-consistent calculations [15]. We also tested the behavior of the superlattice samples under bias before putting them into the magnetic field. These tests revealed that at zero bias the band structure of the superlattice is in fact slightly tilted, and an external collector voltage of $V_c \approx 500$ mV is needed to provide genuine flatband condition. This can also be seen directly in the measurement of the transfer ratio α in dependence of V_c for a constant emitter voltage (in the miniband regime, e.g. $V_E = -1.06$ V). After subtraction of a roughly exponential

background these curves exhibit a peak at flatband condition (see inset of Fig. 2(a)), indicating the transport through the miniband (the structure was designed in such a way that only one miniband exists below the AlGaAs barrier height). For flatband condition the onset voltage in the BEE spectra for this type of sample corresponds very well with the calculated lower edge of the miniband. A detailed description of the BEE spectra as well as a comparison with STM based BEES data can be found in [16].

The next step was to investigate the influence of the transverse magnetic field on the ballistic current. As one can already clearly see from the raw data in Fig. 2(a), the peak height in $\alpha(V_c)$ decreases with increasing magnetic field. This can already be explained by using the simple classical model of a charged particle in a transverse magnetic field (see Fig. 2(b)). The Lorentz force couples the k_y (parallel to the interface) and k_z (orthogonal to the interface) components of the electron momentum, whereas k_x, the component parallel to the B-field, stays unaffected. Due to the B-field, an electron can therefore lose k_z and gain k_y (and vice versa). Whether an electron is able to go through the superlattice or not depends on its kinetic energy associated with k_z, i.e. E_z. Electrons with an initial value of $k_y > 0$ can gain E_z via this mechanism, while all other electrons will always lose E_z. This diminishes the number of electrons with the right energy to pass the superlattice and leads to the observed change in the transmission.

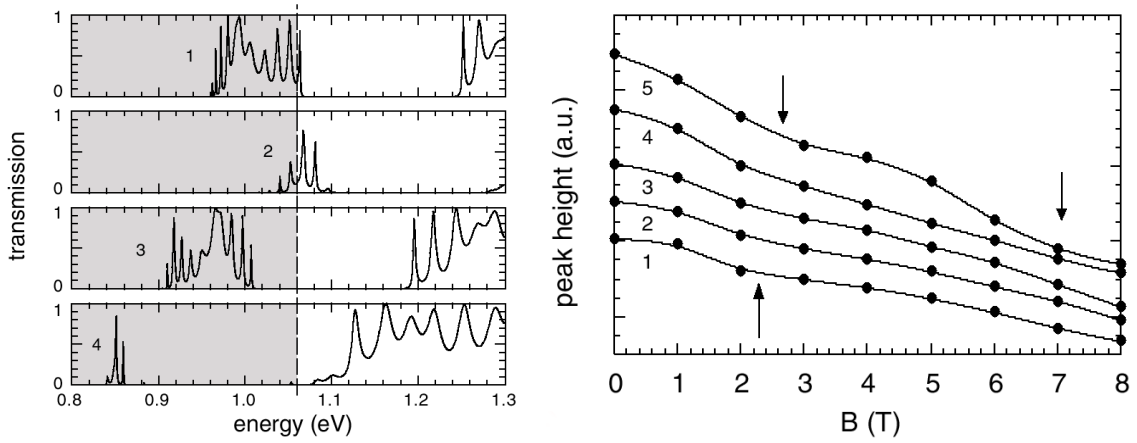

(a) (b)

Fig. 3: (a) Transmission coefficient of the superlattice for several parameter sets.
1: B = 0 T, E_y = 0 meV; **2**: B = 3 T, E_y = 0 meV; **3**: B = 3 T, E_y = 60 meV;
4: B = 8.2 T, E_y = 210 meV. The dashed line indicates the position of the Fermi energy in the emitter for V_E = –1.06 V.
(b) $\alpha(V_c)$ peak amplitude vs. B-field. The solid line is just a guide for the eye. Curves 1–5 correspond to V_E = –1.04, –1.05, –1.06, –1.07, and –1.08 V respectively. The phonon associated features are marked by arrows.

In the quantum mechanic treatment the B field results in an additional term in the Schrödinger equation, which can be treated as a magnetic field induced potential. With this, the transmission can be calculated using conventional transfer matrix methods [16]. Fig. 3(a) shows the transmission coefficient of our superlattice structure at flatband condition as a function of E_z, calculated for different magnetic fields and different initial values of k_y. Curve 1 was calculated for B = 0 T and $k_y = 0$. As one can see, the miniband is located between 0.96 and 1.07 eV. If B is increased the transmissive regime for

electrons with $k_y = 0$ is shifted to higher energy and becomes smaller (curve 2). However, in our experiment also electrons with positive and negative initial k_y values are injected. Electrons with $k_y < 0$ will be reflected back already at small B fields. On the other hand, electrons with positive k_y will gain E_z, which means that the transmissive range is shifted to lower values of E_z (curve 3). Despite this fact, more and more electrons are reflected back. Thus, the coherent current decreases, as it is observed experimentally. Curve 4 shows the situation for B = 8.2 T, E_y = 210 meV, and $E_z = V_b$, where V_b is the Schottky barrier height. Note that this is the highest possible E_y for V_E = -1.06 eV. For this case only a narrow transmission range exists just above V_b. If B is increased further (B > 8.5 T), the transmission is inhibited for all electrons below $e \cdot V_e$ = 1.06 eV.

Plotting the peak height in $\alpha(V_c)$ (after background subtraction, see inset in Fig. 2(a)) vs. B, we observe a decrease for all emitter voltages (see Fig. 3(b)). This decrease is not completely linear, but exhibits one or two kinks, which can be interpreted as a result of sequential LO-phonon emission inside the superlattice. Simple classical estimations show that without magnetic field, the electron transfer time through our superlattice structure (≈100 fs) is just somewhat smaller than the LO-phonon emission time (≈150 fs). In a transverse magnetic field, the transfer time increases, since the average z component of the electron velocity decreases. If the LO-phonon scattering time is exceeded, scattering will occur and the scattered electrons will no longer contribute to the coherent current. Thus, the peak amplitude decreases faster than normal. If B is increased further, a second scattering can occur, provided the electron energy is still high enough. The miniband is about 100 meV broad, therefore in principle allowing the emission of 3 phonons. At V_E = –1.08 V, where the Fermi energy in the emitter is approximately aligned with the top of the miniband, we see two kinks in the data, while for the other curves the second kink is not observable. The second peak at low emitter bias does probably not occur because at high B-field and low injection energy most of the electrons are already below the LO-phonon energy after the first scattering. The third peak is probably missing even at higher energies, since at 8 T the transfer time might still be too small for three sequential phonon emissions.

4. Conclusion

We have developed a MIM injector structure for BEES and used it to investigate the ballistic transport through a superlattice in a transverse magnetic field. We explained the observed behavior quantitatively with an extended transfer matrix method. Furthermore, indications for sequential LO-phonon scattering inside the superlattice, facilitated by the magnetic field via increased transfer times, can be observed.

Acknowledgements

This work was sponsored by the "*Fonds zur Förderung der wissenschaftlichen Forschung*" as project No. P12925-TPH and by the "*Gesellschaft für Mikroelektronik*".

References

[1] W. J. Kaiser and L. D. Bell, *Phys. Rev. Lett.*, **60**, 1406 (1988).

[2] L. D. Bell and W. J. Kaiser, *Phys. Rev. Lett.*, **61**, 2368 (1988).

[3] W. J. Kaiser et a.l., *Phys. Rev. B*, **48**, 18324 (1993).

[4] H. Sirringhaus, E. Y. Lee, and H. von Känel, *Phys. Rev. Lett.*, **73**,577 (1994).

[5] R. Ludeke, M. Prietsch, and A. Samsavar, *J. Vac. Sci. Technol. B*, **9**, 2342 (1991).

[6] M. Prietsch and R. Ludeke, *Phys. Rev. Lett.*, **66**, 2511 (1991).

[7] T. Sajoto et al., *Phys. Rev. Lett.*, **74**, 3427 (1995).

[8] J. Smoliner, R. Heer, C. Eder, and G. Strasser, *Phys. Rev. B*, **58**, 7516 (1998).

[9] R. Heer, J. Smoliner, G. Strasser, and E. Gornik, *Appl. Phys. Lett.*, **73**, 3138 (1998).

[10] M. E. Rubin et al., *Phys. Rev. Lett.*, **77**, 5268 (1996).

[11] W. Wu, J. R. Tucker, G. S. Solomon, J. S. Harris, Jr., *Appl. Phys. Lett.*, **71**, 1083 (1997).

[12] M. Heiblum et al., *Phys. Rev. Lett.*, **55**, 2200 (1985).

[13] C. Rauch et al., *Phys. Rev. Lett.*, **81**, 3495 (1998).

[14] J. P. Spratt, R. F. Schwarz, and W. M. Kane, *Phys. Rev. Lett.*, **6**, 341 (1961).

[15] R. Heer, et al., *Appl. Phys. Lett.*, **73**, 3138 (1998).

[16] D. Rakoczy, J. Smoliner, R. Heer, and G. Strasser, *J. Appl. Phys.*, **88**, 3495 (2000).

Infrared Quantum Cascade Laser

W. Schrenk, N. Finger, S. Gianordoli, L. Hvozdara, E. Gornik, and G. Strasser

Institut für Festkörperelektronik, Technische Universität Wien
Floragasse 7, 1040 Wien, Austria

We report on quantum cascade lasers in the AlGaAs material system grown on GaAs. The emission wavelength is in the range of $\lambda \sim 9.5$ - 13 μm. Both, first and second order distributed feedback laser have been fabricated. A metallized surface-relief grating is used for feedback to achieve single-mode emission. The emission wavelength is continuously tunable with the heat sink temperature. The second order distributed feedback lasers are efficient surface emitters with low beam divergence. Further, continuous wave operation at cryogenic temperatures has been achieved for a chirped superlattice active region.

1. Introduction

A quantum cascade laser (QCL) is a semiconductor laser involving only one type of carrier and which is based on two fundamental phenomena of quantum mechanics, namely, tunneling and quantum confinement. In conventional semiconductor diode lasers (as used, e.g., in compact disk players), the light originates from the recombination of electrons and holes, and the emission wavelength is determined by the bandgap. However, in QCLs the light generation is based on intersubband transitions within the conduction band (or valence band). So far, QCLs are demonstrated only in two material systems, the InGaAs/InAlAs material system grown on InP [1] and the AlGaAs/GaAs grown on GaAs [2]. Spontaneous emission from quantum cascade structures has been achieved in some other materials [3], [4]. Recently, room temperature operation of AlGaAs based QCL [5] has been demonstrated for Fabry Perot lasers, which is an important step towards commercial applications. Up to this, room temperature operation was a privilege for QCL grown on InP. Continuous wave operation of QCL is so far restricted to low temperatures [6], also for QCL grown on InP [7] – [9]. However, for absorption measurements like gas sensing, single mode lasers are favored. Therefore, distributed feedback (DFB) QCL [10] – [13] have been realized soon after the invention of QCLs. Some demonstration of infrared spectroscopy of gases [14] – [16] (single- or multiple pass absorption), liquids [17] or photoacoustic spectroscopy [18] show the potential for commercial applications. In this letter, we report on distributed feedback quantum cascade lasers in the AlGaAs material system grown on GaAs.

2. Experimental

The energy band diagram (conduction band) of a typical QCL is shown in Fig. 1. The electrons are injected into the upper laser level 3 by an electron funnel (injector). Inversion is achieved by fast depopulation of level 2 by LO-phonon emission (lifetime ~0.3 ps). Therefore the energy spacing of level 2 and level 1 is designed close to the LO-

phonon energy of GaAs (36 meV). The lifetime of the upper laser level is in the range of 2 ps, allowing fast direct modulation.

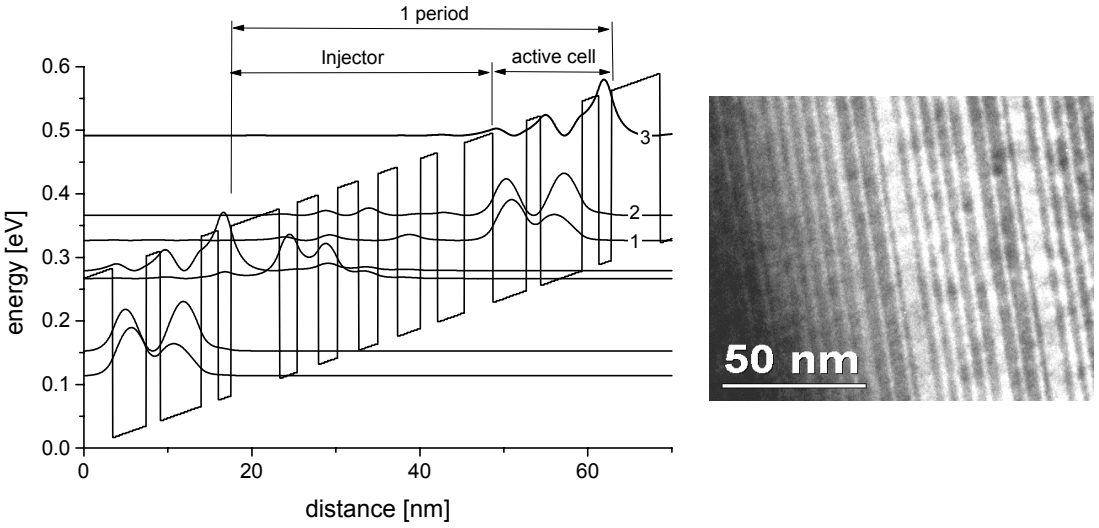

Fig. 1: Left: Energy band structure and moduli square of the most relevant wave functions of a QCL. The laser transition is the transition 3–2, and the energy separation of the level 2 and 1 is close to the LO-phonon energy. Right: Transmission electron microscope picture of a MBE grown QCL.

We have used $Al_{0.33}Ga_{0.67}As$ or AlAs as barrier material and GaAs or $In_{0.04}Ga_{0.96}As$ as well material for our lasers. The active cell is formed by three quantum wells or by a chirped superlattice. The superlattice is chirped in order to get flat minibands for the design field. The conduction band discontinuity and the energy of the upper laser level determines the leakage current into the continuum, which restricted the very first $Al_{0.33}Ga_{0.67}As$/GaAs based QCL to low operation temperatures as the upper laser level is close to the barrier energy (Fig. 1). In the first structures we used $Al_{0.33}Ga_{0.67}As$ as barrier material, where the X-valley is higher in energy than the Γ-valley in order to get rid of multi valley effects as the crossover from a direct to an indirect semiconductor occurs for $Al_xGa_{1-x}As$ at x~0.45. We have also investigated InGaAs as well material, which increased the band offset in respect to $Al_{0.33}Ga_{0.67}As$ [19]. The lattice mismatch of $In_xGa_{1-x}As$ grown on GaAs allowed only low In contents. Then we used AlAs as barrier material, where the overall Al concentration is small and the AlAs layers are very thin (down to 2 monolayers) so that the electrons remain around the Γ-valley. In this case, the lowest energy levels for the X-valleys (GaAs and AlAs) are higher than for the Γ-valley. An AlAs/GaAs chirped superlattice laser material showed the first time continuous wave operation for GaAs based QCL.

Our laser material is grown by solid source molecular beam epitaxy on n-doped GaAs (100). A double plasmon enhanced waveguide is used for all lasers. 30 to 40 periods of active cell/injector are cascaded and embedded into low doped GaAs (Si, $4x10^{16}$ cm^{-3}, d ~ 3.5 μm) layers, forming the low loss waveguide core. The cladding layers are formed by highly doped GaAs (Si, $4x10^{18}$ cm^{-3}, d ~ 1.0 μm).

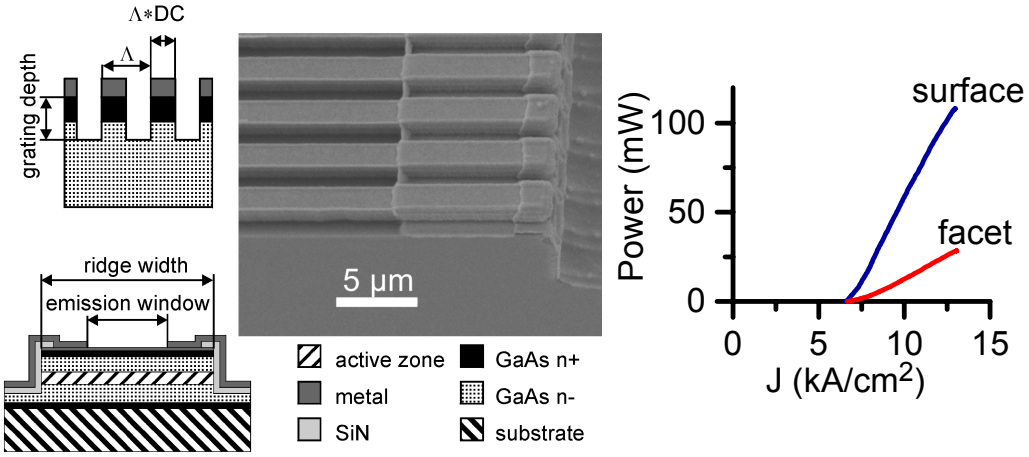

Fig. 2: Left: Schematic cross section of the grating region and the ridge waveguide, and a SEM picture of a fabricated laser. Λ denotes the grating period and DC is the duty cycle of the grating. Right: Emitted power via surface and one facet for a 2.99 mm long and 45 µm wide laser in pulsed mode operation (100 ns, 5 kHz).

We have fabricated DFB laser from several laser materials [6], [13], [20]. A metallized surface relief grating is used for feedback, resulting in a large contact area and avoiding the need of regrowth. The coupling coefficients and losses are calculated based on Floquet Bloch analysis [21]. The Floquet Bloch fields are rigorously calculated at resonance and a connection to the coupled mode theory is made by a perturbation method, as the optical intensity in the grating region is small. In the case of first order DFB laser the whole grating is covered with metal whereas in the case of the second order DFB laser only the grating peaks (Fig. 2) are covered with metal allowing efficient transmission of the TM polarized light through the metal stripe structure. We have fabricated ridge waveguides where we etched through the active region. The lateral light confinement is almost unity whereas the vertical light confinement by the plasmon enhanced waveguide (in growth direction) is in the range of 0.3 – 0.5.

The absolute average power is measured with a slow thermopile detector. The pulse peak power in pulsed mode operation (pulse length 100 ns) is in the several 100 mW range (Fig. 2). Spectral measurements where performed with a Fourier transform infrared (FTIR) spectrometer equipped with a mercury-cadmium-telluride (MCT) detector. As the current heats the active region, the emission wavelength is shifted to longer wavelengths during a pulse causing a broadening of the emission in pulsed mode operation. The current heating can be neglected for short pulses and low pulse repetition rates. The emission wavelength is in this case only a function of the heat sink temperature. The emission wavelength shifts according to the Bragg wavelength and the temperature dependence of the refractive index at a rate of $(d\lambda/dT)/\lambda \sim 1x10^{-5}/K$ (Fig. 3). In continuous wave operation the emission tunes with the current (Fig. 3) corresponding to temperature within the laser cavity.

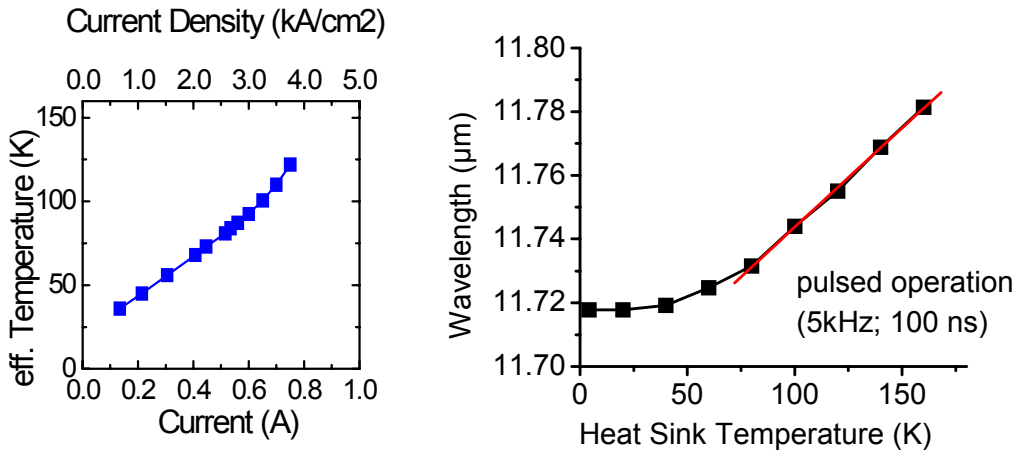

Fig. 3: Left: Effective temperature in the laser cavity for continuous wave operation as obtained from the emission wavelength (heat sink temperature 4.2 K). Right: Emission wavelength in pulsed mode operation (100 ns, 5 kHz) as a function of the heat sink temperature for the same laser.

3. Conclusion

In conclusion, we have achieved single mode emission in the mid-infrared from quantum cascade lasers grown on GaAs. The emission wavelength is continuously tunable by the temperature. We have developed an analysis which allows the accurate prediction of the coupling coefficient and the losses of the waveguide grating structure, including the surface emission of second order DFB lasers. Further, continuous wave operation at low temperatures has been achieved for a DFB laser emitting at 11.7 µm.

Acknowledgements

This work was partly supported by the European Community by the research projects SUPERSMILE IST-1999-1493 and UNISEL (Brite Euram III) BE97-4072 and the FWF Austria.

References

[1] J. Faist, F. Capasso, D. L. Sivco, C. Sirtori, A. L. Hutchinson, and A. Y. Cho, " Quantum Cascade Laser", *Science* **264,** 1994, pp. 553.

[2] C. Sirtori, P. Kruck, S. Barbieri, P. Collot, J. Nagle, M. Beck, J. Faist, and U. Oesterle, "GaAs/$Al_xGa_{1-x}As$ quantum cascade lasers", *Appl. Phys. Lett.* **73**, 1998, pp. 3486.

[3] G. Dehlinger, L. Diehl, U. Gennser, H. Sigg, J. Faist, K. Ensslin, D. Grützmacher, and E. Müller, "Intersubband Electroluminescence from Silicon-Based Quantum Cascade Structures", *Science* **290**, 2277 (2000).

[4] C. Becker, I. Prevot, X. Marcadet, B. Vinter, and C. Sirtori, "InAs/AlSb quantum-cascade light-emitting devices in the 3-5 μm wavelength region", *Appl. Phys. Lett.* **78**, 2001, pp. 1029.

[5] H. Page, C. Becker, A. Robertson, G. Glastre, V. Ortiz, and C. Sirtori, "300 K Operation of a GaAs based Quantum Cascade Laser at λ = 9 μm", *Appl. Phys. Lett.*, in print.

[6] W. Schrenk, N. Finger, S. Gianordoli, E. Gornik, and G. Strasser, "Continuous-wave operation of distributed feedback AlAs/GaAs superlattice quantum-cascade lasers", *Appl. Phys. Lett.* **77**, 2000, pp. 3328.

[7] J. Faist, F. Capasso, C. Sirtori, D. L. Sivco, A. L. Hutchinson, and A. Y. Cho, "Continuous wave operation of a vertical transition quantum cascade laser above T=80 K", *Appl. Phys. Lett.* **67**, 1995, pp. 3057.

[8] R. Köhler, C. Gmachl, A. Tredicucci, F. Capasso, D. L. Sivco, S. N. G. Chu, and A. Y. Cho, "Single-Mode Tunable Quantum Cascade Lasers in the Spectral Range of the CO_2 Laser at λ = 9.5-10.5 μm", *Appl. Phys. Lett.* **76**, 2000, pp. 1092.

[9] A. Tahraoui, A. Matlis, S. Slivken, J. Diaz, and M. Razeghi, "High-perfomance quantum cascade lasers (λ~11 μm) operating at high temperature (T ≥ 425 K)", *Appl. Phys. Lett.* **78**, 2001, pp. 416.

[10] C. Gmachl, J. Faist, J. N. Baillargeon, F. Capasso, C. Sirtori, D. L. Sivco, S. N. G. Chu, and A. Y. Cho, "Complex-Coupled Quantum Cascade Distributed-Feedback Laser", *IEEE Photonics Technol. Lett*. **9**, 1997, pp. 1090.

[11] J. Faist, C. Gmachl, F. Capasso, C. Sirtori, D. L. Sivco, J. N. Baillargeon, and A. Y. Cho, "Distributed feedback quantum cascade lasers", *Appl. Phys. Lett.* **70**, 1997, pp. 2670.

[12] D. Hofstetter, M. Beck, T. Aellen, and J. Faist, "High-temperature operation of distributed feedback quantum-cascade lasers at 5.3 μm", *Appl. Phys. Lett.* **78**, 2001, pp. 396 – 398.

[13] W. Schrenk, N. Finger, S. Gianordoli, L. Hvozdara, G. Strasser, and E. Gornik, "GaAs/AlGaAs distributed feedback quantum cascade lasers", *Appl. Phys. Lett.* **76**, 2000, pp. 253.

[14] C. R. Webster, G. J. Flesch, D. C. Scott, J. E. Swanson, R. D. May, W. S. Woodward, C. Gmachl, F. Capasso, D. L. Sivco, J. N. Baillargeon, A. L. Hutchinson, and A. Y. Cho,"Quantum-cascade laser measurements of stratospheric methane and nitrous oxide" *Appl. Optics* **40**, 2001, pp. 321.

[15] L. Hvozdara, S. Gianordoli, G. Strasser, W. Schrenk, K. Unterrainer, E. Gornik, C. S. S. S. Murthy, M. Kraft, V. Pustogow, B. Mizaikoff, A. Inberg, N. Croitoru, "Spectroscopy in the Gas Phase with GaAs/AlGaAs Quantum-Cascade Lasers", *Appl. Optics* **39**, 2000, pp. 6926 – 6930.

[16] A. A. Kosterev, F. K. Tittel, C. Gmachl, F. Capasso, D. L. Sivco, J. N. Baillargeon, A. L. Hutchinson, A. Y. Cho, "Trace-gas detection in ambient air with an thermoelectrically cooled, pulsed quantum-cascade distributed feedback laser"*Appl. Optics* **39**, 2000, pp. 6866 – 6872.

[17] B. Lendl, J. Frank, R. Schindler, A. Müller, M. Beck, and J. Faist, "Mid-Infrared Quantum Cascade Lasers for Flow Injection Analysis", *Analytical Chemistry* **72**, 2000, pp. 1645 – 1648.

[18] B. A. Paldus, T. G. Spence, R. N. Zare, J. Oomens, F. J. M. Harren, D. H. Parker, C. Gmachl, F. Capasso, D. L. Sivco, J. N. Baillargeon, A. L. Hutchinson, A. Y. Cho, " Photoacoustic spectroscopy using quantum-cascade lasers ", *Optics Lett.* **24**, 1999, pp. 178 – 180.

[19] S. Gianordoli, W. Schrenk, L. Hvozdara, N. Finger, G. Strasser, and E. Gornik, "Strained InGaAs/AlGaAs/GaAs-quantum cascade lasers", *Appl. Phys. Lett.* **76**, 2000, pp. 3361.

[20] W. Schrenk, N. Finger, S. Gianordoli, L. Hvozdara, G. Strasser, and E. Gornik, "Surface-emitting distributed feedback quantum-cascade lasers", *Appl. Phys. Lett.* **77**, 2000, pp. 2086.

[21] N. Finger, W. Schrenk, and E. Gornik, "Analysis of TM-Polarized DFB Laser Structures with Metal Surface Gratings", *IEEE J. Quant. Electron.* **36**, 2000, pp. 773.

Multi-Wavelength Laser Diode Array Based on Surface Mode Coupling

P.O. Kellermann, N. Finger, E. Gornik

Institut für Festkörperelektronik, Mikrostrukturzentrum, TU Wien, Floragasse 7, 1040 Wien, Austria

M. Ost, F. Scholz

4. Physik. Institut, Univ. Stuttgart, Pfaffenwaldring 57, 70550 Stuttgart, Germany

Multi-wavelength emission from a visible red GaInP/AlGaInP laser diode array has been achieved with the contradirectional surface mode coupling technique. The wavelength control is attained by postgrowth adjustment of the thickness of a surface waveguide. The horizontal cavity lasers show both edge and surface emission (beam divergence $0.1° \times 10°$). The individual elements show single-mode emission with a spectral linewidth of less than 0.1 nm and a sidemode suppression ratio up to 30 dB. The wavelength spacing between the elements is 0.76 ± 0.08 nm yielding a total range across the array of 5.4 nm (from 681.5 nm to 686.9 nm). The thermal red-shift of the wavelength is 0.028 ± 0.002 nm/K.

1. Introduction

The *wavelength division multiplexing* (WDM) scheme is utilized to increase significantly the transmission rate of optical communication systems. Monolithic arrays of multi-wavelength laser diodes are considered as a compact choice for WDM light sources. Lasers in the visible regime are suitable to be used as emitters in optical short-range data transmission since the attenuation minimum of *polymethylmethacrylate* (PMMA) fibers lies near 650 nm.

Wavelength shift in *distributed feedback* (DFB) laser arrays is achieved by changing the grating period of the individual elements requiring a very precise definition of the grating period [1]. Also, arrays of multi-wavelength *vertical cavity surface emitting laser* (VCSEL) diodes have been attained. The optical thickness of their layers is varying in the lateral direction on the wafer. The resonance wavelength of the microcavity can be adjusted after the epitaxial growth by oxidation of an AlGaAs adjustment layer [2] or the local growth rate of all the epilayers is controlled with the help of a topographically patterned substrate [3].

2. Experimental

We have developed a multi-wavelength surface emitting laser array with horizontal cavities. The wavelength of single array elements can be adjusted after the processing by just changing the optical thickness of a *surface waveguide* (SWG). If the Fabry-Perot mirrors are etched (not cleaved) the wavelength of laser groups can be monitored and adjusted automatically on the chip. The principle of the laser diodes is based on *surface*

mode coupling (SMC). Phase matching of the surface mode (propagating in the dielectric SWG) and the laser mode is achieved by a surface relief grating in the top cladding of the laser waveguide. The grating causes radiation losses of the laser mode (dominated by the emission into the substrate). The losses are reduced significantly in a narrow spectral range by the excitation and feedback process of the surface mode. The linewidth of this resonance is comparable to the longitudinal Fabry-Perot mode spacing of the laser cavity, thus providing an effective mode selection mechanism, which leads to single-mode emission. By adapting the thickness of the SWG phase matching of the surface and the laser mode is achieved at another emission wavelength. By choosing the appropriate grating period either co- (the laser and surface mode propagating in the same direction are coupled) or contradirectional (the counterpropagating modes are coupled) coupling is achieved. The surface mode couples both to the active region and into the vacuum light cone resulting in surface emission.

Recently, we have shown that a SMC laser exploiting contradirectional coupling leads to an increased SMSR [4]. This can be explained by the fact that the slopes of the intersecting dispersion curves differ much more and hence the resonance is five times narrower than for the codirectional SMC concept. The wavelength shift induced by a change of the SWG thickness is five times smaller for contradirectional SMC. This eases the wavelength adjustment and improves the insusceptibility against longitudinal variations of the SWG thickness. In this work, we realized for the first time a multi-wavelength laser array with the contradirectional SMC concept. The adjusting span was increased from 1.2 nm in Ref. 4 to 5.4 nm, the SMSR from 26 dB to 30 dB.

The GaInP/AlGaInP-lasers were grown by low-pressure metalorganic vapour-phase-epitaxy (MOVPE). Asymmetric cladding layers (by the aspect of thickness and refractive index) shift the electric field distribution of the laser mode towards the surface to achieve sufficient coupling. The second-order grating for the SMC is defined by holographic exposure of a spin-coated photoresist on the p-side of the laser structure. The pattern is etched into the top layers by ion milling (Λ = 270 nm, height 100 nm). The evaporation of semitransparent Au/Zn/Au stripes (5/5/20 nm, orientated perpendicularly to the surface grating) with a width of 10 µm defines the stripe-contacts of the lasers.

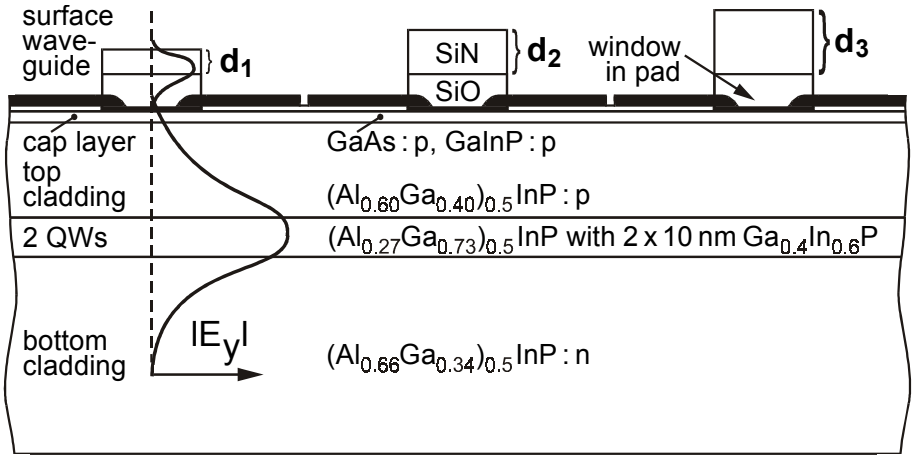

Fig. 1: Cross-sectional sample structure of three array elements. The semiconductor layers, surface waveguides (with different thicknesses), contact pads, windows, and optical mode profiles are indicated. The stripe-contacts are orientated perpendicular to the plane of the drawing. Different SiN-layer thicknesses of the surface waveguides result in different emission wavelengths.

Contact pads are evaporated on a polymid isolation and on the stripe contacts leaving a 5 µm wide window in the center of the contacts. Next the lasers are coated with ~170 nm SiO_x below ~335 nm SiN_x forming the SWG, which supports the TE_0 surface mode. The combination of one low- (SiO_x) and one high-index (SiN_x) dielectric layer avoids excessive leakage losses into the high-index substrate. The SWG thickness of individual lasers is adjusted by ion milling and photolithography. Thicknesses descending from ~505 to ~450 nm in steps of ~8 nm are realized on the finally cleaved laser bars. In Fig. 1 the cross-sectional sample structure of three array elements is sketched. The semiconductor layers, surface waveguides (with different thicknesses), contact pads, windows, and optical mode profiles are indicated. The stripe-contacts are orientated perpendicular to the plane of the drawing.

Single-mode edge emission is observed both in pulsed driven (AC) and continuos wave (CW) operation. The SMC laser diodes showed a threshold current density of 1 kA/cm^2 at a temperature of 10°C in AC and at –5 °C in CW operation. Spectra of an array with seven wavelengths due to seven different thicknesses of the SWG are shown in Fig. 2 (CW, 1.6 kA/cm^2, 0 °C). In the spectral center of the array the SMC-resonance (and thus the wavelength of the laser) falls together with the maximum of the active layer gain spectrum (~684.2 nm). This leads to a SMSR up to 30 dB as shown in the inset on the right side. With increasing distance to the gain maximum the light output intensity and the SMSR decrease. The smallest SMSR of 19 dB is depicted in the inset on the left side. The spectral linewidth achieved is <0.1 nm.

An average wavelength spacing between neighbored lasers of 0.76 ±0.08 nm is found yielding a total range across the array of 5.4 nm (from 681.5 to 686.9 nm). The SWG thickness increases in small steps of 7.9 ± 0.3 nm from 450 to 505 nm (as measured with a profilometer).

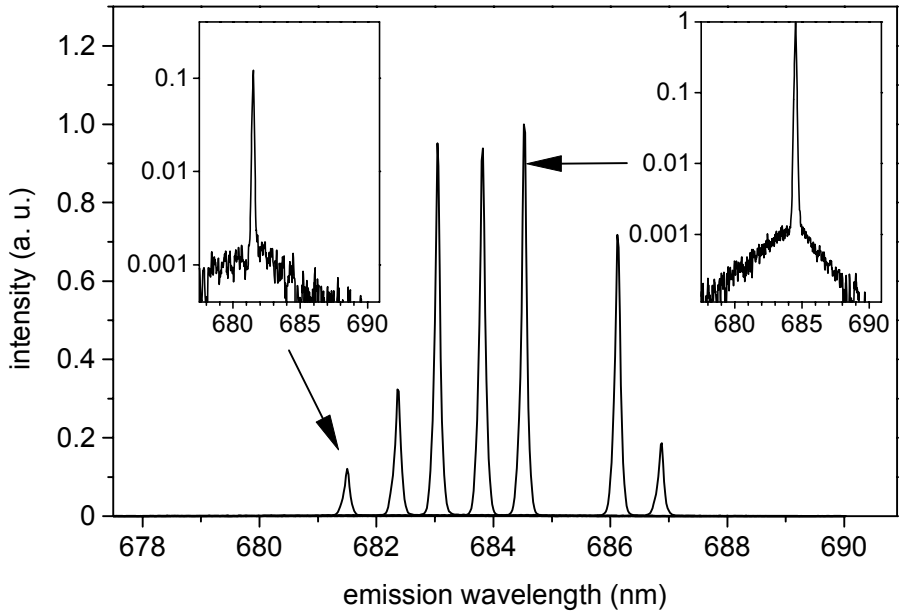

Fig. 2: Emission spectra of seven SMC lasers with seven different thicknesses of the SWG all joining the same array (CW, 1.6 kA/cm^2, 0 °C). Spectra with the smallest (19 dB) and highest (30 dB) SMSR are shown with a logarithmic scale in the insets.

The far-field pattern of the lasers was measured by scanning from one cleaved facet along the stripe contact to the other facet. The surface emission for a laser that emits at 683.7 nm is observed at $\alpha = \pm 47.5°$ with a beam divergence of 0.12°. The divergence in the azimuthal direction is 10°. The other array elements show a shift in α due to their different wavelengths. The shift in α between neighbored lasers is ~0.25°. The intensity emitted per solid angle via the surface beam is five times larger than the one at the edges. Presently a fraction of 2% of the whole light output power (7 mW at 1.6 kA/cm^2, 0 °C, CW) is emitted via the surface.

The thermal behavior $\partial\lambda/\partial T$ of an SMC-laser was compared with a Fabry-Perot laser, which was prepared on the same array. The wavelength of the SMC-laser increases with 0.028 ± 0.002 nm/K. The Fabry-Perot laser shifts with 0.12 ± 0.01 nm/K according to the bandgap shift. The small red-shift of the SMC-lasers is due to the fact that the wavelength is "locked" to the SMC resonance.

3. Conclusion

In conclusion, the contradirectional SMC technique for obtaining a multi-wavelength surface emitting single-mode laser array has been demonstrated with visible red GaInP/AlGaInP lasers. The wavelength control is achieved by postgrowth adjustment of the thickness of a surface waveguide. The wavelength spacing between the individual lasers is 0.76 ± 0.08 nm yielding a total range across the array of 5.4 nm. A SMSR up to 30 dB is reached.

An optimization of the red SMC laser array with the help of index- instead of gain-guiding is under progress. Increased surface emitted power, increased SMSR and a wider wavelength span are expected.

Acknowledgements

This work is partly supported by the Volkswagen-Stiftung (Germany).

References

[1] Y. Muroya, T. Nakamura, H. Yamada, and T. Torikai: "Precise wavelength control for DFB laser diodes by novel corrugation delineation method", *IEEE Photon. Technol. Lett.*, vol. 9, 1997, pp. 288 – 290.

[2] A. Fiore, Y. A. Akulova, J. Ko, V. Hegblom, and L. A. Coldren: "Postgrowth tuning of semiconductor vertical cavities for multiple-wavelength laser arrays", *IEEE J. Quantum Electron.*, vol. 35, 1999, pp. 616 – 623.

[3] S. Q. Luong, G. G. Ortiz, Y. Zhou, Jun Lu, C. P. Hains, J. Cheng, H. Q. Hou, and G. A. Vawter: "Monolithic wavelength-graded VCSEL and resonance-enhanced photodetector arrays for parallel optical interconnects", *IEEE Photon. Technol. Lett.*, vol. 10, 1998, pp. 642 – 644.

[4] P.O. Kellermann, N. Finger, W. Schrenk, E. Gornik; R. Winterhoff, H. Schweizer and F. Scholz: "Wavelength adjustable surface-emitting single-mode laser diodes with contradirectional surface-mode coupling", *Appl. Phys. Lett*., vol. 75, 1999, pp. 3748 – 3750.

Scanning Capacitance Microscopy on Epitaxial Si Layers

J. Smoliner[1], B. Basnar[1], S. Golka[1)], E. Gornik[1], B. Löffler [2], M. Schatzmayr[2], H. Enichlmair[2]

[1] Institut für Festkörperelektronik, TU Wien, Floragasse 7, 1040 Wien, Austria

[2] Austria Mikro Systeme International AG, Tobelbader Strasse 30, 8141 Unterpremstätten, Austria

In this work, the physical processes leading to contrast in Scanning Capacitance microscopy (SCM) are investigated both experimentally and theoretically. Using a p-type silicon epitaxial staircase structure we show that a monotonic dependence of the SCM signal on the doping level is only obtained if the tip bias is adjusted in a way that the sample is either in accumulation or depletion. In the transition region, the SCM signal is non monotonic because depending on bias, any doping concentration can yield a maximum SCM signal size. We also show that this behavior is in excellent agreement with the conventional model of a metal-oxide-semiconductor junction.

1. Introduction

Scanning Capacitance Microscopy [1] (SCM), an extension of conventional Atomic Force Microscopy (AFM), is a promising tool for semiconductor device characterization. The main application of this method is two-dimensional carrier profiling for failure analysis or process control especially on cross-sectional samples. The current state of the art of this technique can be found in the review articles [2] – [4]. However, SCM is not an easy and straightforward to use technique. In detail, quantitatively reproducible measurements are a serious problem, since sample preparation has a dramatic influence on the results especially in cross-sectional measurements. According to the literature, best results are obtained on samples polished with silica slurry [5], [6], followed by a low temperature oxidation in an oven [7], [8]. Usually temperatures below 350 °C are used to avoid diffusion processes which would lead to a broadening of the investigated doping profiles. Alternatively, irradiation with UV light and simultaneous oxidation through *in-situ* generated ozone [9], or a combination of these two approaches [10], [11] is employed.

In addition to these technical problems, the physical processes leading to contrast in SCM images are not fully understood. Recently, a non-monotonic behavior of the SCM signal for large dynamic range samples was observed, and the influence of the applied DC bias [12] was studied qualitatively. Further an influence of light on the SCM signal [13] was found. Apart from this, the influence of adsorbed water on the sample surface on the resolution has been published [14], [15].

To obtain quantitative results, calibration samples such as epitaxial staircase structures [16], [17] are often used. However, simple calibration attempts immediately fail when the investigated structure size reaches the order of the depletion length in the semicon-

ductor, or the diameter of the AFM-tip. Thus, intensive simulations were carried out to study the limitations of the calibration curve method for determining doping profiles [18]. In general it turns out that quantitative 2D doping measurements on small structures are obviously impossible without inverse modeling [19] or detailed simulations using empirical databases [20] – [22].

2. Experimental

In this work, we investigate the physical processes leading to SCM contrast both experimentally and theoretically. Using conventional Metal-Oxide-Semiconductor (MOS) theory [23], [24] and epitaxial staircase structures we show that the maximum SCM signal strongly depends both on doping and the applied bias. The sample we used was a CVD-grown doping staircase prepared by AMS (*Austria Mikro Systeme International AG*) and consists of five nominally 400 nm thick p-type Si-layers having doping concentrations of 2.1×10^{15}, 2.0×10^{16}, 1.7×10^{17} 2.2×10^{18} and 9.1×10^{18} cm^{-3}, respectively. The highest concentration is located at the sample surface. The substrate is p-doped silicon with a concentration below 1×10^{15} cm^{-3}. The dopant concentrations were determined by a SIMS measurement the result of which is shown in Fig. 1. To avoid the usual problems related to sawing and polishing procedures in sample preparation for cross-sectional AFM/SCM measurements the samples were cleaved and subsequently oxidized in UV-light [9] – [11]. For the back contact, sputtered aluminum was employed. The capacitance measurements were performed using the Dimension-3100 system with integrated SCM sensor (Digital Instruments, USA). The probes implemented for the investigations were conducting diamond tips (Nanonsensors, Germany) which turned out to be superior to metal coated tips due to their high resistance against abrasion. Space charge effects in such tips can be neglected as long as the dopant concentration in the tip (10^{20} at/cm^3) is much higher than in the sample.

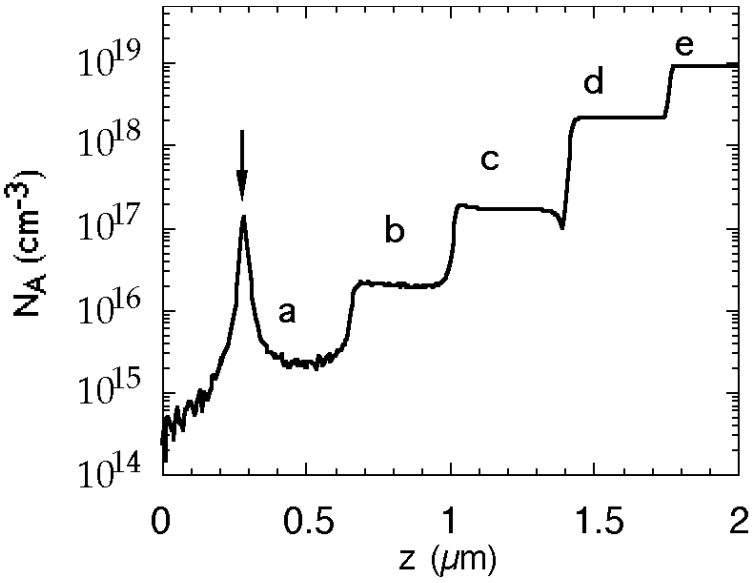

Fig. 1: Doping profile of our epitaxial staircase structure determined by SIMS. The sample surface is on the right hand side. The peak at z = 0.25 μm is an unintentional artifact of the epitaxial process.

Before we discuss our SCM data, we have to introduce the following important convention concerning the bias polarity: In analogy to textbooks on conventional MOS theory [23], [24], the bias in this work is always plotted in a way as if it would be applied to the AFM tip. In reality this is not the case, since in the DI-3100 SCM the bias is applied to the substrate for technical reasons. Finally, it needs to be mentioned that the SCM only measures the derivative of the capacitance, dC/dV, and not the capacitance itself.

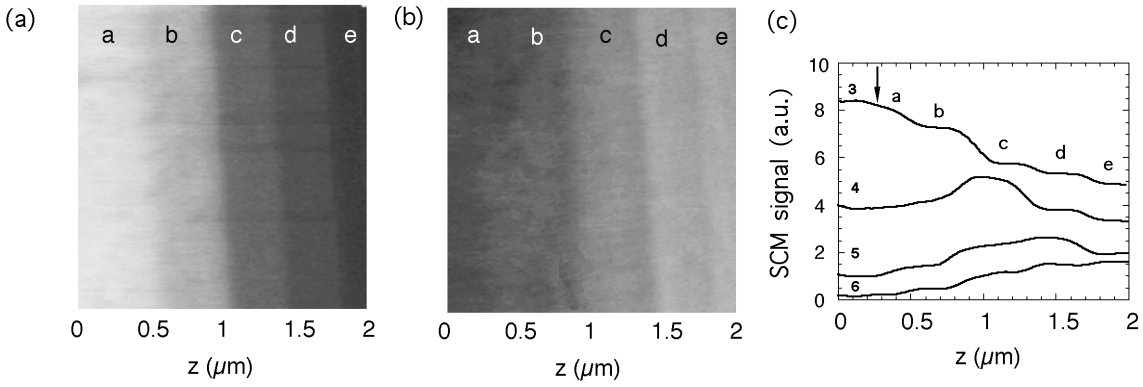

Fig. 2: (a) SCM image of our sample taken at a bias of –1.9 V. Image (b) was recorded at +0.8 V. The regions (a), (b), (c), (d) and (e) have doping concentrations 2.1×10^{15}, 2.0×10^{16}, 1.7×10^{17} , 2.2×10^{18} and 9.1×10^{18} cm^{-3} , respectively. (c): Sections through SCM images taken at a bias of +0.8 V, 0 V, –0.5 V and –1.9 V (curves 3-6). The numbering of the curves corresponds to the numbering in Figure 3.

Figure 2 shows cross sectional SCM images of our sample measured at two different bias values. The sample surface is on the right hand side. Figure 2(a) was measured at a tip bias of –1.9 V and Fig. 2(b) at V = +0.8 V. As one can see, the contrast between these two images is reversed. Figure 2(c) shows sections through SCM images perpendicular to the growth direction and measured at four different bias values. Two features are evident: First, the 400 nm wide differently doped layers are clearly visible as well defined steps in the SCM signal (see curve (3) e.g.). As a consequence we conclude that geometry effects of the tip can be neglected otherwise the steps would be washed out. This washout, however is nicely seen for the doping spike at the substrate interface, the position of which is marked by an arrow both in curve (3) and the SIMS data (Fig. 1). As the spike is much narrower than the steps and already in the same order as the radius of the tip (100 nm), only a small dip is observed in curve (3) instead of the expected well pronounced minimum.

As second feature in Fig. 2(c), the contrast dependence as a function of bias, can be seen in detail. At –1.9 V (curve 3), the SCM signal decreases with increasing doping. At +0.8 V (curve 6), however, this behavior is reversed and the SCM signal increases monotonically with increasing doping concentration For bias values of –0.5 V and 0 V the behavior is non monotonic, and the maximum of the SCM signal is observed in regions (c) and (d), respectively.

Although the bias induced contrast reversal was already reported in the literature [12], a detailed study of this behavior was not carried out up to now. To explain the origin of this behavior, we consider an ideal p-Si/SiO_2/Al junction as model system and use con-

ventional MOS theory. Figure 3 (a) shows the corresponding C(V) and dC/dV curves, where the y-axis of the dC/dV was flipped for better comparison with the experimental data. For the calculation an acceptor concentration of $N_A = 1x10^{16}$ cm^{-3}, an oxide thickness of 3 nm (a typical thickness for SCM), and no traps or surface charges were assumed. Other parameters could also be chosen, but have no qualitative influence on the obtained result. At low bias, the sample is in accumulation, which means that the capacitance is high, because it is mainly determined by the oxide thickness. The dC/dV peak marks flatband conditions, and above 0.9V, the area under the gate becomes depleted. To explain the non-monotonic behavior of the SCM contrast, we simply calculate dC/dV as a function of the acceptor concentration N_A at various constant bias values both in the accumulation and the depletion regime. As our considerations apply for n- and p-type samples and the sign of the SCM output depends on the phase adjustment of the built in lock-in amplifier, we consider the absolute value of dC/dV for convenience. The result of this calculation is shown in Fig. 3 (b) where the curve numbers correspond to the bias values marked by arrows in Fig. 3 (a). In accumulation (curves 1 – 3), the SCM signal always decreases exponentially with increasing doping. Further, the signal increases when the bias approaches the region of the maximum in the dC/dV curve. Under depletion conditions (curves 4 – 6), the situation is complex. For bias values close to the dC/dV maximum, the SCM signal shows a clear maximum for doping concentrations around $N_A = 1x10^{16}$ cm^{-3} (curve 4). This maximum shifts to higher concentrations when the sample goes deeper into depletion (curves 5, 6). In addition, the signal size decreases. At a bias of 1.1 V (curve 6) a situation is achieved where the maximum is close to $N_A = 1x10^{19}$ cm^{-3}. Above that bias, the SCM signal becomes very small but monotonically increases in the whole regime between $N_A = 1x10^{15}$ cm^{-3} and $N_A = 1x10^{19}$ cm^{-3}.

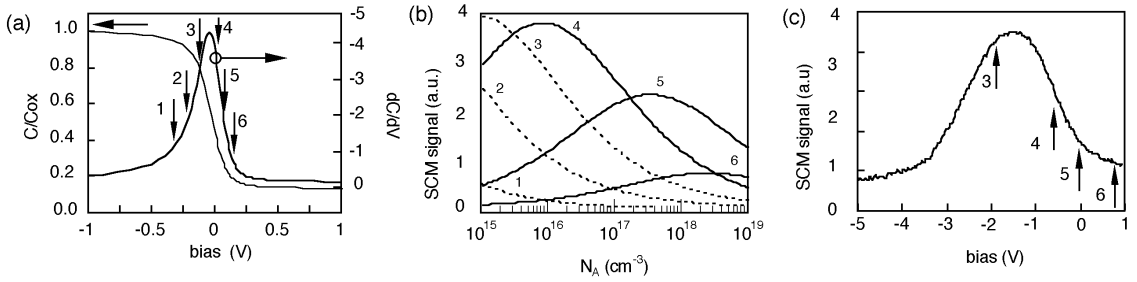

Fig. 3: (a) calculated C(V) and dC/dV curves of an ideal p-Si/SiO_2/Al junction. The y-axis of the dC/dV plot was flipped for better comparison with the experimental data. (b): SCM signal plotted as a function of N_A for different constant bias values as labeled in Figure 3(a). (c) typical dC/dV curve measured with our SCM. The arrows labeled with (3-6) indicate those bias values at which curves (3 – 6) in Fig. 2 (c) were taken.

If we now compare the measured SCM signal in the differently doped areas with the calculated behavior in Fig. 3(b), one can see that the experimental curves (3 – 6) in Fig. 2(c) clearly correspond to the calculated curves (3 – 6) of Fig. 3(b). Thus, it becomes clear why the SCM signal decreases with increasing doping concentration in accumulation and vice versa in depletion. In the transition regime, any doping concentration can yield highest contrast depending on bias.

To verify this further, we also measured dC/dV curves using our SCM. Figure 3(c) shows typical data. Again, the absolute value of the SCM signal is plotted for convenience. Compared to the calculated dC/dV curve of an ideal p-Si/SiO_2/Al junction (see Fig. 3(a)), the position of the peak is shifted to negative bias, which is due to surface charges and the use of a diamond tip having a different surface barrier height than aluminum. In addition, the peak is much broader, which is mainly due to the tip geometry [25]. The arrows (3 – 6) indicate the bias positions where curves (3 – 6) of Fig. 2(c) were measured. As one can see, bias positions (4 – 6) are located on the right hand side of the dC/dV peak, which is the bias regime where the sample moves from accumulation into depletion. At bias position (3) the sample is still completely in the accumulation regime. This good agreement nicely shows that the experimental situation indeed qualitatively corresponds to our idealized model system.

For practical SCM applications some conclusions can now be drawn: To obtain unambiguous results, the bias position of the maximum in dC/dV has to be known. Then, the bias should be chosen in a way that the sample is either in accumulation or depletion. According to our experience, the accumulation region yields more reproducible results, probably due to the fact that deep depletion is difficult to achieve because of the influence of the laser beam necessary for the AFM feedback control. Note that the dC/dV maximum shifts with doping concentration so that one has to stay in a save distance from the dC/dV maximum in order to avoid to enter the transition regime between accumulation and depletion by accident. Finally, care should be taken on samples where both p-type and n-type regions exist. If the bias is adjusted in a way that the sample is in accumulation in the p-type regions, it will be in depletion in the n-type regions. As a consequence, the contrast is reversed in the n-type region and also the signal will be small. Moreover, measurements at zero bias, as often found in the literature on pn-junction imaging, might yield unpredictable contrast behavior.

3. Conclusion

In summary, we have investigated the bias dependent SCM contrast on a p-type silicon doping staircase. We have found, that a monotonic behavior of the SCM signal as a function of doping is only obtained if the sample is either in sufficient accumulation or depletion. In the transition region, the behavior is non-monotonic, and the maximum SCM signal size depends both on doping concentration and applied bias. The observed behavior is in good agreement with conventional MOS theory and theoretically applies for p- and n-type samples.

Acknowledgements

This work was sponsored by: *Östrreichisches Bundesministerium für Verkehr, Innovation und Technologie*, *Fonds für innovative Projekte an der TU Wien*, *Gesellschaft für Mikroelektronik* (GMe) and *Fonds zur Förderung der wissenschaftlichen Forschung* (FWF) project No. Z24-TPH.

References

[1] D.D.Bugg, P.J.King, J.Phys. E21, 147 (1988)

[2] V.V. Zavyalov, J.S. McMurray, C.C. Williams, Rev. Sci. Instr. 7, 158 (1999)

[3] P. De Wolf, R. Stephenson, T. Trenkler, T. Clarysse, T. Hantschel, W. Vandervorst, J.Vac. Sci. Technol. B18, 361 (2000)

[4] R.Stephenson, P.DeWolf, T.Trenkler, T.Hantschel, T.Clarysse, P.Jansen, W.Vandervorst, Vac. Sci. Technol. B18, 555 (2000)

[5] F. Giannazzo, F. Priolo, V. Raineri, V. Privitera, Appl. Phys. Lett. 76, 2565 (2000)

[6] J.S. McMurray, J. Kim, C.C. Williams, J. Vac. Sci. Technol. B15, 1011 (1997)

[7] G.H. Buh, H.J. Chung, C.K. Kim, J.H. Yi, I.T. Yoon, Y. Kuk, Appl. Phys. Lett. 77, 106 (2000)

[8] J. Schmidt, D.H. Paoport, G. Behme, H.-J. Fröhlich, J. Appl. Phys. 86, 7094 (1999)

[9] J.J. Kopanski, J.F. Marchiando, B.G. Rennex, J. Vac. Sci. Technol. B18, 409 (2000)

[10] V. A. Ukraintsev, F.R. Potts, R.M. Wallace, L.K. Magel, H. Edwards, M.-C. Chang, AIP Conf. Proc. 449, 736-740 (1998)

[11] V.V. Zavyalov, J.S. McMurray, S.D. Stirling, C.C. Williams, H. Smith, J. Vac. Sci. Technol. B18, 549 (2000)

[12] R.Stephenson, A.Verhulst, P.DeWolf, M.Caymax, W.Vandervorst, Vac. Sci. Technol. B18, 405 (2000)

[13] C.C.Williams J.Slinkman, W.P.Hough, K.Wickramasinghe, Vac. Sci. Technol. A8, 895 (1990)

[14] N.Nakagir, T.Yamamoto, H.Sugimura, Y.Suzuki, Vac. Sci. Technol. B14, 887 (1996)

[15] S.Lany, Surf. Interface Anal. 27, 348 (1999)

[16] T.Clarysse, M.Caymax, P.DeWolf, T.Trenkler, W.Vandervorst, J.S.McMurray, J.Kim, C.C.Williams, J.G.Clark, G.Neubauer, Vac. Sci. Technol. B16, 394 (1998)

[17] J.S.McMurray, J.Kim, C.C.Williams, Vac. Sci. Technol. B15, 1011, (1997)

[18] J.F.Marchiando, J.J.Kopanski, J.Albers, J. Vac. Sci. Technol. B18, 414 (2000)

[19] Y.Huang, C.C.Williams, J.Slinkman, Appl. Phys. Lett. 66, 344 (1995)

[20] J.F.Marchiando, J.J.Kopanski, J.R.Lowney, J. Vac. Sci. Technol. B16, 463 (1998)

[21] L.Ciampolini, M.Ciappa, P.Malberti, W.Fichtner, V.Ranieri, (preprint, submitted)

[22] J.J.Kopanski, J.F.Marchiando, J.R.Lowney, J. Vac. Sci. Technol. B14, 242 (1996)

[23] S.M. Sze, Physics of Semiconductor Devices, John Wiley & Sons Ltd, New York, 1981

[24] E.H. Nicollian, J.R. Brews, MOS (metal oxide semiconductor) physics and technology, John Wiley & Sons Ltd, New York 1982

[25] L.Ciampolini, private communication

Laser-Interferometric Investigation of Triggering Behavior in CMOS and Smart Power ESD Protection Structures

M. Litzenberger, C. Fürböck, R. Pichler, S. Bychikhin, D. Pogany, E. Gornik

Institute for Solid State Electronics, Vienna University of Technology, Floragasse 7, 1040 Wien, Austria,

K. Esmark, G. Groos, H. Gossner, M. Stecher

Infineon Technologies, Munich, Germany

We report on noninvasive laser-interferometric thermal and free carrier mapping in electrostatic discharge (ESD) protection devices during a high current stress. The method is based on monitoring the changes in the silicon refractive index due to thermo-optical and plasma-optical effects. We study the homogeneity of bipolar transistor triggering along the device width in CMOS and smart power technology devices. The measured optical phase shift due to temperature and concentration changes is in a good agreement with the results of device simulation.

1. Introduction

Protection of electronic circuits against electrostatic discharge (ESD) is becoming a more and more important issue with the scaling down of technologies [1] and using the electronics in steadily harsher environment as e.g. in automotive applications [2]. Due to the high energy dissipated during the ESD pulse, the self-heating effect is a dominant failure cause in the ESD protection devices [1]. Due to non-linearities in bipolar conduction, the current flow in the device may be inhomogeneous leading to destructive hot spots. Therefore, thermal mapping is of great importance for hot spot identification and for experimental verification of simulation models [2] – [4]. We have recently developed a laser-interferometric thermal mapping technique for non-invasive investigation of thermal distribution and free carrier concentration changes in ESD protection devices under high current stress [5] – [7]. In this contribution we present the study of triggering homogeneity, thermal and free carrier distribution, and dynamics in CMOS and smart power technology ESD protection devices.

2. Results and Discussion

Devices studied are grounded gate- (gg) n-MOSFETs of 0.35 μm process (gate width is 100 μm) [3] and smart power ESD bipolar transistor protection devices [2] (see Fig. 1). The thermal energy distribution and free carrier concentration changes in devices are studied using a heterodyne interferometric technique [5], [6]. The temperature or carrier concentration change during a high current stress causes a modulation of the silicon refractive index which results in a phase shift of an infrared laser beam probing the device from the polished backside. The phase shift is a superposition of thermal and free carrier contributions. They can be distinguished by sign and different time evolution of the

phase signal [6]. The devices were stressed by rectangular current pulses using a transmission line pulser or a DMOS high-current switch. All measurements are performed under the snapback operation where the bipolar conduction occurs in the device.

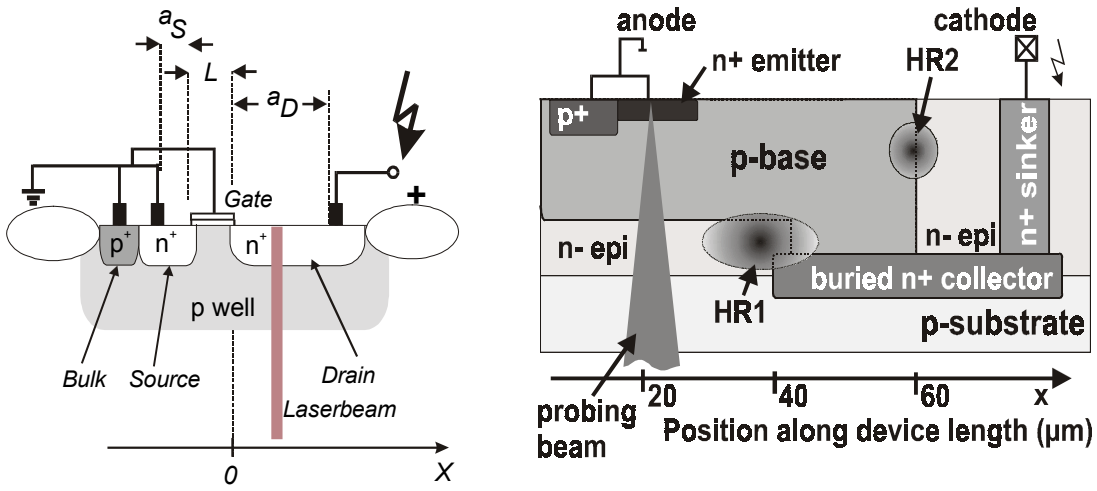

(a) (b)

Fig. 1: Cross section of (a) gg-n-MOSFET and (b) smart power ESD protection devices. Probing beam is indicated. HR1 and HR2 in (b) indicate the location of regions with dominant heating.

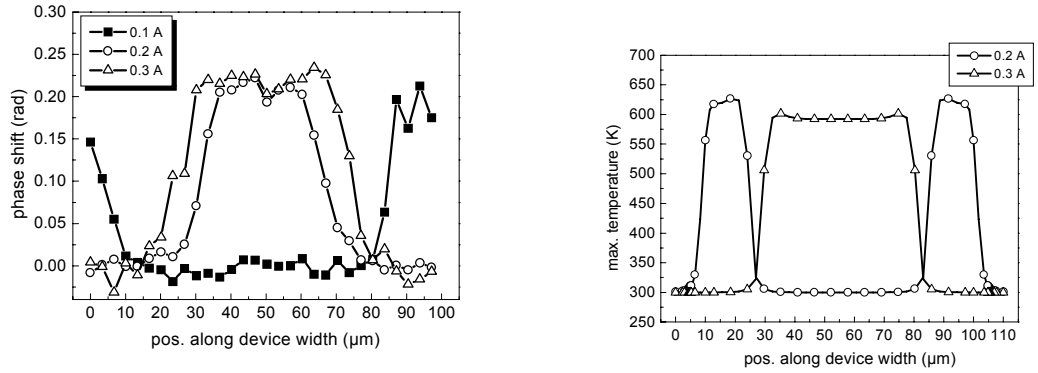

(a) (b)

Fig. 2: (a) Phase shift distribution at the end of 100ns ESD pulse along the width of a gg-n-MOSFET with the stress current as parameter. (b) Simulated current density distribution in the same device.

The trigger homogeneity along the gate width in gg-n-MOS devices is studied at low stress currents. The probe beam is located on position where heat dissipation along the device length is maximal (i.e. at the drain edge of the channel, see Fig. 1(a)). Figure 2(a) shows the measured phase shift distribution along the device width as a function of the stress current. As the holding voltage is nearly current independent, the phase shift represents, in the first approximation, the current density (current per unit of device width). At low stress currents (I_S = 0.1 A) the device triggers preferentially at corners. This is

due to a high electric field at the drain/bulk junction curvature at the corners, and consequently higher hole base current density, which promotes the transistor triggering at the corners. When I_S increases, the triggered place switches to the middle of the device. With a further increase in I_S the triggered width increases, until the device is completely triggered. The change of triggering place from the corner is caused by a lower distributed drain resistance in the device middle, which makes the current conduction in the center energetically more favorable. This trigger behavior can qualitatively be reproduced by an isothermal three-dimensional device simulation using DESSIS^{ISE} (see Fig. 2(b)). At even higher stress currents, when the device is completely triggered, the current conduction along the width is homogeneous until the stress level (I_S > 1 A) where the device fails due to a formation of destructive current filaments [8].

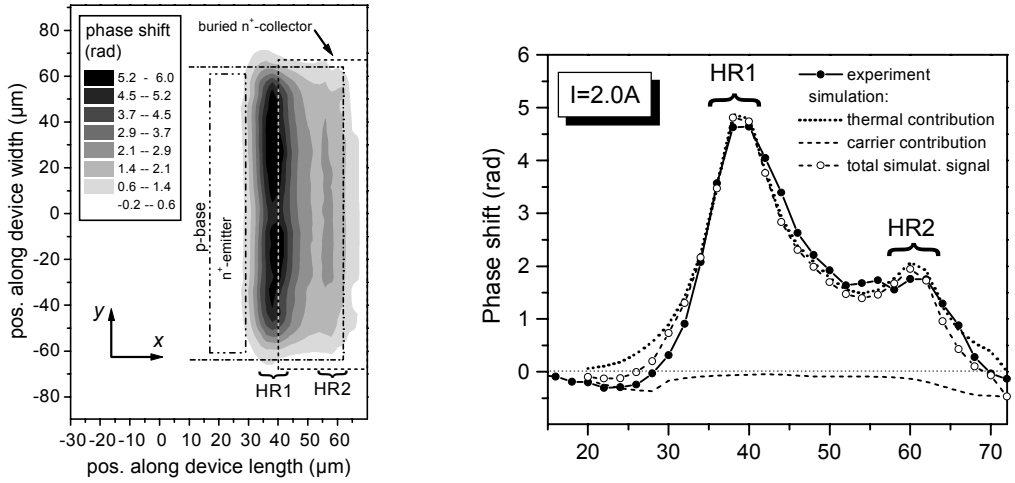

(a) (b)

Fig. 3: 2D distribution (a) and a cross section (b) of phase shift at the end of a current pulse of 170ns duration and I_S = 2A in a smart power ESD protection device (cf. Fig.1(b)).

Because of a larger characteristic feature size in smart power ESD devices, the trigger homogeneity in these devices is studied by performing two-dimensional phase shift mapping in lateral directions. The phase shift distribution along the device length at the end of the stress pulse of I_S = 2 A shows one dominant heat dissipated region (HR 1) and a region with a smaller local temperature maximum (HR 2), see Fig. 3(a). The temperature distribution along the device width is nearly homogeneous, with a slight temperature increase at device corners, probably due to lateral current crowding effect (Fig. 3(a)). Figure 3(b) shows a phase shift distribution along the device length in the middle of the device (y = 0, cf. Fig. 3(a)). The two hot regions HR1 and HR2 can clearly be distinguished. In addition, a region with a negative phase shift can be found under the emitter region. The latter is attributed to a negative phase shift contribution caused by electron injection from the emitter to the base. The electro-thermal two-dimensional device simulation using DESSIS has revealed that the region HR1 (HR2) is related to the heat dissipation due to a vertical current flow from the emitter to the buried layer (due to a subsurface lateral current flow between the p-base and n-sinker), see Fig. 1(b). As the devices at this stress current level trigger homogeneously, the experimental phase shift can be compared to a simulated phase shift. The latter was calculated as a sum of

thermal and free carrier contributions, using the integrals of simulated temperature and free carrier distribution along the optical beam path. The agreement between the simulation and experiment is excellent (see Fig. 3(b)). For better distinction of the free carrier and thermal contributions to the total phase shift, these are also given in the figure.

3. Conclusion

The laser interferometric method is a useful characterization tool for study of thermal and free carrier distribution and dynamics in ESD protection devices in ns time domain. An inhomogeneous triggering at low stress currents has been found and explained in gg-n-MOSFET devices. Two hot spots due to a lateral and vertical current path have been revealed in the smart power ESD protection devices. The results are in good agreement with the simulation.

References

[1] Amerasekera A and Duvvury D. ESD in silicon integrated circuits. J Wiley & Sons, 1995.

[2] Gossner H, Müller-Lynch T, Esmark K and Stecher M, "Wide range control of the sustaining voltage of ESD protection elements realized in a smart power technology. *Proc. EOS/ESD Symp.*, 1999, pp. 19 – 27.

[3] K. Esmark, W. Stadler, M. Wendel, H. Gossner, X. Guggenmos, W. Fichtner: "Advanced 2D/3D ESD device simulation- A powerful tool already used in a pre Si Stage", *Proc. EOS/ESD Symp.*, 2000, pp. 420 – 429.

[4] K. Esmark, C. Fürböck, H. Gossner, G. Groos, M. Litzenberger, D. Pogany, R. Zelsacher, M. Stecher, and E. Gornik, "Simulation and experimental study of temperature distribution during ESD stress in smart-power technology ESD protection devices", *Proc. Int. Reliab. Phys. Symp. (IRPS'2000)*, San Jose, California, April 10 – 13, (2000), pp.304 – 309.

[5] C. Fürböck, D. Pogany, M. Litzenberger, E. Gornik, N. Seliger, H. Gossner, T. Müller-Lynch, M. Stecher, and W. Werner, "Interferometric temperature mapping during ESD stress and failure analysis of smart power technology ESD protection devices", *J. Electrostatics*, Vol. 49, 2000, pp.195 – 213.

[6] C. Fürböck, K. Esmark, M. Litzenberger, D. Pogany, G. Groos, R. Zelsacher, M. Stecher, and E. Gornik, "Thermal and free carrier concentration mapping during ESD event in smart power ESD protection devices using an improved laser interferometric technique", *Microel. Reliab.*, Vol.40, 2000, pp. 1365 – 1370.

[7] M. Litzenberger, K. Esmark, D. Pogany, C. Fürböck, H. Gossner, E. Gornik, and W. Fichtner, "Study of triggering inhomogeneities in gg-nMOS ESD protection devices via thermal mapping using backside laser interferometry", *Microel. Reliab.*, vol 40, 2000, pp.1359 – 1364.

[8] D. Pogany, K. Esmark, M. Litzenberger, C. Fürböck, H. Gossner and E. Gornik, "Bulk and surface degradation mode in 0.35µm technology gg-nMOS ESD protection devices", *Microel. Reliab.*, Vol. 40, 2000, pp. 1467 – 1472 (2000).

Microelectronics Technology — Cleanroom Linz

Micro- and Nanostructure Research: Cleanroom Linz

G. Bauer, H. Heinrich, H. Thim, G. Brunthaler
Institut für Halbleiter- und Festkörperphysik, and
Institut für Mikroelektronik,
Johannes Kepler Universität Linz, A-4040 Linz, Austria

The micro- and nanostructure research in the cleanrooms of the Institut für Halbleiter- und Festkörperphysik and the Institut für Mikroelektronik is supported by the Society for Microelectronics (GMe). In the field of Si/SiGe heterobipolar transistors, compatibility issues with conventional Si technology were investigated. Silicon/Germanium structures were also used for the investigation of strain distributions in nanostructures and for the investigation of the metal-insulator phase transition at low temperatures. In GaAs technology, a hot electron injection field effect transistor in 0.5 μm technology with a transit frequency of 32 GHz was realized. Also Nanostructures were prepared in AlGaAs layers by use of electron beam lithography. In the field of optoelectronics, silicon light emitting diodes were achieved by doping with erbium and oxygen. Furthermore, in IV-VI semiconductor compounds, optically pumped surface emitting lasers were realized. Growth processes of semiconductor II-VI compounds were in-situ measured by Reflection Difference Spectroscopy and magnetic properties of iron layers on GaAs were investigated with respect to spin electronics.

The funding of the activities in the two cleanrooms at the University of Linz which are jointly used by three groups is of vital importance for our micro- and nanostructure research activities. This basic funding allows for investigations which are made possible through additional funding coming from the FWF, the FFF, the European Commission, as well as through cooperations with industrial groups as listed in the report.

A short overview is given in the following on the achievements made in the year 2000 in the cleanrooms in Linz. The basic equipment which is available in these clean rooms allows for MBE growth of Si-based heterostructures, of II-VI and IV-VI heterostructures, for the deposition of ferromagnetic layers like Fe on II-VI as well as III-V compounds, as well as for MOCVD growth of III-V compounds like GaAs/GaAlAs and GaAs/GaInAs. Apart from *in situ* and *ex situ* structural characterization, lateral patterning is made possible through equipment like optical, holographic, and electron beam lithography. Processing includes also facilities for the deposition on insulating as well as contact layers. The transmission electron microscope, purchased through funds of the Federal Ministry of Education, Science and Culture, became operational this year.

The research efforts were concentrated on high frequency electronic and optoelectronic devices as described in the following.

Si-SiGe heterobipolar transistors are now widely introduced in the production for high speed bipolar and BiCMOS circuits, offering a great speed advantage over standard Silicon technologies. In Linz steps towards the optimization of the of doping and composition profiles for the SiGeC HBT technology were made in a collaboration with Austria Microsystems, Unterpremstätten. In the production process, incompatibilities due to the

insertion of Ge become an important issue. For example, a transient enhanced diffusion (TED) of boron out of the SiGe base layer upon thermal activation of the poly-emitter implant occurs. As a remedy, the use of a carbon co-doped base has been proposed, in order to suppress the diffusitivity. On the other hand, C-complexes may introduce electrically active states in the band gap and thus degrade the electrical properties of the devices. Thus quantitative measurements of substitutional carbon and SiC were performed on MBE grown $Si_{1-y}C_y$ layers. In the IR transmission spectra, optical absorption from coherent and incoherent β-SiC was observed. The precipitation behavior of C to β-SiC in $Si_{1-y}C_y$ layers was then studied with the FTIR technique. In addition, the impact of carbon in a SiGeC HBT structure with a poly-Si emitter was studied. Complete suppression of TED of B was obtained by carbon doping of the base with 0.2% substitutional carbon.

Silicon and Si/Ge structures were also used in the investigation of strain distributions by x-ray methods. The strain in Si substrates underneath laterally patterned periodic SiO_2 stripes was measured by the grazing incidence diffraction technique. This method enhances the sensitivity in the near interface regions compared to conventional x-ray methods. A tensile and two compressively strained regions were found below and close to the edges of the stripes, respectively. These data have relevance for electronic transport. In Si/Ge islands, the strain and composition distribution was investigated. It turned out that although pure Ge has been deposited during island growth, the Ge composition varies due to intermixing processes between 0.5 and 1.

Silicon/Germanium quantum well structures were further used to investigate a basic physical problem, the behavior of potential fluctuations near the metal-insulator transition at low temperatures. For this purpose, the free electrons were detected by electron spin resonance (ESR). From the ESR signal, the potential fluctuations and the Thomas-Fermi screening efficiency were deduced. At the critical density of the metal-insulator transition, the potential fluctuations diverge leading to a strong increase in resistivity.

Hot electron injection field effect transistors (HEIFET) were realized in GaAs technology. In such a device the usual ohmic source contact is replaced by an injection limiting contact in order to inject fast electrons into the channel region. Consequently, the electron transit time through the channel is reduced and the transistors upper frequency limits are raised. As a result, a 0.5 μm device with a transit frequency of 32 GHz could be realized.

Different types of nanostructures were fabricated in AlGaAs layers. Narrow lateral regions were defined in a two-dimensional electron gas by deep groove etching or by top gate structures with the help of electron beam lithography. In such structures the lateral quantization of electron waves was observed. The investigation and understanding of quantum effects in nanostructures is important as the continuing miniaturization will lead to similar effects in future semiconductor devices.

In the field of optoelectronics, silicon light emitting diodes (LED) were achieved by co-doping of erbium (Er) and oxygen (O). The LED's emit at room temperature at a wavelength of 1.54 μm. The doping profile and electrical activity were investigated in order to optimize the structure for room temperature luminescence.

Optically pumped vertical-cavity surface emitting lasers were fabricated from narrow band gap IV-VI semiconductor compounds. High reflectivity PbEuTe/EuTe multilayers are used as mirrors for the laser cavity. The stimulated emission occurs between 3 and

4.5 μm and is generated either in PbTe quantum wells or in self-organized PbSe quantum dots. PbTe on PbSe was also used for nano-scale dislocation patterning studied by a scanning tunneling microscope.

Furthermore, surface processes in molecular beam epitaxy were investigated *in situ* during growth by the Reflection Difference Spectroscopy method on II-VI semiconductor compounds in order to develop an all-optical feed-back system for controlling the growth. In this method, the measured signal is the difference between the near normal incidence reflectance of light linearly polarized along the two principal axes. The signal is recorded as a function of time, photon energy and/or surface conditions. In CdTe/ZnTe the *in situ* stress relaxation during growth was observed for the first time.

Finally, thin iron films were deposited on GaAs substrates and ZnSe epilayers in order to investigate their magnetic properties in the initial surface reconstruction process. The incorporation of magnetic layers in semiconductor heterostructures is an increasingly active area of study for spin electronics. The magnetization versus magnetic field hysteresis curve for iron on GaAs shows a single irreversible jump whereas the irons films on ZnSe exhibit two such jumps if the thickness is between 60 and 120 nm.

Project Information

Project Manager

ao.Univ.Prof. Dr. Gerhard Brunthaler

Institut für Halbleiter-und Festkörperphysik, Johannes Kepler Universität Linz, A-4040 Linz, Austria

Project Group

Last Name	First Name	Status	Remarks
Bauer	Günther	University professor	
Heinrich	Helmuth	University professor	
Jantsch	Wolfgang	University professor	
Schäffler	Friedrich	University professor	
Thim	Hartwig	University professor	
Brunthaler	Gerhard	Associate professor	
Diskus	Christian	Associate professor	
Helm	Manfred	Associate professor	
Krenn	Heinz	Associate professor	
Palmetshofer	Leopold	Associate professor	
Springholz	Gunther	Associate professor	
Sitter	Helmut	Associate professor	
Bonanni	Alberta	Assistant professor	
Fromherz	Thomas	Assistant professor	
Heiss	Wolfgang	Assistant professor	
Kolmhofer	Erich	Assistant professor	
Lübke	Kurt	Assistant professor	
Binder	Fritz	Technician	
Fuchs	Othmar	Technician	
Hinterreiter	Marion	Technician	
Kainz	Ursula	Technician	
Katzenmayer	Hans	Technician	
Rabeder	Klaus	Technician	
Wirtl	Elisabeth	Technician	½ paid by GME
Balderas	Raul	Guest researcher	University de San Louis Potosi, Mexico
Hingerl	Kurt	Guest researcher	Austrian Academy of Sciences + Company Profactor

Last Name	First Name	Status	Remarks
Stepikhova	Margarita	Guest researcher	
Stifter	David	Guest researcher	Company Profactor
Daniel	Anke	Ph.D. student	
Himmelbauer	Karin	Ph.D. student	
Kocher	Gudrun	Ph.D. student	
Montaigne-R.	Alberto	Ph.D. student	
Mühlberger	Michael	Ph.D. student	
Pinczolits	Michael	Ph.D. student	
Prechtl	Gerhard	Ph.D. student	
Raab	Anneliese	Ph.D. student	
Roch	Tomas	Ph.D. student	
Sandersfeld	Nils	Ph.D. student	
Schelling	Christoph	Ph.D. student	
Schwarzl	Thomas	Ph.D. student	
Stangl	Julian	Ph.D. student	
Wiesauer	Karin	Ph.D. student	
Zhuang	Yan	Ph.D. student	
Berer	Thomas	Diploma student	
Gruber	Daniel	Diploma student	
Landsiedl	Michael	Diploma student	
Lengauer	Gunther	Diploma student	
Pillwein	Georg	Diploma student	
Raiser	Stefan	Diploma student	
Schraml	Stefan	Diploma student	

Publications in Reviewed Journals

Published:

1. G. Bauer
"Magnetotransport in SiGe/Si structures"
In: "Properties of Silicon Germanium and SiGe: Carbon", EMIS Data Review Series No. 24 , edited by Erich Kasper and Klara Lyutovich, University of Stuttgart, Germany. INSPEC (London) 2000, p. 228-243, ISBN 0 85296 783 7

2. M. Berti, D. De Salvador, A.V. Drigo, M. Petrovich, J. Stangl, F. Schäffler, S. Zerlauth, G. Bauer, A. Armigliato
"Metastability of $Si_{1-y}C_y$ epilayers under 2 MeV a-particle irradiation"
Micron 31, 285-289 (2000)

3. A. Daniel, V. Holy, Y. Zhuang, T. Roch, J. Grenzer, Z. Bochnicek, G. Bauer
"GID study of strains in Si due to patterned SiO_2"
J. Phys. D: Applied Physics 34, 1-6 (2001).

4. D. De Salvador, M. Petrovich, M. Berti, F. Romanato, E. Napolitani, A. Drigo, J. Stangl, S. Zerlauth, M. Mühlberger, F. Schäffler, G. Bauer, P.C. Kelires
"Lattice parameter of SiGeC alloys"
Phys. Rev. B 61, 13 005-13 013 (2000)

5. D. De Salvador, M. Tormen, M. Berti, A. V. Drigo, F. Romanato, F. Boscherini, J. Stangl, S. Zerlauth, G. Bauer, L. Colombo, S. Mobilio
"Local lattice distortion in $Si_{1-x-y}Ge_xC_y$ epitaxiial layers from x-ray absorption fine structure"
Phys. Rev. B 63 (2001)

6. M. Helm, W. Hilber, G. Strasser, R. DeMeester, F.M. Peeters, A. Wacker
"Interminiband spectroscopy of biased superlattices"
Physica E 7, 274 (2000).

7. V. Holy, J. Stangl, G. Springholz, M. Pinczolits, G. Bauer, I. Kegel, T.H. Metzger
"Lateral and vertical ordering of self-assembled PbSe quantum dots studied by high-resolution x-ray diffraction"
Physica B 283 (1-3), 65-68 (2000).

8. W. Jantsch, Z. Wilamowski, N. Sandersfeld, F. Schäffler
"Electric and magnetic field fluctuations in modulation-doped Si/SiGe quantum wells"
Physica E 6, 218-221 (2000)

9. Z. Kovats, T.H. Metzger, J. Peisl, J. Stangl, M. Mühlberger, Y. Zhuang, F. Schäffler, G. Bauer
"Investigation of ß-SiC precipitation in $Si_{1-y}C_y$ epilayers by x-ray scattering at grazing incidence"
Appl. Phys. Lett. 76, 3409-3411 (2000)

10. M. Mühlberger, C. Schelling, N. Sandersfeld, H. Seyringer, F. Schäffler
"High-Speed Transport in $Si/Si_{1-x-y}Ge_xCy$ Heterostructures"
Thin Solid Films 369, 306-311 (2000)

11. C. Penn, F. Schäffler, G. Bauer, P. C. M. Christianen, J. C. Maan, S. Glutsch
"Magnetoluminescence Investigations of $Si/Si_{0.76}Ge_{0.24}$ Quantum Wells"
Phys. Rev. B 61, 13 055-13 059 (2000

12. C. Penn, T. Fromherz, G. Bauer
"Energy gaps and band structure of SiGe and their temperature dependence"
In: "Properties of Silicon Germanium and SiGe: Carbon", EMIS Data Review Series No. 24 , edited by Erich Kasper and Klara Lyutovich, University of Stuttgart, Germany. INSPEC (London) 2000, p. 125-134, ISBN 0 85296 783 7.

13. C. Penn, G. Bauer, F. Schäffler, S. Glutsch
"Band ordering of the pseudomorphic $Si_{1-x}Ge_x/Si$ heterostructure: the fundamental role of excitons"
Thin Solid Films 369, 394-397 (2000)

14. C. Penn, P.C.M. Christianen, F. Schäffler, J.C. Maan, G. Bauer
"Type II band alignment and exciton wave-functions in $Si/Si_{1-x}Ge_x$ quantum wells"
Physica E 7, 550-554 (2000)

15. A. Prinz, V. M. Pudalov, G. Brunthaler, G. Bauer
"Metal-insulator transition in Si-MOS structures"
Superlattices and Microstructures 27, No. 5/6, p. 301-310 (2000).

16. A. Raab, G. Springholz
"Oswald ripening and shape transitions of self-assembled PbSe quantum dots on PbTe (111) during annealing"
Appl. Phys. Lett. 77, 2991-2993 (2000)

17. C. Rosenblad, J. Stangl, E. Müller, G. Bauer, H. von Känel
"Strain relaxation of graded SiGe buffers grown at very high rates"
Materials Science and Engineering B71, 20-23 (2000)

18. R. Rupprecht, H. Pascher, H. Krenn, W. Faschinger, G. Bauer
"Coherent Raman spectroscopy of CdTe/MnTe short period superlattices"
Phys. Rev. B 63 (2001)

19. N. Sandersfeld, W. Jantsch, Z. Wilamowski, F. Schäffler
"ESR investigations of modulation-doped Si/SiGe quantum wells"
Thin Solid Films 369, 312-315 (2000)

20. C. Schelling, G. Springholz, F. Schäffler
"New kinetic growth instabilities in Si (001) homoepitaxy"
Thin Solid Films 369, 1-4 (2000)

21. C. Schelling, G. Springholz, F. Schäffler
"Kinetic vs. strain-induced growth instabilities on vicinal Si(001) substrates"
Thin Solid Films 380, 20-24 (2000).

22. G. Springholz, T. Schwarzl, M. Aigle, H. Pascher, W. Heiss
"4.8 μm vertical emitting PbTe quantum-well lasers based on high-finesse EuTe/$Pb_{1-x}Eu_xTe$ microcavities"
Appl. Phys. Lett. 76, 1807-1809 (2000)

23. G. Springholz, M. Pinczolits, V. Holy, P. Mayer, G. Bauer, H.H. Kang, L. Salamanca-Riba
"Tuning of vertical and lateral correlations in self-organized PbSe/$Pb_{1-x}Eu_xTe$ quantum dot superlattices"
Phys. Rev. Lett.84, 4669-4672 (2000)

24. G. Springholz, M. Pinczolits, V. Holy, P. Mayer, K. Wiesauer, T. Roch, G. Bauer
"Self-organized growth of three-dimensional IV-VI semiconductor quantum dot crystals with fcc-like vertical stacking and tunable lattice constant"
Surface Science 454-456, 657-670 (2000)

25. G. Springholz, J. Stangl, M. Pinczolits, V. Holy, P. Mikulik, P. Mayer, K. Wiesauer, G. Bauer, D. Smilgies, H.H. Kang, L. Salamanca-Riba
"Nearly perfect 3D ordering in IV-VI quantum dot superlattices with ABCABC... vertical stacking sequence"
Physica E 7, 870-875 (2000)

26. G. Springholz, M. Pinczolits, V. Holy, S. Zerlauth, I. Vavra, G. Bauer
"Vertical and lateral ordering in self-organized quantum dot superlattices"
Physica E 9, 149-163 (2001)

27. J. Stangl, T. Roch, V. Holy, M. Pinczolits, G. Bauer, I. Kegel, T.H. Metzger, J. Zhu, K. Brunner, G. Abstreiter, D. Smilgies
"Strain-induced self-organized growth of nanostructures - from step bunching to ordering in quantum dot superlattices"
J. Vacuum Science & Technology B 18, 2187-2192 (2000)

28. G. Strasser, L. Hvozdara, S. Gianordoli, W. Schrenk, K. Unterrainer, E. Gornik, M. Helm
"Intersubband and interminiband GaAs/AlGaAs quantum cascade lasers at 10 microns"
Physica E 7, 709 (2000).

29. K. Wiesauer, G. Springholz
"Fabrication of semiconductor nanostructures by nanoindentation of photoresist layers using atomic force microscopy"
J. Appl. Phys. 88, 7289-7297 (2000)

30. Y. Zhuang, C. Schelling, J. Stangl, C. Penn, S. Senz, F. Schäffler, T. Roch, A. Daniel, J. Grenzer, U. Pietsch, G. Bauer
"Structural and optical properties of Si/$Si_{1-x}Ge_x$ wires"
Thin Solid Films 369, 409-413 (2000)

31. Y. Zhuang, C. Schelling, T. Roch, A. Daniel, F. Schäffler, G. Bauer, J. Grenzer, U. Pietsch, S. Senz
"Investigation of inhomogeneous in-plane strain relaxation in Si/SiGe quantum wires by high resolution x-ray diffraction"
Mat. Res. Soc. Symp. Proc. 590, 207-212 (2000)

32. Y. Zhuang, U. Pietsch, J. Stangl, V. Holy, N. Darowski, J. Grenzer, S. Zerlauth, F. Schäffler, G. Bauer
"In-plane strain and shape analysis of Si/SiGe nanostructures by grazing incidence diffraction"
Physica B 283, 130-134 (2000).

33. Y. Zhuang, A. Daniel, C. Schelling, F. Schäffler, G. Bauer, J. Grenzer, S. Senz
"Optical and structural properties of Si/SiGe wires grown on patterned Si substrates"
Thin Solid Films 380, 51-53 (2000).

34. M. V. Stepikhova, B.A. Andreev, V.B. Shmagin, Z.F. Krasil´nik, V.P. Kuznetsov, V.G. Shengurov, S.P. Svetlov, W. Jantsch, L. Palmetshofer, H. Ellmer
Properties of Optically Active Si:Er and Si1-xGex Layers Grown by the Sublimation MBE Method
Thin Solid Films **369**, 426 (2000)

35. G. Springholz, T. Schwarzl, M. Aigle, H. Pascher, W. Heiss
4.8 μm Vertical Emitting PbTe Quantum-Well Lasers Based on High-Finesse EuTe/$Pb_{1-x}Eu_xTe$ Microcavities
Appl. Phys. Lett. **76** (14), p. 1807-1809 (2000)

36. T. Schwarzl, W. Heiss, G. Springholz, M. Aigle, H. Pascher
6 μm Vertical Cavity Surface Emitting Lasers Based on IV-VI Semiconductor Compounds
Electronic Letters **36** (4), p. 322-324 (2000)

37. K. Bierleutgeb, H. Sitter, H. Krenn, H. Seyringer
A Comparative Study of Iron Films on II-VI and III-V Semiconductors
Phys. stat. sol. (b) **220**, 41 (2000)

38. R.E. Balderas-Navarro, K. Hingerl, W. Hilber, D. Stifter, A. Bonanni, H. Sitter
In Situ Reflectance Difference Spectroscopy of Doped CdTe and ZnTe Grown by Molecular Beam Epitaxy
J. Vac. Sci. Technol. B **18**(4), 2224-2228 (2000)

39. K. Bierleutgeb, H. Sitter, H. Krenn
The Influence of Interface and Surface Effects on the Magnetic Properties of Thin Iron Films
Proc. European Magnetic Materials and Application Conf., Kiev, June 2000

40. W. Heiss, T. Schwarzl, G. Springholz
Lead Salt Based Bragg Mirrors and Microcavities for the Mid Infrared
Proc. 9th Int. Conf. NGS, Berlin 1999, ed. by N. Puhlmann, H.-U. Müller, M. v. Ortenberg, ISBN 3-00-005993-8 (2000)

41. T. Schwarzl, W. Heiss, G. Springholz
High Finesse Mid Infrared Microcavities Based on Lead Salts
Physica E **7**, 636 (2000)

42. D. Stifter, A. Bonanni, M. Garcia-Rocha, M. Schmid, K. Hingerl, H. Sitter
In Situ Reflectance Difference Spectroscopy of p-type ZnTe:N Grown by MBE
Thin Solid Films **373,** 41 (2000)

43. E. K. Miller, K. Hingerl, C. Brabec, A. J. Heeger and N. S. Sariciftci,
Ultrathin, Oriented Films of Conjugated Polymers: Reflectance Anisotropy Spectroscopy as a Nondestructive Characterization Technique
Jour. Chem. Phys. 113, (2000) p.789-92.

44. R. E. Balderas-Navarro, K. Hingerl, W. Hilber, D Stifter, A. Bonanni, and H. Sitter,
In situ reflectance-difference spectroscopy of doped CdTe and ZnTe grown by molecular beam epitaxy
Journ. Vac. Sci Techn B18, (2000); p.2224-8

45. A. Bonanni; K. Hingerl; H. Sitter; D. Stifter
Reflectance difference spectroscopy: a powerful tool for in situ investigations of II-VI compounds with Mn
Thin Solid Films. 367, (2000); p.216-19.

46. A. Bonanni; K. Hingerl; H. Sitter; D. Stifter
In situ reflectance difference spectroscopy of intra-Mn transitions in highly N-doped II-VI diluted magnetic semiconductors
Jour. of Cryst.-Growth. 214-215; (2000); p.163-6.

47. K. Hingerl, R. E. Balderas-Navarro, W. Hilber, A. Bonanni, and D. Stifter
Surface-stress-induced optical bulk anisotropy
15 (2000), Phys. Rev. B62, 13048

48. C. G. Diskus, A. Stelzer, C. Gamsjaeger, K. Luebke, E. Kolmhofer, H. W. Thim,
A 35 GHz Six-Port Receiver for Radar Applications,
Proceedings of SPIE, International Conference on *Subsurface Sensors and*

Applications (SSA '99), July 19–21, 1999, Denver, Colorado, USA, SPIE Proceedings Series Vol. 3752, pp. 355–365. ISSN 0277-786X, ISBN 0-8194-3238-5

49. A. Stelzer, C.G. Diskus, K. Lübke, H. W. Thim, "A Microwave Position Sensor with Submillimeter Accuracy", *IEEE Transactions on Microwave Theory and Techniques*, Vol. 47, No. 12, Dec. 1999, pp. 2621–2624. ISSN 0018-9480, SCI: 2449

Submitted / in print:

1. M. Aigle, H. Pascher, M. Pinczolits, G. Springholz, T. Schwarzl, W. Heiss, G. Bauer *"Optical characterization of self-organized PbSe/$Pb_{1-x}Eu_xTe$ quantum dot superlattices"* Physica Status Solidi, in print (2001).
2. G. Brunthaler, A. Prinz, G. Bauer and V.M. Pudalov, *"Temperature limits for quantum effects in the 2D metallic state of high-mobility Si-MOS structures"* Cond-Mat/0007230, in print.
3. G. Brunthaler, A. Prinz, G. Pillwein, G. Bauer, K. Brunner, G. Abstreiter, T. Dietl, V.M. Pudalov *"Semiclassical origin of the 2D metallic state in high mobility S-MOS and Si/SiGe structures"* Proc. 25th International Conference on the Physics of Semiconductors, Sept. 2000, Osaka, Japan, in print.
4. A. Daniel, V. Holy, Y. Zhuang, J. Stangl, T. Roch, G. Bauer, J. Grenzer, Z. Bochnicek *"X-ray diffraction study of lateral strain modulations in Si substrates arising from patterned periodic SiO_2 stripes"* Phys. Rev. B, submitted.
5. V. Holy, J. Stangl, G. Springholz, M. Pinczolits, G. Bauer *"High resolution x-ray diffraction from self-organized PbSe/PbEuTe quantum dot superlattices"* Journal of Physics D, submitted.
6. V. Holy, J. Stangl, G. Springholz, M. Pinczolits, G. Bauer *"Lateral and vertical ordering of PbSe self-assembled quantum dots in PbSe/PbEuTe superlattices"* MRS Proceedings, in print.
7. H. H. Kang, L. Salamanca-Riba, M. Pinczolits, G. Springholz, V. Holy, G. Bauer *"TEM investigation of self-organized PbSe quantum dots as a function of space layer thickness and growth temperature"* MRS Proceedings, in print.
8. H. Kepa, J. Blinowski, P. Kacman, G. Springholz, G. Bauer, C.F. Majkrzak, K.I. Goldman, T.M. Giebultowicz *"Interlayer exchange in antiferromagnetic-nonmagnetic semiconductor superlattices"* Proc. ICPS Jerusalem 2000, submitted.

9. M. Meduna, V. Holy, T. Roch, J. Stangl, G. Bauer, J. Zhu, K. Brunner, G. Abstreiter
"X-ray reflectivity of self-assembled structures in SiGe multilayers and comparison with Atomic Force Microscopy"
J. Appl. Phys., in print.

10. A. Raab, G. Springholz
"Oswald ripening of facetted self-assembled PbSe quantum dots during annealing
Physica Status Solidi, in print.

11. G. Springholz
"Molecular Beam Epitaxy of IV-VI Heterostructures and Superlattices"
In: "Lead Chalcogenides: Physics and Applications", eds. D. Khoklov, Gordon and Breach, in print.

12. G. Springholz, M. Pinczolits, G. Bauer, H.H. Kang, L. Salamanaca-Riba
"Phase diagram of lateral and vertical ordering in self-organized PbSe quantum dot superlattice grown MBE"
J. Crystal Growth, in print.

13. G. Springholz, T. Schwarzl, W. Heiss, M. Aigle, H. Pascher
"Molecular beam epitaxy of lead-salt-based vertical cavity surface emitting lasers for the 4-6 mm spectral region"
J. Crystal Growth, in print.

14. G. Springholz, M. Pinczolits, V. Holy, P. Mayer, G. Bauer, H.H. Kang, L. Salamanca-Riba
"Controlling of lateral and vertical order in self-organized PbSe quantum dot superlattices
Proc. ICPS 25, submitted.*"*

15. G. Springholz, M. Pinczolits, V. Holy, P. Mayer, G. Bauer, H. Kang, L. Salamanca-Riba
"Self-assembled molecular beam epitaxy of PbSe quantum dots"
Proceedings APF 6, Japan 2001, in print.

16. Z. Wilamowski, N. Sandersfeld, W. Jantsch, D. Többen, F. Schäffler
"Screening breakdown on the route toward the metal-insulator transition in modulation doped Si/SiGe quantum wells"
In: Cond-mat/ 0010077

17. Y. Zhuang, V. Holy, J. Stangl, S. Zerlauth, F. Schäffler, G. Bauer, U. Pietsch, N. Darowski
"Inhomogeneous strain relaxation in dry etched Si/SiGe wires: a high resolution x-ray diffraction study"
Phys. Rev. B, submitted.

18. Y. Zhuang, A. Daniel, C. Schelling, F. Schäffler, G. Bauer, J. Grenzer, S. Senz
"Optical and structural properties of Si/SiGe wires grown on patterned Si substrates"
Thin Solid Films, submitted.

19. Z. Wilamowski, N. Sandersfeld, W. Jantsch, D. Tübben, F. Schäffler
Screening Breakdown Near the Metal-to-Insulator Transition in Modulation-Doped Si/SiGe Quantum Wells

20. W. Heiss, G. Prechtl, G. Springholz
Giant tunability of exciton photoluminescence emission in antiferromagnetic EuTe
Phys. Rev. B , in print

21. T. Schwarzl, W. Heiss, G. Springholz, M. Aigle, H. Pascher, K. Biermann, K. Reimann
Lead salt based VCSELs for the 3-6 micron range
SPIE Proceedings Vol. 4286 in print

22. W. Heiss, G. Prechtl, G. Springholz
Magnetic field tunable excitonic photoluminescence transitions in antiferromagnetic EuTe layers with an effective g factor in excess of 1000
Submitted to Appl. Phys. Lett.

23. W. Heiss, T. Schwarzl, G. Springholz, K. Biermann, K. Reimann
Above-room-temperature mid-infrared lasing from vertical cavity surface emitting PbTe quantum-well lasers
Appl. Phys. Lett., in print

24. W. Heiss, G. Prechtl, G. Springholz
Giant tunability of excitonic photoluminescence transitions in antiferromagnetic EuTe epilayers
World Scientific, in print

25. W. Heiss, G. Prechtl, G. Springholz
Giant tunability of excitonic photoluminescence transitions in antiferromagnetic EuTe epilayers induced by magnetic polarons
Physica E, in print

26. G. Springholz, T. Schwarzl, W. Heiss, M. Aigle, H. Pascher
Molecular beam epitaxy of lead-salt based vertical cavity surface emitting lasers for the 4-6 μm spectral region
J. Cryst. Growth, in print

27. M. Aigle, H. Pascher, M. Pinczolits, G. Springholz, T. Schwarzl, W. Heiss, G. Bauer
Optical characterization of self-organized PbSe/$Pb_{1-x}Eu_xTe$ quantum dott superlattices
Phys. Stat. Solidi, in print

28. W. Jantsch, Z. Wilamowski, N. Sandersfeld, F. Schäffler
Evidence for Screenign Breakdown Near the Metal-to-Insulator Transition in Two Dimensions
World Scientific, in print

29. Z. Wilamowski, W. Jantsch
Antiferromagnetic Phase of the Two-Dimensional Electron Gas
World Scientific, in print

30. W. Jantsch, G. Kocher, L. Palmetshofer, H. Przybylinska, M. Stepikhova, H. Preier
Optimization of Er Centres in Si for Reverse Biased Light Emitting Diodes
Mat. Sci. and Eng. B, in print

31. H. Przybylinska, W. Jantsch, A. Kozanecki
Site Selective Excitation of Er-Implanted GaN
Mat. Sci. and Eng. B, in print

32. K. Hingerl et al.
In-situ observation of stress relaxation in CdTe/ZnTe heterostructures by reflectance-difference spectroscpy,
Appl. Phys. Lett (2001). Accepted (submitted 2000).

33. K. Hingerl, R.E. Balderas-Navarro, A. Bonanni, P. Tichopadek and W. G. Schmidt
On the Origin of Resonance Features in Reflectance Difference Data of Silicon
Appl. Surf. Science, in print

34. R. E. Balderas-Navarro, K. Hingerl, A. Bonanni, and H.
In situ observation of the onset of dislocations in CdTe/ZnTe heterostructures
Appl. Phys. Lett., in print

Presentations

Invited Talks:

1. G. Bauer
"Si-Ge based heterostructures for optoelectronic applications"
Conference on IV-VI Heterostructures, Universitée Paris Sud, Orsay, 06.-07. Juli 2000.

2. G. Bauer, V. Holy, J. Stangl, G. Springholz, A.A. Darhuber, M. Pinczolits
"Strain-induced self-organized growth of nanostructures: from step-bunching to ordering in quantum dot superlattices"
27th Conference on the Physics and Chemistry of Semiconductor Interfaces, Salt Lake City, Utah, 16.-20. Jan. 2000.

3. G. Brunthaler
"Metal-insulator Phase Transition in Two Dimensions"
Instituts Kolloquium, Ørsted Institut, Kopenhagen, Dänemark, 16. Feb. 2000.

4. G. Springholz
"Controlling of vertical and lateral ordering in self-organized PbSe quantum dot superlattices "
Fall Meeting of the Materials Research Society, 26.11.-1.12.2000, Boston, USA.

5. G. Springholz, M. Pinczolits, V. Holy. P. Mayer, G. Bauer, H. Kang, L. Salamanca-Riba
"Vertical and lateral correlations formed in self-organized quantum dot superlattices"
25th International Conference on the Physics of Semiconductors, 17.-22.9.2000, Osaka, Japan.

6. G. Springholz, M. Pinczolits, V. Holy and G. Bauer
"Lateral and vertical ordering in self-organized quantum dot superlattices "
18th General Conference of the Condensed Matter Division of the European Physical Society, 13.-17.3.2000, Montreux, Switzerland.

7. G. Springholz, M. Pinczolits, V. Holy and G. Bauer
"Vertical and lateral correlations in self-organized quantum dot superlattices"

Spring Meeting of the German Physical Society, 26.-31.3.2000, Regensburg, Germany.

8. G. Springholz, M. Pinczolits, V. Holy and G. Bauer
"Vertical and lateral correlations in self-organized quantum dot superlattices"
11th International Winterschool on New Developments in Solid State Physics – Low Dimensional Systems: Fundamentals and Applications, 21.-25.2.2000, Mauterndorf, Austria.

9. G. Springholz
"Vertikale und Laterale Ordnung in selbst-organisierten Halbleiter-Quantenpunkt Übergittern"
Seminar at the Phyiscs Department of the Ludwig-Maximilians Universität München, 25.5.2000

10. G. Springholz *(seminar talk)*
"Molecular beam epitaxy of self-organized semiconductor nanostructures"
Institut für Festkörperphysik der Technischen Universität Graz, 14.1.2000, Graz, Austria.

11. W. Jantsch
Towards Si optoelectronics
Physikkolloquium Universität Amsterdam, 27. 2. 2000

12. W. Jantsch
ESR-Untersuchungen an zweidimensionalen Halbleiterstrukturen
Seminar Universität Regensburg, 9. 6. 2000

13. W. Jantsch, G. Kocher, L. Palmetshofer, H. Przybylinska, M. Stepikhova, H. Preier
Optimization of Er centres in Si for reverse biased light emitting diodes
E-MRS 2000

14. A. Kozanecki, B.J. Sealy, K. Homewood, S. Ledain, W. Jantsch, D. Kuritsyn
Sensitization of the 1.54 pm luminescence of Er in SiOg films by Yb and Si nanocrystals
E-MRS 2000

15. W. Jantsch, Z. Wilamowski, N. Sandersfeld, F. Schäffler
Conduction electron spin resonance – a new tool to investigate the two-dimensional electron gas
Mesospin 2000, Cortona, Italy

16. K. Hingerl
Influence of anisotropic strain on critical point resonances in reflectance interfaces
Workshop on Optical Characterization of Semiconductor Interfaces
Park City, Utah, Oct. 2000

17. T. Schwarzl, W. Heiss, G. Springholz
IV-VI semiconductor based vertical Bragg microcavities
Seminar Universität Bayreuth, 8. 6. 2000

18. K. Hingerl, R.E. Balderas-Navarro, A. Bonanni
I*nfluence of Anisotropic strain oN Critical Point Resonances in Reflectance Difference Data*

Park City, Utah, Workshop on Optical Characterization of Semiconductor Interfaces, 15.-18.10. 2000

Conference presentations (talks and posters):

1. M. Aigle, H. Pascher, G. Springholz, M. Pinczolits, T. Schwarzl, W. Heiss, and G. Bauer
   "Optical characterization of self-organized PbSe/PbEuTe quantum dot superlattices"
   International Conference on Semiconductor Quantum Dots, 31.7.-3.8.2000, München, BRD.
2. A. Daniel, V. Holy, Y. Zhuang, T. Roch, J. Grenzer, Z. Bochnicek, G. Bauer
   "Grazing incidence study of strain modulations in Si due to patterned SiO_2"
   X-TOP, Ustron, Polen
3. A. Daniel, Y. Zhuang, T. Roch, J. Stangl, G. Bauer, C. Schelling, F. Schäffler, J. Grenzer, U. Pietsch, V. Holy
   "Study of depth dependent in-plane strain relaxation on Si/SiGe and SiO_2 wires using grazing incidence diffraction" (Poster)
   HASYLAB User Meeting, Hamburg, Deutschland, Januar 2000.
4. V. Holy, J. Stangl, G. Springholz, M. Pinczolits, G. Bauer
   "X-ray scattering from self-organized PbSe quantum dots in PbSe/PbEuTe superlattices"
   5th Biennial Conference on High Resolution X-ray Diffraction and Topography (X-TOP 2000), 13-15th September 2000, Ustron-Jaszowiec, Polen
5. A. Prinz, G. Brunthaler, G. Bauer and V.M. Pudalov
   "On the borders for quantum effects in high-mobility Si-MOS structures",
   25th Int. Conf. on the Physics of Semiconductors, Osaka, Japan 2000.
6. A. Raab and G. Springholz, (poster)
   "Oswald Ripening of facetted self-assembled PbSe quantum dot during annealing"
   International Conference on Semiconductor Quantum Dots, 31.7.-3.8.2000, München, BRD.
7. T. Roch, V. Holy, J. Stangl, E. Höflinger, A. Daniel, G. Bauer, I. Kegel, H. Metzger, J. Zhu, K. Brunner, G. Abstreiter
   "Structural investigations on self-organized Si/SiGe islands by grazing incidence small angle x-ray scattering",
   International Conference on Semiconductor Quantum Dots, July 31- August 3, 2000, Munich, Germany
8. T. Roch, V. Holy, A. Daniel, E. Höflinger, M. Meduna, T.H. Metzger, G. Bauer, J. Zhu, K. Brunner, G. Abstreiter
   " X-ray Scattering Studies on Self-organized Wires in SiGe/Si Multilayers",
   5th Bienial Conference on High Resolution X-ray Diffraction and Topography, 13-15 September 2000, Ustron-Jaszowiec, Poland,
9. T. Roch, A. Daniel, E. Höflinger, G. Bauer, J. Zhu, K. Brunner, G. Abstreiter
   "X-ray reflectivity on self-organized Si/SiGe wires" (Poster)
   HASYLAB User Meeting, Hamburg, Deutschland, Januar 2000.

10. G. Springholz, V. Holy, P. Simicek, P. Mayer, M. Pinczolits, and G. Bauer
"Modeling of vertical and lateral correlations in self-organizes quantumd dot superlattices: Finite size effects and the influence of the elastic anisotropy"
International Conference on Semiconductor Quantum Dots, 31.7.-3.8.2000, München, BRD.

11. G. Springholz, T. Schwarzl, W. Heiss, M. Aigle, and H. Pascher
"Molecular beam epitaxy of lead salt-based vertical cavity surface emitting lasers for the 4 - 6 μm spectral region"
11th International Conference on Molecular Beam Epitaxy, 10.15.9.2000, Beijing, China

12. G. Springholz, M. Pinczolits, V. Holy, P. Mayer, G. Bauer, H. Kang, and L. Salamanca-Riba
"Phase diagram and tuning of lateral and vertical order in self-organized PbSe quantum dot superlattices"
11th International Conference on Molecular Beam Epitaxy, 10.15.9.2000, Beijing, China

13. G. Springholz, V. Holy, P. Mayer, and G. Bauer
" Modeling of vertical and lateral ordering in self-organized quantum dot superlattices: Finite size effects and the influence of the elastic anisotropy"
11th International Conference on Molecular Beam Epitaxy, 10.15.9.2000, Beijing, China

14. G. Springholz, W. Heiß, and G. Prechtl
"Giant tunability of excitonic photoluminescence transitions in antiferromagnetic EuTe epilayers"
Fall Meeting of the Materials Research Society, 26.11.-1.12.2000, Boston, USA.

15. G. Springholz, T. Schwarzl, W. Heiss, M. Aigle and H. Pascher
"Molecular beam epitaxy of vertical cavity surrface emitting PbSe quantum dot lasers for the mid infrared spectral region"
Fall Meeting of the Materials Research Society, 26.11.-1.12.2000, Boston, USA.

16. G. Springholz, M. Pinczolits, V. Holy, P. Mayer, G. Bauer, H. H. Kang, L. Salamanca-Riba (Poster)
"Scaling behavior and phase diagram of lateral and vertical ordering in self-organized
PbSe quantum dot superlattices"
International Conference on Semiconductor Quantum Dots, 31.7.-3.8.2000, München, BRD.

17. J. Stangl, T. Roch ,A. Daniel, M.Pinczolits, G. Springholz, G. Bauer, I. Kegel, T.H. Metzger
"Investigations of quantum dot multilayers with grazing incidence small angle scattering: shape and ordering",
10th ESRF Users' Meeting, 8.-12.2.2000, Grenoble

18. J. Stangl, T. Roch, A. Daniel, M. Pinczolits, G. Bauer, I. Kegel, T.H. Mtezger, D. Smilgies
"Investigation of quantum dot multilayers with grazing incidence small angle scattering: shape and ordering" (Poster)
ESRF User Meeting, Grenoble, Frankreich, Februar 2000.

19. J. Stangl, A. Daniel, V. Holy, G. Bauer, I. Kegel, T.H. Metzger, T. Wiebach, O.G. Schmidt, K. Eberl
"Composition and strain in freestanding Ge islands" (Poster)
MRS Boston, USA

20. J. Stangl, V. Holy, A. Daniel, T. Roch, G. Bauer, T.H. Metzger, J. Zhu, K. Brunner, G. Abstreiter
"Shape and size of buried SiGe islands"
25th International Conference on the Physics of Semiconductors, 17.-22.9.2000, Osaka, Japan.

21. K. Wiesauer and G. Springholz
"Scaling behavor in spiral growth of PbTe (111) under conditions far from thermodynamic equilibrium"
Spring Meeting of the German Physical Society, 26.-31.3.2000, Regensburg, Germany.

22. K. Wiesauer and G. Springholz
Spiral growth in molecular beam epitaxy far from thermodynamic equilibrium: Scaling behavior and growth mode transitions
11th International Conference on Molecular Beam Epitaxy, 10.15.9.2000, Beijing, China

23. H. Przybylinska, W. Jantsch, A. Kozanecki
Site selective excitation of Er-implanted GaN
E-MRS 2000

24. Z. Wilamowski, W. Jantsch
Aniferromagnetic phase of the two-dimensional electron gas
ICPS 25, Osaka, Sept. 2000

25. W. Jantsch, Z. Wilamowski, N. Sandersfeld, F. Schäffler
Evidence for screening breakdown near the metal-to-insulator transition in two dimensions
ICPS 25, Osaka, Sept. 2000

26. Z. Wilamowski, W. Jantsch
Spin resonance properties of the two-dimensional electron gas
PASPS 2000, Sendai, Sept. 2000

27. W. Jantsch, Z. Wilamowski, N. Sandersfeld, F. Schäffler
Conduction electron spin resonance – a new tool to investigate the two-dimensional electron gas
50. Jahrestagung der ÖPG, Graz, Sept. 2000

28. E. Thor, M. Mühlberger, L. Palmetshofer, F. Schäffler, M. Gritsch
Capacitance-voltage profiling and deep-level transient spectroscopy on epitaxially grown Si, SiGe, SiC, SiGeC heterostructures
50. Jahrestagung der ÖPG, Graz, Sept. 2000

29. K. Hingerl, R. Balderas-Navarro, W. Hilber, A. Bonanni
A model for resonance features at critical points in reflectance difference data
ICSFS-10, Princeton University, Princeton, USA, July 2000

30. R.E. Balderas-Navarro, K. Hingerl, W. Hilber, D. Stifter, A. Bonanni, H. Sitter
In situ reflectance-difference spectroscopy of doped CdTe and ZnTe grown by molecular beam epitaxy
27th Conf. Physics and Chemistry of Semiconductor Interfaces, Salt Lake City, Utah, Jan. 2000

31. G. Springholz, T. Schwarzl, W. Heiß, M. Aigle, H. Pascher
Two-color vertical cavity surface emitting PbSe quantum dot laser for the mid infrared
Material Research Society (MRS) 2000 Fall Meeting, Boston, USA, November 27 - December 1, 2000

32. G. Springholz, T. Schwarzl, W. Heiss, M. Aigle, H. Pascher
Molecular beam epitaxy of lead-salt based vertical cavity surface emitting lasers for the 4-6 μm spectral region
11th International Conference on Molecular Beam Epitaxy (MBE-XI), Beijing, China, September 10-15, 2000

33. T. Schwarzl, G. Springholz, M. Aigle, H. Pascher, W. Heiss
4-6 μm vertical cavity surface emitting lasers based on lead salt compounds
European Conference on Lasers and Electro-Optics Europe 2000 (CLEO/Europe), Nice, France, September 10-15, 2000

34. M. Aigle, H. Pascher, M. Pinczolits, G. Springholz, T. Schwarzl, W. Heiss, G. Bauer
Optical characterization of self-organized PbSe/$Pb_{1-x}Eu_xTe$ quantum dot superlattices
International Conference on Semiconductor Quantum Dots (QD 2000), Munich, Germany, July 31 - August 3, 2000

35. T. Schwarzl, W. Heiß, G. Springholz, M. Aigle, H. Pascher
Lead salt based vertical cavity surface emitting lasers for the 4 – 6 micron wavelength range
42nd Electronics Materials Conference 2000 (EMC), Denver, USA, June 21 – 23, 2000

36. T. Schwarzl, W. Heiss, G. Springholz, S. Gianordoli, G. Strasser, M. Aigle, H. Pascher *Strongly detuned IV-VI microcavity and microdisk resonances: mode splitting and lasing*
25th International Conference on the Physics of Semiconductors (ICPS 25), Osaka, Japan, September 17 – 22, 2000

37. T. Schwarzl, W. Heiß, G. Springholz, M. Aigle, H. Pascher
Lead salt based vertical cavity surface emitting lasers for the 4 - 6 μm wavelength range
11th International Winterschool on New Developments in Solid State Physics: "Low-Dimensional Systems: Fundamentals and Applications", Mauterndorf, February 21 – February 25, 2000

38. G. Springholz, W. Heiss, G. Prechtl
Giant tunability of excitonic photoluminescence transitions in antiferromagnetic EuTe epilayers
MRS-2000 Fall Meeting, Boston, USA, (November 27-December 1, 2000)

39. W. Heiss, G. Prechtl, G. Springholz
Giant tunability of excitonic photoluminescence transitions in antiferromagnetic EuTe epilayers
25th International Conference on the Physics of Semiconductors, Osaka, Japan (September 17-22, 2000)

40. W. Heiss, G. Prechtl, G. Springholz
Giant tunability of excitonic photoluminescence transitions in antiferromagnetic EuTe epilayers induced by magnetic polarons
The Int. Conf. on the Physics and Application of Spin-Related Phenomena in Semiconductors 2000, Sendai, Japan (September 13-15, 2000)

41. W. Heiss, G. Prechtl, G. Springholz
Giant tunability of excitonic photoluminescence transitions in antiferromagnetic EuTe due to magnetic polarons
Euroconference Spin Effects in Mesoscopic Systems, Cortona, Italy (June 28 – July 2, 2000EuTe epilayers
25th International Conference on the Physics of Semiconductors, Osaka, Japan (September 17-22, 2000)

42. W. Heiss, G. Prechtl, G. Springholz
Giant tunability of excitonic photoluminescence transitions in antiferromagnetic EuTe epilayers induced by magnetic polarons
The Int. Conf. on the Physics and Application of Spin-Related Phenomena in Semiconductors 2000, Sendai, Japan (September 13-15, 2000)

43. W. Heiss, G. Prechtl, G. Springholz
Giant tunability of excitonic photoluminescence transitions in antiferromagnetic EuTe due to magnetic polarons
Euroconference Spin Effects in Mesoscopic Systems, Cortona, Italy (June 28 – July 2, 2000)

44. K.Hingerl*, R. Balderas, W. Hilber and A. Bonanni
A Model for Resonance features at critical points in reflectance difference data
International conference on solid films and surfaces
Princeton University Princeton, USA, July 9 - 13, 2000 ICSFS-10

45. 23. R. E. Balderas-Navarro, K. Hingerl, W. Hilber, D. Stifter, A. Bonanni and H. Sitter
In situ reflectance-difference spectroscopy of doped CdTe and ZnTe grown by molecular beam epitaxy
27th Conference on the Physics and Chemistry of Semiconductor Interfaces.Salt Lake City, Utah 16-20 January 2000

46. C. G. Diskus, A. Stelzer, C. Gamsjäger, E. Kolmhofer, K. Lübke und H.W. Thim,
Phasenmessungen an Mikrowellensignalen
Beiträge der Informationstagung Mikroelektronik, ME'99, Wien, Österreichischer Verband für Elektrotechnik, ÖVE-Schriftenreihe Nr. 23, S. 189–196. ISBN 3-85133-019-6

47. A. Stelzer, C. G. Diskus, A. Fischer, K. Lübke und H. W. Thim,
Direkte Frequenzmessung an Mikrowellensignalen
Beiträge der Informationstagung Mikroelektronik, ME'99, Wien, Österreichischer

Verband für Elektrotechnik, ÖVE-Schriftenreihe Nr. 23, S. 233–240. ISBN 3-85133-019-6

48. C. G. Diskus, A. Stelzer, K. Lübke, H.W. Thim,
A Ka-Band Detector Diode with High Sensitivity
Proceedings of the Seminar Current Developments of Microelectronics 1999, organized by the Society for Microelectronics (Gesellschaft für Mikroelektronik - GMe), 3rd–6th March 1999, Bad Hofgastein, Austria, pp. 29–33. ISBN 3-901578-04-8

49. H. W. Thim,
MMIC Research and Development at Austrian Universities
Proceedings of the Seminar Current Developments of Microelectronics 1999, organized by the Society for Microelectronics (Gesellschaft für Mikroelektronik - GMe), 3rd–6th March 1999, Bad Hofgastein, Austria, pp. 25–27. ISBN 3-901578-04-8

50. E. Kolmhofer, M. Bergmair, C. Diskus, K. Luebke, A. Stelzer, and H. Thim,
Hot Electron Injection Field Effect Transistor
Digest to the 23rd Workshop on Compound Semiconductor Devices and Integrated Circuits (WOCSDICE '99), May 26–28, 1999, Chantilly, France, p. 145

Patents

1. H. Thim, K. Lübke,
„Feldeffekttransistor mit injektionsbegrenzendem Sourcekontakt (Hot Electron Injection Field Effect Transistor HEIFET)“
Österreichisches Patent Nr. 407.451, erteilt am 6.12.2000

Doctor's Theses

1. Dipl.Ing. Michael Pinczolits
“Self-Organized Epitaxial Growth of IV-VI Quantum Dots and Quantum-Dot Crystals”
2. Dipl.Ing. Julian Stangl
“High-resolution X-ray Diffraction Studies of Self-organized SiGe(C) Islands”
3. Dipl. Phys. Christoph Schelling
„Growth and characterization of self-organized and ‚organized’ Si and $Si_{1-x}Ge_x$ nanostructures“
4. Dipl.Ing. Heinz Seyringer
„Nanostrukturierung und Charakterisierung von Si/SiGe Heterostrukturen“
5. M.Sc. Yan Zhuang
“Fabrikation und Charakterisierung von lateral strukturierten Si/SiGe-Heteroschichten”
6. Dipl.-Ing. Karin Bierleutgeb:
Herstellung und Charakterisierung ferromagnetischer Schichten

7. Dipl.-Ing. Andreas Stelzer, "Aufbau eines Mikrowellenmeßsystems mit Sub-Millimeter Genauigkeit unter Verwendung direkter Frequenzmessung und Six-Port Phasenbestimmung", Linz, 2000.

Cooperations

1. Siemens München, Dr.Heide
2. Daimler Benz Reserach Laboratories Ulm, Dr. Presting, Dr. König
3. VOEST ALPINE, Linz, Dr.Angerer,
4. INFINEON Villach,
5. AMS Unterpremstätten
6. KEBA, Linz, Ing.G.Krippner
7. Institut für Halbleiterphysik, Frankfurt/Oder
8. Sektion Physik, Ludwig-Maximilians Universität München
9. Physics Department, Cornell University
10. ETH, Zürich
11. ESRF Grenoble
12. DESY, Hasylab, Hamburg
13. FOM Institute Rijnhuizen, Niederlande
14. Walter Schottky Institut, TU München
15. IBM Research Center, Yorktown Heights
16. Institut für Festkörperelektronik, TU Wien
17. Philips Almelo, Niederlande
18. Heriot Watt University, Edinburgh, Scotland
19. University of Southampton, England
20. High Pressure Research Center, Warschau, Polen
21. Institue of Physics, Polish Academy of Sciences, Warschau
22. TU Berlin, Institut für Festkörperphysik
23. Universität Würzburg
24. Universität Bayreuth
25. Universität Bremen
26. Purdue University, Lafayette, IN, USA
27. MIT, Cambridge, MA, USA
28. NIST, Gaithersburg, MD, USA
29. Nanoelectronics Research Center, University of Glasgow, Scotland
30. University of Warwick, Coventry, England

31. North Carolina State University, NC, USA
32. IAF Freiburg
33. CENG Grenoble
34. Universität Paderborn
35. INSA, Lyon
36. Université de Montpellier
37. ELETTRA, Triest
38. Universiteit Instelling, Antwerpen, Niederlande
39. TASC Triest
40. ENEA, Roma
41. CNRSM-PASTIS, Brindisi
42. Akademie der Wissenschaften, Troits, Moskau
43. High Magnetic Field Lab., Grenoble
44. Siemens München, Zentrale Technik, Bereich Halbleiter
45. Fraunhofer-Institut (IAF) Freiburg (Chiptechnologie)
46. TU-München (Mikrowellentechnik)
47. Profactor, Steyr, Upper Austria

Characterization of Si/SiGeC Heterostructures for Device Applications

D. Gruber, T. Fromherz, M. Mühlberger, C. Schelling, L. Palmetshofer, F. Schäffler

Institut für Halbleiter- und Festkörperphysik, Johannes Kepler Universität, Altenbergerstraße 69, 4040 Linz, Austria

1. Introduction

With the commercial introduction of the Si/SiGe hetero bipolar transistor (HBT) into mainstream integration technologies, process incompatibilities become an important issue. A basic problem is, for example, the transient enhanced diffusion (TED) of boron out of the SiGe base layer upon thermal activation of the poly-emitter implant. As a remedy, the use of a carbon co-doped base has been proposed, in which a carbon concentration of a few tenths of an atomic percent have been show to very effectively suppress TED. On the other hand, great effort has been dedicated in the past to reduce the carbon concentration in Si ingots as far as possible, because of the propensity of C to form complexes and β-SiC precipitates. In contrast to substitutional C, some of these complexes are known to introduce electrically active states in the band gap. It is therefore important to characterize the microscopic configuration in which C is present after processing of SiGe:C HBTs. In this work, we address this problem with a combination of Fourier Transform Spectroscopy (FTIR), x-ray diffraction (XRD) and SIMS studies.

With the FTIR technique, one is able to probe the local surroundings of carbon atoms in the silicon crystal. In order to detect the absorption from carbon, a silicon reference spectrum has to be subtracted because of the strong Si phonon absorption in the interesting spectral region. The process of subtraction of the Si background is very sensitive to differences in thickness between sample and Si reference, making numerical correction necessary. This is done by measuring the thicknesses by Fabry-Perot interference fringes.

2. Measurement of Substitutional Carbon / Silicon Carbide

FTIR is the standard method for the measurement of substitutional C in bulk-Si. Despite the high concentrations in epitaxially grown $Si_{1-y}C_y$ layers, the integrated amount of C is small compared to bulk material. With a method for correction of differences in thickness between sample and Si reference, quantitative measurements on thin layers are possible as shown in Fig. 1.

It is also possible to measure the β-SiC concentration by FTIR. A defined amount of C was deposited on a Si substrate followed by a thin Si cap layer. During an annealing step at 1000 °C, the carbon forms β-SiC, which can be identified by its characteristic phonon absorption.

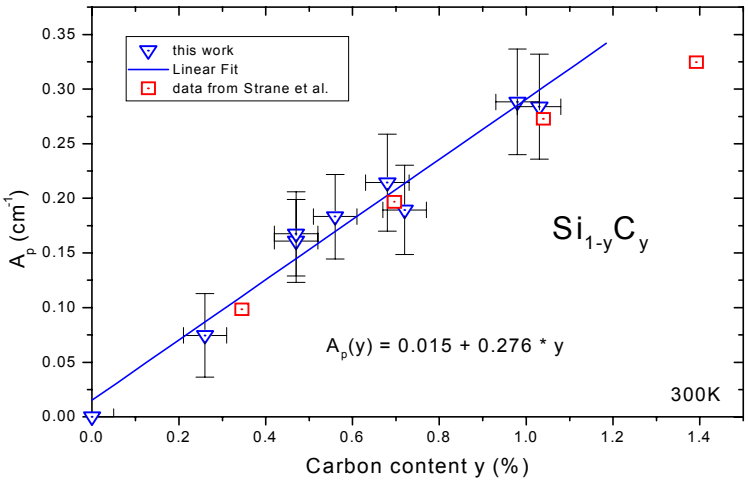

Fig. 1: Dependence of the integrated peak for substitutional carbon from the FTIR measurement as a function of carbon content measured by XRD. The layers are MBE grown with a thickness of 1000 Å.

3. Precipitation Behavior

Since the solid solubility of C in Si is about 0.0001%, the epitaxially grown layers are metastable and tend to relax their strain by forming β-SiC precipitates. The process can be studied by FTIR spectroscopy. Substitutional carbon (607 cm^{-1}) leaves the lattice and forms small precipitates which are coherently bound to the Si crystal (750 cm^{-1}).

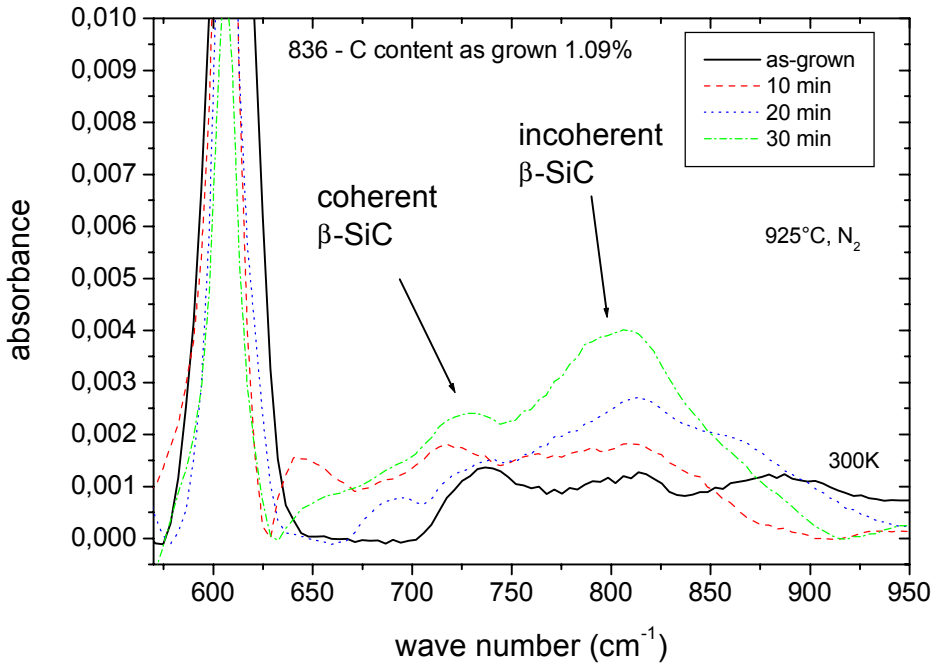

Fig. 2: Time evolution of the different peaks for a 1000 Å thick $Si_{0.99}C_{0.01}$ layer which has been annealed at a temperature of 925 °C for different amounts of time.

If the temperature is high enough, more strain can be relaxed, if the bonds between Si atoms and precipitate break up and the coherence with the neighboring Si atoms is lost. Phonon absorption from β-SiC can then be seen at 820 cm^{-1}.

The precipitation process is very sensitive to the as-grown situation. The above figure shows the time evolution of spectra from a $Si_{1-y}C_y$ sample annealed at 925 °C for different periods of time. At the same time, the expansion of the vertical lattice constant can be monitored by XRD.

4. Impact of C on TED in a SiGeC: HBT

The influence of C on TED of B was studied for an HBT structure with graded Ge base. Pieces of two samples, one with (0.2%) and one without C doping in the base have been annealed at different RTA temperatures. The slope for the sample with C doping is, within the accuracy of the measurement, constant. TED of B is completely suppressed in this structure. Electrical measurements suggest no negative influence of carbon on device characteristics.

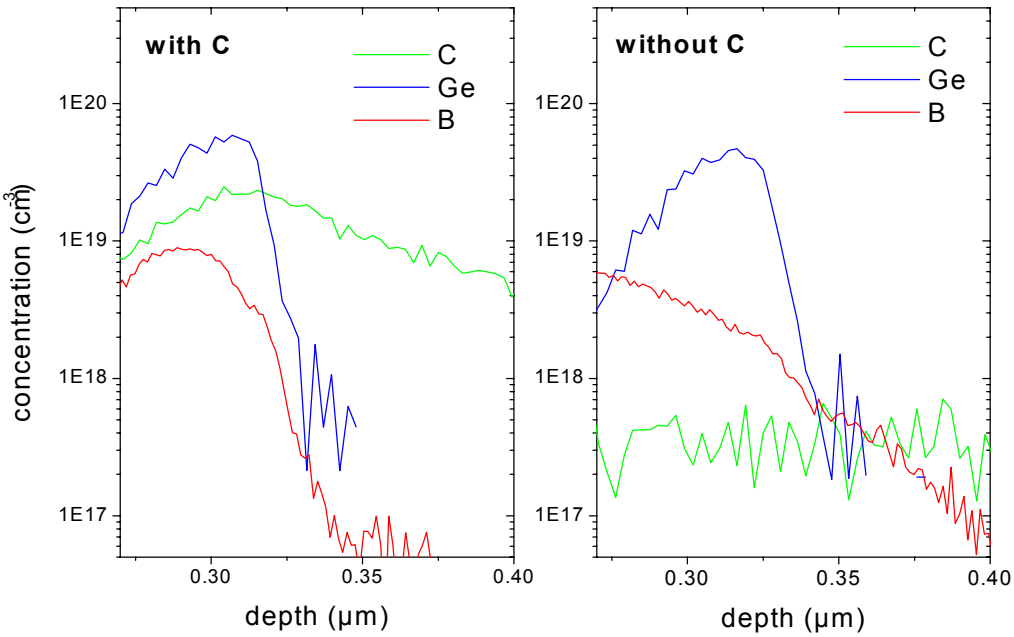

Fig. 3: Comparison of the B profile at the base-collector junction for a SiGe drift-HBT with and without carbon co-doping of the base.

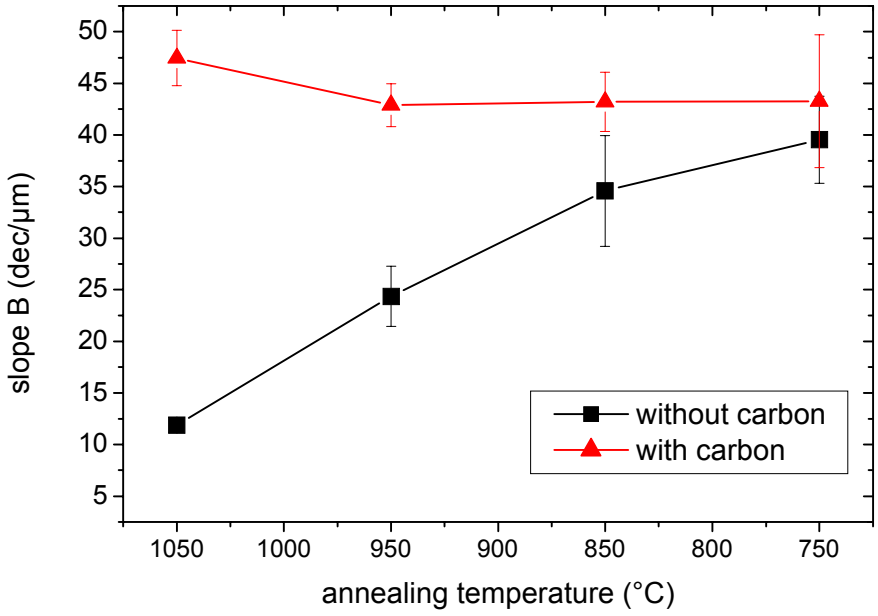

Fig. 4: Slope of the boron profile as a function of annealing temperature for the sample with and without C doping.

5. Conclusions

Quantitative measurements of substitutional carbon and SiC were performed on MBE grown $Si_{1-y}C_y$ layers. In the IR transmission spectra, optical absorption from coherent and incoherent β-SiC was observed. The precipitation behavior of C to β-SiC in $Si_{1-y}C_y$ layers was then studied with the FTIR technique.

As a second experiment, the impact of carbon in a SiGeC HBT structure with a poly-Si emitter was studied. Complete suppression of TED of B was obtained by carbon doping of the base with 0.2% subst. C.

References

[1] P A Stolk, H-J Gossmann, D J Eaglesham, and J M Poate, Mat. Sci. Eng. B **36** (1996), no. 1 – 3, p. 275.

[2] J W Strane, H J Stein, S R Lee, S T Picraux, J K Watanbe, and J W Mayer, J.Appl. Phys. **76**, no. 6, p. 3656.

[3] R Scholz, U Gösele, J-Y Huh, and T Y Tan, Appl. Phys. Lett. **72** (1998), no. 2, 200.

Strain and Composition of SiGe Islands on Si (001)

J. Stangl, A. Daniel, V. Holý, T. Roch, G. Bauer

Institut für Halbleiter- und Festkörperphysik, Johannes Kepler Universität, Altenbergerstr. 69, 4040 Linz, Austria

We have investigated the strain and composition distribution in uncapped SiGe islands on Si (001) by x-ray diffraction. In order to be sensitive to the dot layer at the sample surface, and at the same time being able to measure in-plane strain and strain in growth direction, we utilized a scattering geometry at grazing incidence angles, but with high exit angles. The measured intensity distribution is compared to simulations based on the strain distribution calculated by the finite element method. It turns out that, although pure Ge has been deposited during island growth by molecular beam epitaxy, the Ge composition varies from 0.5 at the island base to 1.0 at the top of the islands. The elastic relaxation reaches only about 50% even at the island top.

1. Introduction

Recent years have seen a series of studies shedding light on the formation of so-called self-organized nanostructures during semiconductor heteroepitaxy. They are formed due to a growth instability in strained heterostructures. After a certain critical thickness of deposited material, in our case Ge on Si, three-dimensional islands form on top of a two-dimensional layer, the so-called wetting layer (WL). These islands can elastically relax and hence reduce their strain energy, which is the driving force of their formation. The main advantage of such islands as compared to nanostructures fabricated, e.g., by etching, is the high areal density and the virtually complete absence of defects [1].

However, it is difficult to control the size, strain and composition of self-organized structures because these quantities depend very sensitively on the growth conditions (substrate temperature, adatom flux, etc.). Transmission electron microscopy (TEM) has been used to investigate the strain distribution within such islands [2], [3]. Recently, also the Ge and Si distributions in uncapped SiGe islands have been investigated using TEM, showing that islands formed during the deposition of pure Ge onto a Si surface are alloyed [4]. On the other hand, TEM investigations on Ge islands grown by chemical vapor deposition of 11 ML of Ge at 600 °C have been interpreted as not giving evidence for significant alloying [5].

X-ray diffraction (XRD) techniques have also been applied to tackle the question of strain and composition [6], [7]. In principle, XRD is the method of choice to measure strains, and often the strain state can be directly related to a composition. This is a standard technique for the investigation of, e.g., SiGe buffer layers with graded composition. However, for objects as small as self-organized islands, the correct spatial localization of a certain strain state is an ambitious task.

2. Experimental

Our investigations focus on a sample (S1183B4) with free-standing SiGe islands grown by MBE on [001]-oriented Si. After growth of a Si buffer layer and a buried SiGe island layer, a layer of Ge islands at the surface was formed by the deposition of 6 ML of Ge. The growth temperature was 600 °C. Here we are interested solely in the surface islands; the buried islands have no influence on the scattered signal due to the low incidence angle $\alpha_i = 0.15°$ (below the critical angle $\alpha_c \approx 0.22°$). With AFM two types of islands have been detected on the sample surface, larger ones with a base diameter of about 175 nm and a height of 30 to 70 nm, but with a low density of about 2×10^7 cm^{-2}, and smaller ones with a high density of about 4×10^9 cm^{-2}, and a height and base diameter of about 13 nm and 110 nm, respectively. Here, we consider only the smaller islands, and neglect the scattering from the larger islands because of their low density.

In order to distinguish between material composition and strain state, we measure not only the in-plane lattice parameter, as in grazing incidence diffraction studies, but also the lattice parameter in growth direction. This can be achieved by measuring reciprocal space maps (RSMs) with the momentum transfer component along growth direction $Q_z > 0$, as illustrated in Fig. 1(a) and (b). RSMs have been recorded around the (202) reciprocal lattice point (RLP) of Si, which is inaccessible in the conventional coplanar geometry at a wavelength of 1.55 Å, but can be accessed by rotating the scattering plane around the scattering vector **Q**, out of the plane of the RSM, as is shown in Fig. 1(c). With this setup, it is possible to keep the incidence angle α_i and hence the penetration depth constant at a value below ac for the entire RSM, in order to be sensitive to the dot layer at the sample surface.

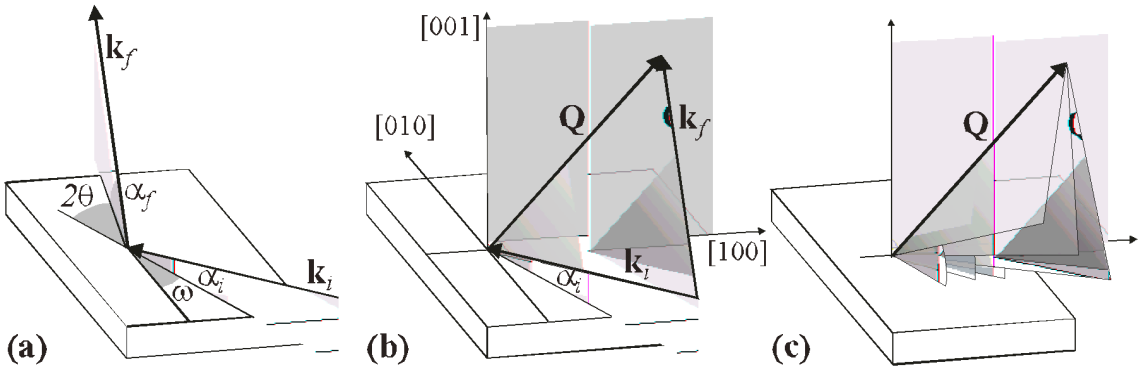

Fig. 1: Illustration of the scattering geometry in real space (a) and reciprocal space (b). (c) Tuning of the incidence angle by rotating the scattering plane around the scattering vector **Q**.

For the determination of the Ge distribution within the islands, we use kind of a "fitting" procedure: we start with an assumption on the Ge distribution and calculate the strain distribution using the finite element method (FEM). With this result the XRD pattern is calculated, and compared to the experimental result. Repeating the procedure while varying Ge distribution and island shape until a good correspondence between experiment and simulation is reached, we are able to establish the distributions of Ge content and strain within the islands. We assumed islands with the shape of a rotational parabo-

loid. With the FEM data, RMSs have been calculated using a kinematic scattering theory, and as well assuming a cylindrical symmetry.

Figure 2(a) shows the measured intensity distribution. Taking simply the peak maximum position Q_{max} and calculating the lattice parameters via the relation $a_{\parallel,\perp} = 2\pi/Q_{x,z}$, we would obtain values for the composition $x_{Ge} = 0.73$ and for the in-plane strain with respect to the substrate $\varepsilon_{\parallel} = (a_{\parallel} - a_{Si})/ a_{Si} = 0.011$. The results of our simulations are shown in Fig. 2(b) – (d). Using a constant composition of the SiGe islands, no good correspondence with the experiment can be obtained: assuming an island with the constant composition of $x_{Ge} = 0.73$, the simulation yields a peak at a different position than the measurement, at the correct value of Q_z, but at a too large value of Q_x (Fig. 2(c)).

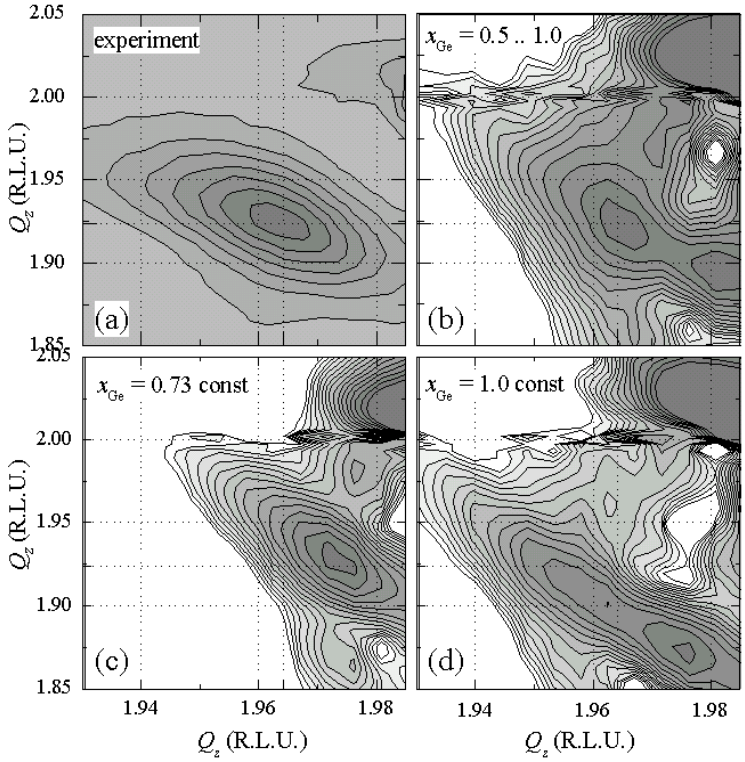

Fig. 2: (a) Reciprocal space map around the (202) Bragg reflection. (b) – (d) Simulations with different assumptions on the Ge distribution within the islands.

The reason for this difference is quite clear: the simple evaluation of the peak position assumes an island with homogeneous composition and homogeneous strain. As the island is grown pseudomorphically on the Si substrate, but relaxed towards the top, at least the latter cannot be true. We varied the composition of the island to obtain a smaller Q_x of the peak maximum. At $x_{Ge} = 1.0$ (Fig. 2(d)), the peak position is almost correct along Q_x, but now Q_z is too small. Hence it is clear that assuming a constant composition, no agreement with the experiment can be achieved. Thus we varied the Ge composition distribution within the island from a value $x_{Ge,1}$ at the base to a value $x_{Ge,2}$ at the top. Within the islands, the Ge content was assumed to be constant laterally, and only a vertical profile, either linear, or increasing like $z^{1/2}$ (i.e., the Ge content increases faster at the bottom of the island than on its top) or z^2 (Ge content increasing faster at the

top of the island than on its base), was assumed. We found the best correspondence between simulation and experiment for a faster increase of the Ge content at the base of the islands. Figure 2(b) shows the calculated RSM for a Ge distribution which reproduces the peak position best, with a maximum content of $x_{Ge,2} = 1.0$ at the top of the island, and $x_{Ge,1} = 0.5$. In contrast to, e.g., InAs Islands on GaAs [7], the maximum in-plane strain at the top of the islands reaches only about 0.02, i.e., the dot is only about 50% relaxed even at the top.

3. Conclusion

In summary, from our study it is evident that albeit pure Ge is deposited during MBE growth, the uncapped islands are alloyed, and the Ge content varies from about $x = 0.5$ at the base to $x = 1.0$ at the top (these particular values will depend sensitively on the growth parameters). We believe that the reduced elastic energy of an interdiffused island, [8] as compared to an island of pure Ge, is the main driving force for the alloying.

Acknowledgements

This project has been supported by SIGENET (EC). We thank D. Smilgies and the staff of TROÏKA II beamline at the ESRF (Grenoble, France) for their support.

References

[1] J.S. Sullivan, E. Mateeva, H. Evans, D.E. Savage, M.G. Lagally: “Properties of $Si_{1-x}Ge_x$ three-dimensional islands”, *J. Vac. Sci. Technol.*, vol. A17, 1999, pp. 2345 – 2350.

[2] S. Christiansen, M. Albrecht, H.P. Strunk, M.J. Maier: “Strained state of Ge(Si) islands on Si: Finite element calculations and comparison to convergent beam electron-diffraction measurements”, *Appl. Phys. Lett.*, vol 64, 1994, pp. 3617 – 3619.

[3] Chuan-Pu Liu, J.Murray Gibson, D.G. Cahgill, T.I. Kamins, D.P. Basile, R. Stanley Wiliams: “Strain Evolution in Coherent Ge/Si Islands”, *Phys. Rev. Lett.*, vol. 84, 2000, pp. 1958 – 1961.

[4] X.Z. Liao, J. Zou, D.J.H. Cockayne, Z.M. Jiang, X. Wang, R. Leon: “Composition and its impact on shape evolution in dislocatedGe(Si)/Si islands”, *Appl. Phys. Lett.*, vol 77, 2000, pp. 1304 – 1306.

[5] P.D. Miller, Chuan-Pu Liu, W.L. Henstrom, J. Murray Gibson, Y. Huang, P. Zhang, T.I. Kamins, D.P. Basile, R. Stanley Williams: “Direct measurement of strain in a Ge island on Si(001)“, *Appl. Phys. Lett.*, vol. 75, 1999, pp. 46 – 48.

[6] Th. Wiebach, M. Schmidbauer, M. Hanke, H. Raidt, R. Köhler, H. Wawra: „Strain and composition in SiGe nanoscale islands studied by x-ray scattering“, *Phys. Rev. B*, vol. 61, 2000, pp. 5571 – 5578.

[7] I. Kegel, T. H. Metzger, A. Lorke, J. Peisl, J. Stangl, G. Bauer, J. M. García, P. M. Petroff: „Nanometer-Scale Resolution of Strain and Interdiffusion in Self-

Assembled InAs/GaAs Quantum Dots“, *Phys. Rev. Lett.*, vol. 85, 2000, pp. 1694 – 1697.

[8] S.A. Chaparro, J. Drucker, Y. Zhang, D. Chandrasekhar, M.R, McCatney, D.J. Smith: “Strain-Driven Alloying in Ge/Si(100) Coherent Islands”, *Phys. Rev. Lett.*, vol. 83, 1999, pp. 1199 – 1202.

Strain Modulations in Si Underneath Patterned Oxide Stripes

A. Daniel, Y. Zhuang, J. Stangl, T. Roch, V. Holý, G. Bauer
Institut für Halbleiter- und Festkörperphysik, Johannes Kepler Universität, Altenbergerstraße 69, 4040 Linz, Austria

We present a characterization method for lateral strain modulations in Si substrates underneath laterally patterned periodic SiO_2 stripes. For the investigations, the x-ray grazing incidence diffraction (GID) technique was applied to enhance the sensitivity to the interface near regions. Apart from a tensilely strained part below the oxide lines, we find two compressively strained regions close to the edges of the stripes. Furthermore, the experimental GID results clearly show the depth dependent in-plane strain distribution. These data are relevant for electronic transport, particularly in short channel structures.

1. Introduction

With the continuing miniaturization of electronic device structures, inhomogeneous strain distributions of various origins become more and more important for the electronic transport. Consequently, information on these surface-near strain distributions in nanostructures has to be obtained with sufficiently high resolution. Among the x-ray diffraction techniques, grazing incidence diffraction (GID) is particularly well suited for such investigations. Several groups [1] – [3] have employed this technique for the study of heterostructures and of buried nanostructures. However, the quantitative analysis of GID data requires the use of either the fully dynamical diffraction theory, which is barely treatable, or as an simpler approach, the distorted wave Born approximation (DWBA) [4] – [5]. As a suitable model system we have chosen a laterally periodic SiO_2 layer on a Si substrate, for the following reasons: (i) Silicon dioxide is widely used for the fabrication of high-density semiconductor integrated circuit devices. In particular, with their shrinking dimensions, the structure and the quality of the interface between the oxide and the Si substrate are crucial for the performance and reliability of the devices. Additionally, the evolution of internal stresses during the conversion of Si into SiO_2 becomes more and more important in these miniaturized structures. These stresses mainly originate from the thermal expansion mismatch created by the oxidation process. (ii) Due to the amorphous nature of the oxide, the scattered intensity distribution in an x-ray diffraction experiment results only from the strain distribution in the single crystalline Si substrate. This clear-cut situation allows to include not only transmission and specular reflection into the undisturbed wave fields in the DWBA-simulations, as it was done previously [2], but also diffraction. Coplanar high angle diffraction technique yields only information on the average strain in the Si substrate, whereas GID provides a depth sensitivity due to incidence and exit angles close to the critical angle of total external reflection [6].

2. Experiment

We started from a Si (001) wafer with a 100 nm thermal SiO_2. In order to estimate the value of the effective linear mismatch $\chi = (\langle a \rangle_{SiO2} - a_{Si})/a_{Si}$ the curvature of the sample was measured using x-ray diffraction in transmission geometry. $\langle a \rangle_{SiO2}$ is the mean distance of the Si atoms in the amorphous SiO_2, and a_{Si} the bulk lattice parameter of silicon. From the curvature we obtain a range of $3.4\times10^{-3} \leq \chi \leq 5.7\times10^{-3}$. The error of the curvature measurements is quite large and does not allow for an accurate determination of χ. After the curvature measurement, the oxide was structured into laterally periodic stripes by holographic lithography and an etching step. The stripes were oriented along the [-110] direction and had a period of about 800 nm. The height of the stripes, examined by atomic force microscopy, was about 100 nm, and the width of the stripes was 350 nm.

Quantitative strain calculations based on the finite element method were performed to obtain the strain distribution in the Si substrate. Since the effective mismatch χ depends sensitively on the particular growth parameters and can only be determined with some uncertainty from the curvature measurements, we use it as a fit parameter. We finally obtained the best correspondence with the x-ray measurements using a value of $\chi = 4.3\times10^{-3}$. Figure 1 shows the resulting contour plots for different components of the strain tensor $\boldsymbol{\varepsilon}$. Directly underneath the SiO_2, a tensile force is exerted in the Si substrate which leads to a larger in-plane lattice constant compared to unstrained bulk Si. In between the SiO_2 stripes the Si in-plane lattice constant becomes smaller than that of unstrained bulk Si, corresponding to a compressed strain state.

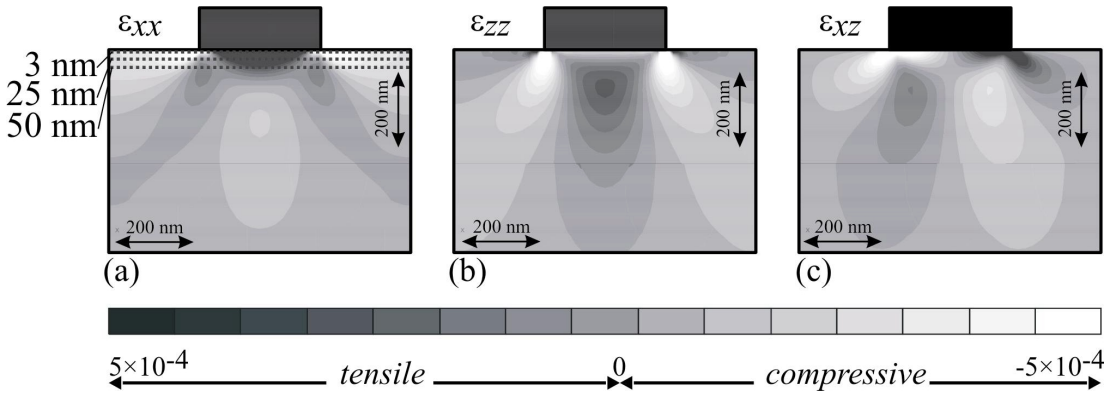

Fig. 1: Contour plots of the strain components (a) ε_{xx}, (b) ε_{zz} and (c) ε_{xz} based on finite element calculations for SiO_2 shadow mask and Si substrate.

Additionally, a compressively strained region appears in a larger depth > 100 nm below the center of the SiO_2 stripes. In the coplanar x-ray diffraction experiments, the whole region contributes to the detected signal, impeding a distinction between regions near and far from the Si–SiO_2 interface. In Fig. 2, ε_{xx} values for different depths in the Si substrate are shown, as indicated in Fig. 1(a).

For obtaining experimental information on such strain gradients in the Si substrate, GID experiments have been performed. In GID, the scattering plane is nearly parallel to the sample surface. If the angles of incidence α_i and exit α_f are close to the critical angle of the total external reflection α_c, the penetration depth of the x-ray beam depends very

sensitively on α_i and α_f. It changes typically from 5 nm for $\alpha_i < \alpha_c$ to several μm for $\alpha_i > \alpha_c$. Moreover, it is possible to choose the diffraction vector **h** either parallel (2-20) or perpendicular (220) to the stripes. In the first case the diffracted intensity depends only on the shape of the stripes.

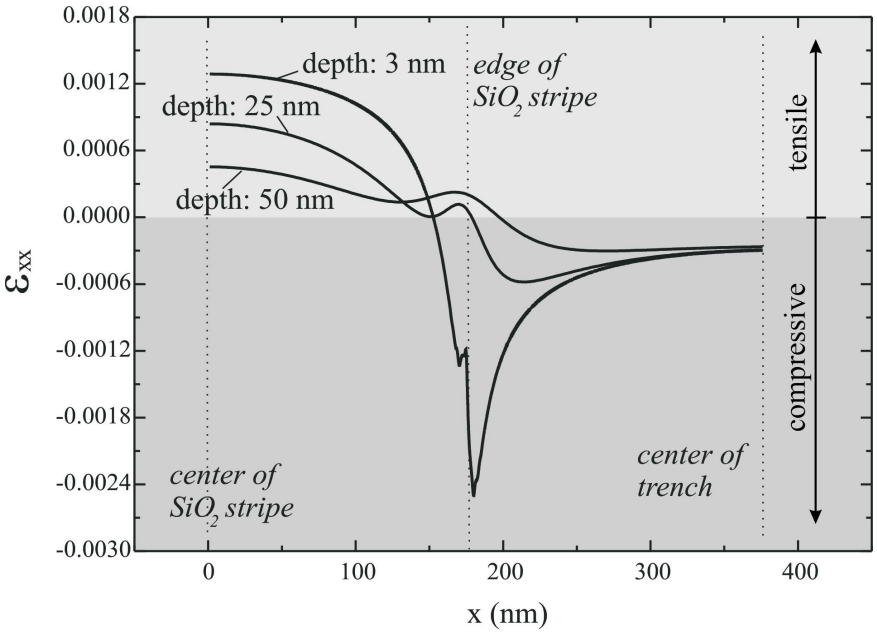

Fig. 2: Dependence of the strain tensor component ε_{xx} on lateral position in Si for three different depths below the interface.

In our case, the stripes are amorphous and thus in this geometry only a central peak at the position determined by the bulk Si lattice constant and no lateral peaks appear. This fact proves that the etching indeed stopped at the Si/SiO_2 interface and the Si substrate remains unpatterned.

In the second case, with the diffraction vector (220) perpendicular to the stripes, the intensity distribution depends both on shape and strain. However, in our case only the strain distribution in the crystalline Si accounts for the diffracted intensity distribution, reflecting both compressively ($q_x>0$) and tensilely ($q_x<0$) strained regions. Figure 3(a) shows longitudinal line scans measured around the (220) reciprocal lattice point for several angles α_i, keeping $\alpha_f = 0.20°$. The appearance of the satellite peaks proves the presence of the lateral periodic strain modulation in the Si substrate with a period of 765 nm. The envelope of the intensity distributions exhibits a slight dependence on the incidence angle α_i. For the simulation of the measured data we have to solve the problem of GID from a periodically strained semi-infinite crystal with a flat surface, since the SiO_2 stripes act only as stressors and they do not contribute to the diffraction process.

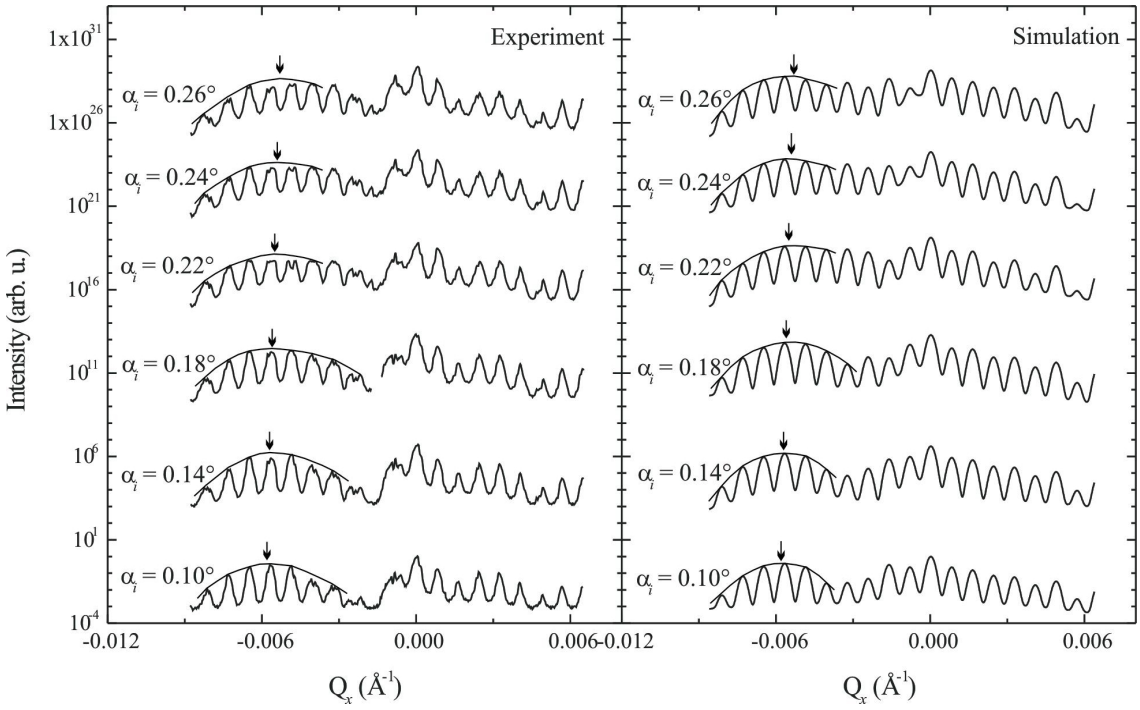

Fig. 3: Longitudinal line scans around the (220) reciprocal lattice point. (a) Experimental data, (b) simulations. For the tensilely strained regions, the envelope curve is indicated.

3. Results and Discussion

We calculated the dependence of the scattered intensity I on q_x using DWBA. A detailed description of the simulation model is given in Ref. [7]. The most significant influence of the effective mismatch χ on the simulations is found for values of $q_x < 0$ corresponding to the tensilely strained Si. Changing χ shifts the envelope curve and the best correspondence was found for $\chi = (4.3\pm0.2)\times10^{-3}$ (see Fig. 3(b)). Furthermore, the experimental data demonstrate clearly the presence of compressively strained regions in Si near the interface to the stripes. While for the tensilely strained regions beneath the stripes the lateral period is the same as for the stripes, two compressively strained regions exist near the surface at each edge of the SiO_2 stripes. Thus the lateral peaks for $q_x > 0$ exhibit an additional modulation. This is qualitatively well reproduced by the simulations.

4. Summary

A periodic array of SiO_2 stripes on the Si surface exerts a periodic stress field on the surface that results in a deformation field periodic in the direction perpendicular to the stripes. We have investigated this deformation field by grazing-incidence x-ray diffraction. The deformation field in the plane perpendicular to the stripes has been calculated by the finite element method. Using this result, the x-ray diffraction patterns were successfully simulated. These simulations have been performed by means of the distorted-wave Born approximation assuming a perfect crystalline substrate as an undisturbed system.

References

[1] T. Baumbach, D. Lübbert, M. Gailhanou, J. Appl. Phys. **87**, 3744 (2000).

[2] A. Ulyanenkov, N. Darowski, J. Grenzer, U. Pietsch, K.H. Wang, and A. Forchel,Phys. Rev. **B60**, 16701 (1999).

[3] S. Tanaka, C.C. Umbach, Q. Shen, and J.M. Blakely, Mat. Res. Soc. Symp. Proc. **405**}, 109 (1996).

[4] S.K. Sinha, E.B. Sirota, S. Garoff, and H.B. Stanley, Phys. Rev. **B38**, 2297 (1988).

[5] V. Holý, U. Pietsch, and T. Baumbach, *High-Resolution X-Ray Scattering From Thin Films and Multilayers*, (Springer Tracts in Modern Physics Vol. 149. Springer-Verlag Berlin, Heidelberg, New York, 1999).

[6] U. Pietsch, T.H. Metzger, S. Rugel, B. Jenichen, and I.K. Robinson, J. Appl. Phys. **74**, 2381 (1993).

[7] A. Daniel, V. Holý, Y. Zhuang, T. Roch. J. Grenzer, Z. Bochnicek, and G. Bauer, J. Phys. D: Appl. Phys, (2000) in print.

Potential Fluctuations in SiGe Quantum Wells

W. Jantsch[1], Z. Wilamowski[2], N. Sandersfeld[1] and F. Schäffler[1]

[1] Institut für Halbleiter- u. Festkörperphysik, Johannes-Kepler-Universität, Altenbergerstraße 69, 4040 Linz, Austria

[2]Institute of Physics, Polish Academy of Sciences, Al Lotnikow 32/46, 0668 Warsaw, Poland

We are able detect the electron spin resonance due to free carriers in modulation doped SiGe/Si/SiGe quantum wells due to its exceedingly small line width of down to 0.03 G. From the ESR we obtain the density of states that allows us to evaluate potential fluctuations and the Thomas-Fermi screening efficiency. The length scale of the fluctuations is estimated from the hyperfine broadening of the ESR. It implies ionized donors in the doping layer as the main source of fluctuations.

1. Introduction

Two-dimensional SiGe structures with particular design exhibit higher mobility than bulk crystals and therefore they allow the construction of devices with higher limiting frequency than Si. The mobilities obtained, however, and thus the maximum frequency, are still below the theoretical limit and therefore it is important to know the limiting processes. In this project, we investigate potential fluctuations in the two-dimensional (2D) channel of a SiGe/Si/SiGe structure by means of electron spin resonance (ESR). We show that these fluctuations limit the electron mobility.

Modulation doped quantum wells of Si embedded between SiGe barriers exhibit in standard X-band ESR an extremely sharp resonance [1] – [3] with a g-factor close to 2.0000. The line width under optimum conditions is 30 mG, *i.e.*, two orders of magnitude narrower than that of donors in Si. We identified this resonance as that of the free carriers in the quantum well on behalf of its two-dimensional symmetry, its scaling with the carrier density and its persistent properties after illumination [2].

In this paper we describe the determination of the magnetic susceptibility of the 2D electron gas (2DEG) from ESR and its evaluation in terms of the Pauli susceptibility. The latter is proportional to the density of states (DOS) of the 2DEG which, for an ideal system, should be constant above the band edge. We observe rather a smooth onset which we attribute to the existence of fluctuations. The Thomas-Fermi screening efficiency is also proportional to the density of states [4], and it is determined thus in the same experiment. Using this quantity we calculate the mobility, and we obtain good agreement with experimental data. This demonstrates that potential fluctuations which are responsible for the band tails are also responsible for the limited mobility. From the ESR line width we derive an average length scale for the fluctuations of the order of 1 μm. Such smooth fluctuations can arise only from remote ionized impurities.

2. Experimental

Modulation doped $Si_{0.75}Ge_{0.25}$/Si quantum wells were grown pseudomorphically on top of a linearly graded, relaxed $Si_{0.75}Ge_{0.25}$ buffer by MBE. To achieve n-type conductivity, an Sb-doped layer (25 nm thick) was placed 12 nm above the quantum well. After cooling in darkness, samples with a volume doping concentration of 7.10^{17} cm^{-3} are insulating. Prolonged illumination increases the electron concentration to 3.10^{11} cm^{-2} and a mobility exceeding 10^5 cm^2/Vs at 4.2 K. For gated samples, a Pd layer was evaporated in order to allow control of the 2DEG density.

Measurements were performed with a standard Bruker X-band spectrometer. We observe a strong increase of the integral CESR absorption with increasing illumination dose after cooling in darkness, and finally for prolonged illumination, the signal saturates. For a gated sample, we see a rather weak signal for zero bias that increases for accumulation and it saturates also for higher positive bias voltage.

In order to determine the carrier concentration *in situ*, we make use of cyclotron resonance (CR) which causes a broad background signal [2] in the standard ESR experiment. The CR amplitude increases and at the same time the CR width decreases persistently with increasing illumination dose. The latter reflects momentum scattering indicating improved mobility as the Fermi level moves up and away from the tail states. The CR signal can be fitted using the Drude expression for the dielectric function taking both the CR-active and the CR-inactive parts into account as it is necessary since linear polarized microwaves are used in our experiments [2]. The carrier concentration is normalized to its saturation value. The latter was determined independently by investigating Shubnikov - de Haas oscillations.

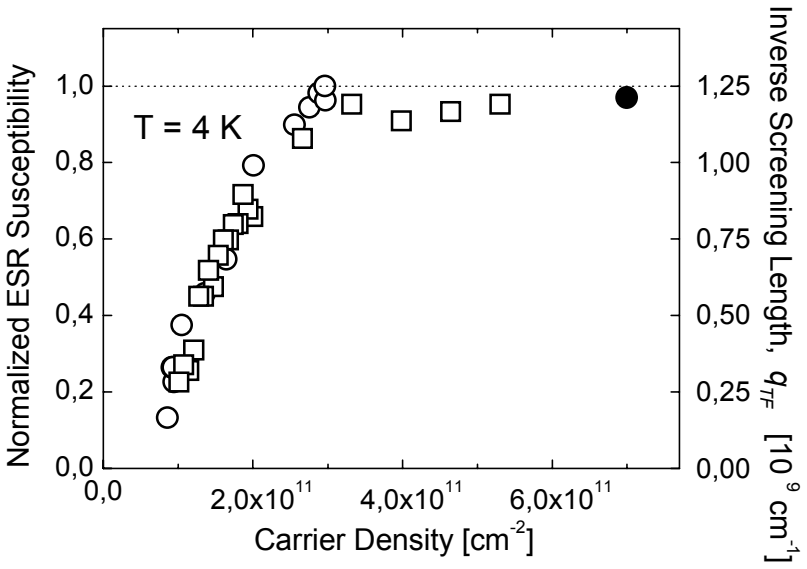

Fig.1: Normalized ESR susceptibility of the 2DEG as a function of carrier density for an ungated sample (circles), the same sample with a gate electrode (squares) and a highly doped sample (dot). The rhs scale gives the value of the Thomas-Fermi screening vector.

For gated samples, we used C-V measurements to determine the carrier density.

The integral ESR absorption is proportional to the magnetic susceptibility. In order to evaluate the DOS quantitatively we normalized the integral CESR signal to its saturation value and we assigned the unperturbed 2D DOS to that value. Typical results for the DOS at the Fermi level, $g(\varepsilon_F)$, are given in Fig. 1 as a function of the 2DEG density. The results show a smooth increase in the density of states instead of the sharp jump expected for an ideal 2DEG. For n_s, it approaches the ideal constant value asymptotically. For an ideal 2D DOS, the saturation carrier density of $n_s \approx 3.10^{11}$ cm^{-2} corresponds to a Fermi energy of about 2 meV above the unperturbed band edge.

Within the Thomas-Fermi model, the screening efficiency q_{TF} (inverse screening length) is also proportional to the density of states at the Fermi level, $g(\varepsilon_F)$ [4]. We are thus able to add another scale to Fig.1 giving that quantity. Both $g(\varepsilon_F)$ and q_{TF} increase gradually with increasing n_s instead of the sharp onset expected for an ideal 2DEG.

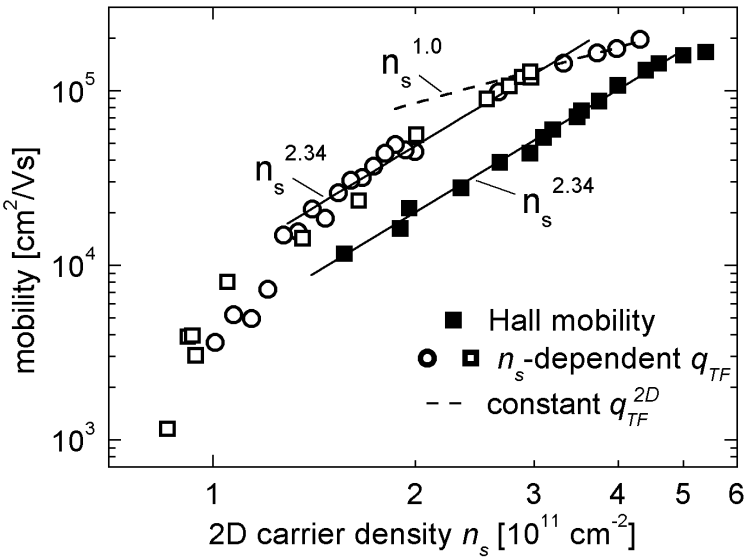

Fig. 2: Hall mobility (solid symbols) and calculated mobility in Thomas Fermi approximation (open symbols) versus n_s. The dashed line represents the ideal 2DCS.

This finding can be explained in terms of potential fluctuations superimposed on the band edge. Such fluctuations may arise from fluctuations of the well width, of the barrier composition, the distribution of ionized donors in the doping layer and residual charged impurities.

In order to test whether these potential fluctuations are the reason for the limited mobility we calculate the mobility within the Thomas-Fermi approach and compare the results to experimental data [5] given in Fig. 2.

As can be seen in Fig. 2, the experimental data differ from the values obtained from q_{TF} by less than a factor of 2 and the exponent is perfectly reproduced.

3. Conclusion

The agreement of the data derived from the ESR susceptibility with the directly measured mobility shows that the mobility is limited by the potential fluctuations that also cause the band tails close to the conduction band edge. The high mobility values seen, at least for high carrier density, show that screening is efficient within the 2DEG. At low carrier density localization occurs and the metal to insulator transition [6], [7] takes place where screening fails and the potential fluctuations tend to diverge [8].

The high mobilities seen indicate rather smooth, long range potential fluctuations. The ESR susceptibility alone does not give direct information on the typical length scale of these fluctuations. There is, however, another quantity which allows to determine a lower limit for the typical extension of the fluctuations in space, namely the ESR line width. The ESR line width is affected by all magnetic moments seen by electrons. This implies a lower limit for the area over which carriers can move freely, because the minimum CESR line width is given by the hyperfine interaction with nuclear spins in the probing area. With the relative abundance of 4.7% of ^{29}Si (the only stable Si isotope with nuclear spin) and the hyperfine constant of P in Si we estimate a minimum extension of the electron wave functions on the order of 1 μm^2. This value is in good agreement with spatially resolved compressibility measurements on GaAs hole channels [9]. Rather large extensions are also consistent with transport experiments on similar samples that revealed in the metallic regime Dingle ratios well in excess of 10. At such high values potential fluctuations are mainly due to the Coulomb potential of the ionized donors in the remote doping layer. These cause inherently smooth fluctuations, and thus large puddles in the insulating regime, since short-range fluctuations decay very fast with increasing spacer thickness.

Acknowledgements

Work supported also by FWF and ÖAD.

References

[1] N. Nestle, G. Denninger, M. Vidal, C. Weinzierl, Phys. Rev. **B56**, R4359 (1997).

[2] W. Jantsch, Z. Wilamowski, N. Sandersfeld and F. Schäffler, Phys. stat. sol. (b) **210**, 643 (1998).

[3] C.F.O. Graeff, M.S. Brandt, M. Stutzmann, M. Holzmann, G. Abstreiter, F. Schäffler, Phys. Rev. **B59**, 13242 (1999).

[4] see *e.g.* J.H. Davies, "The Physics of Low-Dimensional Semiconductors", Cambridge University Press, New York 1997, p353 ff.

[5] D.Többen, F.Schäffler, A.Zrenner, G.Abstreiter, Phys. Rev. B **46**, 4344 (1992), and D.Többen, Ph.D Thesis, Technical University Munich, (1995).

[6] S.V. Kravchenko, W.E. Mason, G.E. Bowker, J.E. Furneaux, V.M. Pudalov, M. D'Iorio, Phys. Rev. B **51**, 7038 (1995).

[7] E. Abrahams, P.W. Anderson, D.C. Licciardello, T.V. Ramakrishnan, Phys. Rev. Lett. **42**, 673 (1979).

[8] Z. Wilamowski, N. Sandersfeld, W. Jantsch, D.Többen, F. Schäffler, cond.matter 0010077.

[9] S. Ilani, A. Yacoby, D. Mahalu, H. Shtrikman, Phys. Rev. Lett. **84**, 3133 (2000).

Hot Electron Injection Field Effect Transistor

E. Kolmhofer, K. Luebke, H. Thim

**Microelectronics Institute, Johannes-Kepler-Universität,
Altenbergerstraße 69, 4040 Linz, Austria**

A new device geometry for a microwave FET with an injection limiting source contact is presented. Through this contact fast electrons are injected into the transistor channel region which leads to a shorter transit time and thereby raised upper frequency limits as compared to a conventional MESFET. Measurement and deembedding methods as well as obtained results are given.

1. Introduction

The purpose of the work reported is to present a new GaAs hot electron injection field effect transistor (HEIFET). In this device the ohmic source contact of a MESFET is replaced by an injection limiting contact in order to inject fast electrons into the channel region. As a consequence the electron transit time through the channel region is reduced, and so the transistors upper frequency limits (f_T and f_{max}) are raised.

2. Experimental

In our HEIFET [1] a hot electron injection contact of the type used in the planar injection limited Gunn diode or "FECTED" [2] replaces the highly doped source contact used in conventional MESFETs. The injection limiting contact which consists of an ohmic contact and an overlapping Schottky gate injects hot and, hence, fast electrons into the FET channel thereby reducing the total transit time throughout the channel. A cross sectional view of the HEIFET is shown in Fig. 1.

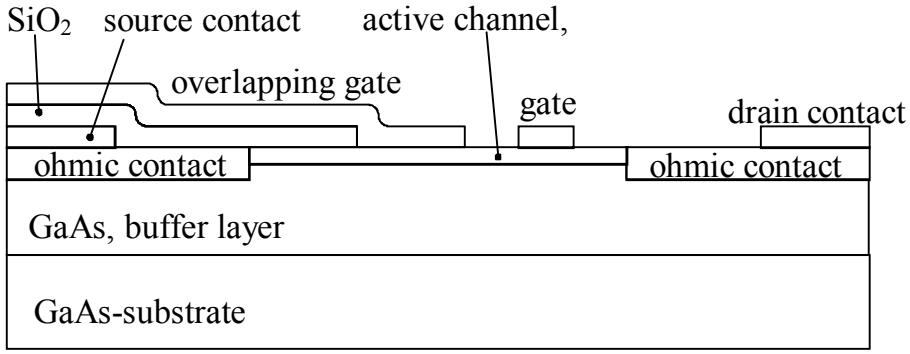

Fig. 1: Cross section of a HEIFET.

In conventional MESFETs the time needed to accelerate electrons leaving the highly doped source region can be as large as a few picoseconds due to the slow energy transfer (energy relaxation) time. This is in our opinion the reason why 0.5 µm gate MESFETs

exhibit a rather low f_T although the time electrons take to traverse a distance of 0.5 µm at saturated velocity (≈10^7 cm/s) is only around 5 ps which is one third of the RF cycle at 60 GHz and which should be short enough to allow efficient operation of a 0.5 µm gate-MESFET at 60 GHz.

3. Measurement Circuit

Our transistors are manufactured by conventional electron beam lithography and lift off techniques in the cleanroom of the Microelectronics Institute. The most critical step in the manufacturing process is the placement of the 0.5 µm gate between the overlapping gate and the ohmic drain contact. In order to need only one gate per transistor an asymmetric layout as shown in figure 1 has been chosen. The transistors are embedded in a coplanar test circuit which allows contacting with a Cascade Microtech waverprober with coplanar HF-tips and so measurement with an HP 8510C vector network analyzer. An overview of the transistor within it's test circuit is given in Fig. 2.

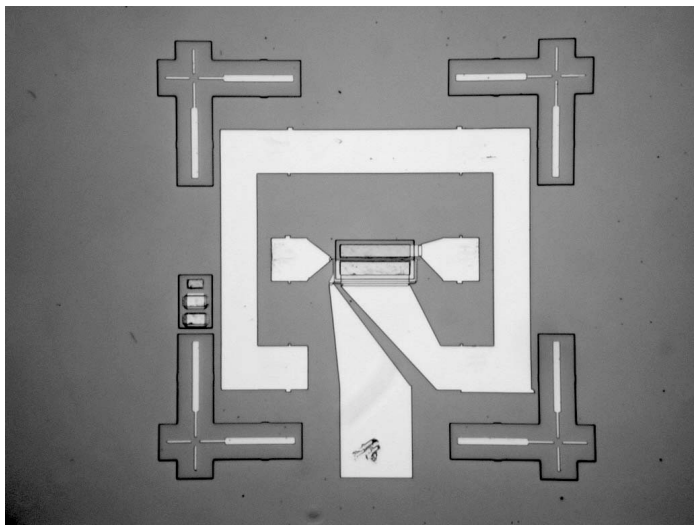

Fig. 2: HEIFET with measurement circuit.

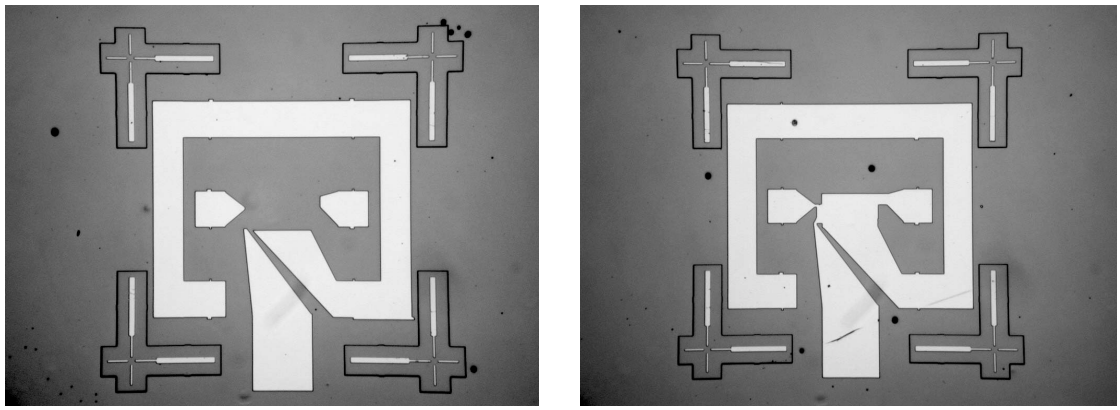

Fig. 3: Open structure (left) and short structure (right) for de-embedding.

4. De-embedding

The only purpose of the test circuit is to enable contacting of the device with coplanar tips during measurement. Since the overall behavior of the transistor is influenced by the test circuit's properties it is necessary to subtract this influence from the measured data. From several available methods to perform this deembedding operation we chose to use one employing separate open and short circuits as shown in Fig. 3 [3].

Following this method the deembedded impedance matrix Z_{TRAN} of the transistor can be calculated by $Z_{TRAN} = \left(Y_{DUT} - Y_{open}\right)^{-1} - \left(Z_{short}^{-1} - Y_{open}\right)^{-1}$. The required values Y_{DUT} for the embedded transistor, Y_{open} for the open structure, and Z_{short} for the short structure can be directly obtained from the measured S-parameters.

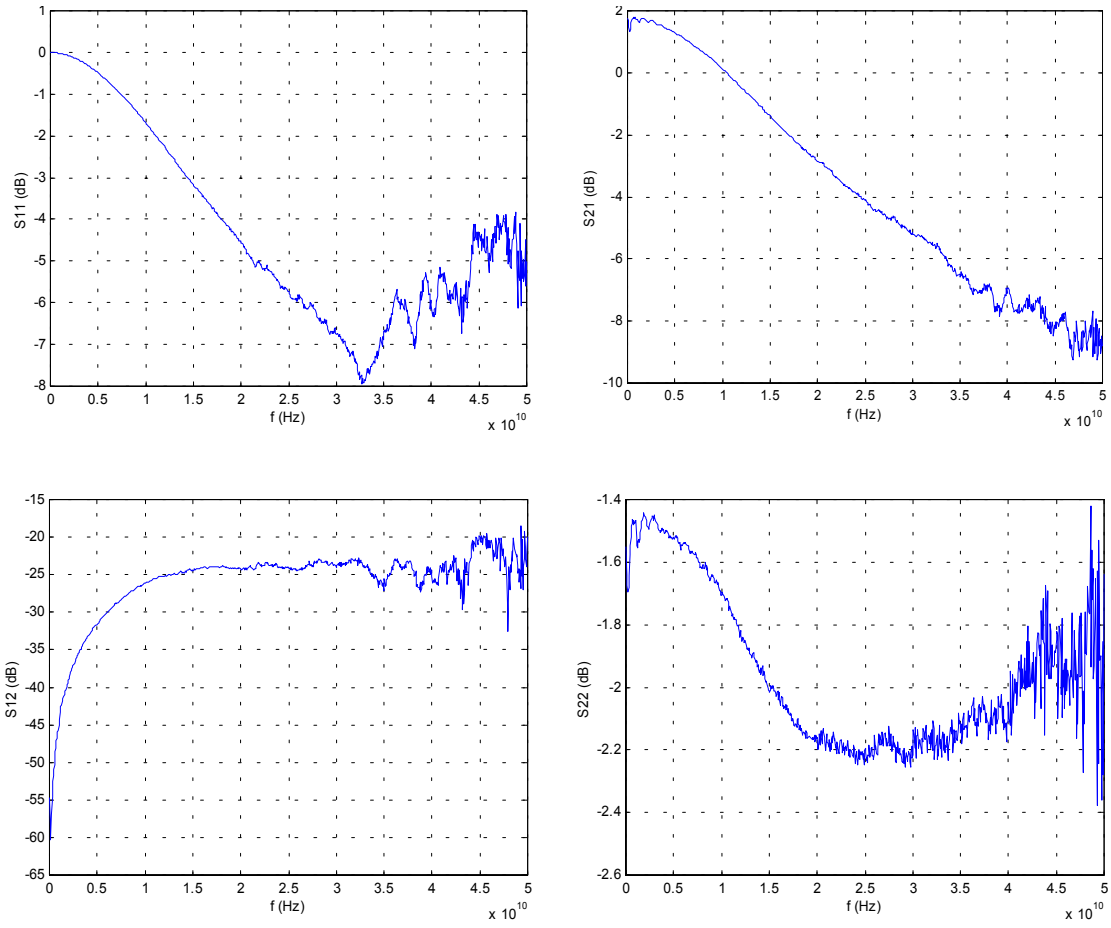

Fig. 4: De-embedded S-parameters of a HEIFET.

5. Results

Using our HP 8510C VNA our transistors have been measured in the frequency range from 45 MHz to 50 GHz. Figure 4 shows the deembedded S-parameters of a HEIFET at a drain voltage of $V_{DS} = 2$ V, gate bias voltage of $V_{GS} = -1.25$ V, and a bias voltage of $V_{BS} = 0.25$ V applied to the overlapping gate. Figure 5 shows the current gain h_{21} calculated from these S-parameters. Therefrom a transit frequency of $f_T = 32$ GHz is deter-

mined for this device. At a frequency of 32 GHz the h_{21} curve departs from its 20 *dB/decade* slope as can be seen in Fig. 5 and continues horizontally. In our opinion this departure from the expected slope is an artifact caused by effects which stem from measuring an asymmetric device with symmetric coplanar tips. Because of the smooth 20 *dB/decade* slope of the curve at lower frequencies we are nevertheless confident that the given value of f_T is reasonable.

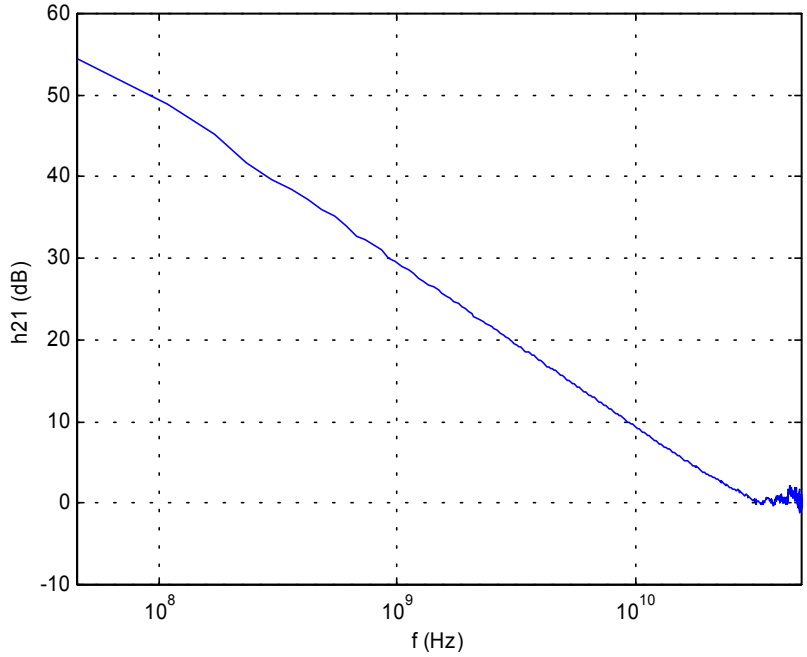

Fig. 5: Deembedded current gain of a HEIFET

6. Conclusion

Despite none of the usual features for improving the upper frequency limit of a FET like gate recess or a mushroom gate have been implemented our transistor shows a transit frequency of 32 GHz which is a good value for a 0.5 µm device. By replacing our current transistor layout with a symmetric one and using an appropriately modified test circuit we hope to extend the range of reliable S-parameter measurement towards higher frequencies. Additionally we hope to raise the f_T of our transistor by optimizing its geometry as well as the parameters of the active channel.

Acknowledgements

The authors would like to thank M. Hinterreiter and J. Katzenmayer for fabricating the devices. This work is supported by the Austrian Science Foundation (FWF) under contract No. P12702 TEC.

References

[1] E. Kolmhofer , K. Luebke , H. Thim, A. Lugstein and E. Bertagnolli: “Hot Electron Injection Field Effect Transistor”,*WOCSDICE 2000*, Aegean Sea, Greece.

[2] A. L. Springer, C. G. Diskus, K. Lübke, and H. W. Thim: “A 60GHz MMIC-compatible TED-Oscillator”, *IEEE Microwave and Guided Wave Letters*, vol. 5, no. 4, April 1995, pp. 114 – 116.

[3] T. E. Ostermann: “Untersuchung des $Si/Si_{1-x}Ge_x$-MODFET für den Einsatz in integrierten Schaltungen”, *Dissertation*, Universität Linz, 1999.

RF Radar Systems

C. G. Diskus[1], A. Stelzer[2]

[1] Microelectronics Institute, Johannes Kepler University, Altenberger Straße 69, 4040 Linz, Austria

[2] Institute for Communications and Information Engineering, Johannes Kepler University, Altenberger Straße 69, 4040 Linz, Austria

After a treatment of standard radar techniques the development of a radar sensor capable of measuring distance with 0.1 mm accuracy is presented. The operating frequency of the front-end is 34 – 36 GHz. The proposed prototype sensor makes use of some new techniques such as direct homodyne receiving and direct frequency measurement.

1. Introduction

The driving force in the field of radar technology has always been the development of military equipment. Especially during the Second World War the existence of operational radar sensors was crucial and fostered research. But the same is true for today's military R&D. Nevertheless, the end of the Cold War had a strong impact on the financial situation of the microwave industry forcing the opening of commercial markets.

Another reason for the rapid growth of the commercial radar market is the availability of microelectronic devices. A radar front-end is no longer a clumsy waveguide device but can be realized in a rather compact way. In addition, new manufacturing processes reduced the cost of such sensors significantly.

1.1 Frequency Allocation

One fundamental problem of every industrial radar application is the limited bandwidth. The resolution of a radar sensor is inversely proportional to the bandwidth. The frequencies that can be used by industrial sensors are restricted to the so called ISM-bands (industrial, scientific, medical). Table 1 shows the allocation of these frequencies.

1.2 Resolution and Accuracy

In contrast to the commonly used nomenclature the word resolution has a different meaning when used in connection with radar techniques. Converting a voltage to a number using an A/D-converter quantizes the information with the least significant digit being the resolution.

The resolution of a radar sensor is defined similar to the resolution of an optical microscope. It quantifies the minimum distance between two resolvable targets. For this reason, the accuracy of a radar measurement of a single target is usually much better than the resolution.

ISM-Band	Frequency range	Bandwidth	Resolution
1	26,957 – 27,283 MHz	326 kHz	460 m
2	40,660 – 40,700 MHz	40 kHz	3750 m
3	433,050 – 434,790 MHz	1,74 MHz	86 m
4	868,000 – 870,000 MHz	2 MHz	75 m
5	2,400 – 2,483 GHz	83 MHz	1,8 m
6	5,725 – 5,875 GHz	150 MHz	1 m
7	24,000 – 24,250 GHz	250 MHz	600 mm
8	61,000 – 61,500 GHz	500 MHz	300 mm
9	122,000 – 123,000 GHz	1 GHz	150 mm
10	244,000 – 246,000 GHz	2 GHz	75 mm

Table 1: ISM-Bands [1] and corresponding radar resolution.

2. Radar Principles

The two physical effects mainly used for measurements are (1) the Doppler effect, which allows the determination of the speed of a target, and (2) the propagation time of a wave for determining the distance to a target. Additional information can be obtained by evaluating other physical effects as attenuation, phase change, or rotation of the polarization plane.

Two different sensors were built at the Microelectronics Institute. A low cost speed sensor [2] using a microwave oscillator [3] and an InGaAs/GaAs detector diode [4] both developed in-house and a high end distance radar capable of measuring distance with an accuracy of 0.1 mm.

3. High Accuracy Distance Radar

On the initiative of the VOEST Alpine Stahl AG a highly accurate level sensor was developed. Due to the rather harsh environment in a steel plant laser sensors do not work satisfactorily, so applying microwaves was the technology of choice. This distance radar should be part of a closed loop control guaranteeing a constant level of liquid steel in a crucible.

3.1 Specifications

Not only the high temperature and the existence of fumes make the design of such a sensor challenging but also the demand for fast measurement cycles. The distance range is 0.5 to 1 m, the accuracy specification 0.1 mm. The sensor will be placed inside a metallic enclosure which allows sweeping the frequency over a larger bandwidth than specified in the ISM-bands.

3.2 Sensor Prototype

As a trade-off between accuracy and costs the frequency of operation was chosen to be 34 to 36 GHz. In this range most devices are commercially available with the exception of direct frequency counters.

To achieve the high accuracy the combination of two modes of operation is necessary: (1) a phase evaluation of the reflected wave at a constant frequency and (2) an analysis of a linear sweep (FM-CW … frequency modulated continuous wave). The phase measurement, which is unambiguous within a quarter of a wavelength, supplies the high accuracy while the coarse FM-CW measurement gives an absolute distance reading.

There are two possibilities of realizing a radar front-end: The conventional way is the application of a highly stable and, hence, expensive signal source. It is not only the stability of the frequency which is an issue but also the possibility of producing a very linear frequency sweep. This is essential for obtaining an accurate distance value using the FM-CW mode. By contrast, the signal source of the presented prototype sensor is a cost-effective varactor tuned Gunn oscillator (VCO … voltage controlled oscillator). The controlling bias of the varactor is provided via a digital/analog converter by a digital signal processor (DSP). After characterizing the control characteristic of the VCO by means of sweeping through the full bandwidth and recording the actual frequency, the generation of a precisely linear sweep is possible. Details of the direct frequency counter were published in [5]. A photograph of the whole radar set-up is shown in Fig. 1.

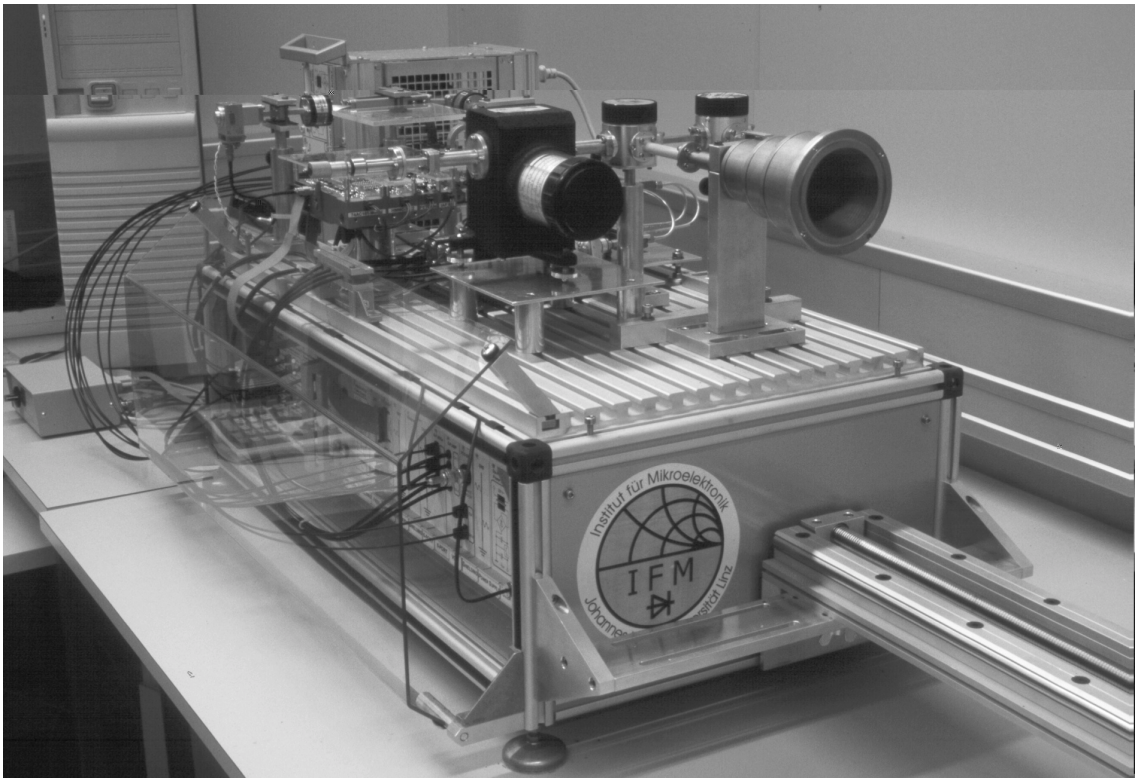

Fig. 1: Radar prototype consisting of waveguide and coaxial components.

The receiving part of the radar front-end is a so called six-port. This device has been used more and more since the early 1970's [6] in laboratories and research establishments and represents an attractive alternative to a conventional heterodyne receiver. The six-port technique is primarily used for measuring magnitude and phase of a received wave. In the proposed sensor the six-port allows measuring the phase of the reflected wave with respect to the incident wave with an accuracy of ±3 degrees which corresponds to about one hundredth of a wavelength.

3.3 Results

The distance measurement is accomplished in two steps. Firstly, a linear frequency sweep is applied yielding the absolute distance with an accuracy of ±1 mm. Note that the resolution of an FM-CW measurement with 2 GHz bandwidth is about 75 mm. Secondly, a constant 35.1 GHz signal is transmitted and the phase of the reflected wave is evaluated. This enhances the accuracy of the distance measurement to ±0.1 mm. The stability of the distance reading is one order of magnitude better [7].

Due to the application of a direct frequency counter the measurement cycle of a 20 bit frequency measurement is 120 µs. These time steps are only necessary for calibrating the VCO. The cycle time during the FM sweep (open loop control) is 6 µs.

4. Conclusion and Outlook

The proposed prototype sensor makes use of some new techniques such as direct homodyne receiving and direct frequency measurement. With these features the sensor operating in the 34 – 36 GHz range is capable of measuring distance with ±0.1 mm accuracy. Future work will concentrate on shrinking the sensor set-up by integrating the six-port and the detector diodes on GaAs.

Acknowledgements

The authors would like to thank K. Lübke and E. Kolmhofer for their support. The technical assistance of J. Katzenmayer and M. Hinterreiter is also greatly acknowledged. The presented projects were supported in part by the Austrian Science Foundation (FWF) and the Upper Austrian Government.

References

[1] A. Heuberger, V. Gehrmann: „Störsichere Übertragung in den ISM-Bändern“, *Elektronik*, Nr. 19, 1999, pp. 74 – 79.

[2] A. A. Efanov, C. G. Diskus, A. Stelzer, H. W. Thim, K. Lübke, and A. L. Springer: “Development of a Low-Cost 35 GHz Radar Sensor”, *Annales des Télécommunications / Annals of Telecommunications*, Special Issue to the International Workshop on Millimeter Waves, Vol. 52, Nr. 3-4, March-April 1997, pp. 219 – 224.

[3] K. Lübke, H. Scheiber, H. Thim: “A Voltage Tunable 35 GHz Monolithic GaAs FECTED Oscillator”, *IEEE Microwave and Guided Wave Letters*, Vol. 1, No. 2, Feb. 1991, pp. 35 – 37.

[4] C. G. Diskus, A. Stelzer, K. Lübke, H. W. Thim: “A Ka-Band Detector Diode with High Sensitivity”, Proceedings of the Seminar *Current Developments of Microelectronics 1999*, GMe, March 3 – 6, 1999, Bad Hofgastein, pp. 29 – 33.

[5] A. Stelzer, C. G. Diskus, K. Lübke: “Fast Frequency Measurement Applied to a Microwave Distance Sensor”, The Society for Microelectronics (Gesellschaft für Mikroelektronik - GMe), *Annual Report 1999*, Vienna, May 2000, pp. 103 – 106.

[6] G. F. Engen: “Application of an Arbitrary 6-Port Junction to Power-Measurement Problems”, *IEEE Transactions on Instrumentation and Measurement*, Vol. IM-21, No. 4, Nov. 1972, pp. 470 – 474.

[7] A. Stelzer, C. G. Diskus: “A Ka-Band Distance Sensor with 0.1 Millimeter Accuracy”, Proceedings of *2000 Asia Pacific Microwave Conference* (APMC 2000), Dec. 3 – 6, 2000, Sydney, Australia, Vol. 1, pp. 465 – 468.

Fabrication of AlGaAs Nanostructures

T. Berer, G. Pillwein and G. Brunthaler

Institut für Halbleiter- und Festkörperphysik, Johannes Kepler Universität, Altenbergerstraße 69, 4040 Linz, Austria

G. Strasser

Institut für Festkörperelektronik, TU Wien, Floragasse 7, 1040 Wien, Austria

In order to investigate the electrical conductivity of nanostructures at low temperatures, different types of nanostructures were fabricated in the AlGaAs material system. The narrow lateral regions were either defined by deep etched grooves or by split gate structures on top of the samples. The electron density in the structures were additionally changed either by illumination or a large top gate Schottky contact. The formation of a 1D electron gas channel was observed.

1. Introduction

The driving force behind the investigation of solid state nanostructures is twofold. On the one hand side, the continuing miniaturization in microelectronics calls for investigation of the lower size limits for devices, on the other hand, nanostructures allow access to new fields in basic physics.

Today's miniaturization in microelectronics can be characterized by Moor's law – every 3 years, the single-chip memory size is increased by a factor of 4. The smallest structure size in this type of semiconductor devices is the gate length, which is 0.18 μm nowadays. This development in miniaturization is expected to continue at least for several years. But finally some hard physical limits will be reached. At least, when one memory unit would have the size of a single atom, a further continuation of miniaturization in the common way is hard to imagine. But other limits will be reached much earlier. If one continues to works with doped semiconductor structures, at much larger length scales one will reach the limit where only a few electrons will be in a single device, which makes the control of such a structure unreliable. Another limit is set by the wavelength of free electrons. As soon as the electrons wavelength becomes comparable with the structure size, interference and quantization effects will occur and strongly influence the functionality of such a device.

The latter limit is the starting point for a manifold of new physical phenomena. The confinement of electrons in nanostructures leads to a quantization in energies and wavefunctions. This allows, at least at low temperatures, the exact control of the state of the electrons and even allows to manipulate them individually. In quantum dots with two connecting tunneling contacts, single electron transmission due to Coulomb blockade can be achieved. Even the realization of quantum computation in solid state structures is considered nowadays.

In order to contribute to research and development in the above mentioned fields, we have established the techniques for the fabrication of nanostructures in the cleanroom

facility in Linz. All necessary steps can be undertaken, including the critical electron beam lithography and etching steps. We have chosen AlGaAs heterostructures a the starting point for the nanostructures fabrication. Figure 1 shows the internal layer structure of a typical sample. The high mobility two-dimensional (2D) electron gas is formed in the GaAs buffer layer at the interface towards the above lying AlGaAs spacer. The doping region is typically 20 nm away from the interface in order to reduce the scattering efficiency and increase accordingly the mobility of the 2D electron gas.

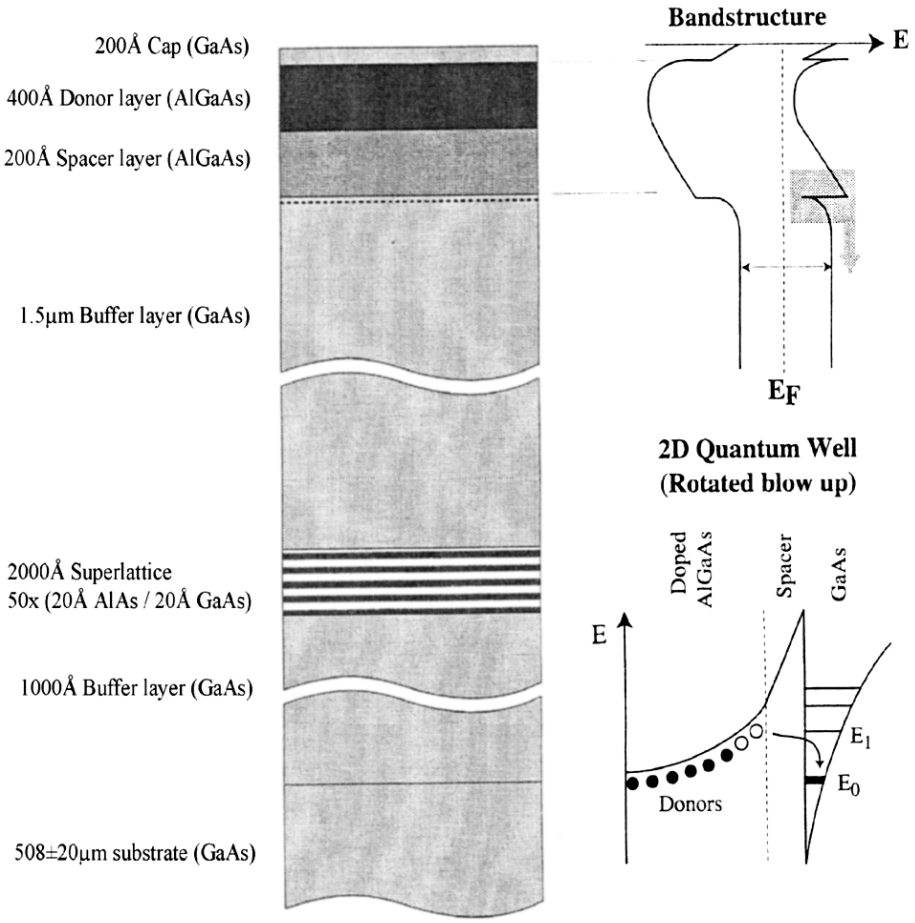

Fig. 1: The scheme on the left hand side shows a typical layer sequence of an AlGaAs heterostructure for achieving a high-mobility two-dimensional electron gas system. The upper diagram on the right hand side shows the band diagram of the heterostructure, the lower diagram displays the energy diagram in the vicinity of the electron gas on an expanded scale.

In order to be able to perform electrical measurements on nanostructures, some geometry for the electrical connections, the ohmic contacts and possible gates have to be prepared. We use a Hall bar geometry, which allows the determination of electron densities and mobilities on the same piece of heterostructure. The ohmic contacts are formed by a sequence of Cr/Ge/Au/Ni/Au which is evaporated onto the sample and annealed for 1.2 minute at 450°C. The Hall bar geometry was defined by a reversal photoresist AZ5218 and etched with CH_4 and H_2 in an "Oxford 80Plus" reactive ion etching system or in a

wet chemical etch process. The different nanostructures are then prepared out of the Hall bar structures.

2. Etched Nanostructures

One kind of nanostructures is prepared by etching deep grooves into the heterostructure, which divide the 2D electron gas layer into different isolated regions. The groove structures were defined on the Hall bar by electron beam lithography with a JEOL 6400 microscope in a PMMA/MA photoresist. The etching of the structures was performed in the reactive ion etching system with CH_4/H_2 gas. The photoresist is then removed in a TEPLA asher. Wire structures with different widths between 100 and 1200 nm were produced, see Fig. 2a and 2b for 500 and 100 nm wide wires. In addition point contacts and ring structures were prepared (Fig. 2c and 2d).

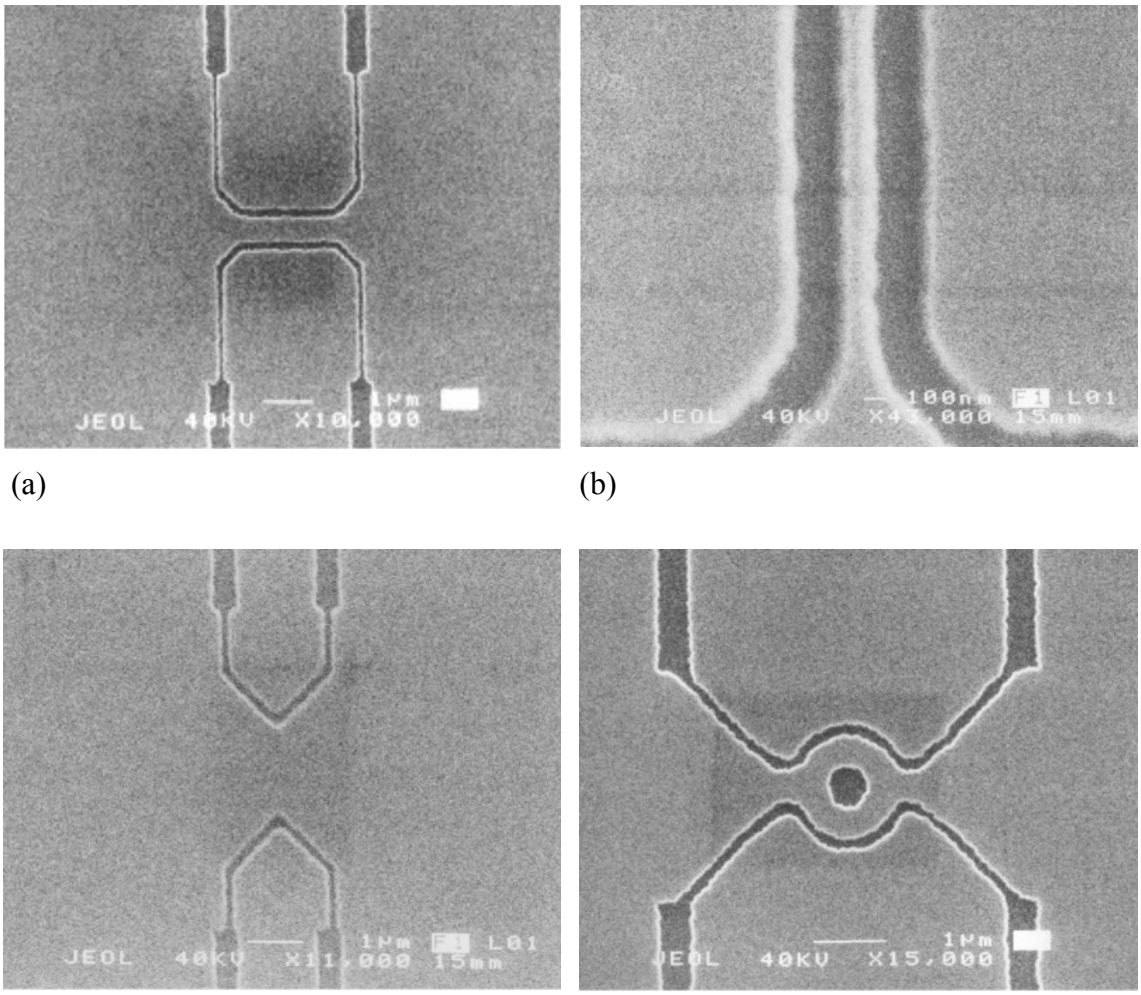

(a) (b)

(c) (d)

Fig. 2: (a) 2 µm long wire structure; (b) detail of a 100 nm wide wire; (c) etched point contact; (d) etched ring structure.

The electrical properties of theses nanostructures were investigated. Most of the narrow structures were not conducting. This is caused by the defect states at the GaAs surface, which have a very high density close to midgap. Free electrons from the neighborhood

go to those defect states leading to a depletion layer. Narrow etched nanostructure channels are thus usually not conducting in the GaAs material system. Only wider structures remain conducting despite the surface depletion.

Figure 3 shows resistivity measurements on a 400 nm wide, 2 µm long wire structure versus applied perpendicular magnetic field at a temperature of 1.5 K. As this sample had no gate, the electron density was varied via illumination with an infrared light emitting diode. Different curves in Fig. 3 correspond to different illumination intensities, where lower resistivity means higher intensity. Several curves show a step-like increase in resistivity at a magnetic field of about 0.6 T. The steps occur approximately between 1/10 and 1/6 of h/e^2 and between 1/6 and 1/4 h/e^2 and thus seem to correspond to transitions between different occupations of electron channels in the one-dimensional (1D) wire [1].

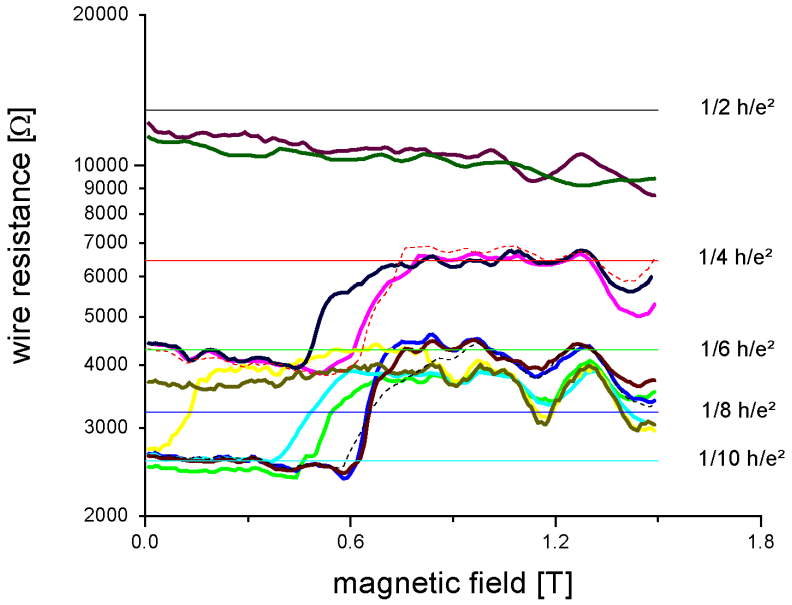

Fig. 3: Wire resistance versus magnetic field for a 400 nm wide, 2 µm long wire structure. Different curves correspond to different illumination intensities of the nanostructure with a infrared light emitting diode.

Due to the persistent photoconductivity effect, caused by DX-centers in AlGaAs structures [2], it is possible to increase the density of 2D electrons with illumination, but the density does not decrease to its previous value after switching off the illumination. Therefore it is difficult to change the density arbitrarily and the use of gated structures is desired.

3. Top Gate

By using a top gate, which covers the whole area of the 2D electrons gas together with the deep etched grooves, the electron density can be varied within a certain range. We have fabricated both a Schottky gate and an insulated metal gate on top of the structures.

The area of the Schottky gate is defined in the usual way by photolithography, an Al metal layer is evaporated and the rest of the photoresist and the metallic layer is removed in the lift-off step. Figure 4 shows a sample where the surface is covered by an Al top gate. The Al layer forms itself a Schottky contact to the GaAs surface. With the Schottky gate, the electron density n could be varied typically between 1.2×10^{11} and 4.2×10^{11} cm^{-2} before the leakage currents became too large. At low electron densities, where the resistivity is strongly increasing, we have observed several steps in the conductance versus gate voltage behavior, which can be attributed to transport in 1D channels.

As the Schottky gate starts to leak when the applied voltage becomes too high, we have also tested a metal gate on top of an insulating layer. As insulating layer, a PMMA/MA photoresist was used as this material is quite stable against thermal stress during cool down of the samples in a cryostat. A Ti/Au or Cr/Au layer was deposited on top of the insulation layer, the Ti (Cr) acts as an adhesive layer, the thicker Au is used as a contact layer for bonding beside the Hall bar. The samples with this kind of gate contact showed only a very small change of the electron density with applied voltage. It seems that lateral currents below the insulating layer shield the gate voltage, and the electron gas is nearly not affected.

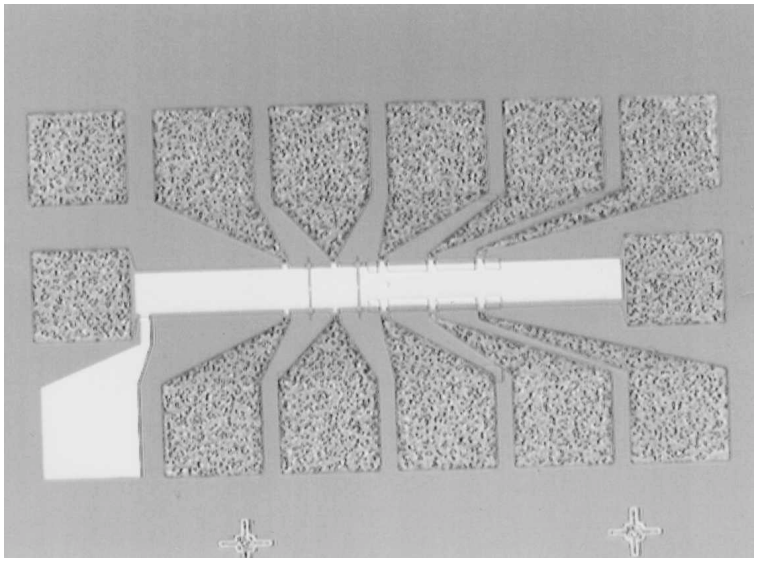

Fig. 4: Hall bar sample, where the 2D electron gas region together with the deep groove etched nanostructures is covered by an Al-Schottky gate.

4. Split Gate Nanostructures

Last but not least, split gate nanostructures were fabricated from the AlGaAs heterostructures. In these samples, a Schottky gate crosses the Hall bar from one side to the other, but leaving a narrow gap of several hundred nm width open. The narrow lateral gap in the gate was defined by electron beam lithography in the two-layer PMMA photoresist. The Al gate was produced in a lift-off step and is shown in a raster electron micrograph in Fig. 5(a).

By applying a negative voltage to both parts of the split gate, the electron density underneath can be reduced until the 2D electron gas is completely suppressed and the two conducting regions are separated. Only in the narrow restriction below the gap in the split gate, the two regions of the 2D gas are electrically connected via a 1D channel. This can be seen in Fig. 5(b) in the resistivity versus gate voltage curve as a plateau. By further increasing the negative gate voltage, also the lateral potential of the 1D channel shrinks, and the resistivity increases further. Small steps, probably due to the quantized conductance in the 1D wire, can already be seen in Fig. 5(b). This resistivity range is most interesting as it contains the conduction through only a few 1D channels and will be investigated in more detail in the future.

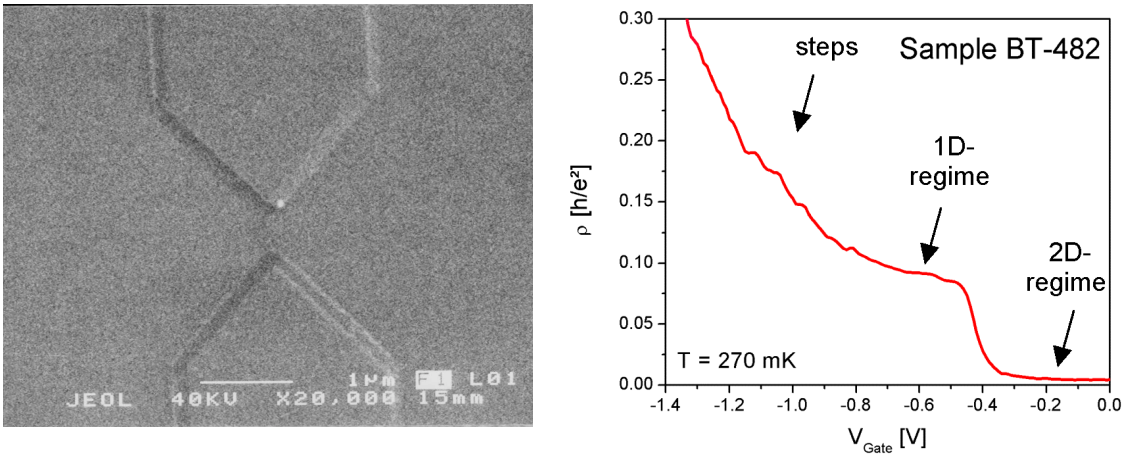

(a) (b)

Fig. 5: (a) Split gate geometry formed by Schottky gate fingers on top of an AlGaAs heterostructure. The restriction has a lateral width of 400 nm. (b) Resistivity versus gate voltage behavior of the top gate structure.

5. Conclusion

We have fabricated several types of nanostructures on high mobility AlGaAs heterostructures. The samples with deep etched grooves suffer from the surface depletion of the GaAs material system, and it is difficult to control the conductivity for narrow lateral structures. Top gate structures worked, but the range in which the electron density can be varied is restricted due to the leakage of Schottky gates. Split gate structures were best suited to change the electron density in a narrow point contact.

Acknowledgements

We thank Poul Erik Lindelof and Rolf Haug for discussions concerning the fabrication and investigation of semiconductor nanostructures. The work was partly supported by the Austrian Science Foundation (FWF Project P13439-TPH).

References

[1] T. Ando: “Quantum point contacts in magnetic fields”, Phys. Rev. B **44**, 1991, pp. 8017 – 8027.

[2] G. Brunthaler, M. Seto, G. Stöger and K. Köhler: "Influence of Coulombic broadened DX center energy levels on free electron concentration in δ-doped AlGaAs/GaAs quantum wells", Appl. Phys. Lett. **65**, 1994, pp. 3084 – 3086.

Erbium in SiO_x Environment: Ways to Improve the 1.54 µm Emission

G. Kocher[1], H. Przybylinska[1,2], M. Stepikhova[1,3], L. Palmetshofer[1] and W. Jantsch[1]

[1] Institut für Halbleiter- u. Festkörperphysik, Johannes Kepler Universität, Altenbergerstr. 69, 4040 Linz, Austria

[2] Institute of Physics, Polish Academy of Sciences, 02-668 Warsaw, Poland

[3] Institute Physics of Microstructures RAS, 603600 Nizhny Novgorod, GSP 105 Russia

Si:(Er,O) based light emitting diodes were developed and fabricated, emitting at room temperature in breakdown regime at a wavelength of 1,54 µm. We investigated doping profiles and electrical activity in order to optimize our structures for room temperature luminescence. We present data from SIMS and Hall effect investigations, which demonstrate significant deviations from TRIM simulations of the implantation profiles and the hitherto assumed electrical activity of Er in such environment.

1. Introduction

It is known that electroluminescence (EL) of erbium in silicon can be achieved by impact excitation with hot electrons injected in a reverse biased (r.b.) diode. Obviously, various Er centers can be excited in the impact excitation process. They can be distinguished by their characteristic luminescence line patterns. It was found, however, that the centers responsible for room temperature luminescence are contained in SiO_x precipitates. Their dominance at high temperature EL becomes apparent in the transformation of the emission spectra from the characteristic sharp line spectra to a less structured band with 20 nm width. The incorporation of Er in SiO_x clusters is achieved by Er and O implantation and subsequent annealing above 950 °C. The latter is necessary in order to initiate the formation of SiO_2:Er precipitates.

Er electroluminescence at room temperature can be realized in diodes operating both in the tunneling and in the avalanche regimes. In tunneling diodes, the Er excitation occurs only at a very small volume, within 15 nm of the depletion edge [1]. Making use of an avalanche process allows us to increase the excitation volume considerably but it is still limited to the space charge region of a pn-junction only.

The fabrication of these diode structures requires accurate control of doping gradients and thus knowledge of the electrical activity and the distribution of the implanted dopants. We present data from SIMS and Hall effect investigations, which demonstrate significant deviations from TRIM simulations of the implantation profiles and the hitherto assumed electrical activity of Er in such environment.

2. Design and Realization of p-n Junctions

An important property of the Er centers is their electrical activity which has to be taken into account in the design of the diodes. For isolated centers a large portion can be electrically active. Electrical activity has been seen also for SiO_2 precipitates. Therefore we investigated the electrical activity of our $SiO_{2-\delta}$:Er precipitates by means of Hall effect measurements on samples prepared by implanting Er into high resistivity Si substrates (Fig. 1). As a result, we estimate an electrical activity of less than 3% for this sample.

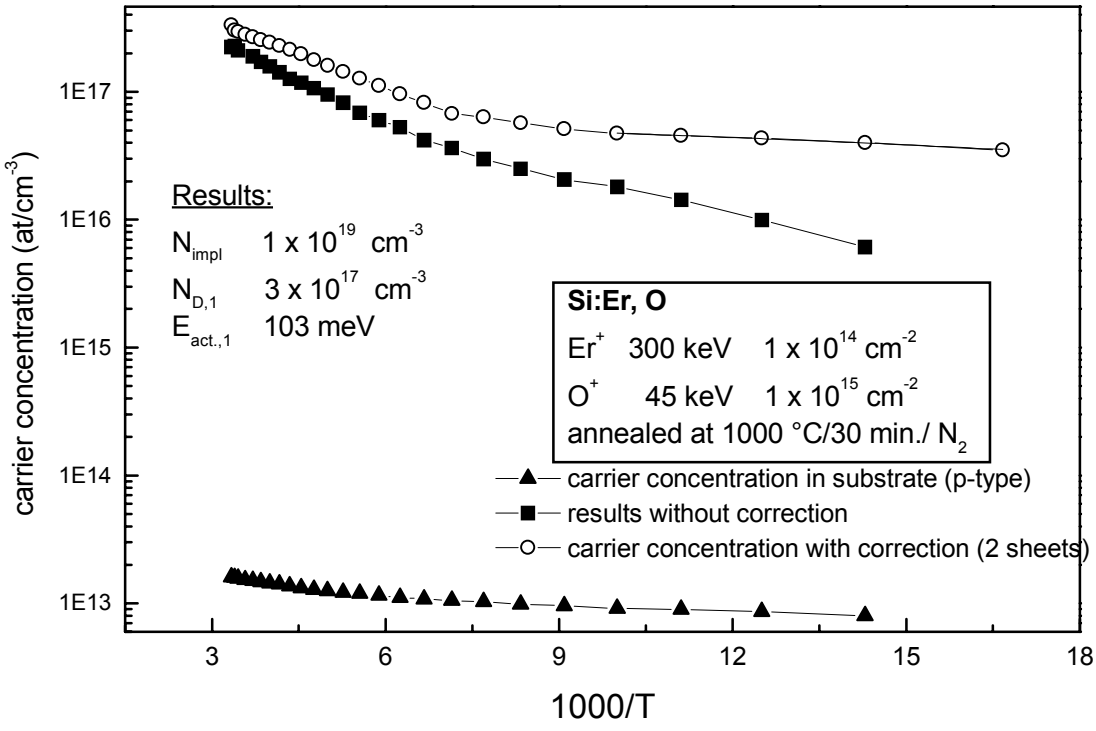

Fig 1: Arrhenius plot of the electron concentration measured by Hall effect on a sample of p-Si ($\rho > 1000\ \Omega\cdot$cm) implanted with Er+O. For the evaluation of the electron concentration a two sheet model was applied in order to correct for the substrate contribution.

The early successful attempts to obtain EL from *r.b.* p-n junctions were performed on diodes with large doping gradients that showed tunneling breakdown [2] – [4]. The problem with this kind of excitation is the short ballistic range of electrons with a energy of more than the 0.8 eV that are required to excite Er [1]. That way only a very small fraction of the incorporated Er can be excited and the total efficiency of such a device would be rather limited. An avalanche breakdown is expected to offer considerable advantages as it occurs in a much wider volume.

The most relevant parameter deciding about the two types of breakdown is the electric field strength which in turn is ruled by the doping gradient. According to Sze, for Si at room temperature the doping gradient must not exceed a value of 10^{23} cm^{-4} if avalanche conditions are desired [5]. This, together with the requirement of a large concentration of optically active Er centers in the avalanche region needs careful design of the implantation parameters and knowledge of the resulting implantation profiles.

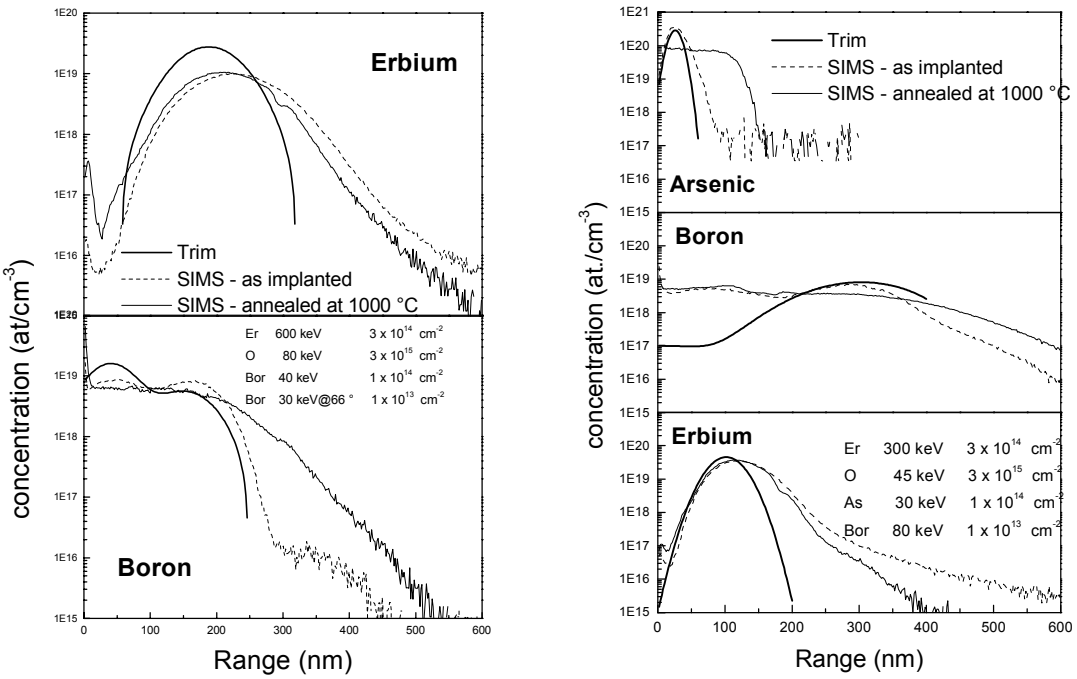

(a) (b)

Fig. 2: Implantation profiles of Er and B into n-Si (a) and Er, As and B into p-Si (b) substrates.

Comparison of the implantation profiles measured by SIMS and those simulated by the TRIM code led to a surprise: the profiles of Er are substantially deeper than expected (see Fig. 2). Since the same discrepancy was found for Er implanted into amorphous SiO_2 [6], channeling effects can be excluded. Because of the low electrical activity of Er under the present preparation conditions this discrepancy may not be crucial for the electronic properties of a diode, but it is important for the optimal spatial overlap of the Er profile and the avalanche excitation volume. More important, however, is the fact that the shallow dopants also start to diffuse substantially at the annealing temperature of 1000 °C (s. Fig. 2). This diffusion has a strong influence on the doping gradient at the p-n junction and therefore realistic profiles have to be taken into account in the design of an avalanche breakdown diode.

Another important design consideration concerns the question of homogeneity of the field strength and thus of the generation rate in the avalanche regime across the diode cross section. It is well known that in an avalanche diode the field strength close to the edge of the contact may exceed the average field strength substantially. Consequently avalanche breakdown occurs already at lower voltage and excitation concentrates at the circumference of the diode whereas the center of the diode remains dark. This effect may lead to an early degradation of such a diode. In order to avoid this effect we apply a guard ring structure as it is also applied in the design of avalanche photon detectors.

3. Conclusion

At present, the only principle yielding stable emission at room temperature employs impact excitation of the Er in a reverse biased p-n junction. It has been shown that thermal quenching of the luminescence can be avoided by producing a particular type of Er center. This type of center exhibits a single inhomogeneously broadened line with two characteristic asymmetrically arranged shoulders. There are several indications for an SiO_2-like surrounding of Er in this type of centers. The SiO_2:Er centers exhibit also larger excitation cross section for hot electrons than the isolated Er centers. We have shown that in the design of such a diode it is essential to control the doping gradient in order to achieve avalanche rather than tunneling breakdown in the diode. It turns out that TRIM simulations are insufficient to describe the Er implantation profile and either diffusion of the shallow dopants has to be taken into account at the necessary formation temperature for the SiO_2:Er clusters of 950 °C or a second implantation and annealing step at lower temperature is necessary. As a result, almost temperature independent emission of 1.54 μm can be achieved in a diode that can be produced in a way compatible with present Si technology. The shortcoming of this type of device is the rather low yield (mW/cm^2), the low efficiency (10^{-4}) and the relatively big linewidth (20 nm).

Acknowledgements

This work is supported by the GMe, FWF, ÖAD, and INTAS

References

[1] S. Coffa, G. Franzo, F. Priolo, Appl. Phys. Lett. 73, 1998, 93.

[2] G. Franzo, S. Coffa, A. Polman, A. Carnera, F. Priolo, Appl. Phys. Lett. 64, 1994, 17.

[3] J. Stimmer, A. Reittinger, J.F. Nützel, H. Holzbrecher, Ch. Buchal, G. Abstreiter, Appl. Phys. Lett. 68, 1996, 23.

[4] S. Coffa, G. Franzo, F. Priolo, Appl. Phys. Lett. 69, 1996, 2077.

[5] S. M. Sze, “Physics of Semiconductor Devices”, (J. Wiley, N.Y. 1981, 2nd ed.) p. 96 ff.

[6] L. Palmetshofer, M. Gritsch, G. Hobler, Material Sience and Engeneering B 56, in print.

Lead-Salt Microcavities for the Mid-Infrared

W. Heiss[1], T. Schwarzl[1], G. Springholz[1], T. Fromherz[1], G. Bauer[1], M. Aigle,[2] H. Pascher,[2] K. Biermann[3], K. Reimann[3]

[1]Institut für Halbleiter- u. Festkörperphysik, Johannes Kepler Universität, Altenbergerstraße 69, 4040 Linz, Austria

[2] Experimentalphysik I, Universität Bayreuth, 95447 Bayreuth, Germany

[3]Max-Born-Institut für Nichtlineare Optik und Kurzzeitspektroskopie, 12489 Berlin, Germany

Operation of optically pumped IV-VI vertical-cavity surface emitting lasers is reported. The microcavity structures were grown by molecular beam epitaxy on BaF_2 (111) substrates. High reflectivity $Pb_{1-x}Eu_xTe$/EuTe multilayers are used as Bragg interference mirrors of the cavity. Stimulated emission at wavelengths between 3 and 4.5 μm is generated either in PbTe quantum wells embedded at the antinode positions of the microcavity or in correlated, self-organized PbSe quantum dots.

1. Introduction

Narrow band gap IV-VI semiconductor compounds (lead salts) are important materials for optoelectronic devices for the mid-infrared (MIR) spectral region (3 – 30 μm). As a result of their favorable band structure, lead salt diode lasers were obtained with cw operation temperatures up to 223 K [1] and up to 60 °C in pulsed mode [2]. This represents the highest cw operation temperature for electrically pumped MIR diode lasers. The major application for such lasers is high resolution and high sensitivity chemical gas analysis as well as atmospheric pollution monitoring. This is due to numerous absorption lines of many gaseous molecules in the MIR range.

Apart from the conventional edge emitting lasers, very recently, surface emitting lead-salt mid-infrared microcavity lasers were demonstrated for the first time [3]. These vertical cavity surface emitting lasers (VCSELs) offer several advantages like a circular output beam with small divergence, single mode operation, and the possibility of high monolithic integration. In addition, VCSELs offer the possibility for reducing the threshold currents and increasing operation temperatures.

In this work, lead-salt VCSELs working in the wavelength range between 3 and 4.5 μm are presented. With optical pumping, pulsed laser operation is demonstrated up to a temperature of 65 °C. In addition, stimulated emission from correlated, self organized PbSe quantum dots, embedded between PbEuTe/EuTe Bragg interference mirrors is shown. This is of high interest since quantum dot lasers have been predicted to yield strongly increased material gain and differential gain, lower threshold currents, higher modulation band widths and better temperature stability as compared to quantum well lasers.

2. Sample details

The microcavity structures were grown by molecular beam epitaxy (MBE) on (111) oriented BaF_2 substrates. Sample 1 consists of a $Pb_{0.94}Eu_{0.06}Te$ cavity with a thickness corresponding to two times the optical wavelength (λ) with nine inserted PbTe quantum wells (QWs). The cavity is embedded between two dielectric Bragg mirrors. The bottom mirror consists of three periods of $Pb_{0.95}Eu_{0.05}Te$/EuTe $\lambda/4$ layer pairs. Because of the very high refractive index contrast of the layers of more than 80 %, this yields a mirror reflectivity of more than 99 %. To enable optical pumping, the top mirror has to be transparent at the pump wavelength. Therefore, the Eu content in the ternary layers of the top mirror was increased to 20 %. This leads to a reduced refractive index contrast, so that four layer pairs had to be used to obtain a reflectivity of 98 %. As active laser material, nine 20 nm wide PbTe QWs were inserted in the cavity close to the five antinode positions of the electric field.

Sample 2 contains a superlattice of correlated, self-organized PbSe quantum dots between the two dielectric Bragg mirrors. These are formed during heteroepitaxial growth of PbSe on $Pb_{1-x}Eu_xTe$ (111) due to the 5.4 % lattice mismatch [4]. Due to the strong increase of the $Pb_{1-x}Eu_xTe$ energy band gap with Eu content ($\Delta E_g/\Delta x_{Eu}$ = 4.48 eV at 4 K), a quantum confinement of the free carriers in the PbSe dots is achieved already for Eu concentrations of a few percent. We have chosen x_{Eu} = 5%, the same concentration as used for the growth of the mirrors. To obtain PbSe dots with an areal dot density of about 5 x 10^{10} cm^{-2}, an average dot height of 120 Å, a width of 300 Å, and a size dispersion of typically around ±15 %, 5 monolayers PbSe were deposited at a substrate temperature of 360° C whereas the mirrors were grown at 260 °C. Fig. 1 shows a cross section of the sample 2, by a sketch in (a), a SEM micrograph of the complete VCSEL structure in (b), and the PbSe dot arrangement in the superlattice by the TEM images of a reference sample grown under identical conditions in (c).

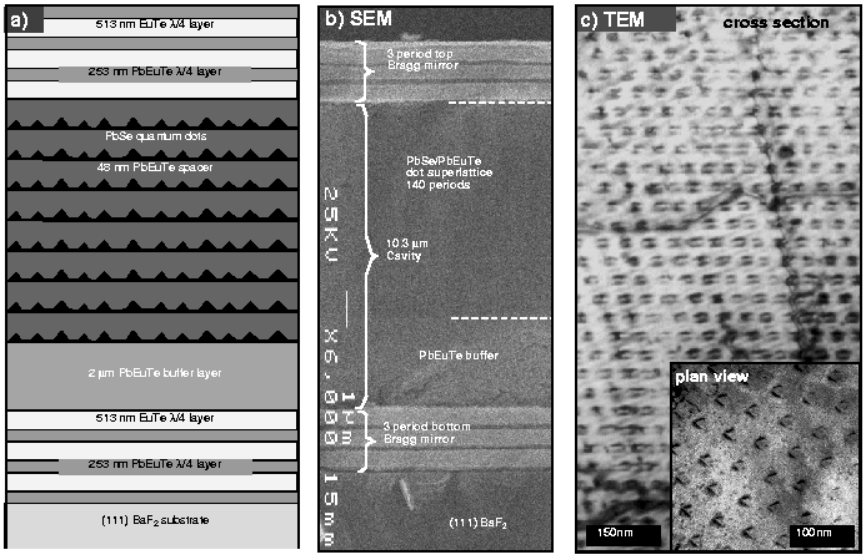

Fig. 1: Schematic representation (a) and cross sectional SEM micrograph (b) of the PbSe quantum dot VCSEL structure. (c) Cross sectional and plan-view TEM micrographs of a PbSe/$Pb_{1-x}Eu_xTe$ dot superlattice reference sample with 5 ML PbSe and 480 Å $Pb_{1-x}Eu_xTe$.

3. Experimental results

For optical pumping of sample 1, we used 100 fs long pulses at a wavelength of 1.97 μm with a repetition rate of 1 kHz. For sample 1 MIR emission can be observed at room temperature. Below laser threshold, the emission spectrum shows a Lorentzian shaped line centered at 3200 cm^{-1} with a width of 160 cm^{-1}. Increasing the excitation density to 1 mJ/cm^2 results in a considerable narrowing of the emission spectrum and a drastic rise of the luminescence intensity. Both effects indicate the onset of stimulated emission. For excitation powers above 1 mJ/cm^2 the line width becomes larger again and the integrated emission intensity of the sample linearly increases with rising pump power. Such a linear dependence is expected for laser emission, and it is shown in detail in Fig. 2(a) giving a laser threshold energy density of 0.83 mJ/cm^2.

The temperature dependence of the emission spectra of sample S1 excited with an energy density of 8 mJ/cm^{-2} is demonstrated in Fig. 2(b). With increasing sample temperature the laser output intensity at first only slowly decreases until about 55°C above which the intensity rapidly decreases and completely quenches at 70°C. As shown in Fig. 2 (a), with rising temperature also the laser threshold increases slightly from 0.83 mJ/cm^2 at room temperature to 1 mJ/cm^2 at 50°C.

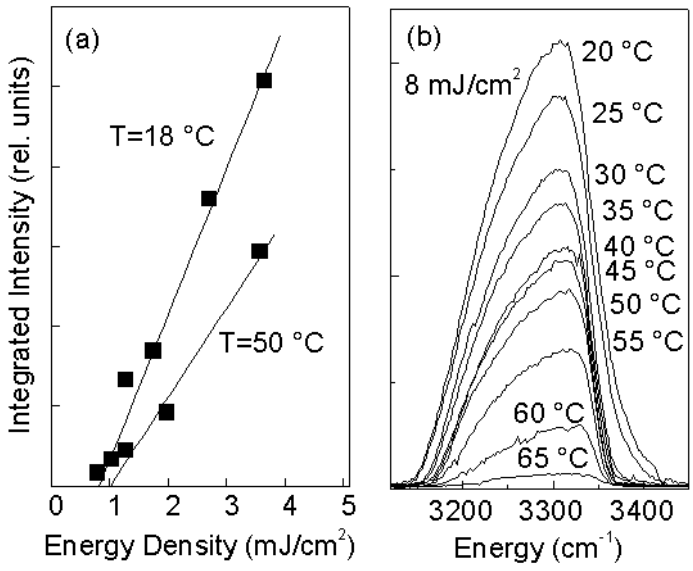

Fig. 2: Dependence of the stimulated emission of sample 1 on excitation intensity (a) and on sample temperature (b). Laser operation is obtained up to 65 °C.

In the following, emission measurements on a superlattice of self-assembled PbSe Stranski-Krastanow islands embedded in a vertical cavity are presented. Because of the large total cavity length of sample 2 a large number of cavity resonance modes are observed within the stop band region. The central m = 28th cavity mode is located at 290 meV (λ = 4.27 μm), corresponding to the low temperature onset of quantum dot absorption measured on PbSe/$Pb_{1-x}Eu_xTe$ reference samples. The stimulated emission spectra of the VCSEL structure induced by optical pumping with a pulsed Nd:YAG laser is shown in Fig. 3. At 1.5 K, simultaneous emission at the m = 28 and 29th order cavity modes at λ = 4.24 and 4.09 μm occurs, with a line width of only 700 μeV. This two-mode laser operation is a result of the inhomogeneous broadening of the quantum

dot gain spectrum to dot size fluctuations. Measurements of the integrated output intensity as a function of pump power indicates an external threshold of P_{th} = 510 kW/cm^2. As shown in Fig. 3, with increasing temperature, the intensity of the 29th mode increases whereas that of the central 28th mode decreases and eventually disappears at a temperature of 40 K. As the temperature is further increased, the 29th emission in turn decreases and at 60K the next higher laser mode turns on. At 70 K, the 29th mode completely disappears, whereas the 30th mode emission persists up to 90 K. This successive switching of the laser emission is explained by the increase of the PbSe band gap with increasing temperature. The envelope of the emission lines is given by the inhomogenously broadened dot gain spectrum with a width of about 18 meV. Similar as in PbTe quantum well VCSELs, the upper limit of operation temperature is caused by the detuning between the gain spectrum and the central cavity modes at higher temperatures. This indicates that much higher operation temperatures can be achieved for the dot lasers by appropriate tuning of the optical cavity modes to the dot emission at higher temperatures.

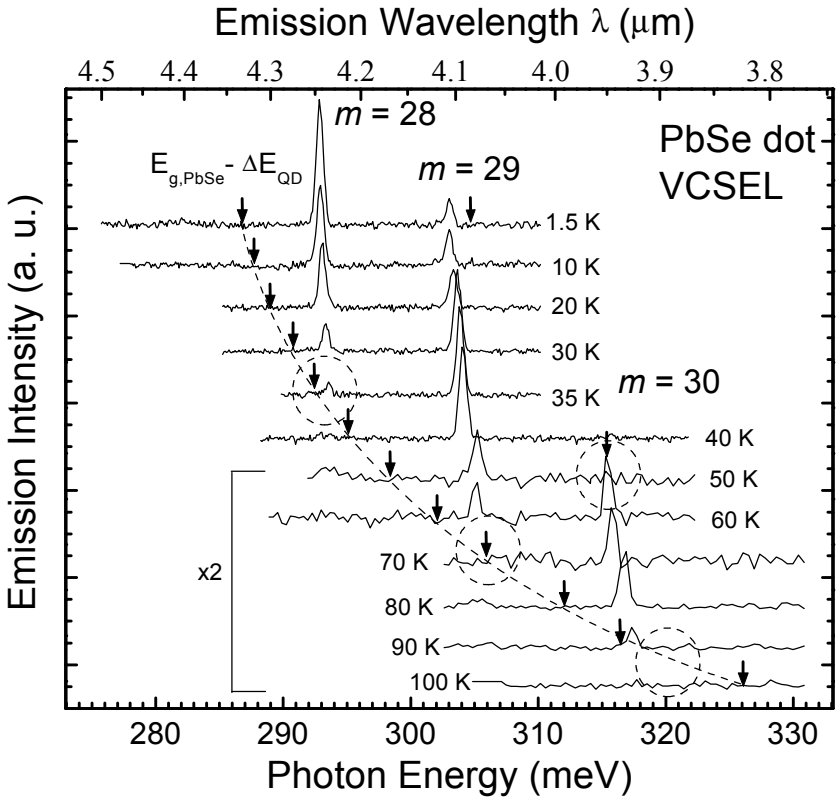

Fig. 3: VCSEL emission spectra at temperatures between 1.5 and 100 K showing the switching of the laser emission to higher cavity modes as the temperature increases. The arrows and dashed line indicate the low energy edge of the quantum dot gain spectrum.

Acknowledgements

This work is supported by the FWF, the Austrian Academy of Sciences, and the Deutsche Forschungsgemeinschaft.

References

[1] Z. Feit, M. Mc Donald, R. J Woods, V. Archambault, P. Mak, Appl. Phys. Lett. **68**, 738 (1996).

[2] P. Schießl, J. Rohr, Infrared Physics. Technol. **40**, 325 (1999).

[3] T. Schwarzl, W. Heiss, G. Springholz, M. Aigle, H. Pascher, Electron. Lett. **36**, 322 (2000).

[4] G. Springholz, V. Holy, M. Piczolits, G. Bauer, Science **282**, 734 (1998).

Mode Splitting and Lasing in Detuned Lead Salt Microcavity and Microdisk Resonances

T. Schwarzl, W. Heiss, G. Springholz

Institut für Halbleiterphysik, Johannes Kepler Universität Linz, Altenbergerstraße 69, 4040 Linz, Austria

S. Gianordoli, G. Strasser

Institut für Festkörperelektronik, Technische Universität Wien, Floragasse 7, 1040 Wien, Austria

M. Aigle, H. Pascher

Experimentalphysik I, Universität Bayreuth, Universitätsstraße 30, 95447 Bayreuth, Germany

PbEuTe/EuTe microcavities and microdisks supporting strongly detuned resonances were fabricated by molecular beam epitaxy and reactive ion milling. For detuned cavity modes, we find a pronounced angle dependent relative polarization splitting of up to 1 % and vertical laser emission at 4.8 μm, for sample temperatures between 35 and 85 K. Furthermore, lateral confinement effects in circular microdisks with diameters below 20 μm are demonstrated.

1. Introduction

Microcavities have attracted immense interest in recent years due to their unique physical properties as well as their high potential for device applications. The very short cavities with lengths comparable to an optical wavelength require high reflectivity mirrors, which are realized by Bragg interference mirrors. Such Bragg mirrors exhibit a stop band with high reflectivity around a certain target wavelength. The width of this stop band is determined by the refractive index contrast between the mirror materials.

We have recently demonstrated PbEuTe/EuTe microcavities with Bragg mirrors having a very high refractive index contrast [1], which is more than four times higher than that of III-V [2] and II-VI [3] mirrors. In these cavities, the mirror stop band width is large enough to sustain Fabry-Perot resonances, which are highly detuned with respect to the stop band center wavelength. The range for this detuning is about six times larger than for III-V Bragg cavities.

In this work, we investigate the angle dependent polarization splitting between the TE and TM modes of detuned resonances (DRs) as well as mid-infrared vertical lasing [4], [5] from a DR. Furthermore, a splitting and a blueshift of resonances in laterally structured planar cavities into microdisks are shown.

2. Experimental

The microcavity samples were grown by molecular-beam-epitaxy (MBE) on (111) oriented BaF_2 substrates. They consist of two high reflectivity $Pb_{0.95}Eu_{0.05}Te$/EuTe Bragg mirrors with only three layer pairs and with (2λ) and (4λ) $Pb_{0.95}Eu_{0.05}Te$ cavities in between. The samples intended for laser emission have inserted several 20 nm thick PbTe quantum wells in the cavity layer as active material. Circular microdisks with various diameters were formed by lateral structuring of the planar cavities by reactive ion milling. The optical characterization of the microcavities was performed with polarization dependent FTIR transmission measurements. For investigation of the microdisks, an IR microscope mounted on the FTIR spectrometer was used allowing spatially resolved reflectivity measurements with a resolution of 8 μm. The laser samples were optically pumped with a pulsed Nd:YAG laser [5].

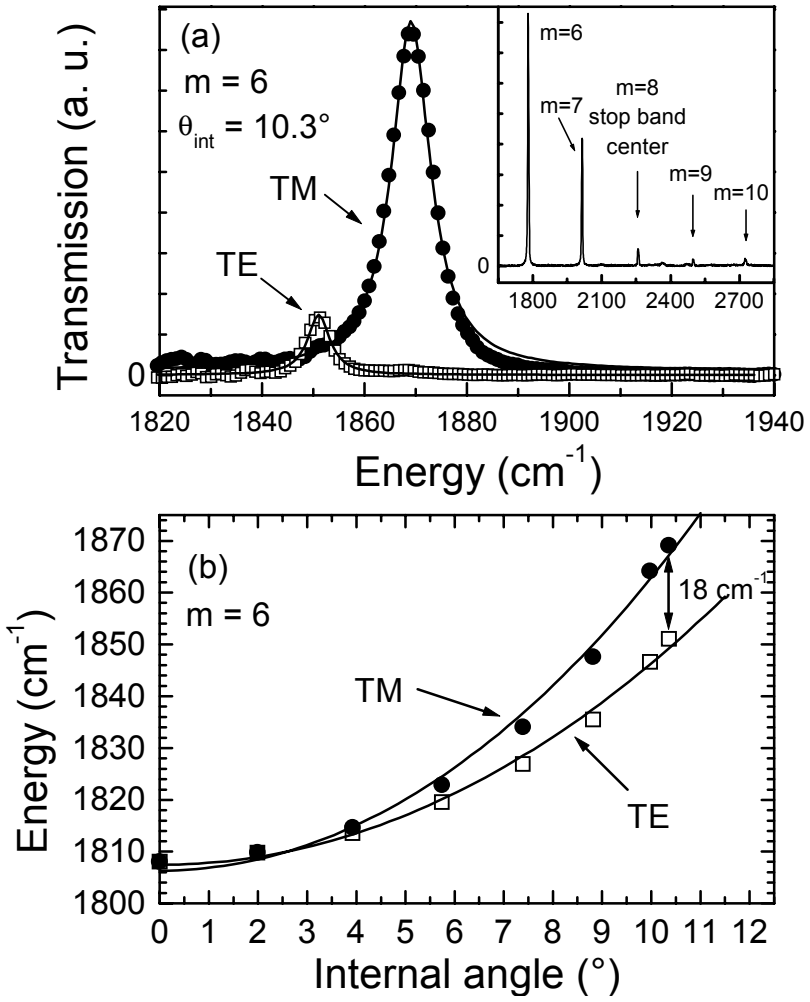

Fig. 1: (a) FTIR transmission of the m = 6 resonance of a 4λ microcavity for TE and TM polarization at an internal angle of 10.3°. Inset: FTIR transmission spectrum of the stop band region of the microcavity. (b) Angle dependent dispersion of the m = 6 mode for TE and TM polarization.

3. Polarization Splitting and Lasing in Microcavities

Our IV-VI microcavity with a length of 4λ supports five cavity resonances, as shown in the inset of Fig. 1(a) by the transmission spectrum of the cavity in the stop band region. The energy of the most detuned resonances with order m = 6 and m = 10 is about 450 cm^{-1} off from the mirror center. Figure 1(a) shows the polarization splitting of the m = 6 mode at 1860 cm^{-1}. At an internal angle of only 10.3° (64° external) it amounts 18 cm^{-1} yielding a relative splitting of 1 %. In comparison, in GaAs/AlAs cavities the tunability of the resonances is limited by the small stop band widths resulting in a polarization splitting of only 0.1 % at an external angle of 60° [6]. For the TE mode we observe, in addition, a considerable larger finesse than for the TM mode, which appears much higher and broader in the transmission spectrum. The difference of the finesse is due to a lower reflectivity for the TM polarization as predicted by the Fresnel formulas. The angular dispersion of the polarization modes of the m=6 resonance is shown in Fig 1(b). Both dispersions are fitted with the same equation [6] by using different values for the effective refractive index (3.55 and 4.25 for TM and TE mode, respectively).

The DRs have a lower quality factor than the central resonances, due to a about 3.5 % lower Bragg mirror reflectivity at the edges of the mirror stop band. Nevertheless, optically pumped lasing has been observed also at DRs, which is in particular important for IV-VI semiconductor lasers exhibiting a strong temperature dependence of the energy band gap. This enables vertical single mode laser operation over a large temperature range via mode hopping between central mode and DRs. This is observed indeed in the (2λ) laser cavity exhibiting three resonances. The sample shows narrow forward directed stimulated emission. At low temperatures around 4 K, emission is observed at the central m = 4 cavity mode at 5.87 µm, whereas at 35 K the emission switches to the m = 5 DR at 4.82 µm. Above 85 K the lasing quenches, because the band gap energy exceeds the energy of the DR [5].

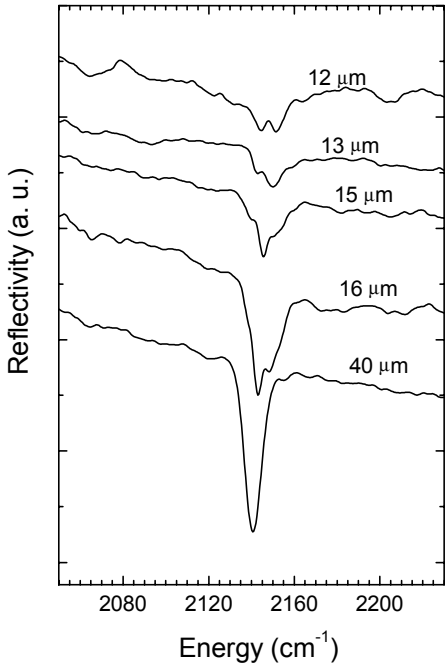

Fig. 2: Reflectivity spectra of circular microdisks with various diameters showing the m = 5 resonance dip.

4. Mode Splitting in Microdisks

The lower quality of the DRs can be improved by laterally structuring of the planar microcavities to obtain three dimensionally confined photonic states [7]. In Fig. 2, the reflectivity of one DR (m = 5) of circular microdisks with different diameters is shown. The disks were structured from a 2λ planar microcavity. For disks with diameters below 20 μm, the resonance dip shows a pronounced splitting into narrower modes.

The distance between the disk modes gets larger with decreasing diameter, as is expected from lateral confinement. Furthermore, the resonances shift to higher energies with decreasing diameter, also indicating lateral confinement. The narrow microdisk modes are attributed to radial-like modes as well as whispering-gallery-like modes [8].

5. Conclusion

In conclusion, we have demonstrated microcavities with strongly detuned resonances with respect to the mirror stop band center. These resonances exhibited a pronounced angle dependent polarization splitting and enable vertical laser emission despite low cavity finesse. Furthermore, circular microdisks showing lateral confinement effects were fabricated by laterally structuring planar microcavities.

Acknowledgements

We thank W. Krepper and O. Fuchs for technical assistance. This work is supported by the FWF P 13330 – TPH, Vienna.

References

[1] T. Schwarzl, W. Heiß, and G. Springholz, *Appl. Phys. Lett.* **75**, (1999) 1246.

[2] R. P. Stanley, R. Houdre, U. Oesterle, M. Gailhanou, and M. Ilegems, *Appl. Phys. Lett*. **65**, (1994) 1883.

[3] E. Hadji, J. Bleuse, N. Magnea, J. L. Pautrat, *Appl. Phys. Lett.* **68**, (1996) 2480.

[4] T. Schwarzl, W. Heiß, G. Springholz, M. Aigle, and H. Pascher, *Electron. Lett.* **36**, (2000) 322.

[5] G. Springholz, T. Schwarzl, M. Aigle, H. Pascher, and W. Heiss, *Appl. Phys. Lett.* **76**, (2000) 1807.

[6] D. Baxter, M. S. Skolnick, A. Armitage, V. N. Astratov, D. M. Whittaker, T. A. Fisher, J. S. Roberts, D. J. Mowbray, M. A. Kaliteevski, *Phys. Rev*. **B 56**, (1997) R10032.

[7] J. P. Reithmaier, M. Röhner, H. Zull, F. Schäfer, A. Forchel, P. A. Knipp, and T. L. Reinecke, *Phys. Rev. Lett.* **78**, (1997) 378.

[8] D. Labilloy, H. Benisty, C. Weisbuch, T. F. Krauss, C. J. M. Smith, R. Houdre, and U. Oesterle, *Appl. Phys. Lett*. **73**, (1998) 1314.

Lateral and Vertical Ordering in Self-Organized PbSe Quantum Dot Superlattices

G. Springholz[1], M. Pinczolits[1], R. Lechner[1], A. Raab[1], P. Mayer[1], V. Holy[1], G. Bauer[1], H. H. Kang[2], L. Salamanca-Riba[2]

[1] Institut für Halbleiter- u. Festkörperphysik, Johannes Kepler Universität, Altenbergerstraße 69, 4040 Linz, Austria

[2] Department of Materials and Nuclear Engineering, University of Maryland, College Park, USA

Self-organized lateral and vertical ordering in PbSe/$Pb_{1-x}Eu_xTe$ quantum dot superlattices is investigated by transmission electron and atomic force microscopy. We observe the occurrence of three different ordered dot structures as a function of the $Pb_{1-x}Eu_xTe$ spacer thickness d_s, namely, (a) a vertical dot alignment with weak hexagonal ordering tendency for small d_s, (b) a well defined trigonal dot lattice with *fcc*-stacking and nearly perfect lateral ordering for intermediate d_s, and (c) uncorrelated and laterally disordered superlattices for large d_s. The formation of these different dot correlations is explained by finite element calculations.

1. Introduction

The spontaneous formation of three dimensional (3D) islands in the Stranski-Krastanow growth mode of highly lattice-mismatched heteroepitaxial layers has recently evolved as a novel technique for the fabrication of self-assembled semiconductor quantum dots [1]. Under appropriate conditions, these islands exhibit sizes in the nanometer regime and are fully coherent (*i.e.*, dislocation free) to the substrate. When embedded in a higher band gap matrix material, quantum boxes with atomic-like optical and electronic properties are formed. Due to the statistical nature of growth, these dots are usually not very uniform in size, shape and spacing, which poses severe limitations for device applications. Multilayering is one possible route for improving the uniformity of self-assembled dots [2] – [4]. This is due to the elastic interactions between the dots across the spacer layers, which leads to the formation of long-range correlations in superlattices.

In the present work, we have investigated the self-organized vertical and lateral ordering in PbSe/$Pb_{1-x}Eu_xTe$ quantum dot superlattices. It is shown that different types of correlations are formed by changes in the spacer thickness. Whereas for small spacer thicknesses, the dots are vertically aligned, an *ABCABC...* stacking sequence is formed for intermediate spacer thicknesses, and no correlations are found for thick spacer layers. The occurrence of the different structures is explained on the basis of finite element calculations of the elastic strain fields induced by the buried PbSe dots, showing a characteristic change when the spacer thickness becomes comparable to the buried dot size.

2. Experimental

A series of superlattice samples was grown by molecular beam epitaxy on PbTe buffer layers predeposited on (111) oriented BaF_2 substrates [4]. The superlattice stacks consisted of 30 periods of 5 monolayers (ML) PbSe alternating with $Pb_{1-x}Eu_xTe$ spacer layers of 200 to 1000 Å in thickness. Due to the -5.4% lattice mismatch with respect to PbTe, PbSe grows in the Stranski-Krastanow mode with the formation of 3D islands once the critical coverage of 1.5 ML is exceeded [5]. During the overgrowth of these islands, a rapid replanarisation takes place such that after 200 Å a smooth 2D surface is regained [4]. Identical growth conditions were employed for all samples with a substrate temperature of 360 ° C and growth rates of 0.08 ML/sec and 3.5 Å/sec for PbSe and $Pb_{1-x}Eu_xTe$, respectively. Thus, the only difference in the superlattices (SLs) was the thickness and composition of the spacer layers, where the latter was adjusted to provide a complete strain symmetrization of the SL stack with respect to the PbTe buffer layer [5]. This prevents misfit dislocation formation and ensures identical strain conditions in all samples.

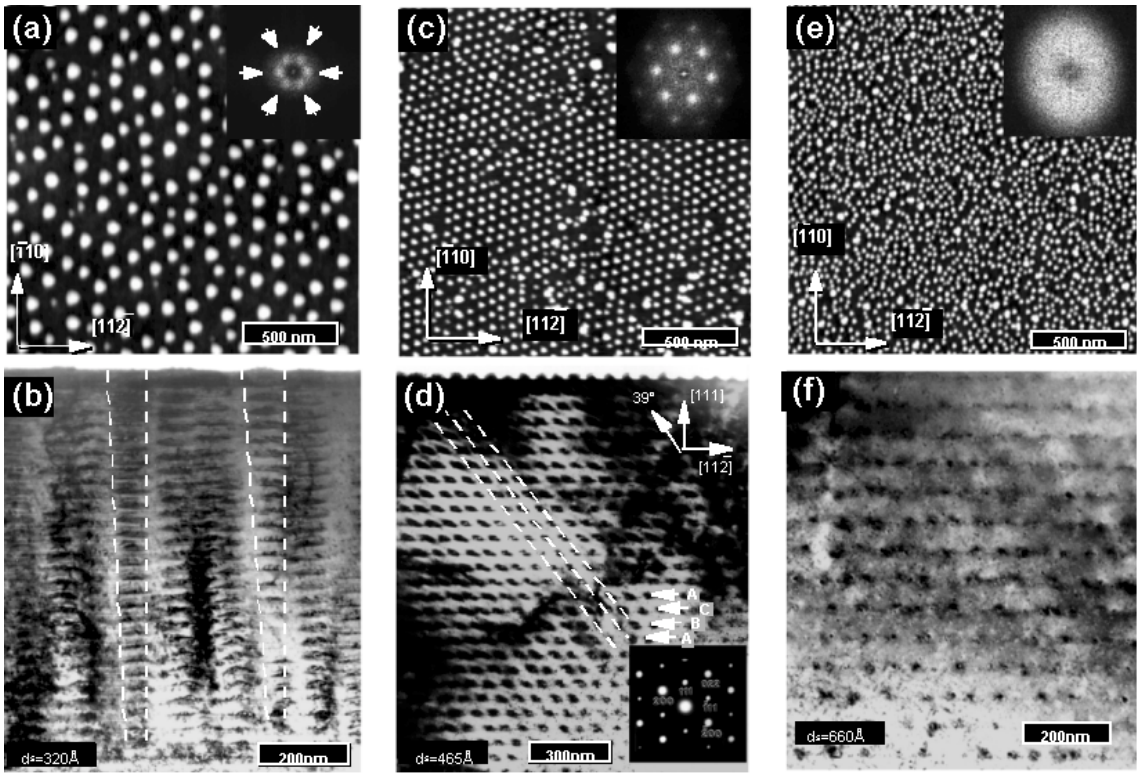

Fig. 1: AFM surface images (top) and cross-sectional TEM micrographs (bottom) of self-assembled PbSe/$Pb_{1-x}Eu_xTe$ dot superlattices with 30 superlattice periods and different $Pb_{1-x}Eu_xTe$ spacer thicknesses of d_s = 320 Å (left), 465 Å (center), and 660 Å (right hand side). For small spacer thicknesses (I) the dots are vertically aligned with weak lateral ordering tendency. For intermediate spacer thicknesses (II) a dot alignment inclined by 39° with respect to the growth direction occurs with an *fcc*-like *ABCABC*... stacking sequence and nearly perfect hexagonal lateral ordering. For thick spacers (III) no vertical dot correlations and no lateral ordering is observed. Inserts in the top panels: 2D FFT power spectra of the AFM images.

3. Results

The atomic force microscopy (AFM) images of the last dot layer and the cross sectional transmission electron microscopy (TEM) images are shown in Fig. 1 for $Pb_{1-x}Eu_xTe$ spacer thicknesses of d_s = 320, 465 and 660 Å. For small spacer thicknesses d_s < 370 Å (Fig. 1(a), (b)), as the number of superlattice periods increases larger and larger PbSe dots are formed on the surface, with a dot density decreasing from the initial value of 550 μm^{-2} for the single layers to about 70 μm^{-2} after 30 SL periods. Correspondingly, the average dot height of 180 Å and base width of 700 Å is much larger as compared to that of single dot layers grown under identical growth conditions. The cross sectional TEM image of this sample (Fig. 1(b)) reveals that the dots are vertically aligned in *columns*, is similar as in InAs/GaAs or SiGe/Si dot superlattices.

Increasing the spacer thickness to 370 – 540 Å leads to a completely different dot arrangement. As shown in Fig. 1(c), a *nearly perfect* hexagonal 2D lattice of dots is formed in this case, with a substantial narrowing of the size dispersion [4]. In addition, the dot density of about 250 μm^{-2} is about four times larger as compared to the samples with thinner spacer layers, with a corresponding decrease of the dot sizes. As demonstrated by the cross sectional TEM of Fig. 1(d), the PbSe dots are now aligned in directions *inclined* by 39° with respect to the growth direction (see dashed lines), and a well ordered trigonal 3D *lattice* of dots with a vertical *ABCABC...* stacking sequence is formed. For spacer thicknesses larger than 550 Å (Fig. 1(e) – (f)), another striking change occurs where the 2D hexagonal dot lattice is replaced by a highly disordered dot arrangement with an even higher dot density of 550 μm^{-2}. The cross-sectional TEM image of this sample (Fig. 1(f)) shows that the PbSe dots in each layer are randomly positioned relative to those in the adjacent layers. Thus, the whole SL structure just represents an uncorrelated repetition of disordered 2D single dot layers.

The different lateral ordering tendency is clearly reflected by the Fourier transformation (FFT) power spectra of the AFM images shown as insets in Fig. 1. For the sample with intermediate spacer thicknesses, many well defined satellite peaks appear in the FFT image (Fig. 1(c)). The clear six-fold symmetry and the large number of higher order peaks indicates the formation of large perfectly ordered 2D hexagonal dot domains. The exceedingly high efficiency of the lateral ordering process is corroborated by the corresponding cross-sectional TEM image, revealing that the lateral ordering sets in already within the first superlattice layers. For spacer thicknesses larger than 550 Å (Fig. 1(e)), only a diffuse ring is observed in the FFT image. This indicates the lack of any lateral ordering tendency and a rather broad dispersion of dot spacings. For samples with small spacer thicknesses $d_s \leq 370$ Å (Fig. 1(a)), although the dots seem to nucleate at random positions, six broad satellite side peaks are still visible in the FFT image (indicated by arrows in Fig. 1(a)). This indicates a weak hexagonal ordering tendency with rather large preferred lateral dot spacing. However, the absence of any higher order FFT satellites shows that only a short-range order exists in this case.

A strikingly different behavior is also found for the scaling of the preferred in-plane dot separation as a function of spacer thickness [6]. For small SL periods $D \leq 380$ Å, the lateral dot separation L is around 1300 Å, varying only slowly as $L = (0.6\ D + L_0)$ with $L_0 = 1080$ Å. At a critical period of $D_1^c = 390$ Å, L drops abruptly by a factor of three to 550 Å, and a nearly perfect 2D dot lattice is formed. In this regime, L scales *exactly* linearly with D as $L = \sqrt{3} \times D \tan \alpha$ [3], where α is the layer-to-layer correlation angle of 39° observed by TEM. For SL periods exceeding a critical value of $D_2^c = 570$ Å, the

mean lateral dot distance again drops abruptly to a value of 450 Å, and remains constant for all larger D. The corresponding dot density then equal to that of single dot layers grown under identical growth conditions. Both structural transitions are not completely abrupt, *i.e.*, for D around 390 Å actually mixed structures with coexisting trigonal and columnar dot regions are observed by TEM. Similarly, the second transition is manifested by a rapid but continuos drop of the layer-to-layer correlation probability.

The formation of different vertical correlations is explained as follows. Due to the lattice distortions around the buried dots a non-uniform strain distribution is imposed on the epitaxial surface. This leads to a preferred island nucleation at the minima of the strain energy on the surface. As shown by our previous work [3], [7], due to the very high elastic anisotropy of the IV-VI compounds and the chosen (111) growth orientation, the strain energy distribution caused by each buried PbSe dots exhibits three pronounced side minima that are laterally displaced from the surface normal direction. The preferred dot nucleation at these strain minima leads to an *ABCABC...* vertical dot stacking sequence [3] as well as to a very efficient hexagonal lateral ordering tendency. This is observed for the superlattices with intermediate spacer thicknesses. To explain the other types of dot correlations, the finite thickness of the spacer layer as well as the finite size of the buried dots has to be taken into account. For this purpose we have performed a series of finite element calculations of the stress distribution around dots located at various depths D below the surface. According to our AFM studies [5], the PbSe dots were modeled as triangular pyramids with (100) side facets. This yields an aspect ratio of b/h = 2.45, where b is the dot base width and h the dot height. Introducing the dimensionless surface coordinates $x' = x/D$ along [-110] and $y' = y/D$ along [-1-12], it turns out that the shape of the energy distribution is only determined by the ratio of D/b, *i.e.*, on the ratio of the depth to the island base width. The results of these calculations are shown in Fig. 2.

For spacer thicknesses larger than the island base $D/b > 1$, the strain energy distributions $E(x',y')$ closely resemble that obtained from a point source model [3], with three well separated minima along the <-1-12> directions. This is exemplified in Fig. 2(b) for D/b = 1.5. The directions of these minima are inclined by $\alpha = 35°$ with respect to the surface normal, in close agreement to the correlation angle observed by TEM. However, when D/b decreases below 1, α rapidly decreases to zero (as is shown in Fig. 2(c)). This means that the three minima are replaced by one central minimum located exactly above the buried dot. This is illustrated by the calculated strain energy distribution shown in Fig. 2(a) for the case of D/b = 0.5. As a consequence, preferential nucleation of new dots then occurs directly above each buried dot, which corresponds to a cross-over from *fcc* stacking to a vertical alignment of the dots, as is observed in the experiments. A more detailed analysis shows that this crossover takes place when the lateral minima separation L becomes smaller than the dot base width. Then, the island size becomes incompatible with the trigonal dot arrangement. Application of this condition to the actual parameters of our experiments leads to an expected critical spacer thickness of D_1^c = 310 Å for this transition, in good agreement with the experiments [6]. On the other hand, as the spacer thickness increases, the depth of these strain minima ΔE_{min} rapidly decreases as $1/D^3$ [6]. As a result, the layer-to-layer dot correlation probability drops to zero at a certain spacer thickness, which is experimentally the case for D_2^c = 560 Å, the upper boundary for the trigonal dot structure.

Due to the changes in the PbSe dot size as a function of the growth conditions, the positions of the critical superlattice periods D^c also change upon changes in the growth con-

ditions. In particular, at lower substrate temperatures, which result in smaller dot sizes, the phase boundaries are shifted to smaller values, which means that an *fcc*-stacking can be also obtained for SL periods smaller than 380 Å. This effect can be utilized in order to extend the tunability range of the trigonal superlattice structure.

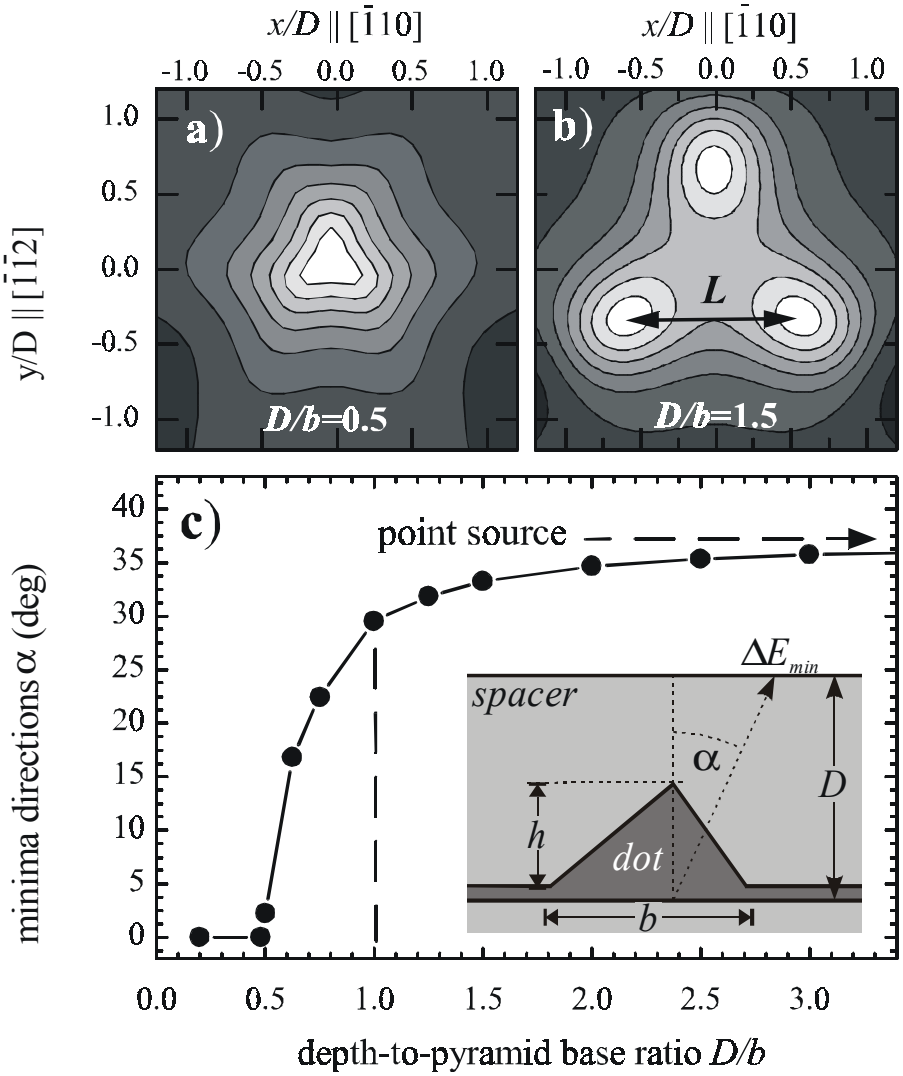

Fig. 2: Surface strain energy distributions above a pyramidal PbSe quantum dot in a PbEuTe matrix derived from finite element calculations and plotted as a function of dimensionless surface coordinates *x/D* for two different dot depths of (a) $D = 0.5 \times b$ and (b) $D = 1.5 \times b$, where *b* is the dot base width. Brighter areas in the contour plots correspond to lower strain energies. (c) Directions α of the strain energy minima on the surface relative to the surface normal plotted as a function of the *D/b* ratio. The dot configuration for the calculations is shown in (c) as insert.

4. Conclusions

In conclusion, different types of vertical correlations are observed in PbSe quantum dot superlattices as a function of the $Pb_{1-x}Eu_xTe$ spacer thickness. The different vertical cor-

relations have dramatic effects on the lateral ordering tendency as well as on the scaling of the lateral dot spacing as a function of spacer thickness. In addition, a different evolution of dot sizes and shapes occurs. The transition between the differently correlated structures is caused by the dependence of the elastic interaction between the dots on the thickness of the spacer layer, as well as by the finite lateral dot sizes. Similar trends are be expected also for other material systems.

Acknowledgements

This work is supported by the *Fonds zur Förderung der wissenschaftlichen Forschung* and the Austrian Academy of Sciences.

References

[1] D. Leonard, M. Krishnamurty, C. M. Reaves, S. P. Denbaar, and P. Petroff, Appl. Phys. Lett. 63 (1993) 3203.

[2] J. Tersoff, C. Teichert, and M.G. Lagally, Phys. Rev. Lett. 76 (1996) 1675.

[3] G. Springholz, V. Holy, M. Pinczolits, and G. Bauer, Science 282 (1998) 734.

[4] M. Pinczolits, G. Springholz, and G. Bauer, Phys. Rev. B 60 (1999) 11524.

[5] M. Pinczolits, G. Springholz, and G. Bauer, Appl. Phys. Lett. 73 (1998) 250.

[6] G. Springholz, M. Pinczolits, P. Mayer, V. Holy, G. Bauer, H. Kang, and L. Slamanca-Riba, Phys. Rev. Lett. 84 (2000) 4669.

[7] V. Holy, G. Springholz, M. Pinczolits, G. Bauer, Phys. Rev. Lett. 83 (1999) 356.

Nano-Scale Dislocation Patterning in PbTe on PbSe (100) Heteroepitaxy Studied by Scanning Tunneling Microscopy

K. Wiesauer and G. Springholz

Institut für Halbleiter- und Festkörperphysik, Johannes Kepler Universität, Altenbergerstr. 69, 4040 Linz, Austria

Heteroepitaxial growth of PbTe on 5.2% lattice mismatched (100) oriented PbSe is investigated using UHV-scanning tunneling microscopy. A 2D growth mode is found, and it is shown that strain relaxation occurs by pure edge type misfit dislocation formation. The early stages of strain relaxation show a lateral injection of dislocation half loops from monolayer step edges on the surface. A rapid increase of the dislocation density with PbTe layer thickness indicates a very effective strain relaxation mechanism with a critical layer thickness below 1 monolayer (ML). At PbTe layer thicknesses above 4 ML we observe the formation of a highly regular network of misfit dislocations with a dislocation spacing of around 10 nm, and a smallest variation of the dislocation separation of only ±12%. Thus, this nano-scale dislocation patterning can serve as template for the fabrication of self-assembled, ordered nanostructures.

1. Introduction

Strain relaxation is a critical process in lattice-mismatched heteroepitaxy. For highly mismatched heteroepitaxial systems, two different strain relaxation mechanisms exist, namely (1) the spontaneous formation of strain-induced coherent 3D islands on the surface, or (2) by misfit dislocation formation at the layer/substrate interface. For the latter, recent work has shown that the formation of interfacial dislocations strongly modifies surface morphology of the epitaxial layers, due to long-range elastic deformations of the lattice and in many cases due to monolayer surface glide steps [1]. In semiconductors, misfit dislocations are usually distributed in a irregular way within the layers, but for special growth geometries highly periodic dislocation arrays occur [2], [3]. This dislocation pre-patterning has been demonstrated as a tool for spatial manipulation of the nucleation sites of self-assembled quantum dots [4], [5], based on the local perturbation of the total free energy of the surface by the subsurface misfit dislocations.

In the present work, we have studied the strain relaxation mechanisms of PbTe on 5.2% lattice-mismatched (100) oriented PbSe substrates, using UHV scanning tunneling microscopy (STM). The non polar (100) surface has the lowest surface free energy in the rocksalt crystal structure, other than the polar (111) surface, where strain relaxation is found to occur by Stranski-Krastanow growth.

2. Experimental

The samples were grown by molecular beam epitaxy using compound sources for PbSe and PbTe. On polished PbSe (100) substrates, a several μm thick PbSe buffer layer was

deposited at a temperature of 380 °C, followed by a PbTe layer, where the PbTe layer thickness was varied from 0.3 to 22.5 ML. After growth, the samples were rapidly cooled down to room temperature and transferred to a separate UHV-STM chamber without breaking ultra-high vacuum conditions.

3. Results

In contrast to (111) oriented growth we find for the growth of PbTe on (100) oriented PbSe substrates a 2D growth mode that persists throughout the heteroepitaxial growth process (Fig. 1). Strain relaxation occurs purely by the formation of misfit dislocations that appear as dark surface depression lines in large-scale STM images (Fig. 1(b) – (d)). Studies of layers with varying PbTe layer thicknesses give a critical layer thickness h_c for the onset of misfit dislocation formation of only 0.8 ML, and STM images of very early relaxation stages show that misfit dislocation half loops are injected laterally from monolayer step edges on the surface (Fig. 1(b)). With increasing PbTe layer thickness the misfit dislocation density increases rapidly, and above about 4 ML PbTe a highly regular, square grid of misfit dislocations with a spacing of the order of 10 nm develops. By measuring the dislocation line density in STM images the relaxed strain in the layers was determined as a function of layer thickness, indicating a very rapid strain relaxation with more than 90% of the 5.2% misfit strain already relaxed at a PbTe layer thickness of 9 ML.

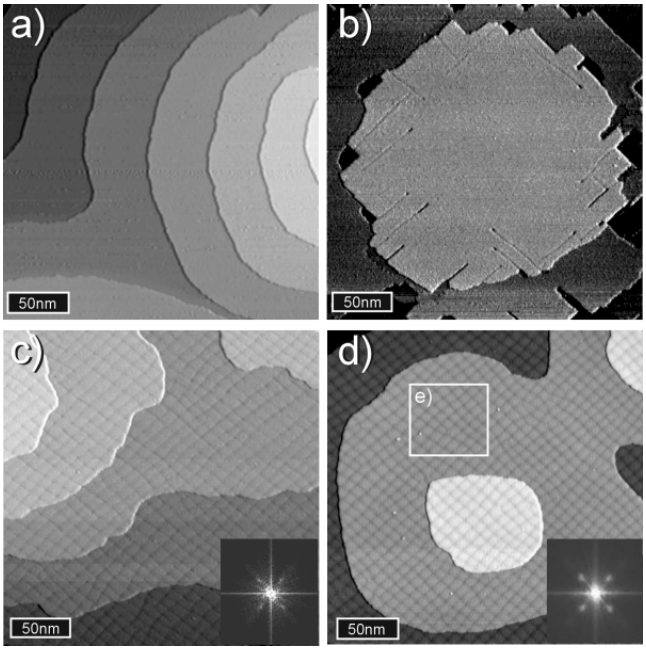

Fig. 1: STM images of PbTe layers on PbSe (100) for different layer thicknesses of (a) 0.3, (b) 0.8, (c) 4.5 and (d) 9 ML. Insert in (c) and (d): FFT power spectra of the STM images. The marked area (e) is shown in Fig. 2 (a) on an enlarged scale.

Atomically resolved STM images of an endpoint of a misfit dislocation (see Fig. 2(b)) show that the Burgers vector **b** is of ½<011> type, as expected for the rocksalt crystal structure of PbSe and PbTe. The Burgers vector is parallel to the heterointerface, and thus, the misfit dislocations cannot be formed by glide but only by climb processes. In

addition, **b** is perpendicular to the misfit dislocation lines that run along the fourfold <1-10> directions. Therefore the misfit dislocations are of pure edge character.

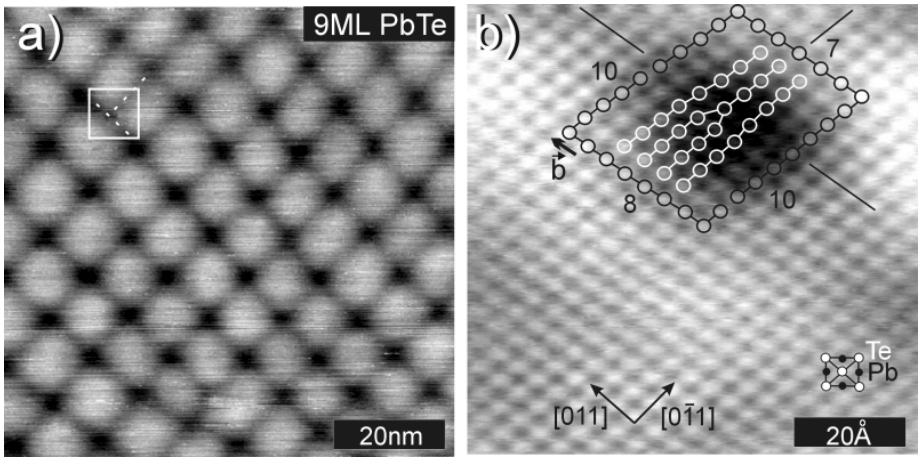

Fig. 2: STM images of a 9 ML PbTe layer on PbSe (100). As shown in (a) a very regular quadratic dislocation array is formed. The atomically resolved STM image of the area in (a) is shown in (b). As indicated by the Burgers circuit, the Burgers vector is equal to ½<011> and the dislocations are formed along the <0-11> directions.

The remarkable regularity of the dislocation network is evidenced by the appearance of satellite peaks in the FFT power spectra of the STM images (insert in Fig. 1(c) and (d)). A statistical analysis of the dislocation spacings for the 4.5 and 9 ML PbTe samples (Fig. 3) indicates a narrowing of the distribution of the dislocation spacings, i.e. a higher regularity of the dislocation network with a variation of the dislocation separation of only ±12% for the 9 ML sample. This is less than the typical variations in size and spacing of self-assembled quantum dots formed by the Stranski-Krastanow growth mode. The high regularity of the dislocation network is explained by the repulsive force between the dislocations and the high dislocation mobility within the heterointerface.

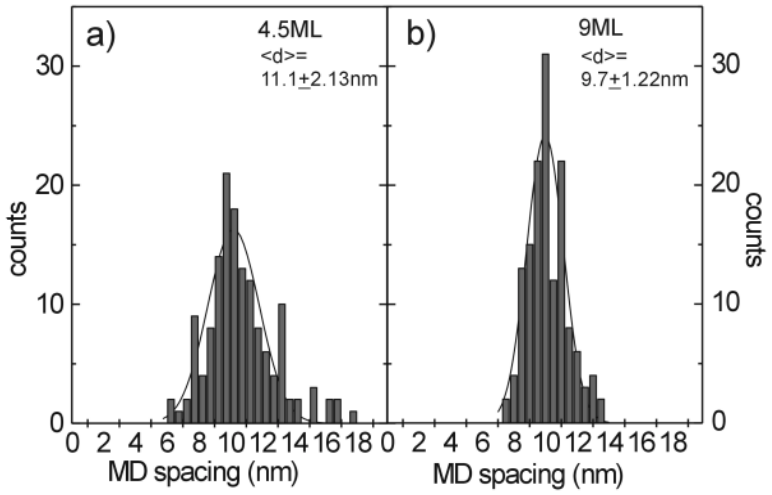

Fig. 3: Histograms of the lateral misfit dislocation spacings for PbTe layer thicknesses of (a) 4.5 ML and (b) 9 ML, indicating that the distributions narrow with increasing layer thickness.

4. Conclusions

For the growth of PbTe on (100) oriented substrates we find a 2D growth mode and a very effective strain relaxation process by the formation of pure edge type misfit dislocations that are formed by a climb process. With increasing PbTe layer thickness, the dislocations form a highly regular, square grid along the fourfold <1-10> directions with a period of the order of 10 nm. Due to the high uniformity of the dislocation network, this dislocation patterning can serve as template for the fabrication of self-organized ordered nanostructures. Because the interaction between dislocations depends strongly on the dislocation separation, similar results can be expected for other highly mismatched heteroepitaxial systems.

Acknowledgements

This work was supported by the *Fonds zur Förderung der wissenschaftlichen Forschung* and the *Österreichische Akademie der Wissenschaften*.

References

[1] G. Springholz, V. Holy, and G. Bauer: “Local surface deformations induced by interfacial dislocations in lattice-mismatched heteroepitaxy of EuTe on PbTe (111)”, *Surf. Sci.*, Vol. 365, 1996, pp. 453 – 460.

[2] J. G. Belk, J. L. Sudijono, X. M. Zhang, J. H. Neave, T. S. Jones, and B. A. Joyce: “Surface Contrast in Two Dimensionally Nucleated Misfit Dislocations in InAs/GaAs(110) Heteroepitaxy”, *Phys. Rev. Lett.*, Vol. 78, 1997, pp. 475 – 479.

[3] A. Trampert, E. Tournié, and K. H. Ploog: “Defect control during growth of highly mismatched (100) InAs/GaAs-heterostructures”, *J. Cryst. Growth*, Vol. 146, 1995, pp. 368 – 373.

[4] S. Yu. Shiryaev, F. Jensen, J. Lundsgaard Hansen, J. Wulff Petersen, and A. Nylandsted Larsen: "Nanoscale Structuring by Misfit Dislocations in $Si_{1-x}Ge_x$/Si Epitaxial Systems", *Phys. Rev. Lett.*, Vol. 78, 1997, pp. 503 – 506.

[5] R. Leon, J. O. Okuno, and R. A. Lawton, M. Stevens-Kalceff, and M. R. Philips, J. Zou, and D. J. H. Cockayne, C. Lobo: "Dislocation-induced changes in quantum dots: Step alignment and radiative emission", *Appl. Phys. Lett.*, Vol. 74, 1999, pp. 2301 – 2303.

Reflection Difference Spectroscopy on II- VI Semiconductors; A Tool to Investigate Surface Processes *in situ* During Growth

Kurt Hingerl

Institut für Halbleiter- und Festkörperphysik, Johannes Kepler Universität, Altenbergerstraße 69, 4040 Linz, Austria

As the materials and structures of semiconductor technology become more complex, interest in developing real time process monitoring techniques during crystal growth is rapidly increasing. Optical Probes are best suited to be applied simultaneously with crystal growth, because they are non-invasive and non-destructive. A technique currently strongly used is *Reflectance Difference Spectroscopy* (RDS), which can monitor in situ surface processes in real time under UHV (MBE, ALE) as well as under atmospheric pressure (CBE, OMCVD) conditions. The measured signal is the difference between the near normal incidence reflectances of light linearly polarized along the two principal axes is investigated as a function of time, photon energy, and/or surface condition. For cubic materials the uninteresting bulk reflection cancels in subtraction, leaving the signal from the lower symmetry surface. However, there are also identified sources for bulk anisotropy for zincblende (001) surfaces which break the 4-fold rotational symmetry. We mention spontaneous ordering, the linear electro-optic effect, dislocations, and quantum confinement.

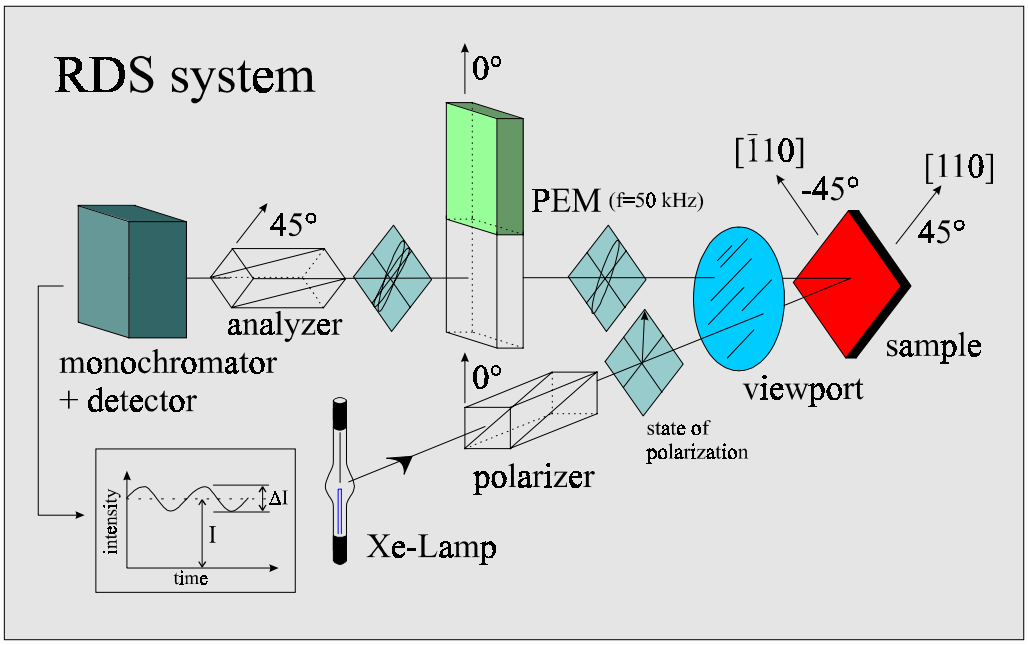

Fig. 1: The alignment of the optical components of the RDS system

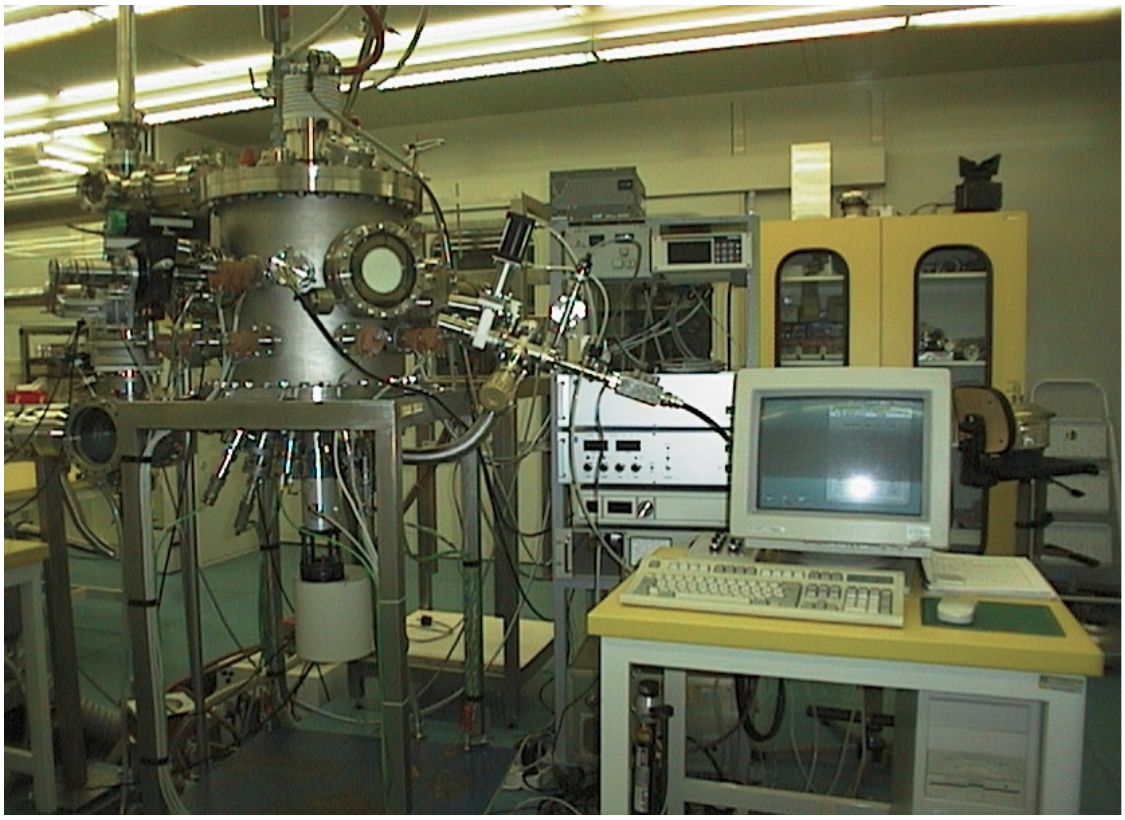

Fig. 2: A photo of the experimental setup of the UHV MBE chamber with the attached RDS in the cleanroom at Linz University (arrow).

Within the last years the understanding of information delivered by RDS and of kinetic RD data has grown considerably, however full exploitation of the power of these optical techniques needs further investigations, particularly when heteroepitaxial systems are concerned. Therefore, since the beginning of the work in February 1997, the major effort was directed onto these topics in II-VI semiconductors:

1. *In situ* determination of in plane stress and strain anisotropy in ZnSe/ZnTe/CdTe (001) Layers on GaAs.
2. On the origin of resonance features in RDS data of silicon.
3. *In situ* observation of stress relaxation in CdTe/ZnTe heterostructures by reflectance-difference spectroscopy at the critical thickness

ad 1) Is there an anisotropic in plane strain occurring due to dimerization for II-VI compounds? Furthermore we tried to find a theoretical description connecting the symmetry of the wave-functions and the polarization dependence of the optical transition matrix elements with the measured spectra (Bikus and Pir Hamiltonian) [6], [10]. Using reflectance difference spectroscopy we showed that Te surface termination on ZnTe induces, due to stress occurring from dimerization and the piezo-optic effect, a dichroism at the E_1 and $E_1+\Delta_1$ critical points of the dielectric function of the ZnTe. The influence of Te dimers on the stress field in the epilayer was proven by comparing with *ex situ* measurements of anisotropically stressed ZnTe layers and *in situ* by enhancing the stress effect by inserting one atomic plane of Cd. Under Zn termination no stress was induced.

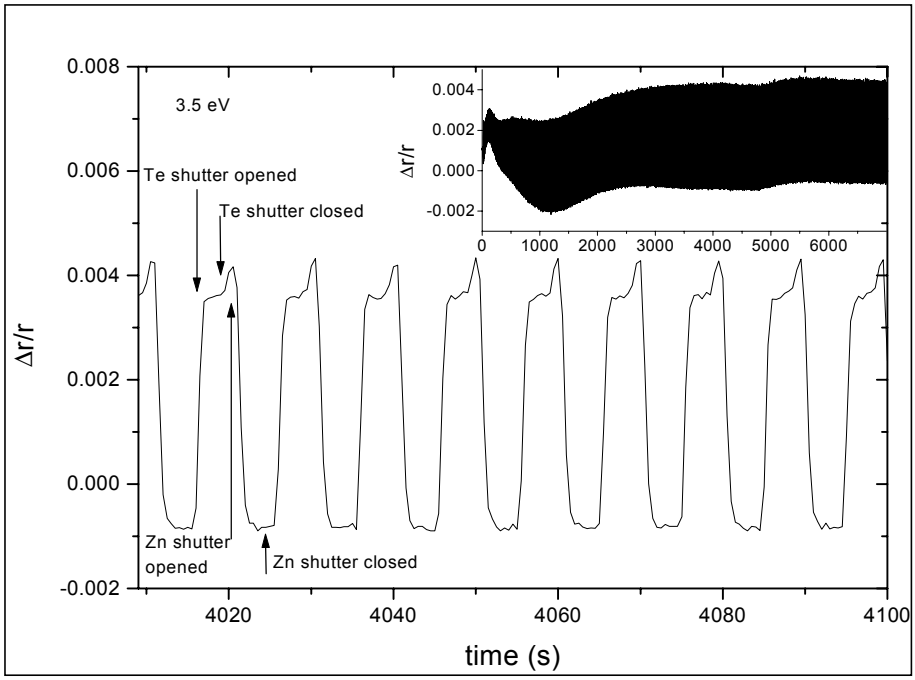

Fig. 3: Kinetic RD data taken during ALE growth of ZnTe (001) grown on GaAs at a photon energy of 3.5 eV. The inset displays RD data on a longer time scale.

ad 2) This also enabled us to shed light on the origin of sharp resonances in reflectance difference spectroscopy (RDS) data at the critical points of the dielectric function of bulk Si: The physical origin of sharp resonances in reflectance difference spectroscopy (RDS) data at the critical points of the dielectric function of bulk Si, previously assigned to surface-bulk transitions, to photon localization or to optical transitions from bound dimer states to excited dimer states was investigated. We show that uniaxial in-plane stress of bulk Si induces sharp resonances at exactly these critical points of Si via the piezo-optic effect. In the recent literature it was shown that surface reconstruction as well as dimerization exerts anisotropic stress, e.g. along the dimer direction, and the resulting strain is extending into the bulk. In our contribution we simulate this surface strain by externally stressing different Si faces and comparing *ex situ* measured RDS data of Si(001), Si(111), and Si(110) surfaces with RDS data measured *in situ* and density functional theory calculations.

ad 3) Understanding where the RDS features come from enabled us also for the first time to observe *in situ* the stress relaxation in CdTe/ZnTe heterostructures by reflectance-difference spectroscopy at the critical thickness. The first stages of epitaxial growth of CdTe on ZnTe and ZnTe on CdTe are monitored with reflectance difference spectroscopy. Spectroscopic reflectance difference data show strong optical anisotropy responses at the critical points of the bulk dielectric function at E_0, E_1 and $E_1+\Delta_1$ interband transitions of ZnTe, respectively CdTe, which indicate that anisotropic in-plane strain occurs during epitaxial growth. Applying a model it is possible to determine the in-plane strain due to the misbalance of 60° dislocations along the $[1\,\bar{1}\,0]$ and $[1\,1\,0]$ directions. Kinetic reflectance difference data taken at the E_1 transition of the respective material exhibit with an accuracy of one monolayer the onset of the formation of misfit dislocations for these material systems. An example of this kinetic behavior is shown in Fig. 5.

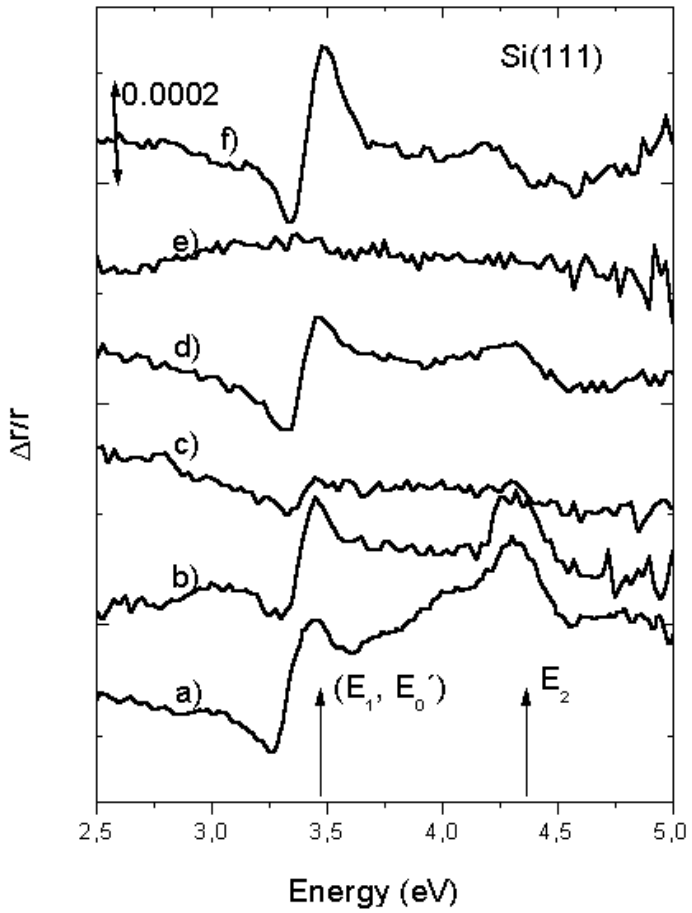

Fig. 4: Comparison between in situ RDS data obtained by other groups and our stress related features for example for the Si(111) surface: (a) displays the RD data of a Si(111): H surface 5° miscut towards the $[1\,1\,\bar{2}]$ direction; (b) shows *ex situ* measured data on Si(111) surfaces covered with natural oxides and 2° miscut; (c) same as Fig. 4(b) with the RDS head rotated by 45° from the $[1\,\bar{1}\,0]$ direction towards the $[2\,\bar{1}\,\bar{1}]$ direction; (d) same as Fig, 4(c) with the application of 25 MPa compressive stress along the $[1\,\bar{1}\,0]$ direction; (e) the RD spectrum of a non miscut Si(111) sample; f) same as Fig. 4(e) with the application of 25 MPa uniaxial stress along the $1\,\bar{1}\,0$ direction.

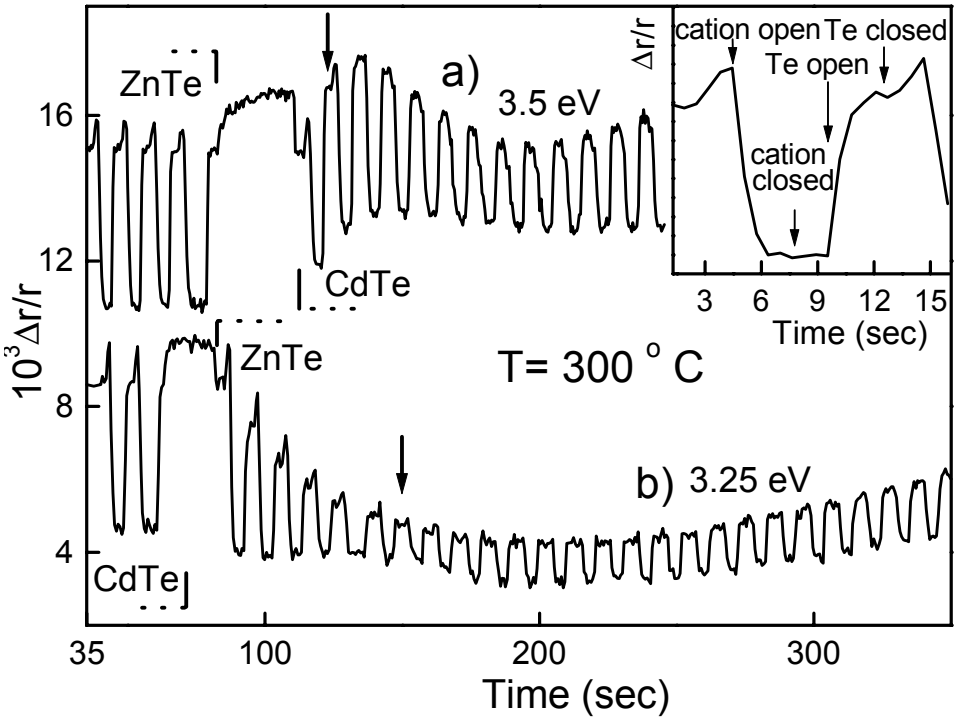

Fig. 5: In situ RD responses at the E_1 critical points during interfaces formation by atomic layer epitaxy growth: a) CdTe on ZnTe(001) and b) ZnTe on CdTe(001). Both curves have been displaced vertically for the sake of clarity. The inset shows the shutter sequences for anion (Te) and cation (Cd or Zn) fluxes prior to interface growth on a shorter time scale.

References:

[1] A. Bonanni, H. Seyringer, H. Sitter, D. Stifter and K. Hingerl: "Control of morphology changes of self-assembled Mn-based nanostructures overgrown with mismatched maetrial", *Appl. Phys. Lett.* 74, 3732, (1999)

[2] D.Stifter, A.Bonanni, M.Garcia-Rocha, M.Schmid, K.Hingerl, H.Sitter: "In situ reflectance difference spectroscopy:Nitrogen-plasma doping of MBE grown ZnTe layers", *J.Cryst.Growth,* 201**,** 132 (1999)

[3] A.Bonanni, D.Stifter, K.Hingerl, H.Seyringer, H.Sitter: "In-situ characterisation of the growth dynamics in MBE of Mn-based II-VI compounds: self-organised Mn structures on CdTe", *J. Cryst. Growth,* 201, 707 (1999)

[4] D.Stifter, M. Schmid and K.Hingerl, A.Bonanni, m. Garcia Rocha and H.Sitter: "In situ reflectance difference spectroscopy of II-VI compounds: A real time study of N plasma doping during molecular beam epitaxy", *Jour. Vac. Sci. & Techn.* **B17,** 1697 (1999)

[5] A. Bonanni, K. Hingerl, H. Sitter, D. Stifter: "Reflectance Difference Spectroscopy of Mn Intra Ion Transitions in p- doped diluted magnetic semiconductors“, *phys. Stat.sol*. 215, 47 (1 999)

[6] T. Hanada, T. Yasuda, A. Ohtake, K. Hingerl, S. Miwa, K. Arai, and T. Yao: "In Situ Observation of Strain Induced Optical Anisotropy of $ZnS_{1-x}Se_x$/GaAs(110) during Molecular Beam Epitaxy”, *Phys Rev.* B60, (8909) (1999)

[7] D. Stifter, K. Hingerl, H. Sitter: “Zerstörungsfreie Messung dünner Schichten mit polarisationsoptischen Methoden”, *e&i, ÖVE*, **116,** 315, (1999)

[8] A.Bonanni, G. Prechtl, W.Heiss, F. Schinagl, S. Holl, H. Krenn , H.Sitter, D.Stifter and K.Hingerl: ”Reflectance Difference Spectroscopy and magneto-optical analysis of digital magnetic heterostructures”, Jour. Vac. Sci. & Techn. **B17,** 1722(1999)

[9] K. E Miller, K. Hingerl, C. Brabec, A. J. Heeger, and N. S. Sariciftci: “Reflectance Anisotropy Spectroscopy of Oriented Films of Semiconducting Polymers”, submitted to J. *Chem. Phys.,* submitted

[10] R. E. Balderas-Navarro, K. Hingerl, W. Hilber, D. Stifter, A. Bonanni, and H. Sitter: “In situ reflectance-difference spectroscopy of doped CdTe and ZnTe grown by molecular beam epitaxy”, submitted to J. Jour. Vac. Sci. & Techn., submitted

Collaborations

PROFACTOR GmbH, Wehrgrabengasse 5, A-4400 Steyr,

Joint Research Center for Atom Technology (JRCAT) ,Tsukuba 305-8562, Japan,

Institute for Materials Research, Tohoku University, Sendai 980-8577, Japan;

Defense Research Agency, UK,

Additional Funding: GME, ÖAW (APART), FWF, ÖAD, EC-Competitive and Sustainable Growth

Magnetic Properties of Thin Iron Films

K. Himmelbauer, H. Sitter, H. Krenn

Institut für Halbleiter- und Festkörperphysik, Johannes Kepler Universität, Altenbergerstr. 69, 4040 Linz, Austria

The incorporation of magnetic layers in semiconductor heterostructures is an increasingly active area of study. There is a great interest in the catalytic, electronic, and magnetic properties of transition metal overlayers on semiconductor substrates in thin film form. Since the metal-semiconductor interface plays an important role in thin film heterostructures, the initial stages of overlayer growth determine the morphology and crystalline structure of subsequent growth. Thin film properties often differ significantly from bulk properties due to surface and interface effects dominating the overall behavior of these films. Iron films show a broad range of magnetic properties depending on film thickness and deposition conditions. We investigate the influence of the initial substrate surface reconstruction on the magnetic behavior of iron films both on GaAs substrates as well as on ZnSe epilayers. Surface reconstruction leads to magnetic anisotropies dominated by an in-plane uniaxial component. We study the growth of ferromagnetic iron to determine the mode of film growth, the interface formation, and the magnetic film properties. Films are characterized by various methods: surface reconstructions are determined by Reflection High Energy Electron Diffraction (RHEED) and magnetic properties by Superconducting Quantum Interference Device (SQUID) measurements with the magnetic field applied along different in-plane directions.

1. Introduction

The growth of single-crystal ferromagnetic films on semiconductor substrates and the incorporation of metal layers in semiconductor heterostructures has attracted considerable attention due to its compatibility with planar electronics (e.g. for inducing magnetic fields in dilute magnetic semiconductors) and due to its potential for spin-sensitive heterostructure devices.

Body-centered cubic (bcc) α-iron is preferentially deposited on GaAs and ZnSe due to the slight lattice mismatch (1.5 % and 1.1 %, respectively). By variation of film thickness and deposition conditions iron films show a broad range of magnetic properties. In this paper we present the influence of the surface reconstruction of the substrate and the influence of the film thickness on the magnetization curves obtained by superconducting quantum interference device measurements.

2. Experimental

A new ultrahigh vacuum chamber, designed for the growth of bcc α-iron and described earlier [1], has been attached to an existing MBE-system allowing us to grow iron directly on (001) GaAs substrates or on ZnSe epilayers.

Prior to growth the (001) GaAs substrates are heated up to 720 °C and kept at that temperature till a streaky RHEED pattern indicates deoxidation of the substrates, usually for a few seconds.

The ZnSe epilayer is grown by ALE (Atomic Layer Epitaxy) [2] in the following way: The shutter of the Zn effusion cell is kept open for 3 sec. After a delay time of 0.5 sec, in which all shutters are closed, the shutter of the Se effusion cell is open for 3 sec. Another delay time of 0.5 sec finishes one growth cycle during which one monolayer of ZnSe is grown. Therefore the substrate with a temperature of 300 °C is exposed to only one kind of source material at one time. The ALE-growth of ZnSe starts with Zn and finishes with Se leading to a Se-terminated surface. The thickness of the ZnSe epilayer is chosen to be 500 Å, which is below the critical thickness at which dislocations start to form.

Figure 1 shows a typical RHEED pattern observed after growth of ZnSe. The distance between the streaks corresponds to a (2x4) reconstruction.

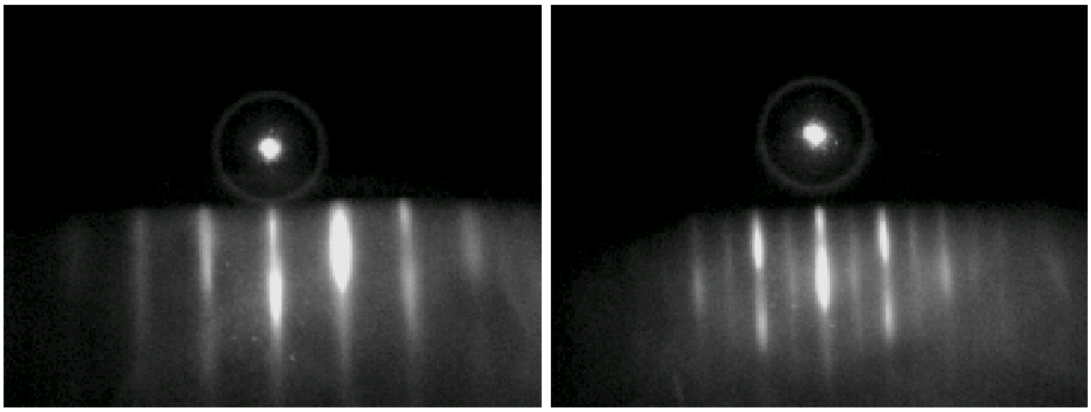

Fig. 1: RHEED pattern along the two [110] directions observed after growth of 500 Å ZnSe in ALE-mode on (001) GaAs.

After ZnSe growth the sample is cooled down to 150 °C and then transferred to the iron chamber via an UHV tunnel without breaking the vacuum. The iron chamber is equipped with an electron beam evaporation source due to the low vapor pressure of iron and the high source temperature required. For details see [1].

The iron layer is grown at a substrate temperature of 165 °C and with a growth rate of approximately 10 Å/min. The thicknesses of the iron films are in the range of 20 – 120 nm. After growth of iron RHEED patterns are taken still in UHV without the effects of oxidation. Then the iron samples, which are not covered with a capping layer, are exposed to air and oxidize. The films are characterized by SQUID measurements with the magnetic field applied along the [100] and [110] in-plane directions.

3. Results and Discussion

Figure 2 shows the results of SQUID measurements taken on a 60 nm thick Fe film on a ZnSe epilayer. There is a shift in horizontal direction due to an offset of the SQUID magnetometer. (Without offset the curves are symmetric with respect to the vertical axis.) For all measurements the magnetic field is applied in the plane of the Fe film.

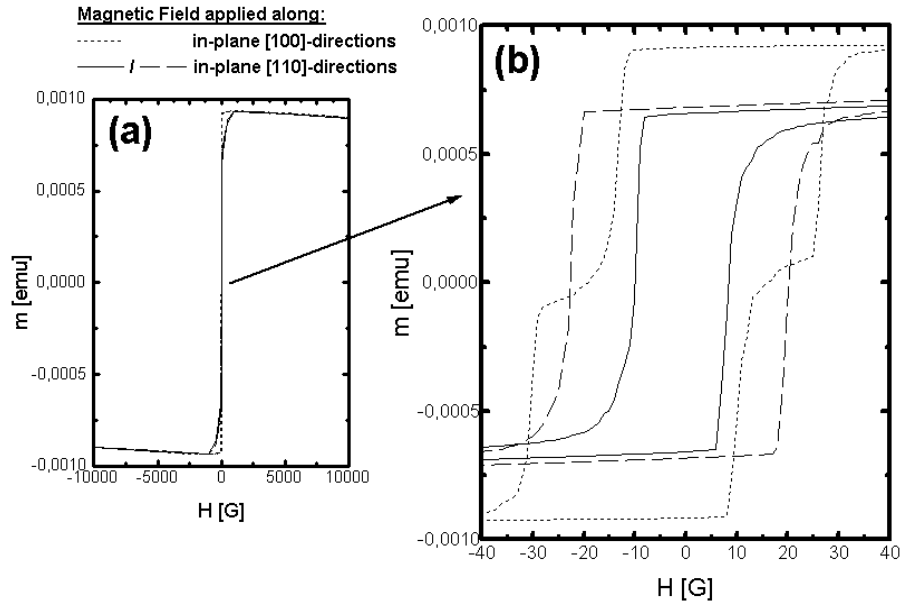

Fig. 2: Magnetic moment, m, versus applied magnetic field, H, obtained from SQUID measurements. (a) Iron film (60 nm thick) on a ZnSe epilayer; (b) magnification of (a) for low magnetic fields.

The curves of magnetization versus applied magnetic field indicate a saturation of magnetization at low magnetic fields (at 50 G and 750 G for the [100] and [110] direction, respectively). It is clearly visible that the [100] axis is the easy axis of magnetization while the [110] axis is the intermediate axis of magnetization as it is expected for a 60 nm thick film [3].

3.1 Magnetic Field Applied Along In-Plane [100] Directions

By taking a closer look at the magnetic behavior for low applied fields (see Fig. 2) we observe no rectangular hysteresis with one jump in magnetization, but a hysteresis containing two irreversible jumps of the magnetization when increasing/decreasing the magnetic field.

This behavior strongly depends on the thickness of the iron layer: For Fe films with a thickness between 20 and 30 nm we observe a hysteresis with only one jump, whereas the Fe films with a thickness between 60 and 120 nm show the two-jump-behavior.

This can qualitatively be explained by evaluating the energy density E of a magnetic thin film with the in-plane magnetization vector $\vec{M}$:

$$E = -\vec{M} \cdot \vec{H} + K_1 \cdot \left(\alpha_1^2 \alpha_2^2 + \alpha_2^2 \alpha_3^2 + \alpha_3^2 \alpha_1^2\right) + K_u \cdot \sin^2\theta$$

where $\vec{H}$ is the applied magnetic field, K_1 is the fourth-order cubic anisotropy, α_i are the direction cosines of the magnetization with respect to the cubic axes, K_u is a uniaxial in-plane second-order anisotropy, and θ is the angle between the magnetization and the in-plane [110] axis.

The ratio K_u/K_1 is crucial for determining the hysteresis. For the magnetic field applied along the [100] direction the hysteresis shows one jump for $|K_u/K_1| > 1$ (range (*1*)), two

jumps for $1 > |K_u/K_1| > 0{,}3$ (range (*2*)) and again one jump for $0{,}3 > |K_u/K_1|$ (range (*3*)) [4]. In range (*1*) the magnetic field, at which the irreversible jump in the magnetization occurs, decreases with decreasing ratio K_u/K_1. In range (*2*) the value of the magnetic field at the first jump increases and for the second jump decreases with decreasing ratio K_u/K_1.

The evolution of the hysteresis with film thickness for our samples exactly agrees with the behavior predicted by the model: Films with thicknesses of 20 and 30 nm show a hysteresis with one irreversible jump of the magnetization with decreasing jump-field for increasing film thickness, whereas films with thicknesses of 60 and 120 nm show two jumps in the hysteresis. By assuming a decreasing ratio K_u / K_1 with increasing film thickness the fields for the jumps behave according to the model described above. Apparently the ratio K_u/K_1 is larger than 1 for Fe films between 20 nm and 30 nm thick while for the thicker films (60 – 120 nm) K_u/K_1 is between 0,3 and 1.

From this thickness behavior we conclude that the uniaxial anisotropy resulting in the inequivalence of the two in-plane [110]-directions is induced by the interface. Another important fact must be mentioned: We observe hysteresis curves with two irreversible jumps only for the Fe films on a ZnSe epilayer, whereas the Fe films grown directly on GaAs show only one jump in the magnetization for the complete thickness range !

This behavior can be explained in the following manner: By deoxidizing the GaAs-substrate prior to growth of iron directly on GaAs, there is no specific background pressure. Therefore after deoxidation we find Ga- and As-dimers at the surface, which are oriented along the $[110]$ and $[\bar{1}10]$ directions [5].

On the contrary by the insertion of a ZnSe epilayer, deposited by atomic layer epitaxy as described in the previous section, we have a Se-terminated surface due to the finishing epitaxy step with the Se shutter open, where the Se-dimers are oriented along the $[\bar{1}10]$-direction [6].

For a (2x4)-reconstruction the dimer bond is parallel to the $[\bar{1}10]$-axis as a result of the orientation of the dangling bonds, and the (2x4)-surface has a pronounced rowlike structure along $[\bar{1}10]$ due to the missing Se-dimer rows. Therefore, the axis perpendicular to the missing dimer rows, which characterize the surface reconstruction of the ZnSe, is an easy axis, whereas the axis parallel to the missing dimer rows is a hard one [5]. Due to the (2x4) surface reconstruction the two in-plane [110]-directions become inequivalent, expressed by the last term in Eq. 1 where θ is the angle between the magnetization and the [110] direction.

The uniaxial anisotropy originates in the interface between ZnSe and Fe and decreases with increasing film thickness, whereas the cubic anisotropy due to the crystal stays is independent of the film thickness. This leads to a decreasing ration K_u/K_1 with increasing film thickness, which has also qualitatively been determined from the evolution of the hysteresis curves.

3.2 Magnetic Field Applied Along In-Plane [110]-Directions

By comparing the hysteresis curves for the magnetic field applied along the two [110] in-plane directions (see Fig. 2), we notice that the magnetic fields of the irreversible jump of the magnetization are different for the two [110] directions by a factor of ap-

proximately 2.4. This also clearly indicates that one of the two in-plane [110] directions is an easy axis for the magnetization, while the other one is a hard axis. This confirms the discussion given above.

In summary there are two contributions determining the hardness of the different in-plane axes: The cubic anisotropy, which distinguishes the [100] (easy) from the [110] (hard) axis, and the uniaxial axis, which leads to the inequivalence of the $[110]$ and the $[\bar{1}10]$ axis. These two contributions combine in a way as theoretically predicted in [7].

4. Conclusion

In summary we have presented (001) iron films with different thicknesses deposited both directly on GaAs as well as on ZnSe epilayers. While the iron films on GaAs show a rectangular hysteresis in the M versus H curves (magnetic field parallel [100]) with one irreversible jump of the magnetization for the whole thickness range, the iron films on the ZnSe epilayer exhibit a different magnetic behavior: The hystereses of thin films (20 – 30 nm) contain only one irreversible jump, but thicker films (60 – 120 nm) lead to hysteresis curves with two irreversible jumps.

This behavior originates in the Fe – ZnSe interface. The ZnSe epilayers are grown by atomic layer epitaxy, where the Se-terminated surface contains a rowlike composition of dimers resulting in inequivalence of the two [110] in-plane directions.

Measurements of M versus H curves with the magnetic field applied along the in-plane [110]-directions are in agreement with the results of the [100]-measurements.

References

[1] K. Bierleutgeb, H. Sitter, H. Krenn, and H. Seyringer: *Phys. Status Solidi B,* 220, 2000, 41.

[2] H. Sitter, and W. Faschinger: *Thin Solid Films* 225, 1993, p. 250.

[3] J. J. Krebs, F. J. Rachford, P. Lubitz, and G. A. Prinz: *J. Appl. Phys.* 53, 1982, p. 8058.

[4] C. Daboo, R. J. Hicken, D. E. P. Eley, M. Gester, S. J. Gray, A. J. R. Ives, and J. A. C. Bland: *J. Appl. Phys.* 75, 1994, p. 5586.

[5] E. M. Kneedler, B. T. Jonker, P. M. Thibado, R. J. Wagner, B. V. Shanabrook, and L. J. Whitman: *Phys. Rev. B* 56,1997, p. 8163

[6] A. Ohtake, T, Hanada, T. Yasuda, K. Arai, and T. Yao: *Phys. Rev. B* 60,1999, p. 8326.

[7] C. Daboo, R. J. Hicken, E. Gu, M. Gester, S. J. Gray, D. E. P. Eley, E. Ahmad, and J. A. C. Bland: *Phys. Rev. B* 51, 1995, p. 15964.